



HAL
open science

Mémoire d'Habilitation à Diriger des Recherches Sorbonne Université

Slavica Stankic

► **To cite this version:**

Slavica Stankic. Mémoire d'Habilitation à Diriger des Recherches Sorbonne Université. Chemical Sciences. Sorbonne Université, 2020. tel-03952647

HAL Id: tel-03952647

<https://hal.science/tel-03952647>

Submitted on 23 Jan 2023

HAL is a multi-disciplinary open access archive for the deposit and dissemination of scientific research documents, whether they are published or not. The documents may come from teaching and research institutions in France or abroad, or from public or private research centers.

L'archive ouverte pluridisciplinaire **HAL**, est destinée au dépôt et à la diffusion de documents scientifiques de niveau recherche, publiés ou non, émanant des établissements d'enseignement et de recherche français ou étrangers, des laboratoires publics ou privés.



Mémoire d'Habilitation à Diriger des Recherches Sorbonne Université

Presented by Slavica STANKIC

CNRS Research Associate (Chargée de Recherche, CNRS)

Institut des NanoSciences de Paris (INSP)

CNRS – (UMR 7588)

Metal oxide nanoparticles as model systems for surface science studies

Defense on December 10, 2020, Paris

Committee:

Xavier Carrier	Examiner
Eric Gaigneaux	Reviewer
Stéphane Jobic	Reviewer
Jacques Jupille	Examiner
Maria Cristina Paganini	Reviewer

TABLE OF CONTENTS

1 Curriculum Vitae	1
Personal data.....	1
Professional experience	1
Education.....	2
1.1 Scientific output.....	2
Publications in international peer-reviewed journals	2
Conferences/ Workshops /Seminars.....	5
Reports for peer reviewed journals or scientific projects	10
1.2 Conference organization	10
1.3 Teaching activity.....	11
1.4 Supervision of students	11
1.5 Participations in projects.....	14
1.6 Staying abroad.....	14
1.7 Collaborations.....	15
2 General introduction.....	16
3 Metaloxide nanoparticles.....	19
3.1 Formation of metal oxide nanoparticles.....	22
3.1.1 Pure metal oxides nanoparticles: MgO as a model system.....	22
3.1.2 Supported noble metal nanoparticles.....	34
3.1.3 Mixed metal oxide (MMOx) nanoparticles	40
3.2 Surfaces of metal oxide nanoparticles	47
3.2.1 Interaction of metal oxide surfaces with probe molecules	49
3.2.2 Interaction of metal oxide surfaces with photons.....	59
3.2.3 Interaction of metal oxide surfaces with photons and surface probe molecules simultaneously.....	63
3.3 Point defects	67
3.3.1 ZnO smoke: Point defects at different processing stages	70
3.3.2 Point defects in ZnO nanopowders in function of synthesis conditions.....	75
3.4 Metal oxide nanoparticles for antimicrobial purposes	81
3.4.1. Metal oxide nanoparticle in aqueous solution	82
3.4.2 Antibacterial activity vs. toxicity of metal oxide nanoparticles	86
4 Summary and perspectives.....	90
Bibliography	100
Annexed articles	110

Curriculum vitae

Personal data

Nationality: Austrian	Slavica STANKIC	stankic@insp.jussieu.fr
Married	CNRS Research Associate	phone: (33) 144274650
Birthdate: October 24th 1974		fax: (33) 144274650
in Baden, Austria		

Professional experience

2007 – **CNRS Research Associate (CR1)**, CNRS, Paris Institute of Nanosciences (INSP), working group Oxides in Low Dimensions.

2005 – 2007 **Post.doc**, Institute of Materials Chemistry, Vienna University of Technology (working group Prof. O. Diwald).

2001 – 2005 **Ph.D Thesis**, Institute of Materials Chemistry, Vienna University of Technology (working group Prof. E. Knoezinger).

2000 – 2001 **Industrial Project**, Institute for Applied Inorganic Chemistry, Vienna University of Technology (working group Prof. U. Schubert).

Education

2001 – 2005 **Ph.D Thesis:** *Light-induced surface processes on MgO and MgO-based nanocrystals*. Supervisor: Prof. Erich Knoezinger, Institute of Materials Chemistry, Vienna University of Technology, Austria.

2000 **Master Thesis:** *Isolation and characterization of Co(II)-complexes*. Supervisor: Prof. Sofija Sovilj, Faculty of Chemistry University of Belgrade, Serbia, Yugoslavia.

1993 – 1999 **Faculty of Chemistry**, University of Belgrade, Serbia, Yugoslavia.

1993 **High school**, option math/physic, Bosnia-Herzegovina, Yugoslavia.

Scientific output 1.1

Publications in international peer-reviewed journals

1. M. Sterrer, T. Berger, S. Stankic, O. Diwald, E. Knözinger: "*Spectroscopic Properties of Trapped Electrons on the Surface of MgO Nanoparticles*"; *ChemPhysChem*, 5 (2004), 1695.
2. T. Berger, M. Sterrer, S. Stankic, J. Bernardi, O. Diwald, E. Knözinger: "*Trapping of photogenerated charges in oxide nanoparticles*"; *Materials Science & Engineering C - Biomimetic and Supramolecular Systems*, 25 (2005), 5-8, 664.
3. S. Stankic, M. Müller, O. Diwald, M. Sterrer, E. Knözinger, J. Bernardi: "*Size-Dependent Optical Properties of MgO Nanocubes*"; *Angewandte Chemie - International Edition*, 44 (2005), 4917.
4. S. Stankic, M. Sterrer, P Hofmann, J. Bernardi, O. Diwald, E. Knözinger: "*Novel optical properties of Ca(2+)-doped MgO nanocrystals*"; *Nano Letters*, 5 (2005), 10, 1889.
5. S. Stankic, J. Bernardi, O. Diwald, E. Knözinger: "*Optical surface properties and morphology of MgO and CaO Nanocrystals*"; *Journal of Physics and Chemistry B*, 110 (2006), 13866.

6. M. Müller, S. Stankic, O. Diwald, E. Knözinger, P. Sushko, P. Trevisanutto, A. Shluger: "*Effect of protons on the optical properties of oxide nanostructures*"; Journal of the American Chemical Society, 129 (2007), 12491.
7. S. Stankic, J. Bernardi, O. Diwald, E. Knözinger: "*Photoexcitation of local surface structures on Strontium oxide grains*"; Journal of Physical Chemistry C, 111 (2007), 8069.
8. M. Müller, A. Sternig, S. Stankic, M. Stöger-Pollach, J. Bernardi, E. Knözinger, O. Diwald: "*Nanoparticles as a support: CaO deposits on MgO cubes*", Journal of Physical Chemistry C 112(25) (2008), 9120.
9. K. Beck, A. Joly, O. Diwald, S. Stankic, P. Trevisanutto, P. Sushko, A. Shluger, W. Hess: "*Energy and site selectivity in O-atom photodesorption from nanostructured MgO*"; Surface Science, 602 (2008), 1968.
10. Riss, T. Berger, S. Stankic, J. Bernardi, E. Knözinger, O. Diwald: "*Charge Separation in layered Titanate Nanostructures: Effect of Ion Exchange induced Morphology Transformation*"; Angewandte Chemie - International Edition, 47 (2008), 1496.
11. Sternig, S. Stankic, M. Müller, J. Bernardi, E. Knözinger, O. Diwald: "*Photoluminescent nanoparticle surfaces: the potential of alkaline earth oxides for optical applications*"; Advanced Materials, 20 (2008), 4840.
12. Stankic, Slavica; Sternig, Andreas; Finocchi, Fabio; Bernardi, Johannes; Diwald, Oliver: "*Zinc oxide scaffolds on MgO nanocubes*"; Nanotechnology, 21(35) (2010), 355603.
13. P. V. Sushko, K. P. McKenna, D. Muñoz Ramo, A. L. Shluger, A. Sternig, S. Stankic, M. Müller, and O. Diwald: "*Photoluminescence Properties of Alkaline-Earth Oxide Nanoparticles*", ECS Transactions 28(3) (2010) 67.
14. Slavica Stankic, Maeva Cottura, Dominique Demaille, Claudine Noguera and Jacques Jupille: "*Nucleation and growth concepts applied to the formation of a stoichiometric compound in a gas phase: The case of MgO smoke*"; Journal of Crystal Growth, 329(1) (2011), 52.
15. Andreas Sternig, Slavica Stankic, Markus Müller, Nicolas Siedl and Oliver Diwald: "*Surface exciton separation in photoexcited MgO nanocube powders*"; Nanoscale, 4 (23) (2012), 7494.
16. Slavica Stankic, Robinson Cortes-Huerto, Nicoleta Crivat, Dominique Demaille, Jacek Goniakowski and Jacques Jupille: "*Equilibrium shape of supported silver clusters*"; Nanoscale, 5 (2013), 2448.
17. Jasmina Vidic, Slavica Stankic, Francia Haque, Danica Ciric, Ronan Le Goffic, Aurore Vidy, Jacques Jupille and Bernard Delmas: "*Selective antibacterial effects of mixed ZnMgO nanoparticles*"; J Nanopart Res 15 (2013), 1595.

18. Jasmina Vidic, Francia Haque, Jean Michel Guigner, Aurore Vidy, Christophe Chevalier and Slavica Stankic: “*Stability of ZnMgO nanoparticles in different biological media*”; Langmuir 30 (2014), 11366.
19. Stefan O. Baumann, Johannes Schneider, Andreas Sternig, Daniel Thomele, Slavica Stankic, Thomas Berger, Henrik Grönbeck, and Oliver Diwald: “*Size Effects in MgO Cube Dissolution*” Langmuir 31 (2015), 2770.
20. Slavica Stankic, Sneha Suman, Francia Haque and Jasmina Vidic: “*Pure and multi metal oxide nanoparticles: synthesis, antibacterial and cytotoxic properties*”, J. of Nanobiotechnology 14 (2016), 73.
21. Francia Haque, Stephane Chenot, Francesc Vines, Francesc Illas, Slavica Stankic and Jacques Jupille: “*ZnO powders as multi-facet single crystals*”; Physical Chemistry Chemical Physics, 19 (2017), 10622.
22. Sandrine Auger, Céline Henry, Christine Péchoux, Sneha Suman, Nathalie Lejal, Nicolas Bertho, Thibaut Larcher, Slavica Stankic, Jasmina Vidic: “*Exploring multiple effects of Zn_{0.15}Mg_{0.85}O nanoparticles on Bacillus subtilis and macrophages*”, Scientific Reports, 8 (2018), 12276.
23. Francia Haque, Fabio Finocchi, Stephane Chenot, Jacques Jupille and Slavica Stankic: “*Towards a comprehensive understanding of heterolytic splitting of H₂ at MgO surface defects: site reactivity, proximity effects and co-adsorption of several molecules*”, JPC C, 122 (2018), 17738.
24. Fabio Finocchi, Francia Haque, Stéphane Chenot, Jacques Jupille and Slavica Stankic: “*Water dissociation on the low-coordinated sites of MgO nanopowders*”, J. Mater. Research, 2019, 408.
25. Miao Zhang, Frederic Aversang, Francia Haque, Patrizia Boghetti, Jean-Marc Craft, Guylene Costentin and Slavica Stankic: “*Defect-related multicolor emissions in ZnO tetrapods: from violet, over green to yellow*”, Nanoscale, 11 (2019), 5102.
26. Selwin Hageraats, Katrien Keunea, Slavica Stankic, Stefan Stanescu, Moniek Tromp and Mathieu Thoury: “*X-ray Nanospectroscopy Reveals Binary Defect Populations in Submicrometric ZnO Crystallites*”, JPC C, 124(23) (2020), 12596.
27. Miao Zhang, Frederic Aversang, Jean-Marc Craft, Patrizia Borghetti, Guylene Costentin and Slavica Stankic: “*Controlled Formation of Native Defects in Ultrapure ZnO for the Assignment of Green Emissions to Oxygen Vacancies*”, JPC C, 124 (23) (2020), 12696.
28. Fabio Finocchi, Francia Haque, Stéphane Chenot, Jacques Jupille, Oliver Diwald and Slavica Stankic: “*Probing site-specific reactivity at MgO surface by Zn²⁺ substitution*”, PCCP, (2020), in submission.

ORAL PRESENTATIONS

S. Stankic, M. Müller, M. Sterrer, J. Bernardi, O. Diwald, E. Knözinger:
"Particle size-dependent optical properties of MgO nanocubes";
Bunsentagung, **2005**, Frankfurt am Main, Germany.

S. Stankic, M. Müller, M. Sterrer, O. Diwald, E. Knözinger:
"Light induced surface processes on MgO and MgO based nanocrystals";
nanoSMat05, **2005**, Aveiro, Portugal.

S. Stankic, M. Müller, M. Sterrer, J. Bernardi, O. Diwald, E. Knözinger:
"Oberflächen-Funktionalisierung von MgO Nanoteilchen";
11. Österreichische Chemietage, **2005**, Leoben, Austria.

S. Stankic, T. Berger, O. Diwald, J. Bernardi, E. Knözinger:
"Manipulation of chemical and optical properties of MgO nanocubes via surface functionalization";
E-MRS Fall Meeting, **2006**, Warsaw, Poland.

S. Stankic, J. Bernardi, O. Diwald, E. Knözinger:
"Zn(x)Mg(1-x)O nanocubes: admixung semiconducting to insulating materials";
106. Bunsentagung, Heterogene Neuartige Kohlenstoffstrukturen", **2007**, Graz, Austria.

S. Stankic, O. Diwald, J. Bernardi, E. Knözinger:
"Manipulation of chemical and optical properties of MgO nanocubes via surface functionalization";
17th International Vacuum Congress (IVC-17): "International Conference on Nanoscience and Technology", **2007**, Stockholm, Sweden.

S. Stankic, A. Sternig, J. Bernardi, F. Finocci, E. Knözinger, O. Diwald:
"Structure and spectroscopic properties of Zn(2+)-doped MgO nanocubes";
CERC3-YCW, **2008**, Vienna, Austria (invited).

A. Sternig, M. Müller, S. Stankic, J. Bernardi, E. Knözinger, O. Diwald:
"Photoluminescent Oxide Particle Surfaces: about the Potential of Alkaline Earth Oxides for optical Applications";
COST D41, Annual Meeting of WG1, **2008**, Paris, France.

M. Müller, S. Stankic, E. Knözinger, O. Diwald, P. Sushko, P. Trevisanutto, A. Shluger:
"Effects of protons on the optical properties of oxide nanostructures";
Bunsentagung, **2008**, Saarbrücken, Germany.

O. Diwald, A. Sternig, M. Müller, S. Stankic, J. Bernardi, E. Knözinger:
"Photoluminescent Nanoparticle Surfaces";
International Conference on Electronic Materials, **2008**, Sydney, NSW, Australia.

O. Diwald, A. Sternig, M. Müller, S. Stankic, J. Bernardi:
"Photoluminescent nanoparticle surfaces: the potential of alkaline earth oxides for optical applications";
SAMIC International: From molecules to nanosystems, **2008**, Commune di Bressanone, Italy.

P. McKenna, P. Sushko, A. Shluger, A. Sternig, S. Stankic, M. Müller, E. Knözinger, O. Diwald:
"Tuning the electronic properties of oxide nanoparticles by surface doping: experimental and theoretical studies of Ca-, Sr-, and Ba-doped MgO";
COST D41, Annual Meeting, **2008**, Barcelona, Spain.

S. Stankic, A. Sternig, J. Bernardi, F. Finochi, E. Knözinger, O. Diwald:
"Zn(x)Mg(1-x)O cubes: structure and spectroscopic surface properties";
COST D41, Annual Meeting, **2008**, Barcelona, Spain.

S. Stankic, A. Sternig, J. Bernardi, F. Finochi, E. Knözinger, O. Diwald:
"Zn(x)Mg(1-x)O Surfaces of MgO Nanocubes";
The 6th International Workshop on Oxide Surfaces (IWOX-VI), **2009**, Schladming, Austria.

A. Sternig, M. Müller, S. Stankic, J. Bernardi, E. Knözinger, O. Diwald:
"Photoluminescent nanoparticle surfaces: the potential of alkaline earth oxides for optical applications";
The 6th International Workshop on Oxide Surfaces (IWOX-VI), **2009**, Schladming, Austria.

F. Finochi, S. Stankic, A. Sternig, O. Diwald:
"Zn segregation and OH vibrations on mixed ZnMgO particles from ab initio calculations";
COST D41, Annual Meeting of the Working Group 1, **2009**, Erlangen, Germany.

A. Sternig, S. Stankic, J. Bernardi, F. Finochi, E. Knözinger, O. Diwald:
"Synthesis and spectroscopy on Zn(x)Mg(1-x)O nanocubes";
E-MRS Spring Meeting **2009**, Strasbourg, France.

A. Sternig, M. Müller, S. Stankic, J. Bernardi, E. Knözinger, O. Diwald:
"Photoluminescent Nanoparticle Surfaces: The Potential Of Alkaline Earth Oxides For Optical Applications"
13. Österreichische Chemietage, **2009**, Vienna, Austria.

A. Sternig, S. Stankic, E. Knözinger, J. Bernardi, F. Finochi, O. Diwald:
"Synthesis and spectroscopy of Zn(x)Mg(1-x)O nanocubes"
13. Österreichische Chemietage, **2009**, Vienna, Austria.

S. Stankic, M. Cottura and J. Jupille:
"Smoke MgO: particles size decrease"
5th NANOSMAT, **2010**, Reims, France.

S. Stankic, N. Crivat, J. Jupille, A. Sternig and O. Diwald:
"Gold nanoparticles supported on smoke MgO"
COST D41, Annual Meeting, **2010**, Torino, Italy.

S. Stankic, R. Cortes, D. Demaille, J. Goniakowski, J. Jupille:
“*MgO nanocubes: ideal system for morphology control and epitaxial growth of Ag nanoparticles*”
XI International conference on nanostructured materials, **2012**, Rhodes, Greece.

Jasmina Vidic, Slavica Stankic, Danica Ciric, Francia Haque, Jacques Jupille, Bernard Delmas:
“*ZnMgO nanoparticles: Are they good antibacterial agents?*”
XI International conference on nanostructured materials, **2012**, Rhodes, Greece.

Slavica Stankic, Robinson Cortes-Huerto, Jacek Goniakowski and Jacques Jupille:
“*Equilibrium shape of supported silver clusters*”,
4th IC4N-2013: International Conference from Nanoparticles and Nanomaterials to Nanodevices and Nanosystems, **2013**, Corfu, Greece.

Slavica Stankic, Robinson Cortes-Huerto, Arianna Minelli, Dominique Demaille, Jacek Goniakowski and Jacques Jupille:
“*Equilibrium shape of supported silver clusters*”;
CMST COST Action CM1104, WG1/WG3 Meeting, **2013**, Vienna, Austria.

Slavica Stankic:
“*Controlling defects in ZnO nanoparticles*”;
International summer workshop “NANOSCIENCE meets METROLOGY”, **2015**, Erice, Italy.

Slavica Stankic:
“*ZnO nano-smoke: defects and colors*”;
6th international conference on NANOstructures and nanomaterials SELF-Assembly, **2016**, Giardini Naxos, Italy.

Zhang Miao, Frederic Averseng, Guylene Costentin and Slavica Stankic:
“*Point defects in ZnO nanopowders*”;
12th International Workshop on Oxide Surfaces (IWOX-XII), **2020**, Lake Placid, NY USA.

INVITED TALKS

“*Metal oxide nanoparticles: playing with size, shape and surface composition*”;
1er colloque scientifique Franco-Serbe, **2012**, Paris, France.

“*Reactive surface sites at metal oxide nanoparticles: from fundamental studies to potential medical application*”;
4th International Conference on Physical and Theoretical Chemistry, **2017**, Dublin, Ireland.

“*Probing surfaces and defects of MgO and ZnO nanoparticles*”;
IUVESTA-ASEVA Workshop, Nanoscale Oxide Systems in Physics and Chemistry, **2018**, Ávila, Spain.

POSTERS

“Novel Surface Properties of Ca Doped MgO Nanoparticles”;
7th Pannonian International Symposium on Catalysis“, **2004**, Srni, Check Republic.

“Oberflächen-Funktionalisierung von MgO Nanoteilchen durch Ca Dotierung“;
38. Jahrestreffen Deutscher Katalytiker, **2005**, Weimar, Germany.

“Chemical and Physical functionalization of MgO nanocubes”;
COST D 19 meeting 2005, **2005**, Torino, Italy.

“Surface functionalization of MgO nanocrystals”;
1st Workshop of COST Action D 41, Inorganic Oxides: Surfaces and Interfaces, **2006**, Vienna, Austria.

“Thermal stability and optical properties of alkaline earth oxide nanoparticle powders”;
107. Bunsentagung, **2008**, Saarbrücken, Germany.

“Optical surface properties of alkaline earth oxide nanoparticles”;
E-MRS 2008, spring meeting, **2008**, Strasbourg, France.

“Thermal Stability and optical Properties of Alkaline Earth Oxide Nanoparticle Powders”;
COST D41, Annual Meeting of WG1, **2008**, Paris, France.

“Photoluminescent nanoparticle surfaces: the potential of alkaline earth oxides for optical applications”;
Bunsentagung, **2009**, Köln, Germany.

“Looking at steps of MgO smoke surfaces in different environments”;
Winter school COST-D41, **2009**, Berlin, Germany.

“Adsorbed and incorporated Ba(2+) ions at MgO nanoparticle surfaces”;
COST D41, Annual Meeting of the Working Group 1, **2009**, Erlangen, Germany.

“Hydrated steps on MgO: smokes versus Ag-supported ultra-thin films”;
COST D41, General Meeting, **2009**, Paris, France.

“Size and Shape Control of Smoke Metal Oxide Nanoparticles”;
COST D41, Annual Meeting of the Working Group 1, **2010**, Munich, Germany.

“Effect of hydrogen on ZnO nanoparticles”;
CMST COST Action CM1104, WG1/WG3 Meeting, **2013**, Vienna, Austria.

“Equilibrium shape of supported silver clusters”;
International summer workshop “NANOSCIENCE meets METROLOGY”, **2015**, Erice, Italy.

“Oxide nanocrystallites with facets of controlled orientation”;
International summer workshop “NANOSCIENCE meets METROLOGY”, **2015**, Erice, Italy.

“Defects in ZnO nano-smoke: a combined structural and spectroscopic study”;
Concluding meeting COST Action CM1104, **2016**, Osnabrück, Germany.

“MgO and ZnO nanoparticles: model systems for probing surface reactivity and crystal defects”;
34e Journées Surfaces et Interfaces, **2020**, Paris, France.

INVITED SEMINARS

“Optical properties of pure and mixed alkaline earth oxides obtained via chemical vapour deposition”;
Polish Chemical Society, Szczecin, Poland, **2006**.

“Optical surface properties of pure and mixed alkaline-earth oxides”;
Seminario Chimica IFM Torino, Italy, Dipartimento di Chimica Inorganica Fisica e dei Materiali, Torino, Italy, **2007**.

“Pure and modified surfaces of MgO Nanocubes”;
Department of Chemical Sciences of the University of Padova, Italy, **2008**.

“Metal oxide nanoparticles: Control of size, shape and surface characteristics”;
INMETRO, Instituto Nacional de Metrologia Normalização e Qualidade Industrial-RJ, UFRJ, Univ. Federal do Rio de Janeiro, Brazil, **2009**.

“Metal oxide nanoparticles: size, shape and surface modification”;
Christopher Ingold Laboratories, Department of Chemistry, University College London, England, **2012**.

“Nanostructured metal oxides”;
Virologie et Immunologie Moléculaires, Institut de la Recherche Agronomique, Jouy en Josas, France, **2013**.

“Pure and mixed metal oxide nanoparticles obtained via gas-phase reactions”;
Laboratoire de Réactivité de Surface, Ivry, France, **2013**.

“Reactive surface sites at metal oxide nanoparticles: from fundamental studies to potential medical application”;
Department of Chemical Dynamics, VINCA Institut of Nuclear Sciences-National Institute of the Republic of Serbia, Belgrade, **2016**.

Journals: Journal of Solid State Chemistry, Journal of Physical Chemistry, Langmuir, Chem. Phys. Lett., Electrochemical and Solid-State Letters, ACS Applied Materials & Interfaces, Journal of Crystal Growth, Crystal Growth & Design, Nanotechnology, RSC Advances, Nanobiotechnology, Optical Materials.

International projects: OPUS 14 (Polish government agency of National Science Centre), REPRISE (Italian Ministry of Education, Universities and Research).

Conference organization 1.2

1st Workshop of COST Action D 41, Inorganic Oxides: Surfaces and Interfaces, Vienna, Austria, November **2006**.

Annual Meeting of WG1, COST D41, Inorganic Oxides: Surfaces and Interfaces, Paris, France, **2008**.

1er colloque scientifique Franco-Serbe, Paris, France, Jun **2012**.

Contribution to Fête de la science

Campus Boucicaut, INSP, **2010**,

Workshop n°1: *La diversité des oxydes – petite manip' avec des cubes d'oxydes*.

Campus Jussieu, **2011**,

Workshop n°4: *L'interaction entre lumière et matière*.

Campus Jussieu, **2013**.

Demonstration for school groups: *Les oxydes métalliques à l'échelle nano*.

Campus Jussieu: on annual basis since **2014**,

Demonstration for school groups and public visitors:

Nanoparticules: petites mais puissantes

Teaching activity 1.3

From 2009 to 2013 I was a member and a coordinator of the experimental project (for international Master program, NANOMAT: nanoscience and materials science) that is a part of the Sorbonne University's Master of Physics and Applications. Four weeks of experimental work (travaux pratiques) entitled:

2009: "High pressure structural transition of ZnO"

2010: "IR on MgO powder"

2011: "Optical properties of ZnO nanoparticles influenced by hydrogen"

2012: "Hydrogen passivation effect on ZnO powder"

2013: "Synthesis and Optical characterization of morphologically different ZnO nanopowders and their interaction with hydrogen"

Evaluation of written report and oral presentation. Contribution in the final exam.

Supervision 1.4

Invited researchers

- (2012) Ph.D Student: Chiara Gionco
 - Università di Torino, Dipartimento di Chimica IFM
 - Starting date: 27/10 Finishing date: 25/11

- (2013) Ph.D Student: Chiara Gionco
 - Università di Torino, Dipartimento di Chimica IFM
 - Starting date: 21/05 Finishing date: 08/06

- (2015) Ph.D Student: Chiara Gionco
 - Università di Torino, Dipartimento di Chimica IFM
 - Starting date: 27/04 Finishing date: 15/05

- (2018) Research Assistant: Natasa Terzic
- University of Belgrade, Department of Chemistry
 - Starting date: 30/10 Finishing date: 20/11

Ph.D students

- Ph.D co-director (2012-2015) Student: Francia Haque
- Title: *Réactivité de nanoparticules d'oxydes d'orientations définies*
 - Starting date: 01/10/2012 Finishing date: 09/10/2015
 - Co-supervising, 50% with J. Jupille

- Ph.D co-director (2014-2017) Student: Miao Zhang
- Title: *Defects in ZnO nanoparticles obtained by gas-phase syntheses*
 - Starting date: 01/10/2014 Finishing date: 16/10/2017
 - Co-supervising, 50% with G. Costentin

Master students

- M1 (2008) Student: Maeva Cottura
- Title: *Etude des fumées de MgO par microscopie à force atomique*
 - 15/05/2008 - 17/06/2008
- M2 (2009) Student: Maeva Cottura
- Title: *Observation de la morphologie des fumées d'oxydes métalliques*
 - 09/02/2009 - 09/06/2009
- M2 (2010) Student: Nicoleta Alexandra Crivat
- Title: *Synthesis of Au/MgO nanocubes as model catalysts*
 - 02/02/2010 - 21/06/2010
- M2 (2012) Student: Francia Haque
- Title: *H₂ doping of ZnO nanoparticles*
 - 06/02/2010 - 29/06/2010

- M2 (2013) Student: Arianna Minelli
- Title: *Supported metallic nanoparticles*
 - 04/02/2013 - 28/06/2013
- M1 (2013) Student: Miao Zhang
- Title: *Comparing optical properties of a typical insulating metal oxide (MgO) and typical semiconducting metal oxide (ZnO) nanoparticles*
 - 28/10/2013 - 29/11/2013
- M1 (2014) Student: Meriem Kebaili
- Title: *Structure, morphologie et propriétés optiques des nanoparticules de $Zn_xMg_{1-x}O$ en fonction du rapport molaire Zn/Mg*
 - 27/05/2014 - 11/07/2014
- M2 (2014) Student: Miao Zhang
- Title: *ZnO nanoparticles: synthesized and studied under different experimental conditions*
 - 03/02/2015 - 20/06/2015
- M2 (2016) Student: Sneha Suman
- Title: *ZnO-based Nanoparticles as Potential Antibacterial Agents: Synthesis and Characterization*
 - 15/01/2016 - 15/06/2016
- M1 (2019) Student: Mohit Patil
- Title: *Interaction of MgO nanocubes with CO and CH₄ investigated by low temperature Infrared spectroscopy*
 - 12/05/2019 - 25/07/2019

Participations in projects 1.5

CNANO (**2007**), Coordinator: S. Stankic (INSP); Partner: Paul Dumas, Soleil. 50 k€

China Scholarship Council (CSC): CSC accepted my proposal for a 3-years financial support for Ph.D thesis of M. Zhang.

Programme de mobilité CHARPAK franco-Indien, (**2016**), Coordinator: S. Stankic (INSP) / J. Panwar (BITS, Pilani)

Programme de mobilité BIO ASIE (**2015-2017**), Coordinator: J. Vidic (INRA), Partners: M. M. Robert (Singapour), M. Angshuman Bagchi (Inde), S. Stankic (INSP)

Programme de mobilité PHC GALILEE **2017**, Coordinator: J. Vidic (INRA), Partners: M. Manzano (Italie), S.Stankic (INSP).

Staying abroad 1.6

17-25 April **2007**: Dipartimento di Chimica IFM, Università di Torino, Italia (group of Prof. Elio GIAMELLO). Short-term scientific mission with the reference code: COST-STSM-D41-02789.

20-31 July **2009**: Universidade Federal do Rio de Janeiro, UFRJ, Brazil (group of Prof. Carlos Alberto ACHETE).

18-24 July **2010**: Lehrstuhl für Feststoff- und Grenzflächenverfahrenstechnik Universität Erlangen-Nürnberg. Institute of Particle Technology (group of Prof. Oliver Diwald). Short-term scientific mission with the reference code: COST-STSM-D41-06025.

Collaborations 1.7

COST D19: Chemical Functionality Specific to the Nanometer Scale (2000-2006).

COST D41: Inorganic oxide surfaces and interfaces (2008-2012).

CMST COST Action CM1104: Reducible oxide chemistry, structure and functions. Working group 2: Synthesis and Characterization, (2012-2016).

Prof. O. Diwald, University of Salzburg, Department of Materials Science & Physics: continued collaboration after my PhD thesis but also in the framework of the COST network resulted in publishing many peer-reviewed manuscripts.

Dr. Guylène Costentin and Dr. Frédéric Averseng (Laboratoire de Réactivité de Surface): collaboration based on co-direction of PhD thesis (Miao Zhang) entitled: “Defects in ZnO nanoparticles obtained by gas-phase syntheses”. Based on this collaboration, two articles were published in peer-reviewed journals and several are in preparation.

Dr. J. Vidic, Institut de la Recherche Agronomique, Unité Virologie et Immunologie, Jouy en Josas, France. Collaboration established on a strong interdisciplinary crosslink between biological systems studied at INRA and fundamental physical chemistry of metal oxide nanoparticles, studied at INSP. The potential of metal oxide nanoparticles as antibacterial agents is studied in function of their toxicological effect. Based on this collaboration several manuscripts were published in peer-reviewed journals.

Prof. D. Opsenica and Dr. Natasa Terzic, Department of Chemistry, University of Belgrade. A recent collaboration established on the basis of a strong interdisciplinary crosslink between potential medical applications of metal oxide nanoparticles. Aimed at the synthesis, characterization and evaluation of biological activity of inorganic-organic hybrids (nano-MOx/organic molecules) a bilateral mobility proposal (Pavle Savic) is approved for two years (2020-2021) under the call within Campus France.

Synchrotron SOLEIL: A recent project that involves researchers from the Rijksmuseum Amsterdam and the local researchers from the HERMES line at the Synchrotron Soleil. The aim is to develop a methodology that is able to simultaneously characterize the defect chemistry and morphology of the sub-micrometric ZnO crystallites that constitute the zinc white pigment in paintings. The approach is based on using the scanning transmission X-ray microscopy in the soft X-ray regime.

2

General introduction

In order to obtain the accreditation to direct research (Habilitation à Diriger des Recherches – HDR) at the Sorbonne Université, this document aims to summarize my scientific output that I have done since receiving my PhD in 2005. Mainly, my research includes fundamental studies on model prototype oxides obtained in the form of nanoparticles. Firstly, this refers to mastering the control over particles size and shape, but in general it encompasses microscopic descriptions of oxide surfaces in terms of the coordination number, orientation, composition, reactivity and crystal defects. Finally, such fundamental approach is extended to potential application of metal oxide nanoparticles as antibacterial agents through studying their antimicrobial activity in parallel to cytotoxicity effects.

In October 2007, I joined the working group “Oxides in low dimensions” (INSP). The main focus of the group was (and still is) to study fundamental physical and chemical properties of metal oxides surfaces. Such research direction was rather well matching with my scientific background obtained within both Ph.D and during my post-doctoral studies. At the same time, the experimental part of the working group was mainly restricted to the scope of “classical” surface science studies. These imply ultra-high vacuum (UHV) conditions i.e. working pressures that are more than 10 orders of magnitude lower than those in real industrial processes (known as *pressure gap*) and, moreover, the use of ideal systems (often single crystal surfaces) which cannot represent well the complex structure of an industrially

supported catalyst i.e. a real system (known as *materials gap*). The strong concern of my scientific program was therefore to extend the concepts of the “classical” surface science to systems that are by far more frequently encountered under real conditions. In that context, an alternative was found in studying the highly dispersed forms of prototype model oxides such as MgO and ZnO, as well as their ternary mixtures ($Zn_xMg_{1-x}O$) – so that the second criterion was fulfilled. Considering the first criterion, some of the existing experimental equipment (FT IR spectrometer) was adapted to provide conditions from UHV to ambient.

For the purpose of synthesis, I have implemented two synthesis chambers in our working group: glove box for combustion (GBC) and chemical vapor synthesis (CVS) reactor. Fundamentally similar, the two synthesis techniques include oxidation of metals in the vapor phase. GBC is a static, closed system where the evaporation and oxidation reaction occur in the same spatial zone. The energy released within rather violent (exothermic) oxidation reaction serves then for further evaporation and affects the growth stage of crystals. As a result, metal oxide nanoparticles of exceptionally regular shapes can be achieved. Yet a significant drawbacks remain within this technique: a relatively high degree of inhomogeneity of the sample (in terms of both the size and shape) whereas in case of ternary oxides instead of mixing the phase separation occurs. In contrast, within the CVS reactor the reactions of evaporation and oxidation are spatially separated while the concentration of reactants in the vapor phase (both, metal atoms and O_2 -molecules) is considerably higher than in GBC. Consequently, the supersaturation occurs quickly which results in the formation of particles smaller than those obtained via GBC. In case of ternary oxides, the two metals are evaporated and mixed before their vapors reach oxygen occurs and, thus, the formation of solid solutions may occur within this approach and in line with the phase diagram of the two oxides foreseen to mix in a ternary compound.

For the purpose of adapting the existing FTIR spectrometer (BRUKER, Vertex 70) to function under UHV conditions, three homemade chambers, all affording a vacuum better than 10^{-9} mbar, were built and added. The first one serves for the introduction of the sample powder, the second allows the necessary thermal annealing and the third, analysis one provides for the introduction of gasses. At the very last stage, the UHV-FTIR setup was equipped also with a cryostat (added into the analysis chamber) which now allows for the adsorption measurements to be studied in a wide range of temperatures (300 K– 60 K).

The manuscript is divided into four parts. The *Chapter 1* is devoted to the administrative part and is followed by general introduction presented in the *Chapter 2*. An effort has been made to synthetically present the different research activities in the *Chapter 3*. This chapter encompasses the studies on pure and ternary metal oxide nanoparticles and covers diverse fields: concepts of nucleation and growth (3.1), the relationship between surface (atomistic) structure and reactivity (3.2) studies on point defects in ZnO nanocrystals (3.3) and an interdisciplinary research activity that combines the fundamental studies on ternary metal oxide nanoparticles with their potential biological activity (3.4). Finally, in *Chapter 4* I will briefly summarize the main research output and elaborate perspectives foreseen for the next couple of years.

Metal oxide nanoparticles

Metal oxides encompass a very heterogenic class of compounds and find applications in many fields of technical interest, from paint pigments and nonlinear optics to sensors and catalysis, as well as in medicine. This is due to the fact that they can be superconductors on the one hand and insulators on the other or the bonding character may be classified as covalent in some cases and highly ionic in other. Finally, when achieved in nano-size, the properties of oxides cover almost all aspects of material science. The properties of most materials are, indeed, intimately connected to the way in which they are ordered on the atomic scale [Brust, 2005]. Macroscopic systems can be accurately represented by the idealized model of an infinitely extended solid exhibiting a periodic arrangement of atoms or ions. However, this approximation usually breaks down in the case of small particles since the additional effects occur in the nano-regime. Nanomaterials are mostly categorized as those which have structured components with at least one dimension less than 100 nm and come in the form of thin films, nanoparticles, nanoporous materials, nanocomposites, and bulk nanocrystalline materials. The properties of nanometer-sized systems are significantly altered compared to their macroscopic analogs since the size of the system is limited. For instance, the mobility of charge carriers (electrons, electron – holes and excitons) is reduced and causes significant changes in electronic properties. Nanoparticles also often expose certain surface facets that are neither predicted by the Wulff construction, nor observed in macroscopic crystals [Feldho

2007]. This is nicely illustrated on nano TiO₂-anatase that is quite different from classical macroscopic anatase. The later one is a tetragonal bipyramid and exhibits more than 95% of its surface as eight facets of the type (101) and may be truncated by two (001) type facets at the tips [Lazzeri 2001; Lazzeri 2002]. Facets of the type (101) and (001), which are widely assumed to make up the majority of exposed facets on anatase surfaces, were found to be in the minority in nanoparticles. Instead, surfaces of powder nanoparticles are rather dominated by facets of the type (100) or (111), and they show also (110), (112), (102), (103), (104), (106), and (108) facets, depending on the particle shape. Finally, the surface to volume ratio is dramatically enhanced in nanosystems and the considerable amount of atoms at the surface influence the entire particle. The presence of a high quantity of low coordinated surface sites becomes responsible for their outstanding activity and the interaction between the surface and the surrounding media becomes a dominant factor to determine the characteristics of nanoparticles. Nevertheless, the occurrence of active surface characteristics in nanoparticles – low-coordinated surface sites, such as corners and edges – is not only determined by particle's size, but it is moreover intimately connected with its morphology. The synthesis of nanoparticles of desired shape and size via easy synthetic routes became, therefore, the most important issue in the growth of nanoparticles.

This Chapter is organized as follows. Formation of nanoparticles will be presented in 3.1. Fundamental issues concerning the nucleation and growth concepts will be discussed on the model system, MgO (3.1.1). Studies devoted to the growth of metallic nanoclusters on metal oxide support will be presented on the Ag/nano-MgO system (3.1.2). This is followed by the issues concerning synthesis of mixed metal oxide nanoparticles (3.1.3). In Chapter 3.2, the surfaces of metal oxide nanoparticles will be discussed in context of their reactivity towards site selective probe molecules, such as H₂ or H₂O, in 3.2.1 or towards the light in 3.2.2. A simultaneous interaction of metal oxide surfaces with photons and surface probe molecules is

presented in 3.2.3. A research related to point defects in metal oxides – studied on model ZnO nanoparticles – will be presented in Chapter 3.3 whereas the last Chapter 3.4 is devoted to studies involving reactions of metal oxide nanoparticles with living organisms – bacteria and human cells – foreseen as their potential use in antibacterial applications.

Formation of metal oxide nanoparticles 3.1

3.1.1 Pure metal oxides nanoparticles: MgO as a model system

To obtain materials with specific physicochemical properties through a control of their size, crystallinity, surface composition and morphology represents a challenge in synthesis of nanomaterials [Daniel 2004, Cushing 2004, Oberdorster 2005]. During the three past decades, new synthetic routes have been developed, and some previous refined, to enable the precise control of these materials characteristics. Nanoparticles can be formed through either the breaking down of larger particles to generate the required nanostructures from them (top down approach i.e. *physical manipulation*) or by controlled assembly processes when single atoms and molecules are integrated into larger nanostructures (bottom up approach i.e. *chemical transformation*). The associated processes usually occur in the solid, aerosol, liquid or in the gas phase. Regarding the synthesis of metal oxide nanoparticles, the medium in which the oxidation reaction takes place is mainly liquid or gaseous. Wet-chemistry syntheses include precipitation of nanoparticles from a solution of chemical compounds. A number of specific methods have been developed and the examples among those that are broadly in use are the following: sol-gel, co-precipitation, (hydro)solvothermal, microwave-assisted, etc. In vapor phase based synthesis the precursors can come in any of the three aggregate states (liquid, solid or vapor) while the association of building units occurs exclusively in the gas phase. The most representative methods are spray pyrolysis, combustion and chemical vapor synthesis.

The effect of the type of the synthesis on materials size, shape and crystal structure can be nicely illustrated on the example of a ternary oxide synthesized in our Lab at the INSP, the

ZnMgO. In Figure 3.1. TEM images and schematic illustrations are presented for its nanoparticles produced via chemical vapor synthesis [Stankic 2010], metal combustion [Vidic 2013; Vidic 2014] and sol-gel [not published]. A uniform size and shape, along with only one a rock salt crystal phase, was observed when these particles were fabricated via CVS. The segregation of Zn into surface and, more specifically, a diffusion into corners and edges of MgO cubes was therefore confirmed by DFT calculations. In contrast, no mixing could be achieved by the GBC synthesis (combustion of Zn/Mg alloy in air at atmospheric pressure) since two types of particle shapes, typical of both ZnO and MgO, could be seen already in TEM images. Besides, analysis of XRD patterns confirmed the phase separation. Similarly to CVS, ZnMgO nanoparticles obtained by wet-chemistry route, a sol-gel, revealed more uniformity in terms of the size and shape.

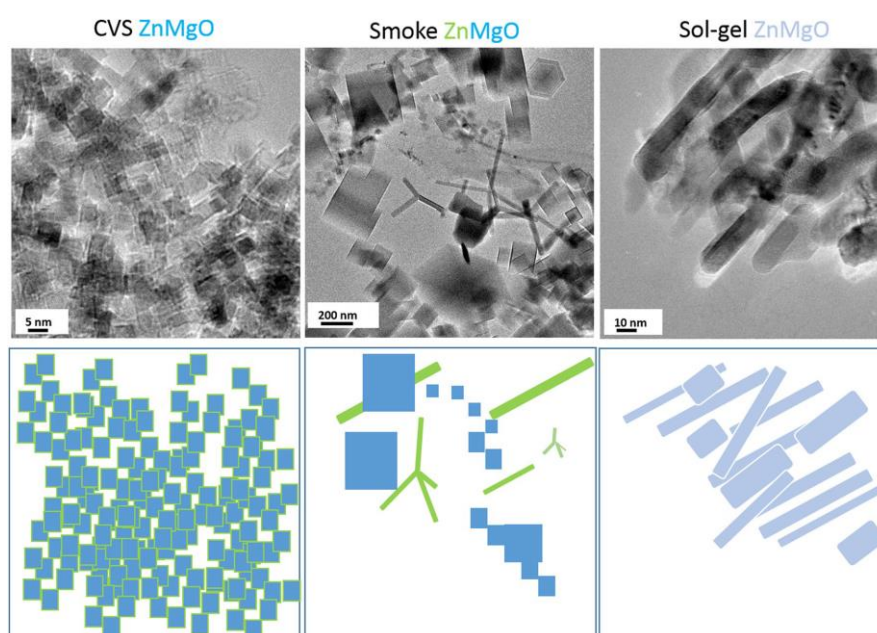
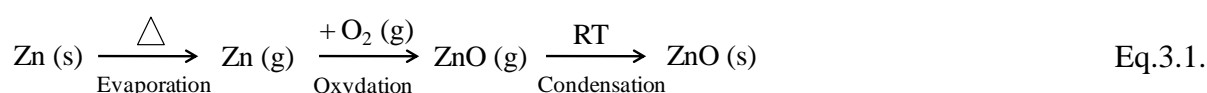


Figure 3.1 TEM images of ZnMgO nanoparticles obtained in our Lab via three different synthesis methods. The illustrations demonstrates differences in the initial morphology resulting from the corresponding fabrication routes.

In our Lab at the INSP, two synthesis methods, metal combustion in a glove box (GBC) and chemical vapor synthesis (CVS) are implemented for the purpose of metal oxide nanoparticles production. In general, both are based on the oxidation reaction in the vapor phase. As illustrated on the example of ZnO (Equation 3.1), the metal is firstly thermally evaporated into the gas phase, where it reacts then with the surrounding oxygen molecules to form monomeric metal oxide. More details and the description of both reactors are given below.



The synthesis of nanomaterials comprises two main stages: nucleation and growth. Nucleation is a first order phase transition process that can take place in vapor, liquid or solid phase and it refers to the first stage of the crystallization process. It can be seen as the process in which building blocks (metal and oxygen atoms in the synthesis of metal oxide nanoparticles) arrange themselves according to the crystalline structure and form a *nucleus* i.e. a cluster consisting of very few atoms of the growing species. Then additional building blocks deposit over the nucleus and the subsequent growth proceeds. The kinetic processes of nucleation and crystal growth requires supersaturation of the medium (either liquid or vapor) in which the system attempts to achieve thermodynamic equilibrium through nucleation and the growth of nuclei. In order for a new phase to appear, an interface must be formed. In the presence of foreign particles when it occurs on pre-existing surfaces (impurities, or ions) the nucleation is facilitated and the process is known as the *heterogeneous nucleation*. Otherwise, in absence of foreign material as well as of crystals of its own type, small embryos in the new phase are being formed and serve as templates for the further growth. Via this process, the nuclei are formed through the *homogeneous nucleation*.

Understanding the mechanisms of nanoparticle's formation is determining for developing skills in nanomaterial's synthesis. In that regard, the concepts of the classical nucleation theory (CNT) represent the fundamental basis. CNT was developed in 1936 and it is based on several approximations [Abraham 1974]. For instance, the condensation nucleus in a supersaturated solution is treated as a small fragment of bulk liquid with the same macroscopic properties as the bulk; such as surface tension and density.

The concepts for nucleation and crystal growth can be generalized also for a supersaturated vapor (or a super-cooled vapor or liquid). Supersaturated vapor possesses a high Gibbs free energy and the overall energy of the system would be reduced by segregating the evaporated units from the vapor i.e. by forming a solid phase and maintaining an equilibrium concentration in the vapor. This reduction in Gibbs free energy is the driving force for both, the nucleation and growth. In general, the CNT provides two parameters from thermodynamic data: critical radius r^* and the nucleation rate. The thermodynamic aspects of the homogeneous nucleation occurring in the vapor phase can be presented as follows: when a spherical nucleus of the radius r and molecular volume v (volume of the growing unit, or monomer) appears in initially supersaturated vapor at pressure P and temperature T , the free energy of the system increases as:

$$\Delta G = 4\pi\sigma r^2 - 4/3 \pi r^3 v \Delta G_v \quad \text{Eq.3.2.}$$

where σ is the specific surface-free energy that is identical to surface tension in case of liquids, $\Delta G_v = RT \ln(S)$ with R being the gas constant per gram of vapor and S is the supersaturation ratio ($S = P/P_0$, P_0 being the saturation vapor pressure at temperature T). The schematic change of volume free energy ΔG_v , surface free energy ΔG_s , and total free energy ΔG , as functions of nucleus radius is shown in Figure 3.2.

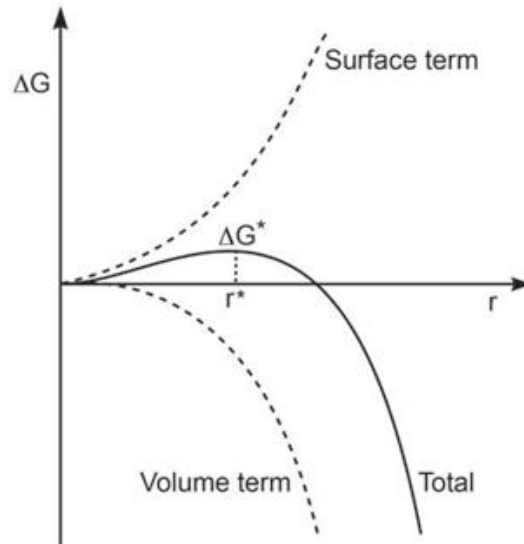


Figure 3.2 The change in the Gibbs free energy (ΔG , solid line) as a function of the nucleus radius (r) and as a sum of the volume (ΔG_v) and surface free energies (ΔG_s) [Mullin 2001].

From the figure, one can easily see that the newly formed nucleus is stable only when its radius exceeds a critical size r^* . The r^* represents the radius at which an equilibrium between condensing and evaporating nucleus has been established. A nucleus smaller than ' r^* ' will dissolve into the solution to reduce the overall free energy, whereas a nucleus larger than ' r^* ' is stable, the condensation rate is greater than the evaporation rate and it continues to grow bigger. At the critical size $r = r^*$ (the inflection point on the curve) ΔG passes through a maximum (which happens at $S \gg 1$), which implies $d\Delta G/dr = 0$. Hence, the critical size r^* and critical energy (the maximal value of ΔG), ΔG^* , are defined as:

$$r^* = 2\sigma v / RT \ln(S) \quad \text{Eq.3.3}$$

$$\Delta G^* = 16 \pi \sigma^3 v^2 / 3(RT \ln(S))^2 \quad \text{Eq.3.4}$$

ΔG^* is the energy barrier that a nucleation process must overcome and r^* represents the minimum size of a stable spherical nucleus. In the synthesis of nanomaterials through nucleation from supersaturated solution or vapor, this critical size represents the limit on how small nanoparticles can be achieved. To reduce the critical size and free energy, one needs to increase the change of Gibbs free energy ΔG_v , and reduce the surface energy of the new phase, σ . From Eq. 3.2 it can be seen that ΔG can be significantly increased by increasing the supersaturation, S ($S= P/P_0$) or by decreasing the temperature. The number of growth units in the critical nucleus, n^* , can be calculated by equating the volume of the critical nucleus, $4/3\pi(r^*)^3$, with the molecular volume of each growing units (v) times the number of growth units per nucleus:

$$4/3\pi(r^*)^3 = n^*v \quad \text{Eq. 3.5}$$

Substituting the previous equations and solving gives:

$$n^* = 32 \pi \sigma^3 v^2 / 3 (RT \ln (S))^3 \quad \text{Eq. 3.6}$$

The main outcome of classical nucleation theory is a prediction for the rate of nucleation i.e. the number of nuclei formed per unit volume per unit time, and it can be expressed as:

$$I = I_0 \exp (-\Delta G^*/RT) \quad \text{Eq. 3.7}$$

Substituting for ΔG^* , it gives:

$$I = I_0 \exp (- 16 \pi \sigma^3 v^2 / 3 R^3 T^3 (\ln(S))^2) \quad \text{Eq. 3.8}$$

where I_0 is the pre-exponential factor. The Eq.3.8 shows that the nucleation rate is governed by the temperature, saturation degree and the surface energy.

The synthesis of nanomaterials requires one to overcome their large surface energies and prevent them from agglomeration. By the liquid-phase routes, relatively monodisperse and

non-agglomerated nanoparticles can be obtained but followed with a small yield of the produced material and contamination issues linked to the remains of the precursors. These drawbacks are compensated in vapor-phase based synthesis techniques. These provide sufficient quantities of highly pure nanoparticles but face other unsolved issues – such as the agglomeration and particle's size non-uniformity. The underlying physics of these issues were studied in depth on the example of MgO that represents a prototype for studying surface processes [Haque 2018, Finochi 2019]. This is mainly due to its simple crystal structure (rock salt) and purely ionic and insulating nature – that has prompted the synthesis of MgO nanopowders by different preparation methods. Nevertheless, whatever the fabrication method, all reported examples of nanostructured MgO have in common the interconnected cubic primary units while particle size and particle size distribution (PSD) were observed to vary. Metal combustion synthesis results in a successful fabrication of MgO powder (MgO smoke) of exceptionally regular shape – with nearly perfect cubes with (100) facets – but a low specific surface area (ranging from 5 to 12 m²g⁻¹) and a broad and bimodal size distribution. For studying these phenomena during the growth from the vapor MgO smoke seemed as a model case with promising potential.

In that respect, we have prepared MgO smoke nanoparticles by combusting metallic Mg under well-controlled O₂/Ar atmosphere [Stankic 2011] – that contrasts the traditional combustion in air i.e. conditions that are far from being controlled. Since the basic mechanism of combustion comprises a fast oxidation of a metal vapor at high temperature, the variation in P_{O₂} was expected to influence the kinetic pathway of the gas-phase reaction already at the nucleation stage and affect in that way the particles size, shape and size distribution.. In general, the combustion of metal occurs in stationary conditions which means at constant temperature and pressure. It has been shown that, within a few percent, all magnesium is oxidized into stoichiometric MgO [Markov 1996] while the heterogeneous reaction of

oxidation of magnesium at the surface of preformed MgO particles is suggested to be marginal [Finnochi 2008, Sun 2002]. Hence, the nucleation of MgO relies only a homogeneous condensation of individual MgO molecules from the supersaturated MgO vapor in a process in which gaseous and condensed species are similar. Finally, the vast majority of the MgO particles adopts the cubic equilibrium shape with (100) facets which minimizes the MgO surface free energy and guarantees a unique value of surface energy. This is assumed to be correct even at the nucleation stage [Scaranno 2004] which fulfils the assumptions for the classical theory of nucleation from a vapor [Markov 1996].

We have rationalized the effect of oxygen partial pressure in terms of basic concepts of monomer formation, nucleation and growth. On the other hand, the concepts of CNT were considered for a cubical form of the growing units (nucleus), instead of spherical, and the previously presented equations for ΔG^* , r^* , n^* and I were adapted. To analyze the particle size dispersion more quantitatively, we have estimated its first and second moments, labeled M_1 and M_2 , respectively, for the samples synthesized in different oxygen partial pressures. They were defined in a standard way as:

$$M_1 = \sum_{n=1}^N P(L_n)L_n$$

$$M_2 = \sum_{n=1}^N P(L_n)(L_n - M_1)^2$$

and are displayed in Table 3.1. A judicious choice of synthesis conditions was shown not only to result in smaller particles but also to significantly improve the monodispersity.

Table 3.1: PSD moment analysis of MgO smoke particles grown by combustion of magnesium in different O₂/Ar ratios.

O ₂ /Ar (%)	M ₁	M ₂
20/80	83	67
40/60	60	20
60/40	44	16
80/20	34	17
100/0	28	20

On the contrary, in case of ZnO the growth can occur via Zn vapor condensation (followed by oxidation) but also via direct condensation of molecular ZnO (whose flux at the surface, although less than that of Zn vapor, is still sufficient to yield an appreciable nanostructure deposit) [Saunders 2011]. The presence of the two growth channels as well as the corresponding equilibrium between them offer a possible explanation for the great diversity of morphologies observed for ZnO nanostructure. In line with this, we observed that the effect of P_{O₂} used during the Zn-combustion affects mainly the particles shape [Zhang 2020]. TEM images recorded on ZnO smokes obtained under different O₂ partial pressures (Figure 3.3) illustrate the shape transformation from typically tetrapod-like in case of ZnO obtained under O₂-poorer atmosphere (O₂/Ar = 5/95 for ZnO-5) to hexagonal prisms achieved in richer O₂-conditions (O₂/Ar = 50/50 for ZnO-50).

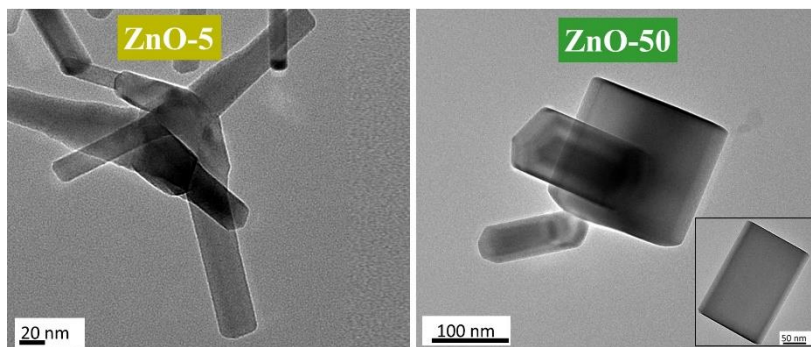


Figure 3.3 TEM images of ZnO smokes synthesized in our Lab at the INSP by combusting Zn in different P_{O₂} (O₂/Ar = 50/50 for ZnO-5 and O₂/Ar = 50/50 for ZnO-50).

Installation of two synthesis chambers. Metal combustion is a fast way to produce metal oxide nanoparticles of high purity. This synthesis requires a thermal activation to initiate the metal evaporation after which the oxidation reaction starts. Then, for the following metal evaporation the required heat is produced *in situ* by oxidation reaction itself. In other words, metal combustion is a type of self-propagating process. For the purpose of metal combustion we have designed and built up a new synthesis reactor in our Lab. It was constructed to provide conditions in which metals can be combusted in a controlled atmosphere – a mixture of an oxidizing agent (O₂, N₂O...) and an inert gas (Ar, N₂...). A homemade stainless-steel chamber is on the one hand connected to a primary vacuum pump to maintain the vacuum (P~ 0.1 mbar) and on the other to necessary gases. A glass window on the top, as well as the gloves allow for the manipulation and powders collection without any exposure to the air. The schematic representation is given in Figure 3.4. For the purpose of metal evaporation, two electrodes are inserted inside the glove box and connected with a thin conducting wire (usually a Ni–Cr wire with 20% Cr, 80% Ni) that is held in contact with an extremity of the metallic ribbon. After the Ni-Cr wire is resistively heated, the metal starts to evaporate and the oxidation occurs in the surrounding oxidizing atmosphere. The heat released upon this reaction is then reused for the further evaporation of the metal. Due to a great temperature gradient between the reaction zone (in flame) and the surrounding, the metal oxide particles formed in the gas phase transform rapidly into the solid. These are collected in a powdered form on the glass plate placed above the reaction zone.

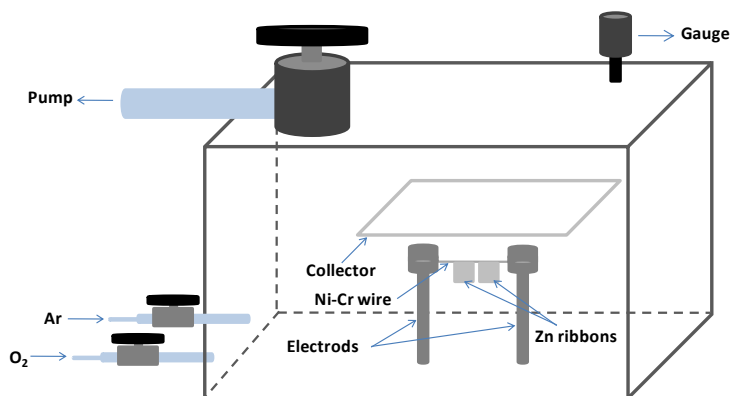


Figure 3.4 The schematic diagram of the glove box used for the synthesis of metal oxide nanopowders in our Lab at the INSP.

Metal combustion is a fast way to produce metal oxide nanoparticles while it also serves for the simultaneous growth of noble metal nanoclusters on a metal oxide support (see 3.1.2). Yet it has several shortcomings. The incomplete burning (i.e. oxidation) of metal precursors or heterogeneity of powders – in terms of both, the morphology and size – are some of them and results mainly from the difficulties to control the synthesis parameters. Furthermore, since the evaporation of metal and the concomitant reaction with O₂ occur almost simultaneously the formation of ternary oxides is usually followed by complete phase separation between the two oxides. Chemical vapor synthesis can nicely overcome some of the issues met within GBC. This especially concerns the synthesis of ternary oxide, which in line to their phase diagram, can be obtained in one crystal phase via CVS. Therefore, to complete the synthesis techniques that occurs in the vapor-phase, we have additionally to GBC installed the CVS synthesis chamber in our Lab (Figure 3.5).

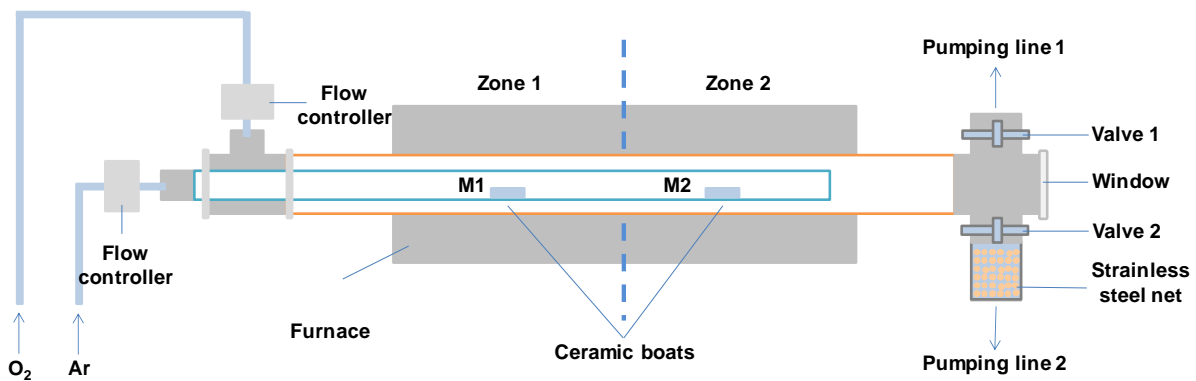


Figure 3.5 Schematic representation of the flow reactor used for the chemical vapor synthesis in our Lab at the INSP.

The chemical vapor synthesis occurs in a flow reactor that consists of a horizontal tube furnace, a quartz glass tube (inner tube) inserted inside another quartz glass tube (outer tube) connected to argon and oxygen, respectively. A typical synthesis of MO_x powder is performed by placing a given amount of the metallic foil into ceramic boats which are positioned in the middle of each heating zone. The reactor is pumped ($P \sim 0.1$ mbar) in order to remove the most of the air from the system and, finally, purged with a flow of high-purity argon. After the oxygen is injected into the outer tube and the pressure of the system set to a desired value (usually 50 mbar) the tube furnace is heated up to the evaporation temperature that corresponds to the desired vapor pressure of the metal. Metallic vapor is then transported by argon flow through the inner tube into the reaction zone filled with oxygen. Metal oxide powder is collected within the stainless steel net for 1 h.

3.1.2 Supported noble metal nanoparticles

Apart from a wide range of applications mentioned above, oxides provide also a large contribution as support for the growth of metal nanoparticles. Supported metal nanoparticles play a pivotal role in areas such as nanoelectronics, energy storage/conversion and catalysis [Prieto 2013]. In particular when deposited on an oxide support they form the basis for most solid catalysts and electrocatalysts, and have important industrial applications such as fuel production, fuels and pollution prevention [Aricò 2005]. The deposition of noble metals on semiconductor oxide surfaces is a commonly adopted method in heterogeneous catalysis and is often found to be beneficial for maximizing the efficiency of photocatalytic reactions by facilitating the charge rectification and promoting interfacial charge transfer [Lahiri 2003]. Such relatively broad spectrum of applications results from properties that are strongly determined not only by the size of metal nanoparticles but moreover by their shape that is defined by the crystallographic orientation of the exposed surface facets. At the same time, it is the interaction between metal nanoparticles and the metal oxide support that can substantially affect the resulting shape of the deposited nanoparticle. Nanoparticles fabricated by nucleation on support's surface are formed by diffusion and aggregation of ad atoms during interaction with the substrate. Morphology of such nanoparticles differ substantially from those achieved as “free” objects (shown in Figure 3.6) since the NPs' equilibrium shape becomes generally determined by the surface energy of the substrate. Two main experimental variables, namely the rate of deposition and the support temperature, provide the way to control the growth progress [Venables 1984].

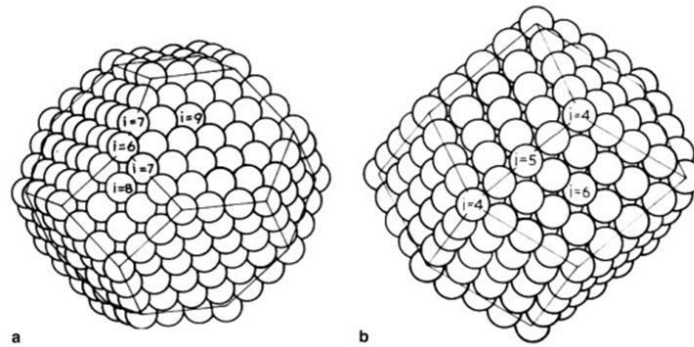


Figure 3.6 Equilibrium shape at 0 K of a) f.c.c.: truncated octahedron (e.g. Au, Ag, Pd) and b) b.c.c.: rhombic dodecahedron (alkali metals) [Henry 2005].

When the metal atoms from the vapor phase are deposited on the oxide surfaces, they can stick to it, diffuse on the surface or re-evaporate – depending on the strength of the interaction with the surfaces, of the kinetic energy of the incoming species and of the amount of thermal energy in the system. In the first stage of adsorption, not all metal atoms stick to the surface. They will be trapped on the surface if they get thermally accommodated to it. A sticking coefficient smaller than one means that the desorption will take place resulting in an incompletely covered surface. This situation is more relevant for elevated surface temperatures. At room temperature, however, the sticking coefficient is already close to one for many transition metal atoms and small aggregates on oxide supports [Hill 1998]. If defect sites are present on the surface, ad-atoms may be trapped at these sites. Thus the growth processes can occur by adding ad-atoms via homogenous nucleation (metal nucleation on a regular site) or heterogeneous nucleation (nucleation at a defect), [Bäumer 1999]. After the saturation density of supported particles has been reached, no further nuclei are formed and all diffusing ad-atoms are captured by existing islands. This is then followed by the growth processes in which either two- or three-dimensional shapes form.

In terms of thermodynamics, the equilibrium shape (ES) of supported metal particles can be described with the help of surface free energies of the metal, γ_{Metal} , the oxide, γ_{Oxide} , and the free energy of the metal-oxide interface, $\gamma_{\text{Interface}}$, [Venables 1984, Zinke-Allmang 1992, Bauer 1958]. When $\gamma_{\text{Interface}} + \gamma_{\text{Metal}} \leq \gamma_{\text{Oxide}}$ the metal wets the oxide at equilibrium, corresponding to a two-dimensional layer-by-layer growth mode (Frank-van-der-Merwe growth). In contrary, when the sum of $\gamma_{\text{Interface}}$ and γ_{Metal} is greater than γ_{Oxide} , wetting is thermodynamically hindered and 3D islands of metal will be achieved via either Stranski-Krastanov (S-K) or Volmer-Weber (V-W) growth mode. The former implies several monolayers to be grown in layer-by-layer fashion before a 3D island is grown while via Volmer-Weber mode the 3D growth occurs immediately without first forming a monolayer. Compared to oxides the surface energies of metals (especially of transition metals) are usually higher [Campbell 1997, Overbury 1975] and, thus, the growth of 3D particles is most likely to occur [Henry 1998, Cambell 1997, Goodman 1995, Persaud 1997, Bäumer 1997]. In the case of a Volmer-Weber growth mode, the equilibrium shape of supported metal particles results from a balance between surface and interface energies. For sufficiently large clusters it is given by Wulff construction and represented by polyhedron [Wulff 1901]. Generally, the equilibrium shape of an unsupported crystal (see figure 3.6) is obtained by minimizing the total surface free energy and this is achieved when h_i , the distance from the center to the face of index i , is proportional to the surface energy γ_i ($\gamma_i / h_i = \text{constant}$). On the other hand, for the prediction of the equilibrium shape of supported particles the effect of the substrate must be included, too. The solution of this problem was solved by Kaishew within the theorem known as Wulff-Kaishew. In that case, the equilibrium shape is a Wulff polyhedron truncated at the interface (shown in Figure 3.7) in accordance with the following equations [Henry 1998, Chatain 1988]:

$$\frac{\Delta h_s}{h_i} = \frac{E_{\alpha d h}}{\gamma_i}$$

while, $E_{adh} = \gamma_{Metal} + \gamma_{Oxide} - \gamma_{Interface}$ where γ_{Metal} is the surface free energy of the corresponding crystal surface i and E_{adh} is the adhesion energy and, as obvious, depends on the metal-oxide interaction.

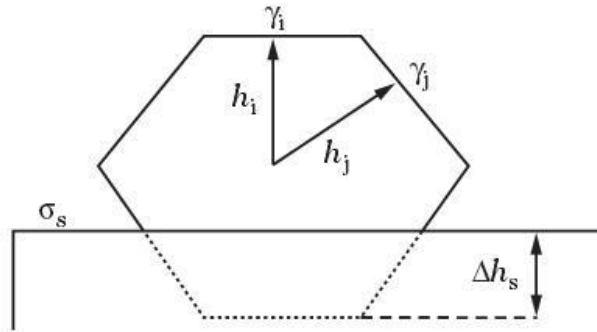


Figure 3.7 Schematic representation of the Wulff-Kaisew construction for an equilibrium shape of a supported crystal with the form of Wulff polyhedron truncated at the interface [Henry 2005].

This approach assumes that the crystal and the support possess equal lattice constants and neglects the epitaxial strain that develops (in both, the crystal and support) in case of a lattice misfit. Indeed, in order to decrease the elastic energy the strain is induced which forces the nanoparticles to grow in height. The crystal tries to reduce the stress by reducing the interface [Muller 2000] and, so, the aspect ratio increases with the size resulting in an equilibrium shape different than predicted without considering the strain energy. This problem has been addressed theoretically by Kern and Müller who have generalized Wulff-Kaisew theorem describing the influence of epitaxial strain on the equilibrium shape of crystals. Since the mechanical equilibrium of the supported crystal is achieved when its free surfaces have no stress components [Landau 1967], the elastic energy density changes with the shape of the crystal and thus can be minimal for a specific shape at a given volume. Therefore, the shape

changes with the size, misfit, adhesion to substrate and the relative stiffness of substrate. Presence of dislocation may induce changes as well. Finally, according to the epitaxial strain value and crystal size, some facets can appear or disappear and the shape of the strained particle may bear little resemblance to that obtained as classical Wulff shape.

Some oxides, like MgO, can act as inert support due to a negligible electronic interaction with most metal over layers. That makes it thermodynamically favored and stable upon deposition which has largely motivated many fundamental studies on metal/ MgO model systems obtained by a controlled metal deposition on a well characterized MgO surface in UHV conditions [Altieri 2007, Ferrari 2007]. We have studied the morphology of silver nanoparticles when supported on complex surfaces of MgO [Stankic 2013]. Indeed, the advantage was taken of MgO smoke which was shown to exhibit particles with surfaces of complex geometries and confinement – such as multiautomic steps and stacked crystallites that share one common contact line (schematically shown in Figure 3.8) – and, thus, provide a suitable support for the growth of metal nanoparticles.

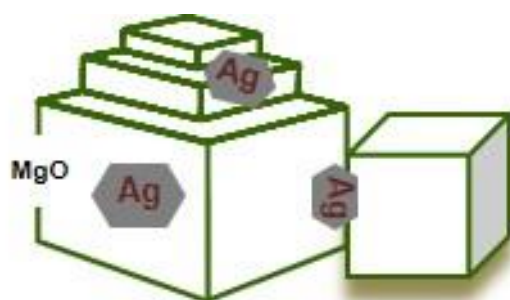


Figure 3.8 Schematic representation of the growth of Ag-nanoclusters at different MgO surfaces: flat (100), multiautomic steps (110) and between two stacked MgO crystallites.

In that respect, we have developed the co-combustion approach (a simultaneous deposition of Ag and formation of MgO by GBC synthesis) in which the high formation heat released upon Mg-oxidation is re-used for the evaporation of metal in parallel. By simultaneous occurrence of the two processes (oxidation and evaporation) the temperature of the support (MgO) is provided to be necessarily high so that the deposition can occur. By combining TEM experiments and atomistic simulations of clusters of realistic size, we could show that the simulated particles reproduce remarkably well the experimental observations and that cluster shapes are consistent with the corresponding equilibrium shapes given by Wulff–Kaishev theorem. An example is shown in Figure 3.9 for Ag clusters grown along the contact line between two stacked MgO crystallites. The matching between the simulated and experimentally observed morphologies strongly implied that silver particles were experimentally achieved close to their local equilibrium. This study also showed that the stabilities of the three considered cluster locations are sensibly different with a clear preference for the location at the contact line between two large MgO(100) facets (see schematic representation shown in Figure 3.9. The related study [Stankic 2013] is represented by the A-1 article, annexed.

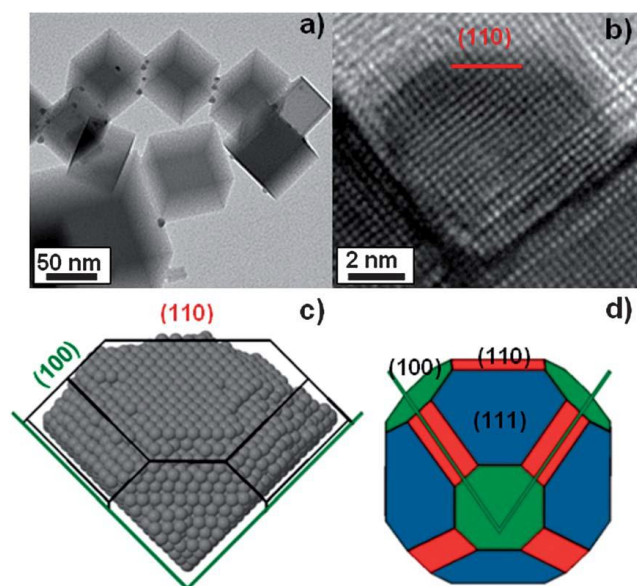


Figure 3.9 (a) TEM and (b) HRTEM images of Ag clusters grown along the contact line between two stacked MgO smoke crystallites; (c) the theoretically simulated atomic structure of a Ag cluster sitting on the contact line between two large MgO(100) facets and (d) the corresponding truncated octahedron shape of the Ag aggregate using the Wulff construction with the indication of facet orientations. In all cases the view direction is along the valley, thus [001] [Stankic 2013].

3.1.3 Mixed metal oxide (MMO_x) nanoparticles

Recent achievements in nanotechnology of metal oxides include elaboration of nanostructured oxides consisting of two or more metallic components. Mixing two (or more) metal oxide components is usually done in order to promote changes in electrical, chemical, optical, or magnetic properties. Combining cations of different size, oxidation state, electronegativity and reducibility, opens up a broad field for modifying one of several above listed properties in the resulting oxide – especially when cations may exist in multiple oxidation states. With respect to single-metal oxides, the chemical behavior of mixed-metal oxides may be different because of several factors. At a structural level, a dopant or second metal can introduce stress into the lattice of an oxide host, inducing in this way the formation of defects that have a high chemical activity. On the other hand, the lattice of the oxide host can impose on the dopant element nontypical coordination modes with a subsequent perturbation in the dopant chemical properties. Finally, metal-metal or metal-oxygen-metal interactions in mixed-metal oxides can lead to electronic properties different from single-metal oxides. Due to the beneficial synergistic effects of each constituent and to nano-dimensionality, the potential applications of such systems are immense. Examples include FeNiO_x and FeCoO_x mixed nanoparticles that reveal a strong synergetic effect on the activity for the electrochemical oxygen evolution

reaction [Pebley 2017, Strickler 2017, Trotochaud 2014] anatase-TiO₂ modified with transition metals reveals an improved photocatalytic performance due to an increase in charge carriers' concentration [Martin 1995]. In case of Ca_{1-x}Mg_xO nanoparticles, a higher thermal stability and new optical properties were reported with respect to those of pure CaO and pure MgO [Stankic 2005(a)]. Mixed metal oxides based on MCo₂O₄ (where M = Cu, Ni, Zn, Mn, Cd, No etc) are fascinating materials possessing spinel structure which, for instance, may provide a better electrical conductivity such as in NoCo₂O₄ [Poonam 2018]. Another example is illustrated on mixed lanthanide oxides whose nanoparticles have magnetic and fluorescent properties that are highly useful for dual imaging in biomedicine [Xu 2012; Das 2011]. An improved thermal stability of ZrO₂ is achieved when mixing with TiO₂, CaO and Y₂O₃ [Gionco 2013]. Moreover, the substitution of Zr²⁺ by Ce²⁺ results in localized energy levels within the band gap of ZrO₂ that makes it photoactive in the visible range.

Specific modifications of properties of well-known materials using small concentrations of the ad atoms and the development of fabrication processes of such nanoparticles are topics of modern material science. Their formation is often thermodynamically preferred over the separate formation of their pure components whereas the synthesis techniques do not principally differ from those described in Chapter 3.1.1. In bulk systems, the outcome of mixing depends generally on the local interactions between the admixed (solute) and host atoms. In the case of weak interactions, the ad atoms are located in random positions in the host lattice which results in fully disordered solid solutions. Formation of solid solutions with short and long range order as well as with phase separations will occur when such interactions are stronger. All these possibilities of mixing can be combined and phase diagrams under which mixing occurs can be derived in function of temperature, pressure, composition, etc. for various MⁿM^mO_x models [Segnit 1965]. Very few solid solutions are ideal and several parameters determine to which extent the solid solution can be achieved. These are: i) size

factor – the atoms or ions must be of similar size, with no more than a 15% difference in atomic radius, in order to minimize the lattice strain, ii) crystal structure – the materials must have the same crystal structure, iii) valence – the ions must have the same valence iv) electronegativity – the atoms must have approximately the same electronegativity.

In case of NPs, the ability to form homogeneous mixed phase and their thermodynamic phase diagram may strongly differ from that of their bulk analogues. This is nicely illustrated on the examples of $\text{SiO}_2 - \text{TiO}_2$ and $\text{CaO} - \text{MgO}$. In both cases, theory predicted positive free energies of formation and thermodynamic instability for all conceivable ordered structures [Cuko 2018; Kohan 1996]. However, NPs of $\text{Si}_{1-x}\text{Ti}_x\text{O}_2$ ($x = 0.3 - 0.5$) were simulated to be stable for sizes below 1 nm. In case of $\text{CaO} - \text{MgO}$, it was experimentally shown that up to 1900 K a complete immiscibility occur [Doman 1963] but a metastable solid solution of CaO in MgO was achieved in the molar fraction range $0 \leq x \leq 0.5$ for $\text{Ca}_{1-x}\text{Mg}_x\text{O}$ nanoparticles produced by CVS [Hofmann 1997; Stankic 2005]. Furthermore, in mixed metal oxide NPs the segregation effects may take place from full phase separation (such as core-shell structures) to partial surface segregation (such as in our CVS-ZnMgO). There are sound thermodynamic reasons that determine whether the segregation will take place or not. For instance, surface energy of either component (i) must be taken into account since those with the lower value tend to segregate at the surface [Berger 2007, Stankic 2010, Myrach 2010]. However, the surface segregation is mostly triggered by mechanic (ii) and/ or electrostatic driving forces in which both, the oxidation states (iii) of the cations as well as their relative electronegativity (iv) are comprised. In the following, each of the (i-iv) examples will be illustrated on certain $\text{M}^3\text{M}'\text{O}_x$ system.

i) Mixed $\text{Zr}_{1-x}\text{Ti}_x\text{O}_2$ NPs of composition up to $x = 0:15$ and sizes 30-100 nm. At low loading, these NPs form solid solutions with the ZrO_2 monoclinic phase in this whole composition range – despite quite different ionic radii. In contrast, above $x = 0:15$ its tetragonal phase is

achieved. A segregation of Ti cations in the subsurface layers is evidenced in the most highly doped material, consistent with a slightly lower surface energy of TiO₂.

(ii) In Ti_{1-x}Ce_xO₂ nanoparticles, the presence of both cations was detected in the surface and subsurface. Yet the degree of mixing was found to be relatively high despite a large difference in ionic radii of Ce and Ti (Ce⁴⁺: 1.01 Å; Ce³⁺:1.15 Å; Ti⁴⁺: 0.56 Å in octahedral coordination). Admixing larger isovalent ions (e.g. Ca, Sr and Ba) into MgO induces significant strain within the lattice, which can be relieved by segregation of the dopant into the surface to MgO. Indeed, this was experimentally confirmed during my Ph.D thesis where we have shown that at higher Ca²⁺ concentrations ($0 \leq x \leq 0.5$) in Ca_xMg_{1-x}O NPs these ions tend to escape the MgO bulk and accumulate at the surface [Stankic 2005(a)]. Similarly, CaO deposits with thicknesses of less than 4 nm on the top of MgO nanocubes were reported for high Ca²⁺ concentrations, i.e. for the concentrations where phase separation is theoretically predicted [Müller 2008]. Early computations provided clues as to reconstruction of BaO rich surface mono- and submonolayers into strongly ruffled arrangements with 50% of the surface segregated Ba²⁺ displaced to locations of low coordination [Masri 1985; Tasker 1985]. More recent theoretical calculations predict that thin BaO layers supported on MgO (001) substrates include a complex dislocation network comprising core structures with screw-edge and pure edge character [Sayle 2002]. In nanoparticulate BaO/MgO composites, however, the formation of hemispherically shaped BaO structures supported on MgO-based nanoparticles, and thus extensive phase separation was demonstrated for Ba²⁺ concentrations exceeding 4 at.% [Sternig 2011]. The illustration of MgO surface functionalization with Ca- and Ba-ions is schematically demonstrated in Figure 3.10.

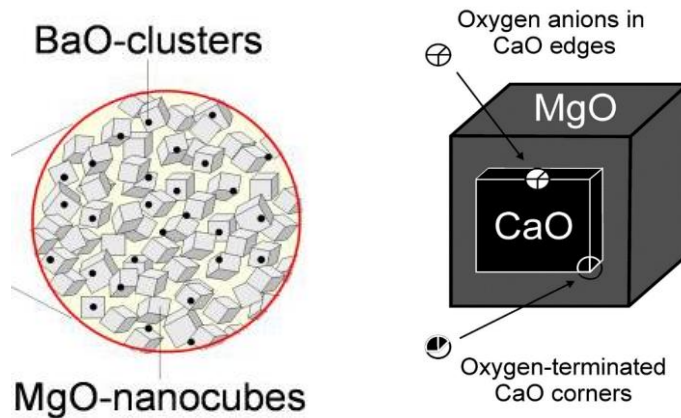


Figure 3.10 Schematic representation of a) hemispherical BaO segregates and CaO deposits on MgO nanocubes [Sternig 2008].

iii) The close ionic radius of Li^+ ($r_{\text{Li}^+} = 0.76 \text{ \AA}$) compared with that of Mg^{2+} ($r_{\text{Mg}^{2+}} = 0.72 \text{ \AA}$) allows for easy substitutional accommodation within the MgO lattice. After thermal treatment, Li^+ ions tend to localize in the surface and near-surface region of the MgO-based crystallites [Aitani 2000]. The experimental data obtained on LiMgO nanoparticles indicated surface segregation of Li-ions already at concentrations below 0.1 at.% with the preferential displacement of lowest coordination ions. Quantum chemical calculations have suggested that Li^+ cations embedded in the MgO nanoparticles segregate during an appropriate annealing procedure into the surface, where they preferentially substitute the lowest-coordinated Mg^{2+} cations to compensate for local deviations from stoichiometry [Nolan 2005]. The dominant mechanism of Li incorporation involves the generation of hole centers, which after segregation into the surface destabilize low-index planes at higher coverages.

iv) The relative electronegativity of the cations plays a role in Zn segregation at the MgO surface. As Zn is less electropositive than Mg, the $\text{Zn}^{2+}\text{-O}^{2-}$ bond is less ionic. This constitutes an important driving force towards the segregation of Zn^{2+} -ions from the bulk into

sites at the surface of the nanoparticles, where the electrostatic (Madelung) potential is weaker. In that respect, we have determined by *ab initio* calculations the surface energies and the preferential substitution of Mg^{2+} selected surface elements by Zn^{2+} ions and confirmed [Stankic 2010]. Moreover, calculations revealed that the enthalpy of segregation ΔH_{segr} is a piecewise function of the surface site coordination number C , which varies by about -20 kJ/mol when passing from C to $C-1$ (Figure 3.11). In the same work, the segregation of Zn^{2+} ions into MgO nanocube edges on $Zn_xMg_{1-x}O$ nanoparticles produced by chemical vapor synthesis was also demonstrated by different spectroscopic techniques.

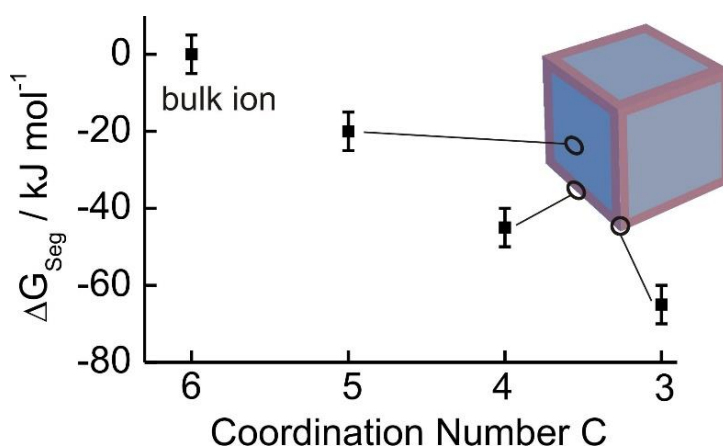


Figure 3.11 Mean free Enthalpy for Zn^{2+} segregation as a function of the Zn^{2+} coordination number C within the $Zn_xMg_{1-x}O$ and, thus, as a function of the topography of the respective surface element [Stankic 2010].

We have attempted to produce ZnMgO nanoparticles by combusting a ZnMg alloy in a glove box but this synthesis led to powders consisting of pure components, MgO nanocubes with FCC crystal structure and wurtzite-ZnO tetrapods – as confirmed by corresponding TEM micrographs and XRD patterns. The observed phase separation is most probably due to the

fact that in the course of this synthesis route the oxidation and the evaporation of Zn and Mg occur physically at the same place. Hence, the mixing of Zn and Mg atoms in the gas phase before they come into the contact with O_2 is hindered and, so, the formation of pure ZnO and MgO is favored – instead of $Zn_xMg_{1-x}O$ mixtures. In contrary, this is avoided through a simultaneous evaporation of the two metals, the oxidation and immediate quenching to room temperature within CVS process. The resulting mixed nanoparticles exhibit a statistical distribution of the two constituents inside the nanocrystal [Schneider 2009] in agreement with their phase diagram. Synthesis of a mixed metal oxide via CVS is schematically presented on the example of ZnMgO in Figure 3.12.

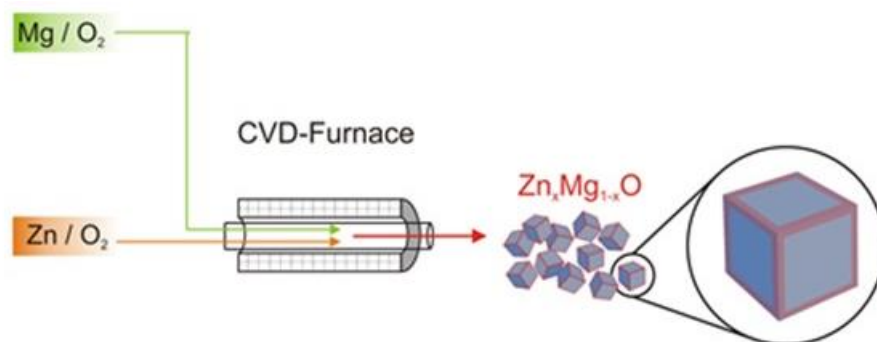


Figure 3.12 Schematic presentation illustrating the synthesis of composite $Zn_xMg_{1-x}O$ nanocubes [Stankic 2010].

Surfaces of metal oxide nanoparticles 3.2

The most fundamental properties that determine the structure-chemical activity relationship of the material include size, shape, defects (which often are subject to a broad distribution of electronic and structural characteristics), crystallographic structure and, in case of multi-compounds the chemical composition. Fundamental understanding of these characteristics as well as of material's surface chemistry provides basis for its further technological applications. The investigation of materials surfaces was traditionally restricted to the systematic use of single crystalline and ultra-high vacuum conditions. Unlike in case of surfaces of pure metals, such *classical surface science* approach encounters several shortcomings when applied to metal oxides – and even more to MO_x nanopowders. A practical difficulty is related to the experimental techniques used by surface scientists. For instance, during the measurements many of these techniques involve at some point the emission or absorption of charged particles (electrons, ions). Since most of the MO_x have negligible bulk conductivity (MgO , Al_2O_3), the samples often cannot be studied. Another principal shortcoming of the *classical surface science* is, in general, the use of single crystals which exhibit relatively reduced concentration of low coordinated surface sites. These sites, however, determine the reactivity and are highly relevant for the materials further use, such as for instance in chemical catalysis. An example is given in an experimental study [Narayanan 2004] where the shape distribution of the platinum catalysts was varied and a particular abundance of low coordinated surface atoms in edges and corners was estimated from geometrical models. Eventually it was found that the measured kinetic parameters of the reaction, like the average rate constant or the activation energy, correlate with the calculated fraction of surface atoms located on the corners and edges in each size and shape.

As a consequence of the above illustrated drawbacks, there existed a strong concern to extend the concepts of classical surface science to systems which at the same time exhibit a high crystal quality and a satisfying concentration of reactive, surface sites. An adequate compromise has been met in polycrystalline materials prepared by non-equilibrium techniques – such as alkaline earth oxides obtained in highly dispersed form. The rock-salt structure leads to particles in the form of nanocubes closed by facets that show a unique (100) family of orientations that can be directly compared to single crystal surfaces. Moreover, they show a considerably enhanced concentration of low-coordinated surface elements i.e., ions in (100) faces (5C), edges (4C), and corners (3C). Among others, MgO became an ideal particulate model system for the investigation of the aforementioned properties of ionic systems. In particular, when produced by CVS it exhibits a specific surface area of ~ 350-400 m²/g, a high crystal quality and highly defined cubic particle morphology. Another appropriate model system for surface science studies on particles is provided by ZnO smoke, which obtained by combustion of Zn exhibits nanoparticles with well-defined surface facets. As such, it enables the in depth analysis of surface crystallographic terminations [Haque 2017] that is not a straightforward task in the case of many oxides.

In well-defined nanoparticulate systems, both, the surface sites and/ or crystallographic orientations become experimentally accessible for the interaction either with properly selected probe molecule or with the photons. A detailed knowledge of the microstructures of stable surface geometries and their interaction with molecules from the gas phase have become accessible in the last several decades via new powerful surface techniques. The reactive sites that populate surface of metal oxide nanoparticles can be preferentially characterized and the correlation between topological surface structures and corresponding physicochemical properties established. Among others, the use of appropriate probe molecules in combination with mid-infrared spectroscopy (4200–400 cm⁻¹) is a powerful approach for obtaining a

detailed description of an oxide surface. With sufficient sensitivity, this technique examines the probe–surface interaction in an indirect sense since the surface is monitored through the perturbation by the probe. The observables are the changes in vibrational frequency and intensity of the probe modes. In some cases it is also possible to follow a reaction-dynamics on the surface [Groppo 2005(a,b), Lamberti 2007]. FTIR spectroscopy of adsorbed probe molecules is one of the most available and well-developed methods for studying the composition and structure of the surface functional groups of supported metal catalysts. As the vibrational spectrum reflects both the properties of the molecule as a whole and the characteristic features of separate chemical bonds, FTIR spectroscopy offers the fullest possible information on the perturbation experienced by a molecule on contact with the solid surface, and often determines the structure of adsorption complexes and of surface compounds. Regarding the molecular probes for IR studies, they are ideally of small size (in order to monitor surfaces in detail), high extinction coefficients (thus resulting in an appropriate detection sensitivity) and interact with the surface weakly (as to avoid alterations of the material under test). Finally, they have to be detectable by IR.

3.2.1 Interaction of metal oxide surfaces with probe molecules

Probing coordination number. The general aim of studying the interactions between surface sites and molecules from the gas phase is to find the relation between structure and reactivity of the samples. MgO is a particularly well-suited model material for the spectroscopic investigation of the properties and chemical reactivity of surface sites. Its cubic shape might suggest that the surface mainly comprises sites in flat (100) planes (Fig 3.13a). However, a realistic surface model of highly dispersed metal oxides was shown to host also a considerable

concentration of highly reactive defects such as steps, step-corners and/ or point defects (anion/ cation vacancies, interstitial sites, cation/anion anti-sites). This is schematically illustrated in Figure 3.13.b.

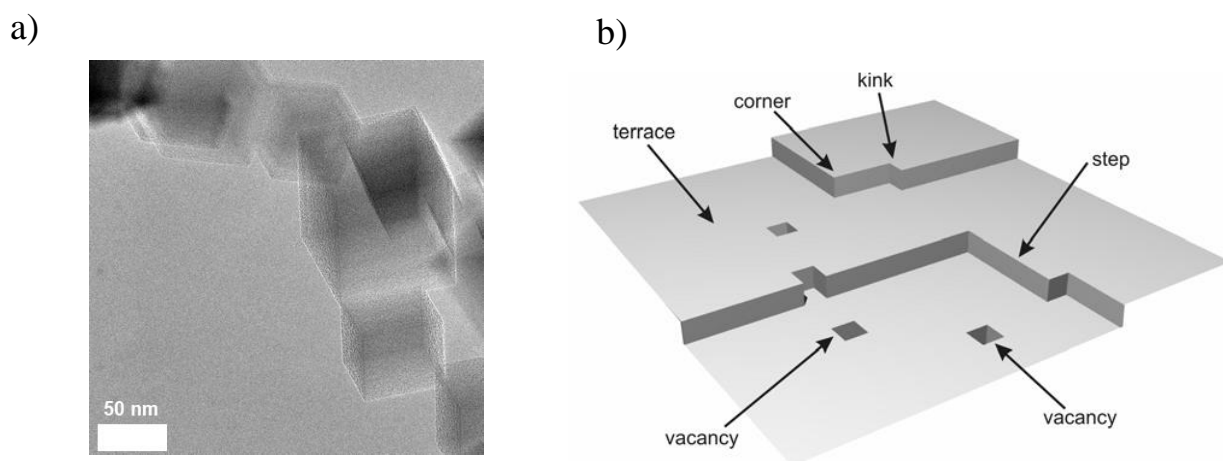


Figure 3.13 a) TEM image of MgO smoke realized at the INSP and b) model of a surface containing steps and point defects.

Regarding the choice of an appropriate probe molecule, hydrogen is often used because of its small dimensions but also being highly sensitive to surface heterogeneity. This is especially true in case of metal oxide surfaces where, due to its amphoteric character, H_2 is able to test both acidic (metal cations) and basic (oxygen anions) surface sites. Moreover, the investigations of H–H bond activation on oxide surfaces are important because of the analogies with C–H bond activation, which occurs in various industrial catalytic processes. Through the interaction with surface centers, already small perturbations of the H–H bond lead to an important shifts of the $\nu_{(HH)}$ stretching mode. One of the first IR evidences on

heterolytic H₂-dissociation and the concomitant formation of hydroxyl and hydride groups over high surface area MgO was provided by Coluccia and coworkers [Coluccia 1980]. The active sites were identified as cation-anion couples in low coordination on MgO surface while in the following series of computational works [Ito 1983, Kobayashi 1990, Shluger 1992, Anchell 1993] their chemical activity was found to be in a strong correlation with their coordination number. In general, on highly dispersed MgO two H₂-adsorption channels with OH/MgH frequencies at 3712/1125 cm⁻¹ (irreversible) and 3460/1325 cm⁻¹ (reversible) were previously evidenced. The corresponding surface geometries (O_{surf}H/Mg_{surf}H) were investigated by several groups, including additional EPR and computational studies. Consensus has been met mostly for the irreversible chemisorption complex: an H⁻ is proposed to sit in an inverse corner (resulting in MgH frequency at 1125 cm⁻¹) with the remaining H⁺ adsorbed on neighboring 4-coordinated oxygen anion (Figure 3.14).

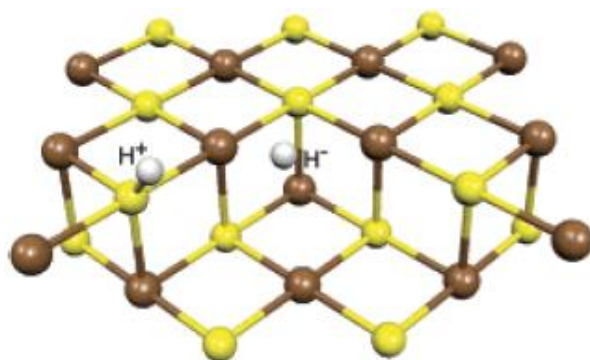


Figure 3.14 Optimal structure of a H₂ molecule dissociatively adsorbed on MgO with the proton adsorbed on a step O_{4C} site and the H⁻ at the inverse corner site. The structure is obtained on the basis of embedded cluster calculations [Ricci 2003].

Low-temperature IR study on H₂ adsorption over MgO surface reported surface configurations responsible for physisorbed hydrogen [Gribov 2004]. In general, a systematic approach combining theory and experiments was usually lacking while on the experimental side several conditions were inappropriate. For instance, the mainly used adsorption pressures of hydrogen were at $P_{\text{H}_2} = 10^{-1} - 100$ mbar which did not allow to test the stability of the observed configurations in the lower pressure regime ($10^{-9} - 10^{-1}$ mbar). Then, the thermal activation of samples – necessary to provide a clean starting surface – was usually performed at high vacuum where the residual pressure of air components is not negligible and the surface, thus, not fully cleaned. Consequently, some of the most reactive sites remain saturated and their vibration fingerprints therefore missed.

To avoid the disadvantages met in the investigation of metal oxide nanoparticles via FTIR spectroscopy, we have constructed a three-chamber set-up and connected it with the standard IR spectrometer. Typical for surface science studies such set-up provides experimental conditions in which also powdered samples can be annealed at UHV pressures. Moreover, the probe molecules can be adsorbed at equilibrium pressures as low as 10^{-9} mbar and these can be increased until ambient pressure in such experimental configuration. In that way, both *the materials* and *pressure gap* could be bridged: highly dispersed, powdered samples could be investigated under conditions typically applied on single crystals and thin films. Based on this strategy, already our first IR studies have shown that the examination of oxide powders in UHV conditions reveals novel surface reactivity and the sites that were never observed by analyses commonly operated under high vacuum could be identified. On both, MgO and ZnO nanopowders the use of ultrahigh vacuum was shown to be essential for identifying the very first adsorption stages while the obtained IR spectra reveal richer complexity than in current state of the art [Haque 2017; Haque 2018]. In case of MgO, beside the identification of thermodynamically most stable surface structures which irreversibly split H₂ molecules in the

lowest pressure regime (up to 10^{-3} mbar), such experimental concept allowed to moreover demonstrate that the population of distant defect sites at the surface proceeds via cooperative adsorption of more than one H_2 molecule. For the first time, a mechanism that includes hybrid surface structures – combined of sites of different reactivity and stability – was proposed for MgO and confirmed via DFT calculation. The theory has proved that whenever H^+/H^- adsorption sites are far apart and not neighbors, the dissociation becomes kinetically hindered, irrespective of the stability of the corresponding adsorption structure. Thus, the co-adsorption approach was demonstrated as indispensable for progressive H^+/H^- population of distant defect sites at MgO surfaces. From the IR spectra shown in Figure 3.15, we can see that such scenario occurs already in the medium range of H_2 pressures (10^{-3} –1 mbar) with the corresponding OH and Mg-H stretching vibrations measured at 3605 and 1225 cm^{-1} , respectively. The importance of such finding can be illustrated by the fact that it finally can occur in a wider range of H-containing molecules, such as for instance as CH_4 . The related study [Haque 2018] is represented by the A-2 article, annexed.

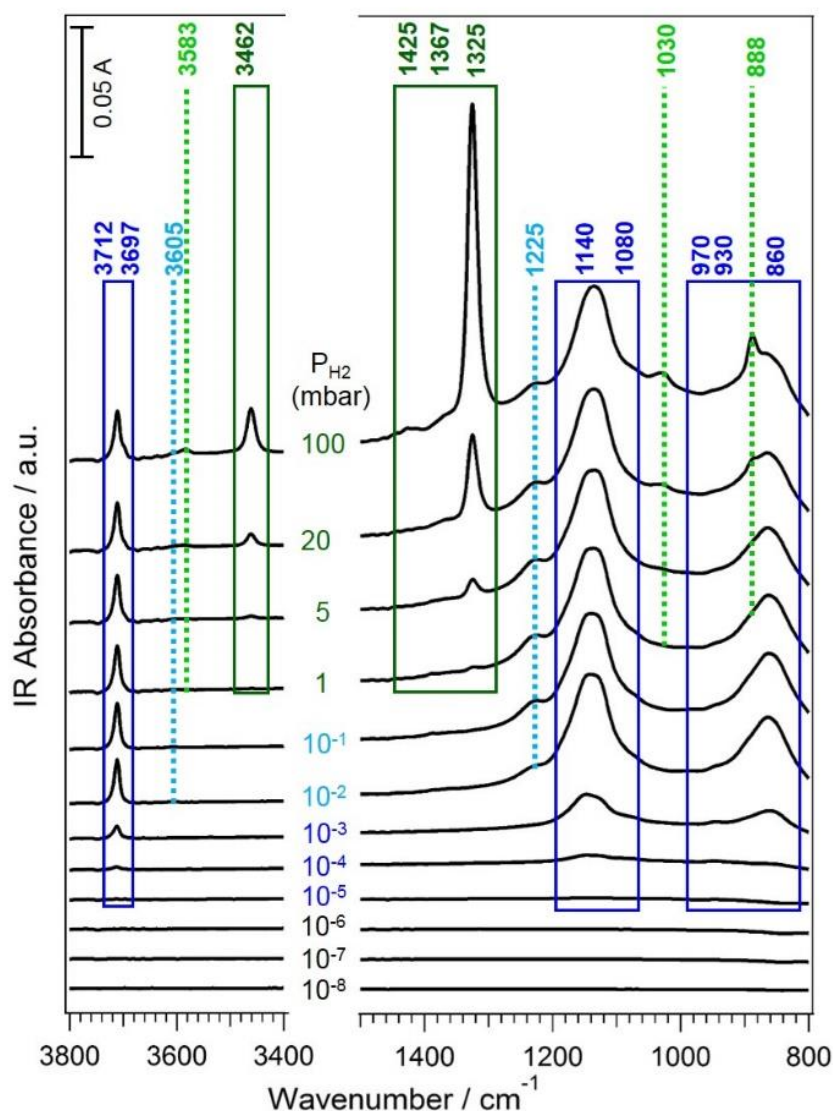


Figure 3.15 Room-temperature FTIR spectra of MgO exposed to $P_{\text{H}_2} = 10^{-8}$ –100 mbar. Three P_{H_2} regimes can be distinguished: low, $< 10^{-2}$ mbar (blue); intermediate, $\sim 10^{-2}$ –1 mbar (cyan); and high, > 1 mbar (green and light green) [Haque 2018].

Probing surface defects. Heterolytic dissociation of H_2 or H_2O is considered to be the rate-determining step in many catalyzed processes since in many of these one or more reaction steps involve hydrogenation/dehydrogenation of the reaction species. As a probe molecule, water does not ideally fulfill all of the above mentioned requirements. Yet IR spectroscopy

provides means for detecting where the water molecules bind on oxide surfaces – either via evolution of O–H stretching modes (dissociative adsorption) of free and hydrogen bonded surface hydroxyl groups or via presence of H₂O bending mode (molecular physisorption). The relative stability of molecularly and dissociatively bound water has been debated for decades on many oxide surfaces and studies have shown that, while water adsorbs molecularly on some oxide surfaces, it completely dissociates on other [Dulub 2005, He 2009, Giordano 1998, Xu 2010, Vittadini 1998]. Once dissociatively adsorbed the principal issue is to precisely determine at which specific surface sites the splitting has occurred. It was generally accepted that water dissociates only on defect sites of oxide surfaces [Kim 2003]. However, several theoretical studies have suggested that a mixed water+hydroxyl layer can be energetically more stable than pure water layers on certain metal oxide surfaces [Giordano 1998, Kim 2003]. Infrared absorption studies on MgO have reported the absence of the bending mode from which it has been deduced that H₂O only chemisorbs on that oxide. Yet for a long time, the expected full dissociation of isolated water molecules on low-coordinated sites on MgO surface remained a pending question. At low partial pressure ($P_{\text{H}_2\text{O}} \leq 10^{-5}$ mbar) water vapor only dissociates on low-coordinated sites of MgO surfaces [Henderson 2002], including steps, corners, and vacancies. At such partial pressure, flat MgO (100) terraces do not dissociate H₂O molecules, while at pressures $P_{\text{H}_2\text{O}} > 10^{-5}$ mbar, the (100) terraces become progressively hydroxylated [Liu 1998, Abriou 1999, Newberg 2011]. Indeed, these findings also implied on the necessity of ultra-high vacuum conditions for the fine analysis of the reactivity of defective MgO surfaces. Moreover, UHV conditions are even more relevant for hygroscopic oxides, such as MgO or in general alkaline earth oxides, that can undergo deep restructuring when exposed to water at a pressure beyond a material-specific threshold [Oncák 2015]. In that context, the conditions applied not only during the measurements but also during the synthesis and concomitant sample's processing, play a crucial role.

Our UHV-connected IR set-up allows for the adsorption of probe molecules at $P_{\text{H}_2\text{O}}$ as low as 10^{-9} mbar. This provides the conditions in which the hydroxylation of (100) terraces, that on MgO occurs at $P_{\text{H}_2\text{O}} > 10^{-5}$ mbar, can be avoided. In such experimental configuration, we have conducted adsorption of water on defective MgO surfaces and followed each adsorption step in UHV by IR spectroscopy [Finocchi 2019]. For that purpose, MgO samples of different relative proportion of surface reactive sites – both, the sites of low-coordination and point defects – were synthesized by CVS and GBC. Moreover, the amount of specific surface sites was tuned by varying the O_2 partial pressure used in the synthesis so that the adsorption experiments could be performed on MgO powders prepared in O_2 -rich or O_2 -poor conditions. Hence, MgO surfaces with point defects (O vacancies and MgO divacancies) and mono- and diatomic steps, either straight or with kinks, that spontaneously dissociate a water molecule were considered within the theoretical models. To unravel the contributions of the main kinds of low-coordinated MgO sites in the hydroxylation process and to determine the nature of the hydroxyl groups, the collected IR data were then compared with numerical simulations. This resulted in the identification of several significant hydroxyls at corners, monoatomic $\langle 010 \rangle$ steps, kinks, and MgO vacancies on monoatomic steps with qualitatively and quantitatively reproduced experimental outcome. These numerical data are gathered in Table 3.2.

Table 3.2 Computed characteristics of the hydroxyl groups on several defects at MgO(100) surfaces: O coordination number, OH bond lengths, hydrogen bond lengths and OH stretching frequencies [Finocchi 2019].

Defect	Hydroxyl groups	OH bond lengths (Å)	Hydrogen bond length (Å)	OH stretching frequencies (cm ⁻¹)
O vacancy @ (100) terrace (F _s center)	No OH groups (vacancy is healed and H ₂ released)			
MgO vacancy @ (100) terrace	O _(4C) -H	0.987	No H bond	3460
	O _(4C) -H	0.987		3460
MgO vacancy @ <010> step	O _(3C) -H	0.971	No H bond	3750
	O _(3C) -H	0.971		3750
<010> step (isolated H ₂ O)	O _(2C) -H	0.971	1.88	3750
	O _(4C) -H	0.993		3290
<010> step (full H ₂ O coverage)	O _(2C) -H	0.969	2.35	3760
	O _(4C) -H	0.984		3510
Kink @ <010> step	O _(2C) -H	0.970	No H bond	3750
	O _(3C) -H	0.972		3735
Kink @ <010> step	O _(2C) -H	0.968	2.25	3760
	O _(4C) -H	0.985		3500
Corner	O _(1C) -H	0.967	1.70	3775
	O _(3C) -H	1.004		3090
Corner	O _(1C) -H	0.967	1.74	3775
	O _(4C) -H	1.010		3005

Probing surface orientation. The importance of the relationship between surface orientation and materials properties can be illustrated on the case example of P-25 titania. This powder reveals significantly higher photocatalytic efficiency than any of its pure phases, rutile or anatase [Hurum 2003]. As demonstrated, this is due to the cooperative mechanism between charge carriers and surface orientations which drive photoreactivity [Pan 2011]. A number of oxides have been synthesized in the form of nanoparticles with well-defined facet orientations for the purpose of tracking down the orientation-dependent properties. In that respect, ZnO represents an almost ideal model system since in the form of powder it exist in a large spectrum of morphologies – sticks, tetrapods, platelets, discs, rings, ribbons and spirals [Campbell 1987, Djurisic 2006]. ZnO smoke, obtained by combustion of Zn in air, exhibits

well-defined *surface facets and behaves* as multi-facet single crystals involving (10-10), (11-20), (0001), and (000-1) surfaces with the polar orientations corresponding to 25% of the total surface area. On such ZnO powder, we have adsorbed water in order to specifically probe oriented facets. We have successfully achieved the identification of water structures also on ZnO (11-20) surface – that was never reported before. Additionally, we have also detected novel water structures on ZnO(10-10). The corresponding atomistic models are shown in Figure 3.16 together with the experimental (recorded after ZnO smoke was exposed to $P_{H_2O}=1$ mbar) and calculated IR spectrum. The related study [Haque 2017] is represented by the A-3 article, annexed.

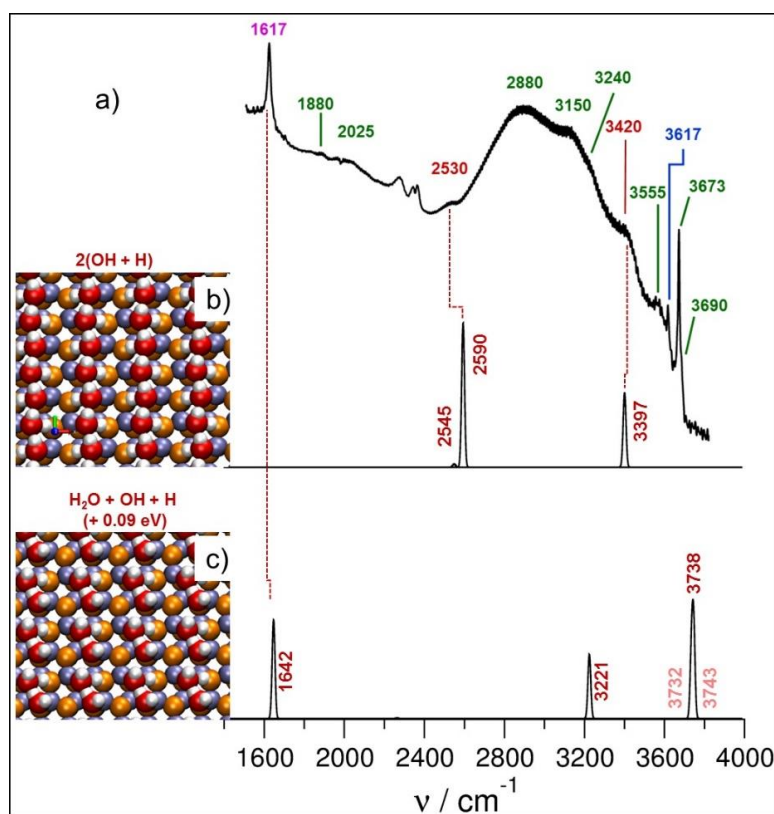


Figure 3.16 Comparison between the a) IR spectrum recorded on ZnO smoke at RT after exposure to $P_{H_2O}=1$ mbar and calculated spectra associated to H_2O ad layer structures determined by DFT approach for ZnO(11-20) surface and representative structures: b)

(2×1)fully-disocc, c) (2×1)half- dissoc. Blue and green highlighted frequencies correspond to ZnO(000-1)-O and ZnO(10-10) orientation, respectively. The deformation frequency (1617 cm^{-1}) of the water molecule is highlighted in violet [Haque 2017].

The above studies prove that when combined with the classical surface science approach, metal oxide nanoparticles can be successfully used as a test bed for studying the reactivity of different surface terminations, sites of defined coordination or point defects towards water and hydrogen.

3.2.2 Interaction of metal oxide surfaces with photons

Site-specific interaction of metal oxides with photons has been firstly investigated in late 70' and early 80' by Zeccina and coworkers [Zecchina 1975, Zecchina 1976, Garrone 1980]. They have used highly dispersed powders of alkaline earth oxides with different concentrations of reactive surface sites to identify their corresponding coordination via associated optical absorption bands. The reported UV diffuse reflectance spectra revealed absorption bands below the band gap of the corresponding bulk material and these were attributed to surface excitons formed at specific low-coordinated surface sites. Their predictions have been later confirmed by theoretical *ab initio* calculations [Shluger 1999] and another series of experimental studies. For instance, the relative intensity of absorption bands of MgO nanocubes were found to strongly depend on particle's size and, thus, relative concentration of low-coordinated surface ions [Stankic 2005 (a,b)]. Optical absorption band specific of 3-coordinated surface ions (corners) that peaks around 4.6 eV (270 nm) was shown to appear with a significantly higher intensity in the spectrum of smaller MgO nanocubes (3 nm vs. 5 nm vs. 10 nm) as a result of an increased ratio between corner and edge ions.

Photoluminescence studies conducted on these oxides [Coluccia 1978] showed that PL emissions could be observed only on high surface area samples ($20\text{--}150\text{ m}^2\cdot\text{g}^{-1}$) while as single crystals they were inactive towards light. The necessary excitations were shown to be achieved by using excitation light of much lower energy than that related to the optical band gaps of their bulk counterparts. Finally, the observed PL emissions were shown to be quenched by introducing molecular oxygen. All of these observations, led them to conclude that the emission as well as corresponding excitation spectra are associated with low-coordinated ions at the surface. Since the seminal works of Garone and Coluccia, a variety of spectroscopic techniques [Spoto 2004, Chiesa 2003, Bailly 2004] and first-principles theoretical calculations [Sushko 2002, McKenna 2007] have been used to investigate the surface properties of alkaline earth oxides of different particle size [Hacquart 2005, Hacquart 2009, Stankic 2011]. Regarding the PL studies on alkaline earth oxides, these were intensified in the working group of Prof. E. Knözinger in Vienna during my Ph.D thesis. Among other findings, the tendency in the PL fingerprints of MgO was found to be similar to the above mentioned dependence of absorption band intensity on the particles size. On the other hand, a comparative PL study conducted on CaO powders [Stankic 2006] of high surface area showed that despite being isostructural with MgO this oxide does not follow the same trends when interacting with light. Photoluminescence effects on CaO are more than a factor of 10 higher in intensity compared to MgO which demonstrates significant differences in the probability for radiative exciton deactivation between two oxides. More importantly, in contrast to MgO the PL process that corresponds to the direct excitation and emission of regular corner sites (3-coordinated) was shown to be absent on larger and morphologically ill-defined CaO particles as a consequence of low abundance of such sites. However, this particular process could be efficiently activated once CaO was obtained in form of small clusters ($< 4\text{ nm}$) as deposits on nano-MgO substrate [Müller 2008]. A new photoluminescence process that was

significantly red-shifted with respect to other CaO-specific spectroscopic fingerprints was detected on such CaO clusters and assigned to photoexcitation of oxygen-terminated CaO corners (Figure 3.17).

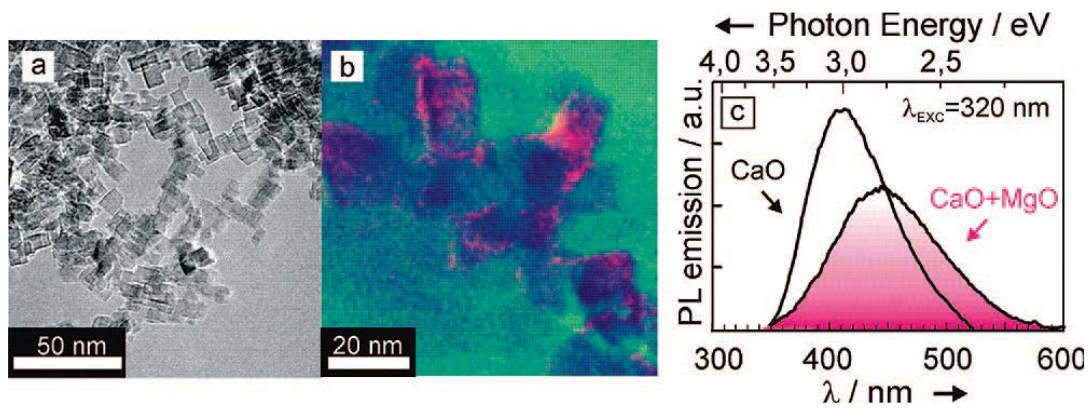


Figure 3.17 Electron microscopy images (a, b) and a photoluminescence emission spectrum of CaO-covered MgO nanocubes (c). (a) TEM image and (b) the energy-filtered TEM where Ca is indicated in pink color. The elemental map represents an overlay over the corresponding TEM micrograph. The photoemission spectrum, acquired at $T > 298$ K and $p < 10^{-5}$ mbar, was obtained on the same powder sample and is compared to that of pure CaO grains using excitation light of $\lambda_{\text{EXC}}=320$ nm [Müller 2008].

A significant PL emission was also reported for SrO nanocrystals [Stankic 2007]. Regardless of the coalescence and the formation of large polycrystalline SrO grains in the course of thermal activation in vacuum, surface anions of different coordination states were again shown to be in the origin of the photoexcitation process. The potential applications of nanostructured AEOs as photoluminescent materials was nicely summarized in our communication article in *Advanced Materials* [Sternig 2008]. Apart from alkaline earth oxides, the interaction of light with and oxide surface was then extended to TiO_2 [Riss 2008]

and the charge-separation processes were investigated by PL/EPR spectroscopies as a function of the oxide's morphology. Two types of morphologies, $\text{Na}_2\text{Ti}_3\text{O}_7$ nanowires and scrolled-up $\text{H}_2\text{Ti}_3\text{O}_7$ nanotubes, observed to reversibly transform into each other by acid/ base treatment were associated with photoluminescence in conjunction with inhibited charge separation (Figure 3.18A). Protonation of octahedral oxygen ions suppresses the radiative deactivation of trapped excitons but the process can reversibly be reinforced by back-exchange with alkali ions that bind only weakly to these units. This is nicely illustrated in the schematic representation in Figure 3.18B.

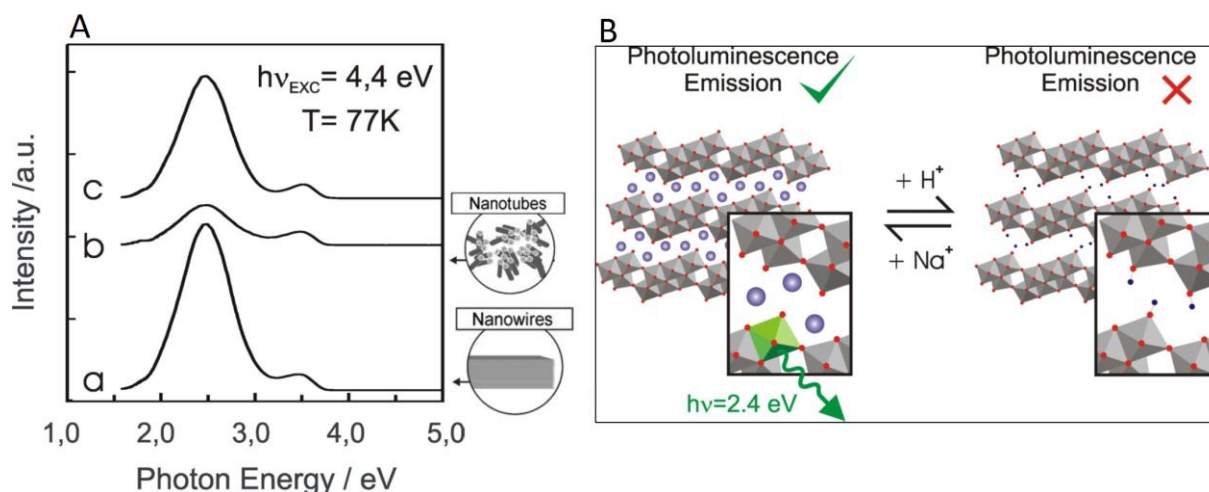


Figure 3.18 A: Photoluminescence emission of (a) Na-Titanate, (b) the material after 5 iterations of HCl treatment and (c) after one re-exchange step with NaOH. The HCl-induced decrease of photoluminescence intensity is almost reobtained after subsequent NaOH treatment. **B:** Scheme of reversible ion exchange within layered titanate nanostructures. In contrast to intercalated Na^+ ions, which are weakly bonded, chemisorbed protons lead to a distortion of the $[\text{TiO}_6]$ octahedron, related to the reduction of trapped exciton deactivation [Riss 2008].

3.2.3 Interaction of metal oxide surfaces with photons and surface probe molecules simultaneously

Finally, examples are given in which we have monitored the interaction of oxide surfaces with photons along with surface modification i.e. during or after an interaction with a selected probe molecule [Müller 2007]. The site-specific functionalization of oxide nanostructures may give rise to novel optical surface properties which can provide deeper insights into the electronic surface structure of the associated materials. As demonstrated above, the excitation ($E_{\text{EXC}} = 4.6 \text{ eV}$) of the fully dehydroxylated MgO nanocubes results in PL emission at 3.2 eV while, both emission and absorption are associated with 3-coordinated oxygen corners. These sites, however, can be selectively modified by protons upon chemisorption of molecular hydrogen – as we have also demonstrated by IR studies [Haque 2018]. We could show that compared to completely clean MgO surface, the selective protonation resulted in an additional photoluminescence feature at 2.9 eV. The excitation spectra of both PL emissions bands, at 2.9 and 3.2 eV (associated with protonated and nonprotonated oxygen corner sites, respectively) nearly coincide with maxima at 4.6 eV – that corresponds to the optical absorption commonly assigned to nonprotonated three-coordinated oxygen sites. We explained these observations with the help of ab initio calculations (summarized in Figure 3.18.): the absorption band at 4.6 eV involves four-coordinated O and Mg ions in the immediate vicinity of the corner sites. The protonation of the 3-coordinated oxygen ions eliminates the optical transitions associated with them and strongly red-shifts other optical transitions associated with neighboring atoms. This study demonstrated that the absorption bands should be assigned not to low-coordinated ions alone but rather to multiatomic topological features as a whole.

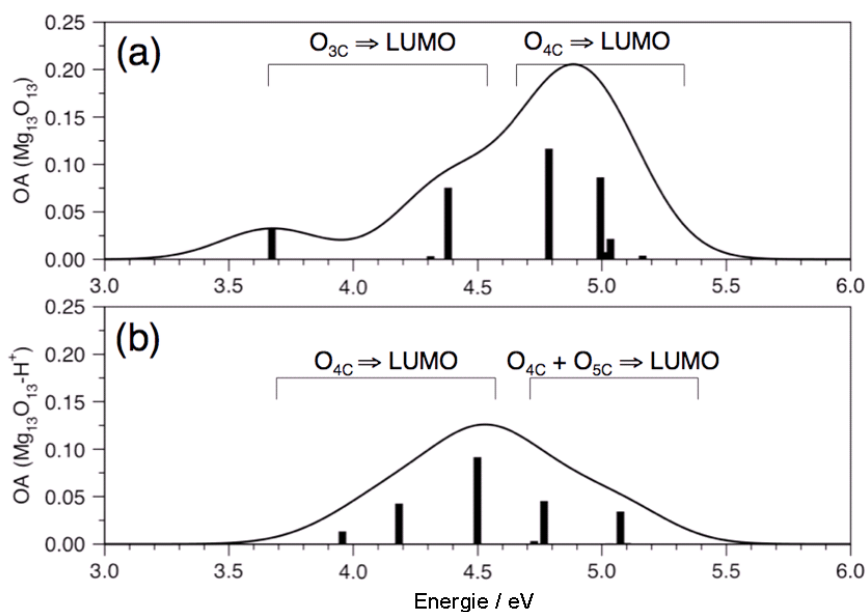


Figure 3.18 Optical absorption of oxygen-terminated corners: (a) non-protonated and (b) protonated sites. The position and height of vertical bars indicate calculated excitation energies and relative intensities of the optical transitions, respectively. The thin solid line shows the convolution of Gaussian-type functions (with dispersion of 0.2 eV) representing transitions in the low-energy part of each spectrum, which corresponds to the 4-4.5 eV range in experimentally obtained absorption spectrum. The qualitative nature of the transitions is also indicated to illustrate the magnitude of the red shift [Müller 2007].

In another study, our aim was to correlate optically active sites of MgO to those of chemical reactivity [Sternig 2012]. We were able to evaluate the proportion between radiative and non-radiative pathways of the exciton deactivation and, thus, to estimate the branching ratio between photoluminescence emission and exciton separation – the latter being related to the production of charge carriers undergoing surface chemical reaction. We used hydroxylated MgO nanocubes and employed in situ photoluminescence spectroscopy to drive and to monitor the reaction at the same time. The excitons that are well known to form in the course

of a photoexcitation on the surface of MgO nanostructures were subjected to additional photon absorption. The subsequent absorption of a second photon led to the separation of an exciton to form an O_3C^- species plus an electron that becomes trapped at surface elements with sufficient electron affinity [Beck 2008, Sterrer 2002]. The key intermediate, i.e. the corner O_3C^- species are highly reactive [Sterrer 2005] and activate molecular hydrogen as well as other H-containing molecules according to:



In the case of H_2 activation, the molecule is split according to eq. (3.9) and it forms surface hydroxyls. The released H atom dissociates at the surface into a proton upon surface hydroxyl formation (eq. 3.10) and an electron which becomes stabilized as the surface trapped electron center (e^-_{trapped}) that reveals a characteristic spectroscopic fingerprints [Sterrer 2004, Chiesa 2006]



In addition, UV light can photolyse surface hydrides upon generation of additional surface trapped electrons.

Our PL study showed (Figure 3.19a) that after UV irradiation with $\lambda_{\text{UV}} = 270$ nm and corresponding photon fluxes of the order of 10^{10} photons $\text{cm}^{-2} \text{s}^{-1}$, only five percent of the PL emission sites related to the photoexcitation of edges and corners of MgO nanocubes are depleted and subject to exciton transformation into reactive charge carriers. This fraction is significantly enhanced by irreversibly bound hydroxyls and hydrides although the underlying sites are not directly involved in PL processes (denoted as A and B processes in Figure 3.19). MgO nanocube edges were found to be efficient absorption sites for UV photons which

correspond to an excitation wavelength of $\lambda_{\text{Exc}} = 240$ nm. Transfer of exciton energy to oxygen ions in corners either led to the radiative surface exciton recombination at corners or to their separation which transforms them into surface radicals. The photochemical reaction pathways were described in detail and the respective insights provide a powerful base for in situ spectroscopic studies which in future can be extended to larger and more complex molecules. A representative schematic illustration is given in Figure 3.19b.

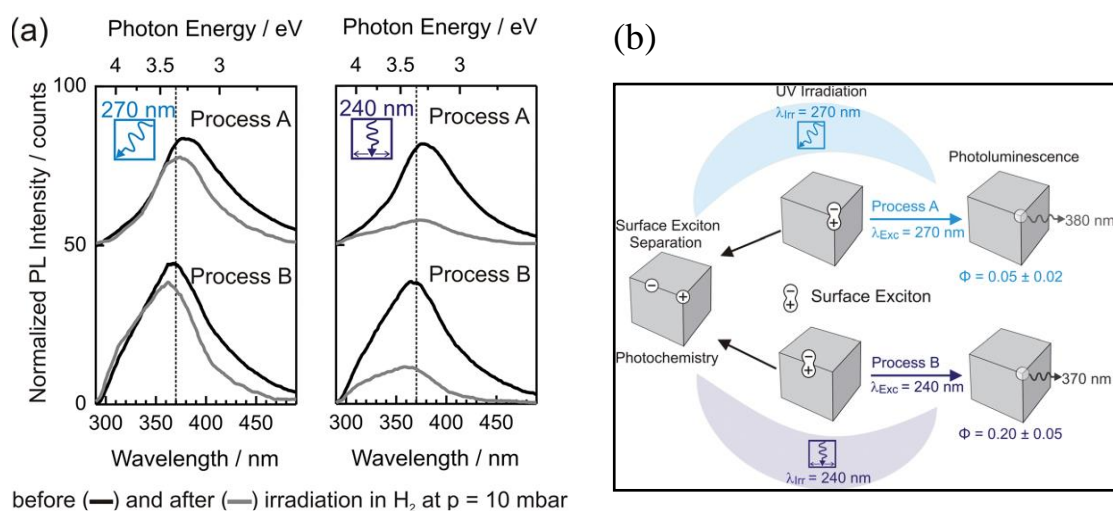


Figure 3.19 (a) PL emission spectra obtained on MgO powders in H_2 atmosphere (a) before (black lines) and after (grey lines) 13 hours of UV irradiation during which all photoinduced surface processes that compete with PL emission have reached saturation. The irradiation wavelengths λ_{irr} are indicated in the plot by the respective icons. (b) Schematic illustration of UV induced processes on MgO nanocubes which occur site-selectively. They give rise to photoluminescence (PL) emission (right side) or to surface photochemistry (left side) [Sternig 2012].

Point defects in metal oxides 3.3

In ideal crystals, the arrangement of atoms or molecules is periodic, and all unit cells line up in space of three dimensions with no distortion. Real crystals, however, generally possess certain number of imperfections where unit cells may have some atoms missing or replaced by other internal or external atoms. Normally, defects can be classified according to their dimensions. Volume defects include voids and precipitates, the scale of which is the largest among the rest of the crystal defects, and are typically deleterious to the properties of materials [Russell 2005]. Planar defects occur at the interfaces between homogeneous regions of the material. The most typical planar defects are stacking faults and grain boundaries. Line defects include edge and screw dislocations and exist at the interfaces between two single crystal regions of different orientations. Point defects are defects where an atom is missing or in an irregular site in the lattice, and they can be divided into two categories: intrinsic and extrinsic defects. Intrinsic defects exist in pure crystals and include vacancies, interstitials and antisites, while extrinsic defects are caused by foreign atoms (present in doped crystals). Point defects exist in different oxidation states with each of them being represented by well-defined energy states within the band gap of semiconducting materials and exhibit. These states have a certain ratio of conduction- versus valence-band character and, therefore, their positions with respect to the valence band maximum (VBM) can be underestimated by a significant amount. This uncertainty affects the prediction of transition levels and formation energies, leading to potentially large errors, especially in the case of wide-band-gap semiconductors such as ZnO.

The formation energy (E_f) of a native defect in a solid determines its concentration through the relation [Kittel 2005] in Eq. 3.11:

$$c = N_{\text{sites}} \exp\left(\frac{-E^f}{k_B T}\right) \quad \text{Eq. 3.11}$$

where N_{sites} is the number of sites (including different configurations) per unit volume the defect can be incorporated in, k_B is the Boltzmann constant and T the temperature. According to this equation, defects with high formation energies will occur in low concentrations. However, the E_f can be strongly affected by growth conditions (Figure 3.20). For example, the formation energy of zinc interstitials is determined by the relative abundance of Zn and O atoms in the environment, as expressed by the chemical potentials μ_{Zn} and μ_{O} , respectively. If the defect is charged, the formation energy further depends on the Fermi level (E_F), which is the energy of the electron reservoir, i.e. the electron chemical potential. Accordingly, in Zn-rich condition, oxygen vacancies as well as zinc excess related defects – like Zn_i and Zn_o – are promoted. In O-rich condition, though, Zn vacancies and other defects associated with oxygen excess (O_{Zn} and O_i) will be formed. Migration barrier, is another parameter that can affect the concentration of native defects, and it determines their annealing behavior [Tuomisto 2005, Erhart 2006].

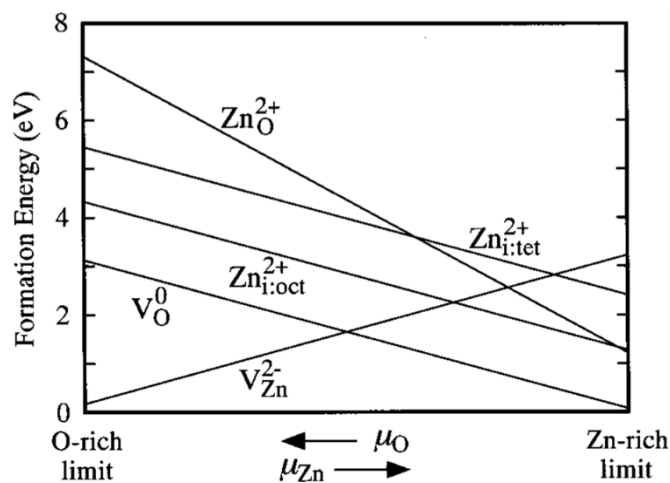


Figure 3.20 Formation energies of native defects as a function of the atomic chemical potentials under n-type condition. For each defect, only the charge state that gives the lowest formation energy is shown [Oba 2001].

Multiple techniques have been used for the identification of lattice defects in ZnO but the combination of photoluminescence spectroscopy and electron paramagnetic resonance spectroscopy, turned out to be the most productive one. Despite a good deal of research that has been carried out to assign the observed PL/EPR spectroscopic features to corresponding intrinsic defects in ZnO the consensus has been rather missed. For instance, for a given EPR signal such as the one with $g = 1.96$, several defects are proposed in the literature (Zn_i , V_o , V_{zn}) and vice versa, several signals (such as 1.96, 1.99, 2.002) can be found as ascribed to one specific defect (V_o). The best illustration is the highly discussed green luminescence centered $\sim 2.17 - 2.5$ eV. This PL emission was controversially assigned to various intrinsic defects in ZnO (V_o , O_{zn} , O_i , V_{zn}) as well as to impurities (H_i , Cu, etc.) introduced either intentionally by doping or unintentionally via inappropriate synthesis conditions [Borseth 2006, Tam 2006, Camarda 2016, Guo 2015, Gurwitz 2014, Lv 2013]. The absence of consensus results from both, an inadequate comparison of samples of different origins (different type of synthesis, different type of samples such as single crystal, thin films, nanoparticles) and/or the variability of experimental conditions applied not only during the synthesis but moreover during the sample's processing and measurements.

To overcome such difficulties encountered in the identification of defects in ZnO we have performed a multiple strategy. Firstly, an advantage was taken out of the two synthesis routes used in our Lab (GBC and CVS). Both of these use pure metallic precursors and highly pure O_2 which assured ZnO powders free of impurities or extrinsic defects. Consequently, the

choice of candidates being potentially responsible for the spectroscopic signal under question became significantly reduced. Moreover, conditions within both of these techniques can be controlled as such to explore the diagram shown in Figure 3.20 which allowed us to obtain ZnO in either an O₂-poor or O₂-rich atmosphere and to direct consequently to the desired type as well as concentration of the point defect. Secondly, high-vacuum conditions were considered as indispensable to be applied at any point of the sample's history: storage, during the measurements and during the annealing treatments which were performed either to clean the particles surface (to access surface defects) or to intentionally generate a defect being specific of the applied annealing treatment. Adopting these precautions, native defects formed during the synthesis under different conditions (by employing different synthesis approaches or by controlling synthesis parameters within given synthesis method) as well as defects generated under specific post-growth conditions (by annealing ZnO nanoparticles in reducing or oxidizing atmosphere) were investigated in ZnO smoke (Sections 3.3.1 and 3.3.2) in a close collaboration with the colleagues from the Surface Reactivity Laboratory (LRS).

3.3.1 ZnO smoke: Point defects at different processing stages

In this study, we combined electron paramagnetic resonance (EPR) and photoluminescence (PL) spectroscopies to investigate the nature of defects natively distributed in ZnO obtained by Zn combustion in air (ZnO smoke). Then, several processing protocols were applied to follow either their transformation or formation of new ones – the conditions specific defects.

Native defects. Apart from green-PL at 2.50 eV (will be discussed in 3.3.2) two pairs of violet-PL/EPR signals (2.88 eV / $g = 1.956$ and 2.80 eV / $g = 1.960$) were observed in the as-synthesized ZnO smoke powder (Figure 3.21 a, b). The intensity of these signals (PL and EPR) was shown to be reduced in the presence of molecular oxygen at the room temperature

whereas another couple, with close PL/EPR values (2.88 eV/ $g=1.96$), remained unaffected. The observed PL maxima (2.80-2.88 eV) match well with the transitions (2.75-2.9 eV) consistently calculated and experimentally observed to arise from energy states related to interstitial zinc (Zn_i) [Zhang 2001, Look 2005, Erhart 2006b, Zeng 2010, Chen 2011, Thapa 2016]. Supported also with our XPS data (performed in UHV conditions) which revealed an excess of Zn ($Zn/O = 1.26 \pm 0.15$) – at least in the first few nanometers (5 nm) – the two PL signals detected in the as-synthesized ZnO smoke powder were attributed to zinc interstitials. Moreover, observed in parallel with the EPR signals that show the same tendency upon molecular oxygen admission, the two PL/EPR couples could be assigned to positively charged zinc interstitials (Zn_i^+). At the same time, such an effect of the molecular O_2 (Figure 3.21 c, d) allowed for the discrimination between surface (2.88 eV/ 1.956) and bulk (2.80 eV/ 1.960) Zn_i^+ . The presence/ absence of the spectroscopic signals depending on measurement's environment proves our concept of performing the measurements under controlled (high vacuum) conditions. Most of the PL/EPR data in the literature do not report about the measurements conditions or otherwise most of those are performed in the air (an O_2 / H_2O containing atmosphere). This, for the consequence, can lead to some signals to escape the detection since the nature of their responsible defects undergoes change in such circumstances and new energy levels become occupied in the gap. This is perfectly represented by the case of PL/EPR = 2.88eV/ $g=1.956$. Moreover, performed either in the presence or absence of O_2 these measurements could prove the location of the responsible defects.

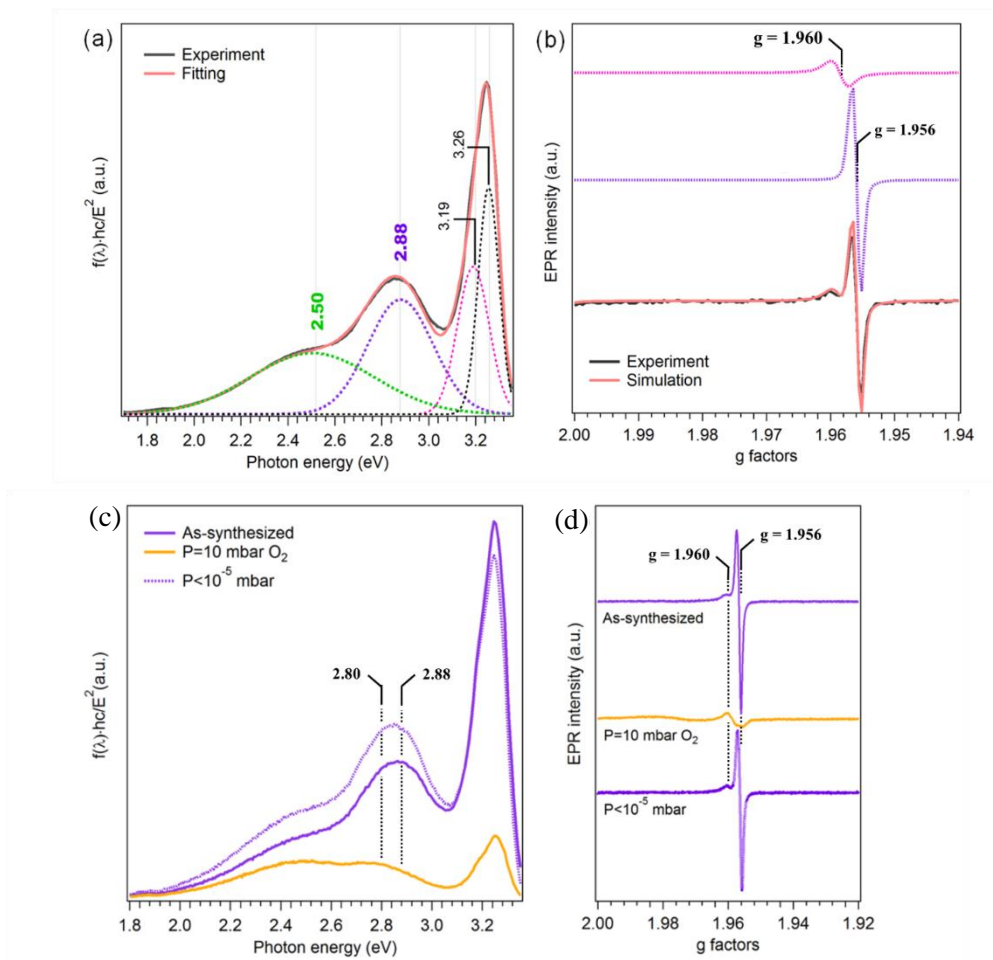


Figure 3.21 (a) As-synthesized ZnO smoke: (a) PL spectra (black curve) and corresponding band-fitting analysis (red). The contribution of each emission is represented by dotted curves in black, magenta, violet and green. (b) Experimental (black curve) and simulated (red curve) EPR spectra. Violet and magenta dotted curves show the contribution of the two paramagnetic species (A and B). PL (c) and EPR (d) spectra of as-synthesized ZnO smoke in vacuum (solid violet curve), in presence of O_2 (solid orange curve, $P_{O_2} = 10$ mbar) and after pumping out O_2 (dotted violet curve, $P < 10^{-5}$ mbar) [Zhang 2019].

Defects developing under annealing in O₂-poor conditions. A new PL/EPR couple was observed at 2.41 eV and $g = 2.002$, respectively, in ZnO smoke annealed under high vacuum ($P < 10^{-5}$ mbar). More importantly, along with this PL/EPR couple we have detected EPR signals specific of superoxide radicals (O_2^-). Normally, such species were reported to form on UHV (or HV) annealed surface of semiconducting material after being intentionally contacted with O_2 . In our case, however, in absence of any external O_2 supply, the oxygen necessary for the creation of notable amount of O_2^- had to be provided by the ZnO lattice itself. Therefore, the PL/EPR couple that develops along could be unambiguously assigned to singly charged oxygen vacancies (V_o^+). Consistently, the same PL/EPR couple was also observed on ZnO smoke annealed in Zn-vapor (again an oxygen poor condition) which additionally proved its V_o -related nature. Furthermore, also in this case an interaction with a probe molecule allowed for the identification of the location of this defects i.e. V_o^+ . Indeed, when the vacuum annealed sample was exposed to water, an intensity decrease was measured for both of the initially detected PL/EPR fingerprints (2.41 eV/ $g= 2.002$). The reactivity towards H_2O , implied that the V_o^+ must have sit at ZnO's surface in order to split water molecule. This type of interaction (metal oxide surface / water) was already discussed in 3.2.1 and it is in generally well established in the literature.

Defects developing under annealing in O₂-rich conditions. Finally, the annealing of ZnO smoke in an O₂-rich atmosphere (high P_{O_2}) resulted in a broad PL emission at ~ 2.07 eV (Figure 3.22) without an EPR counterpart. The yellow luminescence (YL) was observed in all forms of ZnO (single crystals [Epie 2016], thin films [Stavale 2013] and nanoparticles [Gheisi 2014, Chandrinou 2011, Sun 2011]). It was systematically detected upon oxygen rich conditions – applied either during the synthesis or as an additional treatment – and assigned to oxygen interstitials (O_i). However, unless previously reported studies, we could additionally

show that after longer pumping time (24 h) this PL band is not anymore present in the PL spectrum of ZnO smoke.

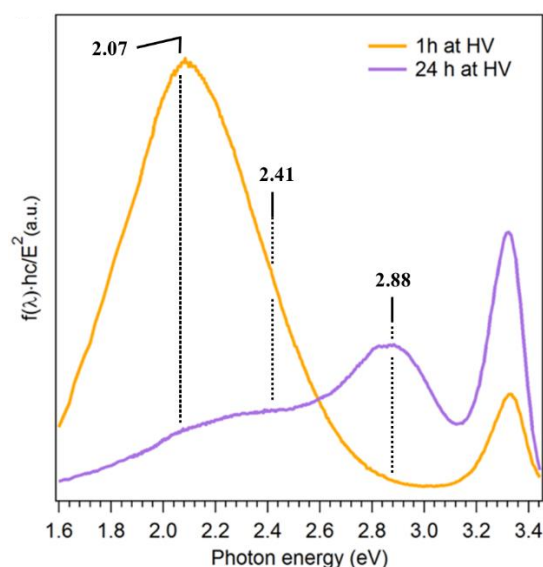


Figure 3.22 PL spectra of ZnO smoke repeatedly annealed in O₂ (3 cycles of T_{ann} = 773 K, P_{O₂} = 100 mbar) then outgassed for 1h at RT (light violet) and for 24h pumping (yellow) [Zhang 2019].

In contrast to the generally accepted picture of YL, being assigned to singly charged oxygen interstitials (O_i⁻), the absence of an EPR counterpart supported the elimination of this defect as a potential candidate for yellow emission [Rauwel 2016, Wu 2001]. Instead, we proposed a peroxide-like entity stabilized at the surface of ZnO nanoparticles where it acts as the recombination center for YL. According to theory [Janotti 2007, Limpijumnong 2005] O_i may be located close to lattice oxygen ions, giving rise to a molecular-like diatomic entity. Such entity would exhibit fully occupied ppπ* orbitals [Janotti 2007, Limpijumnong 2005], with an electronic structure similar to that of O₂²⁻ peroxide species. Not dissociated, such peroxide-species can easily leave the surface as it was confirmed by the disappearance of YL upon more efficient pumping suggesting that the underlying defect is weakly bound to ZnO. This

study demonstrated that under controlled conditions ZnO nanoparticles can serve as an appropriate model system for investigating crystal defects. In addition, considering the investigated condition-specific defects and, thus, PL emissions that range from violet (Zn_i^+), over green (V_o^+) to yellow (O_2^{2-}), ZnO smoke covers almost the whole visible spectrum and represent a good candidate for color specific optical materials. This is illustrated by graphical abstract in Figure 3.23. while the related study [Zhang 2019] is represented by the A-4 article, annexed.

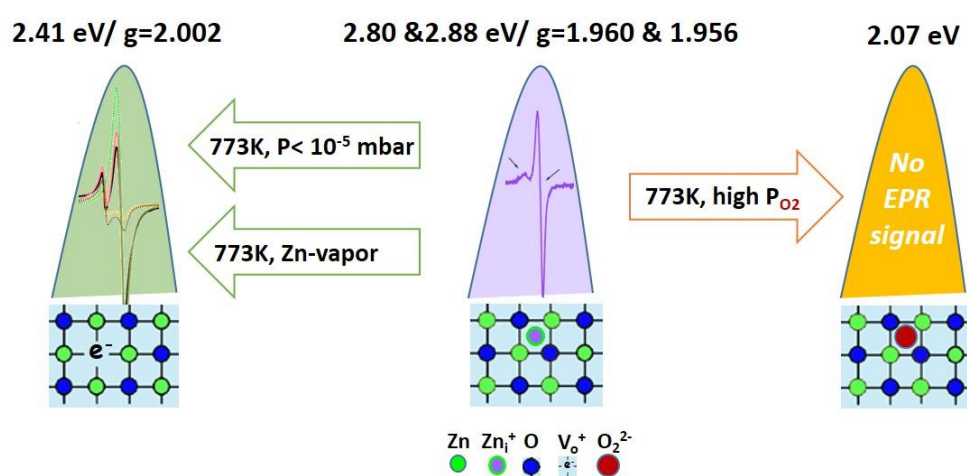


Figure 3.23 Schematic illustration of native defects in ZnO smoke nanopowders, their evolution and formation of new, condition-specific ones [TOC, Zhang Nanoscale 2019].

3.3.2 Point defects in ZnO nanopowders in function of synthesis conditions

As demonstrated in 3.3.1, ZnO smoke reveals two green luminescence bands: at 515 nm (2.41 eV), provoked by an additional thermal annealing, and 495 nm (2.50 eV) already present in PL spectrum of the as-synthesized sample. The former one was attributed to V_o^+ but the nature of the native defect in origin of GL at 2.50 eV remained uncertain. The occurrence of

native defects is strongly dependent on synthesis parameters such Zn and/or O₂ partial pressures in case of ZnO. To unravel the origin of this native defect, we conducted a comparative study on ZnO samples prepared by Zn-combustion either in a glove-box (smoke-samples) or via chemical vapor synthesis (CVS-samples). The former route comprised variations of Ar/O₂-ratios whereas the total pressure in the glove-box was fixed to 1 bar. On the contrary, in CVS flow-reactor the total pressure was reduced to 50 mbar and the partial pressure of oxygen was tuned by varying the Ar/O₂-flows. Four representative samples were selected for this study: smoke-50 and smoke-5 were obtained at Ar/O₂ = 50/50 and Ar/O₂ = 95/5, respectively. CVS samples were produced under the same Ar-flow (1000 sccm) while the oxygen flow was increased from 500 sccm to 1000 sccm during the synthesis of CVS-1 and CVS-2, respectively. As emphasized several times, all of the ZnO powders fabricated by synthesis routes available in our Lab, are free of extrinsic defects. High-vacuum conditions ($P < 10^{-5}$ mbar) during the storage, handling and all spectroscopic characterizations were respected as to avoid the interaction of native defects with environmental molecules (O₂, H₂O, CO₂ etc.) – shown to otherwise lead to the transformation either of defect's oxidation state ($Zn_i^0 \xrightarrow{O_2} Zn_i^+$) or chemical identity ($V_o \xrightarrow{H_2O} OH$) [Kunat 2003, Hu 2013].

The corresponding TEM images of the studied samples (Figure 3.24) reveal that tetrapod-like shapes dominate in all nanopowders except in smoke-50 (Figure 3.24a) – the sample obtained in O₂-richest conditions. The morphology of this sample is mostly dominated by hexagonal prismatic flat rods (Figure 1a) some of which look like pseudo-cubes yet tetrapods can be observed to some extent (inset in Figure 3.24a).

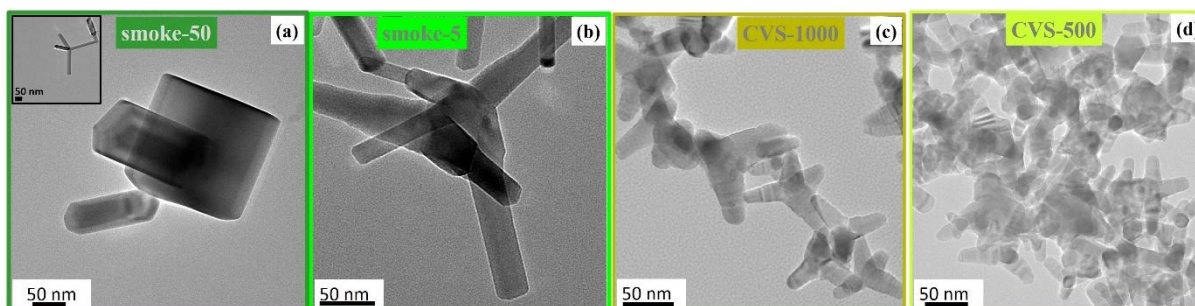


Figure 3.24 TEM images of ZnO nanopowders. (a) smoke-50, (b) smoke-5, (c) CVS-2and (d) CVS-500. The order of samples matches with the decrease of P_{O_2} used for the synthesis [Zhang 2020].

According to HRTEM images and XRD patterns, crystal structure of all the samples was shown to be consistent with wurtzite. The PL/EPR couple ($2.8 \text{ eV}/g=1.96$) previously shown to be related to Zn_i^+ [Zhang 2019] was observed in all – only their corresponding intensities were shown to strongly depend on the P_{O_2} applied during the synthesis. In addition, two green PL bands at 2.5 eV and 2.2 eV were detected without corresponding EPR counterparts. Regarding the UV-Vis absorption properties, smoke-5 and the two CVS samples revealed a red shifted absorption edge compared to that of smoke-50 (Figure 3.25a). Band gap energy of that sample was determined from the Tauc plot E_{BG} (3.26 eV) to be quite close to that reported for ZnO smoke-air (3.25 eV). However, it shifts to 3.23 eV and 3.17 eV for smoke-5 and the two CVS samples, respectively. The shift of the band gap towards visible light – that is observed along with as samples coloration for smoke-5 (pale yellow) and both CVS-samples (almost orange) – is accordingly to DFT and other experimental studies correlated to oxygen vacancies [Kumar 2012, Cuscó 2007].

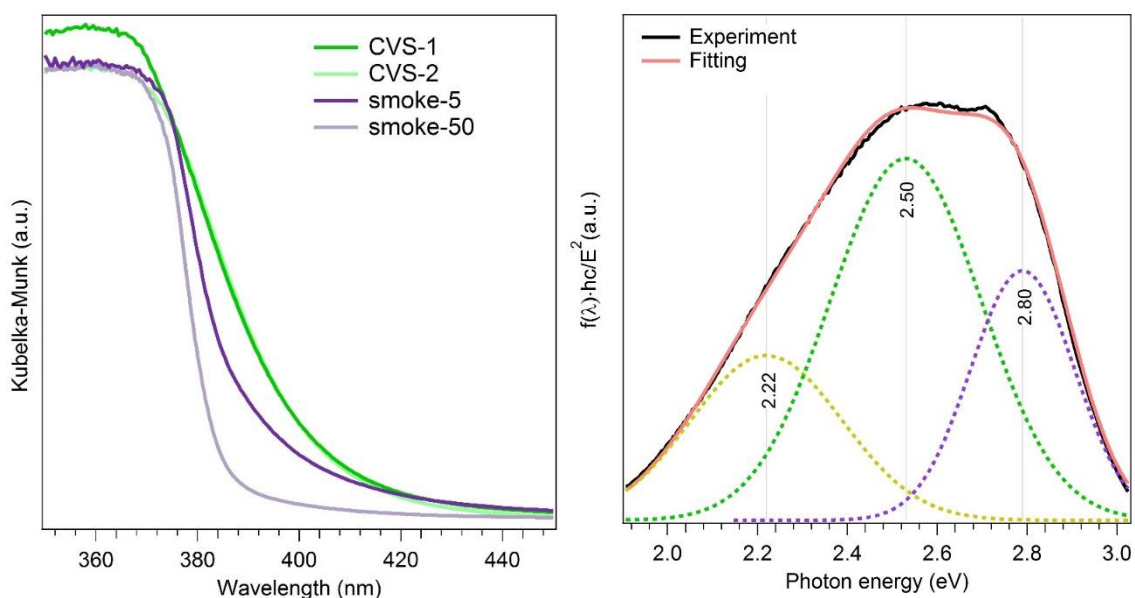


Figure 3.25 (a) DR UV-Vis spectra of smoke-5, smoke-50, CVS-2 and CVS-1. (b) Band fitting analysis of PL spectrum of smoke-5 recorded at $E_{\text{EXC}} = 3.10$ eV (400 nm). Dashed curves correspond to the fitted contributions for individual emission components [Zhang 2020].

Being the most pronounced between smoke-5 and smoke-50, the E_{BG} shift towards lower energy (i.e. towards visible light) was investigated by PL upon using $E_{\text{EXC}} < E_{\text{BG}}$ (Figure 3.25b). From this experiment, we could conclude that in samples with shifted absorption band edge, the contribution of the PL at 2.22 eV is increased. Moreover, this PL contribution was shown to be indispensable to reproduce PL spectra of all the samples – even when the applied excitation energy was higher than the band gap ($E_{\text{EXC}} > E_{\text{B}}$). The corresponding contributions of different visible bands presented in all samples are shown in Table 3 with the contribution of PL at 2.22 eV being clearly favored in samples obtained under lower P_{O_2} .

Table 3: Integration area and relative proportions deduced from fitting of the PL spectra ($E_{Exc}=4.13$ eV) of the smoke and CVS samples.

ZnO sample		←----- PO ₂ ----->			
		smoke-50	smoke-5	CVS-2	CVS-1
Area of PL	2.8 eV	0.83	2.77	4.90	4.32
contribution (x 10 ⁸)	2.50 eV	0.60	1.31	5.51	10.10
	2.22 eV	0.21	0.37	0.42	0.70
Total area (x 10 ⁸)		1.64	4.45	10.83	15.12
Relative proportions	2.8/2.5/2.22	50/37/13	62/30/8	45/51/4	28/67/5

An enhanced contribution of GL emissions at 2.50 and 2.22 eV in samples fabricated at significantly lower P_{O₂} (i.e. in CVS samples) supports their assignment to defects that typically form in such conditions, namely zinc interstitial or oxygen vacancy. Zn_i-related transitions that rather match with violet-blue emission spectral range (405-465 nm i.e. 3.06-2.66 eV) were discarded and EPR inactive oxygen vacancies (V_O²⁺ and V_O⁰) remained the only candidates that could contribute in PL bands at 2.50 eV and 2.22 eV. A lack of oxygen in samples synthesized in lower P_{O₂}, and thus the potential existence of V_O-defects, was further confirmed by Raman and XPS spectroscopies. Finally, the discrimination among V_O²⁺ and V_O⁰ in regard of the two green emission was based on their different formation energies and the difference whether they contain electrons or not. The lowest formation energy in Zn rich conditions among the three types of oxygen vacancies was calculated for V_O²⁺ [Thapa 2016, Li 2013, Knutsen 2012]. Thus, it is expected to prevail over the neutral one (V_O⁰) in our ZnO samples. In all the samples (including smoke-air), GL at 2.50 eV is detected with an intensity higher than that at 2.22 eV, and on this basis associated with V_O²⁺. V_O⁰, considered as a deep donor [Polarz 2005] was consequently linked to the GL at 2.22 eV. Moreover, both DFT and experimental studies [Kumar 2012, Polarz 2005, Erhart 2006b] ascribed the extension of

absorptions towards visible light (Figure 3.25a) to oxygen vacancies, in particular to V_{O}^0 . Indeed, electron containing states within the band gap (which is typically the case for V_{O}^0) are required in this absorption process and lead to sample's coloration.

Finally, Wulff shape constructions of wurzite ZnO was applied on the atypical shape of smoke-50 seen in TE diffractograms. The satisfying matching could be obtained by reducing the contribution of the one of two non-polar facets in ZnO. This is shown in Figure 3.26 where for the sake of clarity, the (11-20) orientation is totally eliminated. Having established the map of naturally occurring defects in ZnO nanoparticles obtained via gas-phase based techniques, this opens up a new relevant research direction in which the stabilization and/ or destabilization of a given surface termination can be investigated in function of the occurring defects.

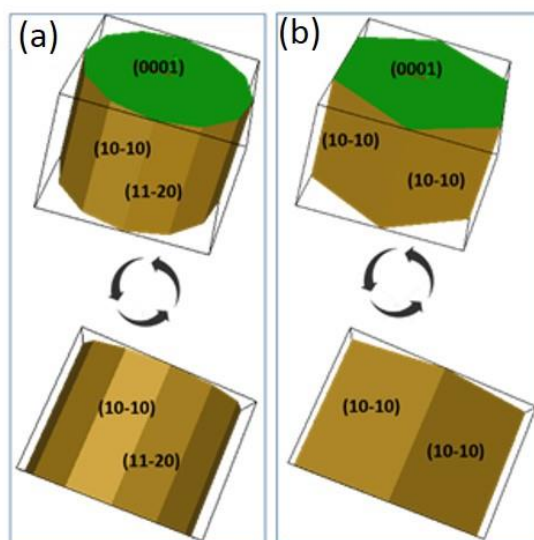


Figure 3.26 Wulff shape constructions for ZnO with different contributions of the non-polar faces: (a) the contribution of the two non-polar faces is equal, (b) the contribution of the (11-20) orientation is negligible. The shapes were rotated in order to illustrate how the hexagonal shape illustrated in (b) can appear as pseudo cubic, such as those observed in TEM images of smoke-50 sample [Zhang 2020].

Metal oxide nanoparticles for antimicrobial purposes 3.4

Apart from the vast applications in fields of technical interest (photonics, energy storage, fuel cells, sensors, paint pigments, catalysis etc.), metal oxide nanoparticles are also widely used in biomedical purposes. These include drug delivery, bio-sensing, imaging and antibacterial therapeutics. To consider nanoparticles for biological applications several key requirements have to be fulfilled. The first is to deal with the engineered nanoparticles of well characterized composition, size, crystallinity and morphology. The second concerns manipulation of stabilized, non-agglomerated nanomaterials in order to control dosing. Finally, the most crucial requirement is their biocompatibility. Presently, microbial resistance to antibiotics has been reaching a critical level. In exploring various options to address this problem, inorganic nanomaterials, like metal oxide nanoparticles, have emerged as promising candidates since they possess greater durability, lower toxicity and higher stability/ selectivity when compared to organic ones. Syntheses of nanoparticles with desired size, shape, morphology, crystal defects and monodispersity provide a rich background for research relevant to antibacterial applications. Characterization of these nanoparticles can be helpful in modifying and tuning their antibacterial and cytotoxic effects. For instance, it has been established that the antibacterial activity increases with decreasing the particles size [Zhang 2007]. In contrast, the crystallographic orientation appears to have no effect on antibacterial activity [Ohira 2008], whereas increasing the lattice constants enhances the antibacterial activity [Yamamoto 2004]. It has also been proposed that different morphologies and crystal growth habits can affect the antibacterial activity [Talebian 2013].

In such context of the studies, we have established a strong collaboration with Dr. J. Vidic, from the Institut de la Recherche Agronomique, Unité Virologie et Immunologie, Jouy en

Josas, France. This collaboration provides a strong interdisciplinary crosslink between biological systems studied at the INRA, on one hand, and fundamental physical chemistry of metal oxide nanoparticles, studied at the INSP. It was further extended within a PHC GALILEE mobility program to the working group of Prof. M. Manzani at the University in Udine.

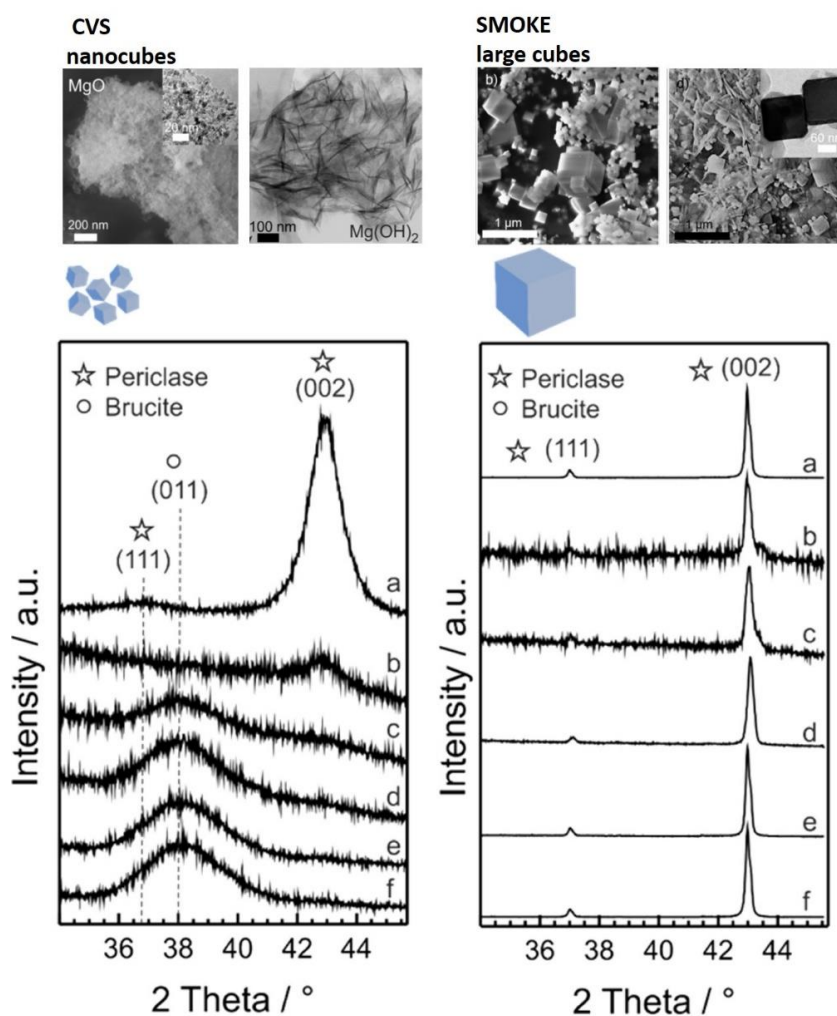
3.4.1 Metal oxide nanoparticle in aqueous solution

As previously illustrated in Section 3.3.1, the way of nanoparticle's synthesis, handling and storage strongly determines their fundamental properties. We could show that by applying the classical surface science approach pristine properties of nanoparticles are preserved. Indeed, through the use of ultra-high vacuum conditions in which the residual pressure of air components is negligible the surface modifications can be avoided. However, when considered for biological applications, nanoparticles are exposed to aqueous environment in which their surfaces typically undergo a series of physico-chemical alterations. Indeed, particle dissolution, aggregation/agglomeration and protein corona formation on the particle surfaces take place in aqueous environment which results in properties that strongly differ from those observed in the as-synthesized forms. Therefore, a prior to biological studies any change caused by water and/ or biological media or fluids, as well as their dispersion and stability, must be understood. In such context, we have shown that in water solutions metal oxide nanoparticles partially dissolve and that this leads not only to their morphological modification but also to formation of new crystallographic phases [Baumann 2015]. Indeed, we have investigated the stability of cubic MgO particles in water and showed that MgO dissolution – proceeding via water dissociation at the oxide surface, disintegration of $\text{Mg}^{2+}\text{-O}^{2-}$ surface elements, and their subsequent solvation – ultimately leads to precipitation

of $\text{Mg}(\text{OH})_2$ nanosheets (see Figure 3.27). At the same time this strongly depends on the particle's size. At an increased pH (≥ 10) CVS-MgO nanocubes with a size distribution below 10 nm quantitatively dissolve within few minutes and convert into $\text{Mg}(\text{OH})_2$ nanosheets. This effect was shown to be significantly different for smoke-MgO with the size distribution ranging from 10 nm to 1000 nm. These, larger cubes were shown to dissolve in water with a significantly lower dissolution rate and undergo etching as demonstrated in previous studies in our group [Hacquart 2009]. Indeed, the (110) faces are formed under etching and these, above a certain face area, dissolve at a rate equal to that of (100) planes. In addition, the delayed solubility of larger, smoke-MgO was shown to be due to the formation of surface hydroxide which consequently induces self-inhibition effects at the (100) and (110)

microplanes. This study confirmed, that the evaluation of stability parameters and dissolution behavior of nanomaterials in aqueous systems is crucial to assess their functionality and fate under environmental conditions and, thus, highly relevant for further biologically oriented research on such systems.

Figure 3.27 TEM images and XRD patterns showing water induced brucite formation in MgO nanocubes (CVS) vs. change in morphology of larger MgO cubes (smoke) [Baumann 2015].



In another study, we have investigated the influence of water and two commonly used cell culture media on the physicochemical properties of a ternary oxide, ZnMgO smoke, and correlated the observed effects to nanoparticles cytotoxicity [Vidic 2014]. ZnO-specific shapes – that could be otherwise seen in TEM images recorded on ZnMgO smoke preserved in high- or ultrahigh vacuum (Figure 3.21a) – could not be detected in powders exposed to water or the Luria–Bertani solution (Figure 3.21b,c,f). At the same time, MgO nanocubes were seen to transform into octahedral form – as underlined by the blue circle in (b).

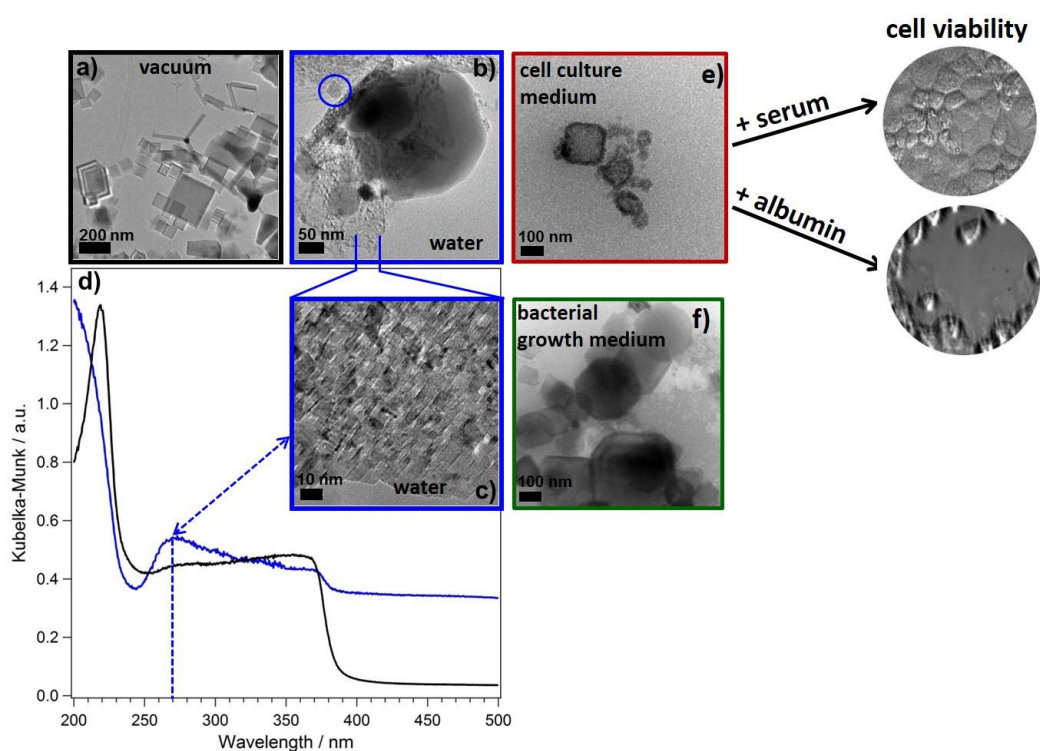


Figure 3.28 TEM images (a–c) and diffuse reflectance UV/vis spectra (d) of as-synthesized ZnMgO smoke (black border and black curve) and water-treated (blue borders and blue curve). Representative Cryo-TEM images of ZnMgO smoke after 24h incubation in RPMI mammalian cell culture medium supplemented with 10% FBS (red) and LB bacterial medium (green), are presented in (e) and (f), respectively. The effect of proteins from biological environment is illustrated in the right panel [Vidic 2014].

The in TEM images observed morphological alternations, caused by water in form of disordered and fragmented structures, were correlated to changes seen in corresponding UV-Vis absorption spectra. This can be best seen at higher magnification as presented in Figure 3.28c in the close-up view where the blue arrow correlates morphological modifications (fragmented structures) with the corresponding change in optical absorption spectrum. In presence of water, the formation of new states within the band gap of ZnO and redistribution of specific sites on MgO surfaces occurs. In mammalian cell culture medium, ZnMgO nanoparticles were shapeless, agglomerated and coated with surrounding proteins (Figure 3.28e) while the serum albumin was found to adsorb as the major yet not the only protein. The investigation on the cytotoxicity showed that in a serum-free medium or a medium containing only albumin ZnMgO was highly toxic. Therefore, the cytotoxicity of an oxide is strongly determined by the surface adsorption of proteins from the surrounding environment through which its biocompatibility can be modulated. Overall, the nanoparticles reach living cells with morphology and surface structure significantly modified in comparison to pristine particles kept in vacuum. The related study is represented by the A-5 article, annexed.

3.4.2 Antibacterial activity vs. toxicity of metal oxide nanoparticles

Pure metal oxide nanoparticles were shown to exhibit different antibacterial mechanisms and effects whereas research in the field of multi-metal oxides still demands extensive exploration. This is understandable given that the relationship between physicochemical properties and biological activity seems to be complex and difficult to generalize even for metal oxide nanoparticles consisting of only one metal component. Also, despite the broad scope that

metal oxide nanoparticles have as antibacterial agents, there arise problems in practical applications taking into account the cytotoxic effects. In this respect, the consideration of polymetallic oxides for biological applications becomes even greater since these can provide synergetic effects and unify the best physicochemical properties of their components. For instance, strong antibacterial efficiency specific of one metal oxide can be complemented by non-cytotoxicity of another. In that context, the antibacterial activity of mixed, ZnMgO nanopowders (smoke-ZnMgO and also those obtained by CVS, $Zn_{0.15}Mg_{0.85}O$) was further studied.

We have studied antibacterial effects of ZnMgO smokes (with Zn content lower than 5 wt%) on Gram-positive (*B. subtilis*) and Gram-negative (*E. coli*) bacteria and compared to those of pure ZnO and MgO smoke nanoparticles [Vidic 2013]. Furthermore, the corresponding toxicological studies have also been conducted on human HeLa cells since an agent can be considered as promising for antibacterial applications only if it is toxic to bacteria but not towards mammalian cells. Among the three studied oxides, ZnO smoke revealed the highest antibacterial efficiency since both types of bacteria were completely eradicated at concentration of 1 mg/mL. At the same concentration, however, this oxide was also found to be toxic towards mammalian cells. On the contrary, MgO smokes are harmless to mammalian cells but only partially inhibit bacterial growth. At the concentration of 1 mg/mL ZnMgO nanoparticles reveal high specific antibacterial activity to Gram-positive bacteria and no human cell damage. Transmission electron microscopy analysis showed that *B. subtilis* cells were damaged after contact with nano-ZnMgO, causing cell contents to leak out. Our study confirmed that mixed oxides reveal synergetic effects of their pure components whereas ZnMgO in particular showed a promising efficient antibacterial efficiency to be considered as a safe new therapeutic for bacterial infections. The antibacterial and toxicological effects of the three studied smoke-oxides are summarized in Figure 3.29 a) and b), respectively.

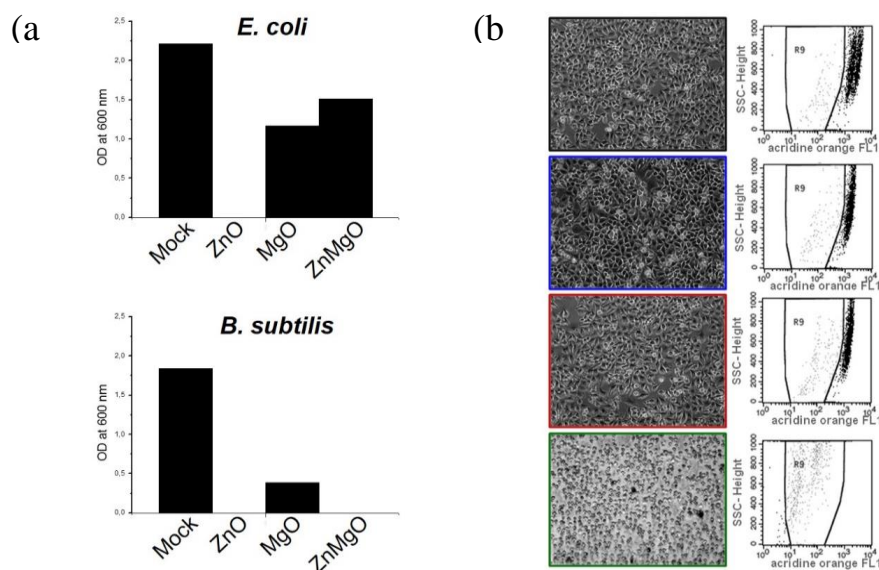


Figure 3.29 (a) Antibacterial efficiency of ZnO (green), MgO (bleu) and ZnMgO (red) nanoparticles at 1 mg/mL tested on *E. coli* (A) and *B. subtilis* (B) after 24 hours incubation. Note that ZnO eliminates completely both bacteria strains while ZnMgO completely eliminated only *B. subtilis*. (b) Optical images of HeLa cells (Mock) and HeLa cells treated with MgO (blue outline), ZnO (green outline) and ZnMgO nanoparticles (24h, mg/mL). Right panel: FACS quantification of nanoparticles cytotoxic effect on HeLa cells [Vidic 2013].

On the other hand, by CVS ZnMgO can be achieved as solid solutions which in line with the Zn-Mg phase diagram [Segnit 1965] exhibit pure rock salt crystal structure – i.e. for Zn concentrations up to 40 at%. As illustrated in Section 3.1.3, such samples consist of ZnO-decorated MgO nanocubes and demonstrate examples of otherwise unstable, high-pressure phase of ZnO. Solid solutions of mixed metal oxides, with, additionally, precise chemical composition, homogeneous size-distribution and well-defined morphology represent model systems that are markedly more useful in the studies related to surface science and those

aimed at biomedical applications. An example is our study on exploring multiple effects of CVS-Zn_{0.15}Mg_{0.85}O nanoparticles on *Bacillus subtilis*, as a model bacterial organism, and on murine macrophages. Zn_{0.15}Mg_{0.85}O powder consist of small monophasic MgO nanocubes whose edges are replaced by Zn-O instead of Mg-O sequences. Homogeneously cubic, small with narrow particle size distribution the Zn_{0.15}Mg_{0.85}O exhibit high surface area and, thus a high concentration of low-coordinated ions and surface defects. As a consequence, this resulted in an enhanced surface reactivity and, hence, an enhanced antibacterial efficiency. Indeed, we could show that Zn_{0.15}Mg_{0.85}O killed planktonic bacterial cells and prevented biofilm formation by causing membrane damages, oxidative stress and metal ions release. Multimode action of Zn_{0.15}Mg_{0.85}O suggested that no single strategy may provide bacterial resistance. Macrophages tolerated Zn_{0.15}Mg_{0.85}O to some extend by both the primary phagocytosis of nanoparticles and the secondary phagocytosis of damaged cells. Bacterial co-treatment with ciprofloxacin and non-toxic amount of Zn_{0.15}Mg_{0.85}O increased antibiotic activity towards *B. subtilis* and *E. coli*. Beside these findings, overall this study shed light on molecular mechanisms involved in metal oxide interactions with bacteria and immunological cells.

4

Summary and Perspectives

Beside a brief summary, the last chapter is devoted to perspectives concerning my future research program. The participation of PhD students, postdocs, and the contribution of research engineers and researchers from the INSP as well as a collaboration with other institutes is foreseen. The project's description is general, it presents main ideas and it is structured with regard to my previous research fields (Chapter 3) covering, thus, stages from the synthesis of metal oxide nanoparticles, over point defects and reactivity to those involving interactions with living organisms. Apart from the continuation in some of the previously described research directions and a new project is foreseen for the next few years with the perspective of expanding the research to 3d transition metal oxide nanoparticles (both, pure and mixed).

The understanding of the mechanisms of particle's formation and growth is indispensable for achieving materials of desired physicochemical properties. In that respect, I could show that the judicious choice of synthesis parameters provides means of controlling over nanoparticle's formation, which is determining for obtaining materials that exhibit predefined: size, shape, crystal structure, type of defects or surface composition and termination.

Type of the synthesis. Firstly, the choice of the synthesis method may itself determine some of these characteristics. This has been nicely illustrated on the example of MgO, which was shown to exhibit cubically shaped nanoparticles of exceptional regularity when produced by combustion in a glove box. On the other hand, via chemical vapor synthesis MgO nanocubes

were achieved much smaller yet with significantly less defined morphology. Regarding ternary oxides, the choice of the synthesis was shown to determine the outcome of mixing. For instance, according to the ZnO-MgO phase diagram, a solid solution with a pure rock salt phase can be formed at maximum Zn concentrations of about 30 at. % and temperatures up to $T \sim 2000^\circ\text{C}$ [Segnit 1965]. However, at higher Zn-concentrations or other T-regime the two oxides form separately – each in its thermodynamically most stable structure i.e. cubic-MgO and wurtzite-ZnO. The first scenario is provided by CVS technique. Powders revealed cubically shaped particles with only one set of XRD peaks, all of them corresponding to rock salt crystal structure. However, powders fabricated by combusting $\text{Zn}_{0.05}\text{Mg}_{0.95}$ alloy in air (GBC route) were shown to consist of cubical and tetrapod-like shapes, typical of MgO and ZnO, respectively, while XRD patterns revealed two crystal phases, cubic and hexagonal – which confirmed the occurrence of the phase separation in this type of ZnMgO powders.

Synthesis parameters. Several parameters can be changed within the two synthesis techniques both of which being based on the combustion of the metal in an oxidizing atmosphere. In case of GBC, this mostly concerns the type and partial pressure of the oxidizing agent (air, O_2 , N_2O). Regarding CVS, the evaporation temperature of metal – that sets its partial pressure – as well as the flow of the transport gas (Ar) and/or the oxidizing agent can be varied. Finally, the system pressure, which usually refers to 1000 mbar in case of GBC or 50 mbar for CVS, can be varied within both techniques. Up to the present, the effect of oxygen partial pressure was mainly studied and it could be demonstrated that an increase in P_{O_2} results in more homogeneous and smaller particles. For instance, by combusting metallic Mg in an argon-oxygen mixture of the ratio corresponding to $\text{Ar}/\text{O}_2 = 80/20$ rather large MgO cubes (~ 80 nm) were obtained while by setting the Ar/O_2 to 20/80 *the size* was able to reduce to ~ 30 nm. At the same time, more homogeneous i.e. powders with narrower particles size distribution was achieved in a more rich O_2 atmosphere during the synthesis.

Apart from the effect on the particle's size, the change in O_2 partial pressure during metal combustion was observed to affect also the ratio of surface terminations which provides means to obtain particles of different *shapes*. An example is given by ZnO that typically exhibits tetrapod-like shapes when produced by GBC synthesis and combusting metallic Zn in air. An increase in P_{O_2} was then shown to result in powders which, apart from tetrapods, reveal in the corresponding TE micrographs also a kind of pseudo-cubical shapes. Deeper analysis of TEM images along with applying Wulff construction implied that these are hexagonal prisms in which one of the non-polar faces was strongly reduced (Figure 3.26).

The change in P_{O_2} – irrespectively if applied within GBC or CVS – was shown to be the determining factor in the formation of specific types of *crystal defects* in ZnO. Their identification was enabled by tracking the qualitative and quantitative changes in the PL and EPR spectroscopic fingerprints as a function of P_{O_2} used during the synthesis. As showed, the same parameter (P_{O_2}) allows to also tune the abundance of a desired defect. In ZnO smoke powders obtained under Zn-rich/ O_2 -poor conditions – typical of combustion synthesis methods – Zn-interstitials (Zn_i) and oxygen vacancies (V_O) were identified as native defects. Overall, ZnO smokes were shown to be richer in Zn_i while the Zn_i/V_O ratio was observed to change with the variation of P_{O_2} . Contrary, in ZnO fabricated under extremely poor O_2 conditions – as provided via specific choice of O_2/Ar flow within CVS – an inversed scenario with V_O defects being dominant over Zn_i was detected. Therefore, by controlling the type and concentration of defects through the synthesis parameters one can obtain ZnO of desired optical properties: ZnO-smokes with dominant Zn_i -defects are more appropriate for violet luminescence whereas CVS powders, which are richer in V_O -defects can be considered for green luminescence.

Supported noble metal nanoclusters. A simultaneous deposition of Ag clusters at MgO surface may be achieved along with the formation of the oxide support. This can be done

within the GBC which provides conditions in which: i) the high formation heat of MgO can be “re-exploited” and, thus, used for Ag-evaporation and ii) the temperature of support (the “just grown” MgO) is as high as necessary for the deposition to take place. Well-defined complex MgO surfaces, including stepped surfaces and contact lines between stacked crystallites, allowed for the growth and analysis of Ag clusters of various orientations. These were seen to systematically adopt the equilibrium shape – the shape of a truncated octahedron –irrespectively of the adsorption site at MgO.

Surface reactivity. Surface chemistry on metal oxides plays an important role in modern society. They are widely used as catalysts, photocatalysts or their interaction with the ambient atmosphere is highly important in the corrosion of metals where the initial stages comprise water adsorption on the surface. Traditionally, the investigation of metal oxide surfaces was, however, restricted to the systematic use of single crystals exposing different crystallographic orientation and the application of ultra-high vacuum conditions. A principal shortcoming of this so called *classical surface science* is that on single crystals the sites that determine the reactivity and, thus, are highly relevant for chemical reactions are present in a relatively low concentration. Alternatively, highly dispersed metal oxides – when obtained by non-equilibrium techniques – exhibit high crystal quality and a considerably enhanced concentration of reactive, low-coordinated surface elements. In that form, as it was shown, they represent suitable models for studying the surface reactivity since reactive surface sites (as well as crystallographic orientations) are experimentally accessible for molecular spectroscopies through which the relationship between topological surface structures and the reactivity can be studied. However, under HV conditions that are typically applied in the studies of highly dispersed systems, the identification of the most reactive sites was rather hindered since they become saturated at much lower pressures and the evolution of their spectroscopic fingerprints masked. This explains why, for instance, only two types of H₂-

chemisorption complexes were initially reported in MgO nanopowders. Studying the surface reactivity while using nanoparticles as model systems in combination with UHV conditions was shown to provide the detection of the very first stages of the adsorption. The adsorption experiments starting at $P_{H_2} < 10^{-8}$ mbar allowed to track an additional OH/MgH pair that was shown to result from H₂-splitting at the most stable sites which are distant at the surface and, hence, kinetically hindered [Haque 2018]. The necessity of UHV conditions was also demonstrated for studying the reactive behavior of surface defects or for the discrimination between different of surface terminations on oxide nanopowders.

Overall, if the synthesis, processing and analysis conditions of metal oxide nanoparticles are strictly controlled, these may represent an adequate model system for studying various surface phenomena. This includes studying the influence of synthesis parameters on particles shape, size, crystal structure, point defects, surface termination etc. The ability to prepare metal oxide nanomaterials of specific size, shape and/ or surface composition (in case of mixed forms) is likely to lead to the development of new antibacterial agents and opens up large field of interdisciplinary based research. Metal oxide nanoparticles represent also suitable models for studying surface reactivity via adsorption of probe molecules or they can be used for the epitaxial growth of noble metal nanoclusters. Apart from the context similar to the above illustrated example studies, the continuation of my research will also include several innovative aspects. Altogether, it can be summarized as following:

i) Fabrication of **tailored nanostructures**

A fundamental understanding of the exposed crystal facets, their surface chemistry and stability as a function of environmental conditions is essential for rational design and improvement of material's synthesis – as well as properties. The stability of a surface is described by its surface energy γ . According to the Gibbs thermodynamic principle, the shape of an equilibrium crystal is obtained by minimizing the total surface free energy associated to

the crystal-medium interface. As a result, most materials minimize their surface energy and produce characteristic equilibrium crystal shapes determined by Wulff's theorem. While liquids exhibit spherical shapes, in the case of solids the minimization of surface energy proceeds via introduction of facets. The surfaces are classified by the net charge Q in a plane and the dipole moment μ of the building block perpendicular to the surface. Surfaces with, $Q \neq 0$ and $\mu \neq 0$ (i.e. they possess the net dipole moment perpendicular to the surface) are polar surfaces and are unstable – due to the diverging electrostatic energy caused by the finite dipole moment in all building blocks. The stabilization of polar surfaces necessarily involve charge modifications of the surface layers through one of the following mechanisms: *surface relaxation, change in surface stoichiometry and adsorption of atoms*. Similarly, such type of mechanisms may also be responsible for favoring or disfavoring of one specific non-polar surface among various.

As demonstrated on the example of ZnO, *changes in surface stoichiometry* may be induced through growth conditions while these are also intimately correlated to the type and concentration of intrinsic defects. Therefore, the surface stability and growth kinetics and, hence, particles morphology, will be investigated in correlation to the intentionally introduced crystal defects whose type and concentration will be controlled via judicious choice of the synthesis conditions. The impact of the *adsorption of atoms* on the morphology of nanoparticles will be studied through the effect of gas phase water from UHV to high water pressures.

- ii) **Surface reactivity** of highly dispersed metal oxides was traditionally studied via FTIR spectroscopy upon adsorbing probe molecules. Never the less, the experimental conditions have generally implied the adsorption at relatively high pressures ($P \geq 10^{-1}$ mbar) which consequently disabled the analysis of the very first stages of the adsorption. In such a way, the identification of the most reactive surface sites – among many and whose reactivity differs

only slightly – was hindered. In addition, a large majority of the reported experiments were performed at the room temperature that made impossible to also evaluate the extent of the molecular vs. dissociative adsorption and, moreover, to estimate the formation enthalpy of the detected adsorption complexes.

Therefore, in the context of surface reactivity, adsorption of diverse probe molecules is foreseen to be studied on model oxide surfaces via IR spectroscopy within the low-temperature regime ($T < 60$ K) and from UHV to atmospheric conditions. This refers to the use of different H-containing molecules (such as H_2 , H_2O , CH_4) as well as to explore in depth the effects of temperature on CO_2 and CO adsorption. The role of crystal defects will be studied in correlation to surface reactivity, too.

The interaction of light with either surface sites or crystal defects in oxide nanoparticles will be further studied via low-temperature photoluminescence spectroscopy. By lowering the temperature, radiationless processes are quenched which results in a better spectral resolution and higher PL yield of the emission processes. This will allow us to explore which part of the broad experimental room-temperature PL signal (in some cases, FWHM ~ 200 nm) is due to vibrations (homogeneous or thermal broadening) and which part is due to the luminescence centers having a different chemical and/or structural environments (inhomogeneous broadening). We then expect to establish an unambiguous correlation between PL processes and the geometric nature of the corresponding optical centers. Moreover, by suppressing exciton transfers at low temperatures both, photo-excitation and photo-emission must occur at originally same centers, which will in addition facilitate their subsequent identification.

- iii) Regarding the **growth of noble metal nanoclusters** on MO_x surfaces, the aim is to move towards systems such Au/MgO and Ag/ZnO . Comparable to previous studies conducted on Ag/MgO , the aim will be to determine surface energies and epitaxial relationships between Au and MgO support as well as to deepen the knowledge of equilibrium shapes of gold

clusters as a function of synthesis conditions. To the present, the Ag/ZnO, which potentially represents an alternative to transparent conductive oxides such as the prototype indium tin oxide, was not much studied. Instead, surface science studies of the epitaxy, morphology, charge transfer and electronic properties of metal deposited on polar ZnO surfaces focused mainly on Cu due to its application as a methanol synthesis catalyst [Martinez-Suarez 2015]. As I could demonstrate, ZnO powders produced by combustion techniques (ZnO smoke) exhibit nanoparticles with well-defined surface facets involving (10 -10), (11 - 20), (0001), and (000-1). Hence, ZnO smokes can be considered as multi-facet single crystals and may provide a good basis for the growth of Ag-nanoparticles and the concomitant analysis of the resulting shape.

- iv) Exhibiting a promising potential for medical applications as an alternative to the existing antibiotics, further continuation of research related to **mixed oxides** is envisaged in a similar context. The bacterial resistance toward antibiotics is an important health issue and the source of serious complications in patient's treatment, even with the fatal ending in the most severe cases. The development of new multifunctional composite nanomaterials (inorganic-organic) for efficient treatment of a given bacterial (for instance *Pseudomonas aeruginosa*) infections represents a crucial task which requests a multidisciplinary approach. A new collaboration with bio-medically oriented research community is recently established with the aim to develop materials composed of ZnMgO-NPs and long chain 4-aminoquinolines and to investigate their anti-virulence and anti-biofilm activity. The given combination of the constituents relies on the following: i) Virulence factors production and biofilm formation are modulated in a cell density-dependent mode through quorum sensing systems (QS) [Whiteley 2017]. Therefore, interference with QS signaling is expected to repress the virulence factors' production leading to less severe infections that could be cleared by the host's immune system. In addition, reducing biofilm formation may increase bacterial susceptibility to antibiotics,

and thus improve the effectiveness of antibacterial therapies. Recently, it was reported that long-chain 4-aminoquinolines (4-AQ) can effectively inhibit biofilm formation and pyocyanin production in *P. aeruginosa* through interference with PQS signaling pathway [Aleksic 2017]. On the other hand, it was also recently reported that $Zn_xMg_{1-x}O$ kills planktonic bacterial cells and, moreover, prevents biofilm formation by causing membrane damages, oxidative stress and metal ions release [Auger 2018] which makes this ternary oxide a suitable candidate as standalone or synergistic agent with other chemotherapeutics.

Studies on MgO-based mixed nanoparticles that are related to more fundamental phenomena such as the surface reactivity (in terms of chemical activity but also interaction with light) are in progress and will be continued as well.

- v) The innovative aspect of my future research is directed to the expanding towards 3d transition metal oxide nanoparticles. The variety of stable oxidation states found with many transition metals results in corresponding oxides of diverse stoichiometries (for example, VO, V_2O_3 , VO_2 and V_2O_5). When obtained in reduced size and low dimensionality their properties are strongly affected, since a large flexibility of their stoichiometry, atomic structure, and electronic characteristics is provided often leading to complex compounds which have no bulk equivalents. Moreover, a large range of applications of their compounds (photovoltaics, photocatalysis, for energy storage and harvesting materials, etc.) is due to the ability of these metals to exist in multiple oxidation states that is particularly important there where upon surface reactions (adsorptions, interactions with light etc.) the oxidation state can be changed. Finally, their potential mixed forms, the combination of two (or more) different 3d transition metals (with cations of different size, electronegativity and reducibility) provide means for the modification of structural (mixing, alloying, janus, core-shell), electronic (band gap engineering) and reactivity characteristics of the parent's oxide. In that context, the modeling of M_2O_3 and mixed $MM'O_3$ structures (with $M, M' = Ti, V, Cr, Fe$) have already been

initiated in our group and a strong dependence of the mixing characteristics on the size and dimensionality of the objects has been predicted [Goniakowski 2019, 2020]. The experimental proof is still missing and, hence, the goal is to fabricate nanostructured forms of these oxides, both in pure and mixed form, and to study their crystal structure (TEM, XRD), surface structure and composition (HRTEM, XPS) and surface reactivity (FTIR via adsorption of small probe molecules: H₂, H₂O, CO etc.). By the synthesis approach available in our Lab (CVS), the particle's sizes can be reduced even down to 2-3 nm. Such reduced dimensions are particularly important when studying the surface structure and composition of mixed metal oxide nanoparticles where several structural motifs can be expected (mixing, alloying, janus, core-shell) as a function of the size.

Finally, development of MgO-TiO₂ based materials for potential recycling of the atmospheric CO₂ is foreseen. Ongoing research in the area of low-carbon technologies mostly relies on materials, which use light and water to transform CO₂ into valuable C1 products. TiO₂ has emerged as an appropriate photocatalytic material for environmental purification yet, it exhibits a poor initial adsorption of CO₂ and, due to its large band gap energy ($E_{BG} \sim 3.2$ eV), it requires UV light for the excitation. The aim is to optimize the drawbacks of bare-TiO₂ by mixing it with MgO. The so far, experimentally unexplored combination is considered on the basis of MgO's basicity whose presence is expected to promote CO₂ adsorption on the TiO₂ surface. In addition, the formation of heterogeneous interfaces in MgO-TiO₂ based system is expected to enhance the interfacial charge transfer rate and spatial separation efficiency of photogenerated charge carriers leading to an improved solar-to-fuel conversion efficiency. The aim is, therefore to provide more fundamental insights into the mechanism of each photoreaction steps upon CO₂ photoreduction over modified TiO₂ in order to optimize such photocatalytic system for a better reduction of CO₂ under solar light and with largely increased quantum yields.

BIBLIOGRAPHY

A

- [**Abraham 1974**] F.F. Abraham; New York, Academic Press, (1974).
- [**Abriou 1999**] D. Abriou and J. Jupille; *Surf. Sci.* 430 (1999) L527.
- [**Aricò 2005**] A.S. Aricò, P. Bruce, B. Scrosati, J-M.Tarascon, W. van Schalkwijk; *Nature Materials* 4, (2005) 366.
- [**Aleksic 2017**] I. Aleksic, S. Segan, F. Andric, M. Zlatanovic, I. Moric, D.M. Opsenica, L. Senerovic; *ACS Chem Biol.* (2017), 12, 1425.
- [**Altieri 2007**] S. Altieri, S. F. Contri, and S. Valeri; *Phys. Rev. B*, 76, (2007) 205413.
- [**Aitani 2000**] H. Aitani, H. Yamada, T. Nishio, T. Shiono, S. Imamura, M. Kudo, S. Hasegawa, T. Tanaka, S. Yoshida; *J. Phys. Chem. B* 104 (2000) 10133.
- [**Anchell 1993**] J.L. Anchell, K. Morokuma, A.C. Hess; *J. Chem. Phys.* 99 (1993) 6004.
- [**Auger 2018**] S. Auger, C. Henry, C. Péchoux, S. Suman, N. Lejal, N. Bertho, T. Larcher, S. Stankic, J. Vidic; *Scientific Reports* (2018) 8, 12276.

B

- [**Bailly 2004**] M.-L. Bailly, G. Costentin, H. Lauron-Pernot, J. M. Krafft, M. Che, J; *Phys. Chem. B* 109 (2004) 2404.
- [**Baumann 2015**] S. O. Baumann, J. Schneider, A. Sternig, D. Thomele, S. Stankic, T. Berger, H. Grönbeck, O. Diwald; *Langmuir* 31 (2015) 2770.
- [**Bauer 1958**] E. Bauer; *Z. Kristallogr.* 110, (1958) 372.
- [**Bäumer 1997**] M. Bäumer, J. Libuda, H.-J. Freund, Chemisorption and Reactivity on Supported Clusters and Thin Films, NATO ASI Series E, Vol. 331; R.M. Lambert, G. Pacchioni (Eds.); Kluwer: Dordrecht, 1997.
- [**Bäumer 1999**] M. Bäumer, H.-J. Freund, *Prog. Surf. Sci.* 61, (1999) 127.
- [**Beck 2008**] K. M. Beck, A. G. Joly, O. Diwald, S. Stankic, P. E. Trevisanutto, P. V. Sushko, A. L. Shluger and W. P. Hess; *Surf. Sci.* 602 (2008) 1968.
- [**Berger 2007**] T. Berger, J. Schuh, M. Sterrer, O. Diwald, E. Knözinger; *Journal of Catalysis* 247 (2007), 61.
- [**Borseth 2006**] T. M. Borseth, B. G. Svensson, A. Y. Kuznetsov, P. Klason, Q. X. Zhao, M. Willander; *Appl. Phys. Lett.* 89 (2006) 262112.

[Brust 2005] M. Brust; *Nature Materials* 4, (2005) 364.

C

[Camarda 2016] P. Camarda, F. Messina, L. Vaccaro, S. Agnello, G. Buscarino, R. Schneider, R. Popescu, D. Gerthsen, R. Lorenzi, F. M. Gelardi; *Phys. Chem. Chem. Phys.* 18 (2016) 16237.

[Campbell 1997] C.T. Campbell; *Surf. Sci. Rep.* 27, (1997) 1.

[Campbell 1987] C. T. Campbell, K. A. Daube and J. M. White, *Surf. Sci.* 182 (1987) 458.

[Chandrinou 2011] C. Chandrinou, N. Boukos, C. Stogios, A. Travlos, *Microelectron. J.* 40 (2009) 296.

[Chatain 1988] D. Chatain, L. Coudurier, N. Eustathopoulos; *Rev. Phys. Appl.* 23, (1988) 1055.

[Chen 2011] M. Chen, Z. Wang, D. Han, F. Gu, G. Guo; *J. Phys. Chem. C* 115 (2011) 12763.

[Chiesa 2003] M. Chiesa, M. C. Paganini, E. Giamello, C. Di Valentin, G. Pacchioni; *Angewandte Chemie International Edition* 42 (2003) 1759.

[Chiesa 2006] M. Chiesa, M. C. Paganini, E. Giamello, D. M. Murphy, C. Di Valentin and G. Pacchioni; *Acc. Chem. Res.* 39 (2006) 861.

[Coluccia 1978] S. Coluccia, A.M. Deane, A.J. Tench, *J. Chem. Soc., Faraday Trans. 1*, 74 (1978) 2913.

[Coluccia 1980] S. Coluccia, F. Boccuzzi, G. Ghiotti, C. Mirra,; *Z. Phys. Chem.* 121 (1980) 141.

[Cuscó 2007] R. Cuscó, E. Alarcón-Lladó, J. Ibanez, L. Artús, J. Jimenez, B. Wang, M. J. Callahan; *Phys. Rev. B: Condens. Matter Mater. Phys.* 75 (2007) 165202.

[Cuko 2018] A. Cuko, M. Calatayud, S. T. Bromley; *Nanoscale* 10 (2) (2018) 832.

[Cushing 2004] B.L.Cushing, V.L. Kolesnichenko, C.O'Connor; *J.Chem.Rev.* 104 (2004) 3893.

D

[Daniel 2004] M.C.Daniel, D.Astruc; *Chem.Rev.*104 (2004) 293.

[Das 2011] G.K. Das, Y. Zhang, L. D'Silva, P. Padmanabhan, B.C. Heng, J.C. Loo, S.T. Selvan, K. K. Bhakoo, T.T.Y. Tan; *Chem. Mater.* 23, 9, (2011) 2439.

[Djurisic 2006] A. B. Djurisic, Y. H. Leung, *Small* 2 (2006) 944.

[Doman 1963] R.C. Doman, J.B. Barr, R.N. Mc Nally, A.M. Alper; *J. Am. Ceram. Soc.* 46 (1963) 313.

[**Dulub 2005**] O. Dulub, B. Meyer, U. Diebold; *Phys. Rev. Lett.* 95 (2005) 136101.

E

[**Epie 2016**] E. Epie, W. Chu; *Appl. Surf. Sci.* 371 (2016) 28.

[**Erhart 2006**] P. Erhart and K. Albe; *Physical Review B*, 73 (2006) 115207.

[**Erhart 2006b**] P. Erhart, K. Albe A. Klein; *Phys. Rev. B: Condens. Matter Mater. Phys.* 73 (2006) 205203.

F

[**Feldho 2007**] A. Feldho, C. Mendive, T. Bredow, and D. Bahnemann; *ChemPhysChem*, 8, (2007) 805.

[**Ferrari 2007**] A. M. Ferrari, C. Roetti, and C. Pisani; *Phys. Chem. Chem. Phys.*; 9, (2007) 2350.

[**Finocchi 2008**] F. Finocchi, R. Hacquart, C. Naud, J. Jupille; *JCP C*, 112 (2008) 13226.

[**Finocchi 2019**] F. Finocchi¹, F. Haque, S. Chenot, J. Jupille and S. Stankic; *J. Mater. Research*, (2019), 408.

G

[**Garrone 1980**] E. Garrone, A. Zecchina, F.S. Stone; *Philos. Mag.* 42 B (1980) 683.

[**Gheisi 2014**] A. R. Gheisi, C. Neygandhi, A. K. Sternig, E. Carrasco, H. Marbach, D. Thomele, O. Diwald; *Phys. Chem. Chem. Phys.* 16 (2014) 23922.

[**Gionco 2013**] C. Gionco, A. Battiato, E. Vittone, M.C. Paganini, E. Giamello; *Journal of Solid State Chemistry*, 201, (2013) 222.

[**Giordano 1998**] L. Giordano, J. Goniakowski, J. Suzanne; *Phys. Rev. Lett.* 81 (1998) 1271.

[**Goodman 1995**] D.W. Goodman, *Surf. Rev. Lett.*, 2, (1995) 9.

[**Gribov 2004**] E.N. Gribov, S. Bertarione, D. Scarano, C. Lamberti, G. Spoto, A. Zecchina; *J. Phys. Chem. B* 108 (2004) 16174.

[**Groppo 2005(a)**] E. Groppo, C. Lamberti, S. Bordiga, G. Spoto and A. Zecchina; *Chem. Rev.* 105 (2005) 115.

[**Groppo 2005(b)**] E. Groppo, C. Lamberti, G. Spoto, S. Bordiga, G. Magnacca, A. Zecchina, *J. Catal.* 236 (2005) 233.

[**Guo 2015**] H.-L. Guo, Q. Zhu, X.-L. Wu, Y.-F. Jiang, X. Xie, A.-W. Xu; *Nanoscale* 7 (2015) 7216.

[Gurwitz 2014] R. Gurwitz, R. Cohen, I. Shalish; *J. Appl. Phys.* 115 (2014) 033701.

H

[Hacquart 2005] R. Hacquart, J.-M. Krafft, G. Costentin, J. Jupille; *Surface Science* 595 (2005) 172.

[Hacquart 2009] R. Hacquart, J. Jupille, *Journal of Crystal Growth* 311 (2009) 4598.

[Haque 2017] F. Haque, S. Chenot, F. Vines, F. Illas, S. Stankic and J. Jupille; *Physical Chemistry Chemical Physics* (2017) 19:10622.

[Haque 2018] F. Haque, F. Finocchi, S. Chenot, J. Jupille and S. Stankic *JPC C*, 122, (2018), 17738.

[He 2009] Y.B. He, A. Tilocca, O. Dulub, A. Selloni, U. Diebold; *Nat. Mater.* 8 (2009) 585.

[Henderson 2002] M.A. Henderson; *Surf. Sci. Rep.* 46 (2002) 1.

[Henry 1998] C.R. Henry; *Surf. Sci. Rep.*, 31, (1998) 231.

[Henry 2005] C.R. Henry; *Progress in Surface Science*, 80, (2005) 92.

[Hill 1998] Th. Hill, M. Mozaffari-Afshar, J. Schmidt, Th. Risse, S. Stempel, M. Heemeier, H.-J. Freund, *Chem. Phys. Lett.*, 292, (1998) 524.

[Hofmann 1997] P. Hofmann, E. Knözinger, O. Diwald, A. Mustafa; *Ber. Bunsenges. Phys. Chem.* 101 (1997) 1722.

[Hu 2013] Hu, H.; Ji, H. F.; Sun, Y., *Phys. Chem. Chem. Phys.* 15 (2013) 16557.

[Hurum 2003] D. C. Hurum, A. G. Agrios, K. A. Gray, T. Rajh, M. C. Thurnauer, *J. Phys. Chem. B* 107 (2003) 4545.

G

[Goniakowski 2019] J. Goniakowski and C. Noguera, *J. Phys. Chem. C* 123 (2019) 7898.

[Goniakowski 2020] J. Goniakowski and C. Noguera, *J. Phys. Chem. C* 124 (2020) 8186.

I

[Ito 1983] T. Ito, M. Kuramoto, M. Yoshioka, T. Tokuda; *J. Phys. Chem.* 87 (1983) 4411.

J

[Janotti 2007] A. Janotti, C. G. Van de Walle, *Phys. Rev. B: Condens. Matter Mater. Phys.* 76 (2007) 165202.

K

[**Knutsen 2012**] K. E. Knutsen, A. Galeckas, A. Zubiaga, F. Tuomisto, G. C. Farlow, B. G. Svensson, A. Y. Kuznetsov; *Phys. Rev. B: Condens. Matter Mater. Phys.* 86 (2012) 121203.

[**Kobayashi 1990**] H. Kobayashi, M. Yamaguchi, T. Ito; *J. Phys. Chem.* 94 (1990) 7206.

[**Kohan 1996**] A.F. Kohan, G. Ceder; *Phys. Rev. B*, 54 (1996) 805.

[**Kim 2003**] Y. D. Kim, T. Wei, J. Stultz, and D. W. Goodman; *Langmuir* 19 (2003) 1140.

[**Kittel 2005**] C. Kittel, Introduction to solid state physics. Wiley: 2005.

[**Kumar 2012**] S. Kumar, P. Sahare; *Nano* 7 (2012) 1250022.

[**Kunat 2013**] Kunat, M.; Girol, S. G.; Burghaus, U.; Woell, C., *J. Phys. Chem. B* 107 (2003) 14350.

L

[**Lahiri 2003**] D. Lahiri, V. Subramanian, T. Shibata, E.E. Wolf, B.A. Bunker, P.V. Kamat, J. Appl. Phys., 93, (2003) 2575.

[**Lamberti 2007**] C. Lamberti, E. Groppo, G. Spoto, S. Bordiga, A. Zecchina; *Adv. Catal.* 51, (2007) 1.

[**Li 2013**] M. Li, G. Xing, G. Xing, B. Wu, T. Wu, X. Zhang, T. C. Sum, *Phys. Rev. B: Condens. Matter Mater. Phys.* 87 (2013) 115309.

[**Limpijumnong 2005**] S. Limpijumnong, X. Li, S.-H. Wei S. Zhang; *Appl. Phys. Lett.* 86, (2005) 211910.

[**Landau 1967**] L.Landau, E.Lifchitz; *Théorie de l'élasticité*, (MIR, Moscow, 1967).

[**Lazzeri 2001**] M. Lazzeri, A. Vittadini, A. Selloni, *Phys. Rev. B*, 63, (2001) 155409.

[**Lazzeri2002**] M. Lazzeri, A. Vittadini, A. Selloni, *Phys. Rev. B*, 65, (2002) 1199011.

[**Look 2005**] D. C. Look, G. C. Farlow, P. Reunchan, S. Limpijumnong, S. Zhang, K. Nordlund; *Phys. Rev. Lett.* 95 (2005) 225502.

[**Liu 1998**] P. Liu, T. Kendelewicz, G.E. Brown, and G.A. Parks; *Surf. Sci.* 287 (1998) 412.

[**Lv 2013**] J. Lv, C. Li; *Appl. Phys. Lett.* 103 (2013) 232114.

M

[**Martin 1995**] S. T. Martin, A. T. Lee, and M. R. Hoffmann; *J. Envir. Sci. Tech.*, (1995) 2567.

- [**Masri 1985**] P. Masri and P.W. Tasker. *Surf. Sci.*, 149 (1985) 209.
- [**Martinez-Suarez 2015**] L. Martinez-Suarez, N. Siemer, J. Frenzel, D. Marx; *ACS Catalysis* 5(7) (2015) 4201.
- [**McKenna 2007**] K. P. McKenna, P. V. Sushko, A. L. Shluger; *Journal of the American Chemical Society* 129 (2007) 8600.
- [**Muller 2000**] P. Muller, R. Kern; *Surface Science*, 457, (2000) 229.
- [**Mullin 2001**] J.W. Mullin, *Crystallization* (Elsevier, 2001) 181.
- [**Markov 1996**] I.V. Markov, World Scientific, Singapore, 1996.
- [**Myrach 2010**] P. Myrach, N. Nilius, S. V. Levchenko, A. Gonchar, T. Risse, K.-P. Dinse, L. A. Boatner, W. Frandsen, R. Horn, H.-J. Freund; *ChemCatChem*, 2, (2010) 854.
- [**Müller 2007**] M. Müller, S. Stankic, O. Diwald, E. Knözinger, P. Sushko, P. Trevisanutto, A. Shluger., *Journal of the American Chemical Society*, 129 (2007), 12491.
- [**Müller 2008**] M. Müller, A. Sternig, S. Stankic, M. Stöger-Pollach, J. Bernardi, E. Knözinger, O. Diwald; *Journal of Physical Chemistry C* 112(25) (2008) 9120.

N

- [**Narayanan 2004**] R. Narayanan and M. El-Sayed, *Nano Letters* 4, (2004) 1343.
- [**Newberg 2011**] J.T. Newberg, D.E. Starr, S. Yamamoto, S. Kaya, T. Kendelewicz, E.R. Mysak, O. Soeren Porsgaard, M.B. Salmeron, G.E. Brown, Jr., A. Nilsson, and H. Bluhm; *J. Phys. Chem. C* 115 (2011) 12864.
- [**Nolan 2005**] M. Nolan, G.W. Watson; *Surf. Sci.* 586 (2005) 25.

O

- [**Oba 2001**] F. Oba, S. R. Nishitani, S. Isotani, H. Adachi, I. Tanaka; *Journal of Applied Physics* 90 (2001) 824.
- [**Oberdorster 2005**] G.Oberdorster, E.Oberdorster, J.Oberdorster; *Environ. Health Perspect.*113 (2005) 823.
- [**Ohira 2008**] T. Ohira, O. Yamamoto, Y. Iida, Z.E. Nakagawa; *J Mater Sci.* 19 (2008) 1407.
- [**Oncák 2015**] M. Oncák, R. Włodarczyk, J. Sauer; *J. Phys. Chem. Lett.* 6 (2015) 2310.
- [**Overbury 1975**] S.H. Overbury, P.A. Bertrand, G.A. Somorjai; *Chem. Rev.*, 75, (1975) 547.

P

- [**Pan 2011**] J. Pan, G. Liu, G. Q. Lu and H.-M. Cheng, *Angew. Chem., Int. Ed.* 50 (2011) 2133.

[Pebley 2017] A. C. Pebley, E. Decolvenaere, T. M. Pollock, and M. J. Gordon; *Nanoscale*, 9 (39), (2017) 15070.

[Persaud 1997] R. Persaud, T.E. Madey, Growth and Properties of Ultra-thin Epitaxial Layers, D.A. King, D.P. Woodruff (Eds.); Elsevier: Amsterdam, 1997.

[Polarz 2005] S. Polarz, A. Roy, M. Merz, S. Halm, D. Schröder, L. Schneider, G. Bacher, F. E. Kruis, M. Driess; *Small* 1 (2005) 540.

[Poonam 2018] K.S. Poonam, S. Navjot, S K Tripathi; *Mater. Res. Express* 6 (2019) 025502.

[Prieto 2013] G. Prieto, J. Zečević, H. Friedrich, K. P. de Jong, P. E. de Jong; *Nature Materials*, 12, (2013) 34.

R

[Rauwel 2016] P. Rauwel, M. Salumaa, A. Aasna, A. Galeckas, E. Rauwel; *J. Nanomater.* 2016 (2016) 19.

[Ricci 2003] D. Ricci, C. Di Valentin, G.F. Pacchioni, P.V. Sushko, A.L. Shluger, E. Giamello; *J. Am. Chem. Soc.* 125 (2003) 738.

[Riss 2008] A. Riss, T. Berger, S. Stankic, J. Bernardi, E. Knözinger, O. Diwald; *Angewandte Chemie - International Edition* 47 (2008), 1496.

[Russell 2005] A. Russell and K. L. Lee, Structure-property relations in nonferrous metals. John Wiley & Sons: 2005.

S

[Saunders 2011] R. B. Saunders, E. McGlynn, M.O. Henry; *Cryst. Growth Des.* 11, 10, (2011), 4581.

[Sayle 2002] Sayle D.C, Maicaneanu S.A, Watson G.W, *Phys. Chem.Chem.Phys.*, 4, (2002) 5189.

[Scarano 2004] D.Scarano, S.Bertarione, F.Cesano, G.Spotto, A.Zecchina, *Surf. Sci.*, 570, (2004) 155.

[Shluger 1992] A. L. Shluger, A. J.D. Gale, C.R.A. Catlow; *J. Phys. Chem.* 96 (1992) 10389.

[Shluger 1999] A. L. Shluger, P.V. Sushko, L.N. Kantorovich; *Phys. Rev. B* 59 (1999) 2417.

[Segnit 1965] E. R. Segnit, A. E. Holland J.; *Am. Ceram. Soc.* 48 (1965) 410.

[Spoto 2004] G. Spoto, E. N. Gribov, G. Ricchiardi, A. Damin, D. Scarano, S. Bordiga, C. Lamberti, A. Zecchina; *Progress in Surface Science* 76 (2004) 71.

[Stankic 2005(a)] S. Stankic, M. Sterrer, P. Hofmann, J. Bernardi, O. Diwald, E. Knözinger; *Nano Lett.*, 5, 10, (2005) 1889.

- [**Stankic 2005(b)**] S. Stankic, M. Müller, O. Diwald, M. Sterrer, E. Knözinger, J. Bernardi; *Angewandte Chemie - International Edition*, 44 (2005), 4917.
- [**Stankic 2006**] S. Stankic, J. Bernardi, O. Diwald, E. Knözinger; *Journal of Physical Chemistry B*, 110 (2006) 13866.
- [**Stankic 2007**] S. Stankic, J. Bernardi, O. Diwald, E. Knözinger; *Journal of Physical Chemistry C*, 111 (2007), 8069.
- [**Stankic 2010**] S. Stankic, A. Sternig, F. Finocchi, J. Bernardi, O. Diwald; *Nanotechnology*, 21(35) (2010), 355603.
- [**Stankic 2011**] S. Stankic, M. Cottura, D. Demaille, C. Noguera, J. Jupille, *J Cryst Growth* 329 (2011) 52.
- [**Stavale 2013**] F. Stavale, N. Nilius, H.-J. Freund; *J. Phys. Chem. Lett.* 4 (2013) 3972.
- [**Sterrer 2002**] M. Sterrer, O. Diwald, E. Knözinger, P. V. Sushko and A. L. Shluger; *J. Phys. Chem. B* 106 (2002) 12478.
- [**Sterrer 2004**] M. Sterrer, T. Berger, S. Stankic, O. Diwald and E. Knözinger; *ChemPhysChem*, 5 (2004) 1695.
- [**Sterrer 2005**] M. Sterrer, T. Berger, O. Diwald, E. Knözinger, P. V. Sushko, A. L. Shluger; *J. Chem. Phys.*, 123 (2005) 064714.
- [**Sternig 2008**] A. Sternig, S. Stankic, M. Müller, J. Bernardi, E. Knözinger, O. Diwald; *Advanced Materials*, 20 (2008), 4840.
- [**Sternig 2012**] A. Sternig, S. Stankic, M. Müller, N. Siedl and O. Diwald; *Nanoscale* 4 (23) (2012) 7494.
- [**Strickler 2017**] A. L. Strickler, M. A. Escudero-Escribano, and T. F. Jaramillo; *Nano Lett.* 17(10) (2017) 6040.
- [**Sushko 2002**] P. V. Sushko, J. L. Gavartin, A. L. Shluger, *Journal of Physical Chemistry B* 106 (2002) 2269.
- [**Sun 2002**] Y. Sun, A. Li, M. Qi, L. Zhang, X. J. Yao, *Mater. Sci.* 37 (2002) 1343.
- [**Sun 2011**] W.-C. Sun, Y.-C. Yeh, C.-T. Ko, J.-H. He, M.-J. Chen; *Nanoscale Res. Lett.* 6 (2011) 556.

T

- [**Tam 2006**] K. H. Tam, C. K. Cheung, Y. H. Leung, A. B. Djurisic, C. C. Ling, C. D. Beling, S. Fung, W. M. Kwok, W. K. Chan, D. L. Philips, L. Ding, W. K. Ge; *J. Phys. Chem. B* 110 (2006) 20865.
- [**Talebian 2013**] N. Talebian, S.M. Amininezhad, M. Doudi.; *J Photochem Photobiol B Biol.* 120 (2013) 66.

[**Thapa 2016**] D. Thapa, J. Huso, J. L. Morrison, C. D. Corolewski, M. D. McCluskey, L. Bergman; *Opt. Mater.* 58 (2016) 382.

[**Tasker 1985**] P.W. Tasker, A.A. Colburn, W.C. Mackrodt; *J. Am. Ceram. Soc.* 63 (1985) 74.

[**Trotochaud 2014**] L. Trotochaud, S. L. Young, J. K. Ranney, and S. W. Boettcher; *J. Am. Chem. Soc.* 136 (18) (2014) 6744.

[**Tuomisto 2005**] F. Tuomisto, K. Saarinen, D. C. Look and G. C. Farlow; *Physical Review B*, 72 (2005) 085206.

V

[**Venables, 1984**] J. A. Venables, G. D. T. Spiller, M. Hanbücken; *Rep. Prog. Phys.*, 47, (1984) 399.

[**Vidic 2013**] J. Vidic, S. Stankic, F. Haque, D. Ciric, R. Le Goffic, A. Vidy, J. Jupille and B. Delmas; *J. Nanopart Res*, 15, (2013) 1595.

[**Vidic 2014**] J.Vidic, F. Haque, J.M. Guigner, A. Vidy, C. Chevalier and S. Stankic; *Langmuir*, 30, (2014) 11366.

[**Vittadini 1998**] A. Vittadini, A. Selloni, F.P. Rotzinger, M. Grätzel; *Phys. Rev. Lett.* 81 (1998) 2954.

W

[**Wu 2001**] X. Wu, G. Siu, C. Fu, H. Ong, *Appl. Phys. Lett.* 78 (2001) 2285.

[**Wulff 1901**] G. Wulff, *Z.; Kristallogr.*, 34, (1901) 449.

[**Whiteley 2017**] M. Whiteley, S.P. Diggle, E.P. Greenberg; *Nature* 551 (2017) 313.

X

[**Xu 2012**] W. Xu, J.Y. Park, K. Kattel, B.A. Bony, W.C. Heo, S. Jin, J.W. Park, Y. Chang, J.Y. Do, K. S. Chae, T.J. Kim, J.A. Park, Y.W. Kwak, G.H. Lee; *New J. Chem.*, 36, (2012) 2361.

[**Xu 2010**] H. Xu, R.Q. Zhang, S.Y. Tong; *Phys. Rev. B* 82 (2010) 155326.

Y

[**Yamamoto 2004**] O. Yamamoto, M. Komatsu, J. Sawai, Z.E. Nakagawa; *J Mater Sci.* 15 (2004) 847.

Z

[Zhang 2001] S. Zhang, S.-H. Wei, A. Zunger; *Phys. Rev. B: Condens. Matter Mater. Phys.* 63 (2001) 075205.

[Zhang 2007] Zhang L, Jiang Y, Ding Y, Povey M, York D; *J Nanoparticle Res.* 9 (2007) 479.

[Zhang 2019] M. Zhang, F. Aversang, F. Haque, P. Boghetti, J-M. Craft, G. Costentin, S. Stankic; *Nanoscale* 11 (2019) 5102.

[Zeng 2010] H. Zeng, G. Duan, Y. Li, S. Yang, X. Xu, W. Cai; *Adv. Funct. Mater.* 20 (2010) 561.

[Zinke-Allmang 1992] M. Zinke-Allmang, L.C. Feldman, M.H. Grabow; *Surf. Sci. Rep.*, 16, (1992) 377.

[Zecchina 1975] A. Zecchina, M.G. Lofthouse, F.S. Stone; *J. Chem. Soc., Faraday Trans. I* 71 (1975) 1476.

[Zecchina 1976] A. Zecchina, F.S. Stone; *J. Chem. Soc., Faraday Trans. I* 72 (1976) 2364.

ANNEXED ARTICLES

A-1: Slavica Stankic, Robinson Cortes-Huerto, Nicoleta Crivat, Dominique Demaille, Jacek Goniakowski and Jacques Jupille: “*Equilibrium shape of supported silver clusters*”; *Nanoscale*, **2013**, 5, 2448.

A-2: Francia Haque, Fabio Finocchi, Stephane Chenot, Jacques Jupille and Slavica Stankic: “*Towards a comprehensive understanding of heterolytic splitting of H₂ at MgO surface defects: site reactivity, proximity effects and co-adsorption of several molecules*”, *JPC C*, **2018** 122, 17738–17747.

A-3: Francia Haque, Stephane Chenot, Francesc Vines, Francesc Illas, Slavica Stankic and Jacques Jupille: “*ZnO powders as multi-facet single crystals*”; *Physical Chemistry Chemical Physics*, **2017**, 19:10622.

A-4: Miao Zhang, Frederic Aversang, Francia Haque, Patrizia Boghetti, Jean-Marc Craft, Guylene Costentin and Slavica Stankic: “*Defect-related multicolor emissions in ZnO tetrapods: from violet, over green to yellow*”, *Nanoscale*, **2019**, 11, 5102–5115.

A-5: Jasmina Vidic, Francia Haque, Jean Michel Guigner, Aurore Vidy, Christophe Chevalier and Slavica Stankic: “*Stability of ZnMgO nanoparticles in different biological media*”; *Langmuir* **2014**, 30, 11366–11374.

Equilibrium shapes of supported silver clusters

Cite this: *Nanoscale*, 2013, 5, 2448Slavica Stankic,^{*ab} Robinson Cortes-Huerto,^{ab} Nicoleta Crivat,^{ab} Dominique Demaille,^{ab} Jacek Goniakowski^{ab} and Jacques Jupille^{ab}

The morphology of silver nanoparticles supported on MgO smoke crystallites was studied by combining Transmission Electron Microscopy (TEM) and atomistic simulations of clusters of realistic size. Advantage was taken of the occurrence of well-defined complex MgO surfaces, including stepped surfaces and contact lines between stacked crystallites, to analyze Ag clusters of various orientations. Silver clusters were seen to adopt systematically the shape of a truncated octahedron irrespective of the support morphology. The (100)Ag/(100)MgO epitaxy was evidenced and (100), (111) and (110) facets were identified. The agreement between observed shapes and simulated profiles demonstrated that the formers were close to equilibrium which allowed the use of Wulff–Kaishev construction to determine the anisotropy ratios $\gamma_{100}/\gamma_{111}$ (1.03 ± 0.03) and $\gamma_{110}/\gamma_{111}$ (1.08 ± 0.03) and the Ag(100)/MgO(100) adhesion energy ($0.58 \pm 0.10 \text{ J m}^{-2}$) for clusters large enough to escape stress effects.

Received 30th November 2012
Accepted 19th January 2013

DOI: 10.1039/c3nr33896g

www.rsc.org/nanoscale

1 Introduction

Metallic nanoparticles embedded in an oxide substrate or supported on its surface are used in a large number of applications. Best known examples are catalysis,^{1–3} environmental chemistry, plasmonics,^{4,5} magnetic information storage and medical applications.⁶ Their broad range of applications results from properties that are strongly determined by the size, shape and crystallographic orientation of exposed facets. For instance, shape-sensitive optical scattering responses of noble metal particles allow surface plasmon resonance to be tuned into a desired wavelength.⁵ Controlling the structure of supported nanoparticles opens a way to promote the reactivity and selectivity of catalysts^{7,8} as well as to tune magnetization.⁶ Therefore, for a rational control and efficient tuning of properties of nanoclusters a pivotal issue is to obtain particles of desired architecture. For this, a prerequisite is to determine surface energies and epitaxial relationships between particles and supports but also to deepen the knowledge of equilibrium shapes.

Equilibrium shapes of supported metal particles result from a balance between surface and interface energies and for sufficiently large clusters they are given by Wulff construction.^{9–12} The fcc late transition and noble metals supported on MgO(100) have attracted much interest in this respect. For those metals that are extensively used for their catalytic,⁷ magnetic⁶ and optical properties,⁵ the combination of abrupt interfaces

with the cube-on-cube epitaxy offers optimal conditions for both measurements^{13–20} and numerical simulations.^{21–27} Direct analyses by TEM of metal–MgO systems were mostly performed on MgO smoke particles.^{13–15,28–30} Free fcc metal clusters show primarily low-energy close-packed (111) facets and (100) facets.³¹ On the other hand, the more open (110) facets tend to disappear during growth. The relatively high surface energy favors high deposition rates so that their existence may be questioned, as in the case of the archetypal silver nanoclusters. By annealing silver clusters in either hydrogen or high vacuum (10^{-3} to 10^{-4} Pa), Sundquist has evidenced shapes that could be represented by a broken bond model involving (111), (100) and (110) facets. However, the orientations of clusters – sizes about $1 \mu\text{m}$ – were not directly evidenced and the presence of impurities could not be neglected.³² The calculated $\gamma_{100}/\gamma_{111}$ and $\gamma_{110}/\gamma_{111}$ anisotropy ratios of the surface energy of silver were found in ranges 1.02–1.15 and 1.06–1.22, respectively.^{33–36} Notably, the latter value (1.22), which is also determined by means of a broken bond approach,³⁵ is the limit at which (110) facets do not show up in the Wulff construction. Finally, cluster nucleation and growth has been often shown to be favored at step sites^{37,38} but very little is known about the impact of support morphology on particle shape, epitaxial relationship with the substrate, conformation of the triple line, and types and proportion of exhibited facets.

The present work reports on the morphology of silver clusters grown on MgO smoke cubes. It combines Transmission Electron Microscopy (TEM) with numerical simulations of clusters of realistic size. MgO smoke crystallites provide a well-defined support to grow the metal nanoparticles. Calculations aim at demonstrating that the observed clusters are close to their equilibrium and escape many effects which can perturb

^cCNRS, Institut des Nanosciences de Paris, UMR7588, 4 Place Jussieu, 75252 Paris Cedex 05, France. E-mail: slavica.stankic@insp.jussieu.fr; Fax: +33 1435 42878; Tel: +33 1442 74650

^bUPMC – Université Paris 06, INSP, UMR 7588, 4 Place Jussieu, 75252 Paris Cedex 05, France

the shape of supported clusters. Advantage was taken of MgO smoke exhibiting particles with multiautomic steps and stacked crystallites – which share one common contact line – to explore the morphology of Ag nanoclusters sitting on sites of complex geometries and confinement.

2 Experimental and theoretical methods

Supported Ag nanoclusters were synthesized by burning magnesium ribbons (Goodfellow, purity 99.9%) wrapped with Ag wires (Goodfellow, purity 99.99%) in such a way that silver crystallites were grown on clean native MgO surfaces at temperatures high enough to provide the equilibrium shape. For the purpose of subsequent transmission electron microscopy (TEM) measurements, a tweezer-type support holding a TEM grid was kept at a constant height (~ 10 cm) above the sampling point, allowing the collection of particles near the generation zone. This procedure is based on previous studies on the synthesis of pure MgO nanopowders.³⁹ The powder was collected straight after the production and kept in a vacuum ($P < 10^{-5}$ mbar) prior to investigation in order to avoid morphology modification by air. TEM analysis was performed on a JEOL 2100 field emission transmission electron microscope operated at 200 kV with a 0.18 nm resolution.

Atomistic simulations of MgO-supported, nano-meter sized Ag particles (6000 atoms with ~ 7 nm of diameter) were performed on a semi-empirical level. Metal–metal interaction was described by the second moment approximation to the tight-binding model^{40–42} with parameterization extended up to the fifth Ag–Ag neighbors, as to additionally improve the calculated surface energies.⁴³ Ag–MgO interaction has been represented by a many-body potential energy surface (PES) adjusted to *ab initio* data,^{22,45} which has already enabled successful studies on equilibrium and growth shapes of Ag/MgO(100) particles^{44–46} and on MgO(100)-induced patterning of Ag films.^{47,48} For the present study, the existing PES of the flat MgO(100) surface was extended by a continuous interpolation between the two adjacent (100) terraces, as to include the [100]-oriented steps. Specificity of MgO edge sites being not taken into account explicitly, such approximation is best suited to large metal particles on MgO substrates with small step density, such that only a small proportion of metal atoms is in contact with MgO edge sites. Since typical global optimization techniques can hardly be applied to such large Ag clusters, both shape optimization and cluster equilibration were performed by molecular dynamics: initial, fairly long runs at high temperature enabled a thorough modification of cluster shapes; shorter runs at room temperature were performed to evaluate the averaged cluster structure and energetics.

3 Results

Equilibrium shapes of silver clusters on MgO terraces, valleys and steps

Powder of MgO smoke consists mostly of nanocubes which show almost perfect (100) facets^{39,49} (Fig. 1) and tend to share common contact lines (Fig. 1a). However, a significant

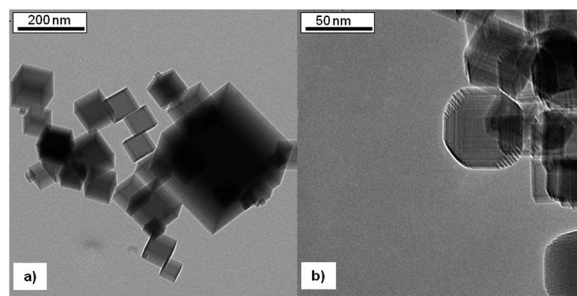


Fig. 1 TEM images of bare MgO smoke nanocubes (a) without and (b) with faceted surface.

proportion of crystallites exhibit also a series of multiautomic steps made of intersecting (100) facets at the vicinity of edges (Fig. 1b).⁴⁹ The experimental protocol used herein leads to MgO powder decorated with Ag clusters of 7 to 50 nm in size. The average shape and size of MgO nanocrystals are not affected by hosting Ag nanoparticles and remain similar to those of bare powder synthesized under similar conditions.³⁹ Ag nanoislands are observed to be present on three types of MgO sites which involve flat (100) terraces, contact lines of stacked cubes and stepped/faceted surfaces. These sites are examined successively in what follows. The TEM image in Fig. 2a shows Ag particles on flat MgO(100) facets. The corresponding HRTEM image (Fig. 2b) reveals an ~ 12 nm large Ag particle, which exhibits a truncated-octahedral profile. The particle is seen along the [011] direction.

Two families of (111) planes with distances of 0.2359 nm and one family of (200) planes with the distance of 0.2043 nm were identified. Measured angles are 70.52° between the two (111) families and 54.74° between (100) family and (111) families. The

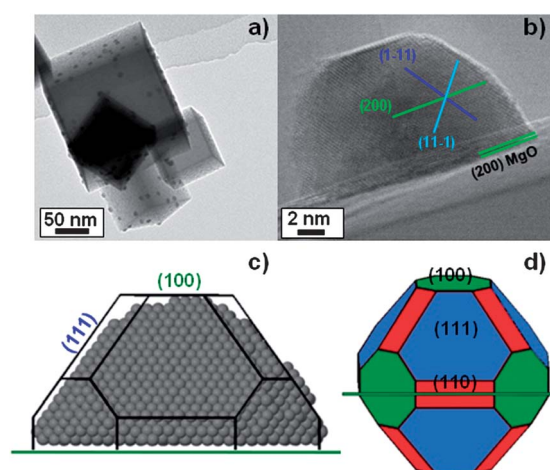


Fig. 2 (a) TEM image of Ag clusters on MgO smoke crystallites; (b) HRTEM image on which traces of (100) (top) and (111) facets exposed by the cluster are shown; (c) theoretically simulated atomic structure of Ag clusters on a flat MgO surface and (d) truncated octahedron shape of a silver nanocluster using the Wulff construction with an indication of (100), (110) and (111) facets that are exposed. Experimentally observed and simulated Ag clusters are analyzed along the [011] axis on flat MgO(100) surfaces.

supported silver particle clearly shows a (100) top facet parallel to the substrate and an adjacent (111) facet. HRTEM analysis evidences also the cube-on-cube epitaxial relationship $(001)\text{Ag}/(001)\text{MgO}$ and $[100]\text{Ag}/[100]\text{MgO}$ that is known to be favored by the rather small mismatch (2.98%) at the Ag–MgO interface – as stated by experimental studies^{18,50} and theoretical calculations.^{26,45,46} Fig. 2c and d present a snapshot of the simulated atomic structure of Ag clusters equilibrated on the flat MgO(100) surface and the deduced schematic representation of the supported particle with the truncated Wulff profile, respectively. In agreement with the experimental profile, the simulated Ag particle exhibits a truncated octahedral shape with (100) epitaxial relationship to the MgO substrate, (100) top facet and four large (111) facets on the cluster sides. In addition, the calculation showed appearance of (110) facets at the edges between adjacent (111) facets (Fig. 2c and d) whereas their presence was not possible to identify in TEM images. Silver clusters grown along contact lines of stacked MgO cubes are shown in Fig. 3a.

The HRTEM image collected along the [001] direction evidences that these clusters are also in the form of a truncated octahedron (Fig. 3b). The main facets – which were identified *via* Fourier transformation – are associated with (100) and (110) planes. The snapshot of the corresponding simulated particle (Fig. 3c) agrees remarkably with the experimental profile. The identification of the (111), (100), and (110) facets (Fig. 3c) gives ground to the schematic truncated Wulff representation (Fig. 3d). Both experimental and simulated silver particles exhibit cube-on-cube epitaxy at Ag–MgO interfaces.

A large proportion of silver clusters sitting along multiatomic steps of MgO crystallites is evidenced in the TEM image shown in Fig. 4. The HRTEM image of such silver clusters located on steps of MgO support is shown in Fig. 4b. In a similar way as in

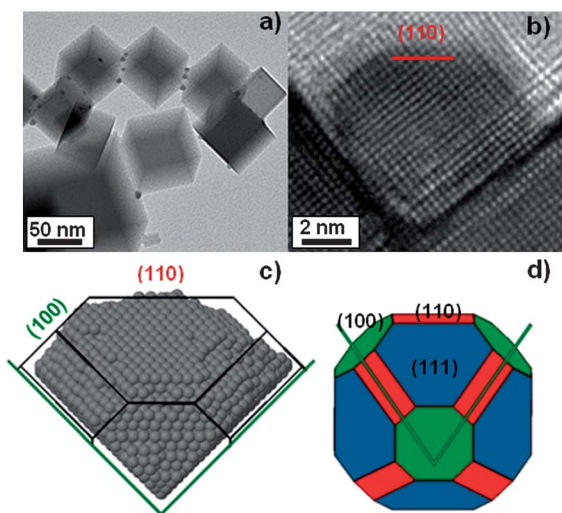


Fig. 3 (a) TEM and (b) HRTEM images of Ag clusters grown along the contact line between two stacked MgO smoke crystallites; (c) the theoretically simulated atomic structure of a Ag cluster sitting on the contact line between two large MgO(100) facets and (d) the corresponding truncated octahedron shape of the Ag aggregate using the Wulff construction with the indication of facet orientations. In all cases the view direction is along the valley, thus [001].

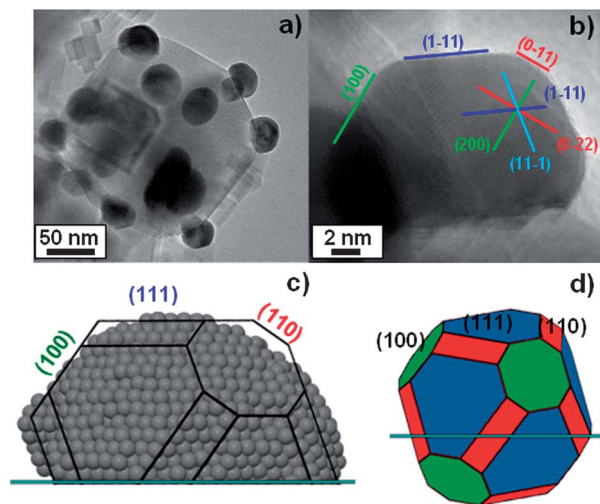


Fig. 4 (a) TEM and (b) HRTEM images of Ag clusters grown on multiatomic steps of MgO smoke crystallites; (c) theoretically simulated atomic structure and the corresponding Wulff shape of the Ag cluster spread over an array of (100) MgO steps, with the indication of facet orientations, including (110); note that the top facet of the Ag cluster is (110); (d) the simulated cluster and the Wulff shape of (c) are rotated to mimic the observed cluster of which image is shown in (b) – in (a) to (c) the view direction is along [011].

cases above, the overall shape is consistent with the truncated octahedron profile. A close inspection of the Fourier-transformed HRTEM image (Fig. 4b) allows for an identification of (111) and (100) planes and, most importantly, for the first time in the series of experimental observations presented herein, a (110) plane is unambiguously observed thanks to a cut through two successive (111) planes separated by a (110) facet. This observation validates the profile that was derived by Sundquist.³² The atomistic model aimed at representing this situation was based on the MgO substrate with equally sized (100) terraces of 2.38 nm to assure that the metal cluster spreads over several steps. The model cluster at equilibrium on a stepped surface preserves the truncated octahedral shape (Fig. 4c) and exhibits cube-on-cube epitaxy on all MgO(100) terraces.

As a consequence, it exposes a top (110) facet parallel to the average orientation of the substrate surface. Since the experimental substrate is much more disoriented with respect to the (100) facets (Fig. 4b), the corresponding cluster shape can be mimicked by rotating the simulated cluster and the corresponding truncated Wulff shape (Fig. 4d). Let us stress that the direct proof of the existence of (110) facets cannot be obtained from the (110) trace seen on clusters in Fig. 2b and 3b since these could only arise from intersections between two adjacent (111) planes. Finally, in all cases the top facet is parallel to the average orientation of the MgO substrate: (100) for flat MgO(100); (110) for clusters sitting at the contact line between two stacked MgO cubic crystallites.

Anisotropy ratios

An excellent agreement between experimental and simulated profiles supports strongly the assumption that the clusters under study are close to their equilibrium. Their shapes are

therefore expected to be ruled by Wulff–Kaishew theorem which enables a well-founded analysis of anisotropy ratios. The HRTEM image of a silver cluster topped by (111) facets with adjacent (110) and (100) facets is presented in Fig. 5a. The case is quite similar to that shown in Fig. 4b but, although the substrate is not clearly seen, the whole profile of the cluster is now visible. Moreover, the particle size is such that the effect of the surface stress can be neglected.⁵¹ In Fig. 5, the identification of three (111) facets allows us to determine the location of the Wulff center *via* straightforward geometry.

As an average over several HRTEM images – similar to that seen in Fig. 4b and 5b – values of $\gamma_{100}/\gamma_{111} = 1.03 \pm 0.03$ and $\gamma_{110}/\gamma_{111} = 1.08 \pm 0.03$ were found, in fair agreement with the values of 1.05 and 1.11 determined by *ab initio* calculations.³⁴ These values correspond to a very small anisotropy. In particular, the surface energies of (111) and (100) facets that dominate the profiles of Ag clusters are almost the same.

The above experiments and simulations demonstrate the existence of (111), (100) and (110) facets on Ag clusters supported on MgO at equilibrium. The finding raises the question of the existence of (110) facets in the Wulff profile of other fcc metals such as Rh, Ir, Ni, Pd, Pt, Cu and Au, of which nano-clusters are involved in many applications. For instance, Ni(110) offers favorable conditions for hydrogenation reaction of CO₂ (ref. 52 and 53) and gold nanobelts with predominant (110) surfaces showing high electrocatalytic activity toward methanol oxidation.⁵⁴ More generally, the open character of the (110) fcc orientation has encouraged specific efforts to synthesize particles that mostly show (110) facets.⁵⁴ Indeed, anisotropies derived from the values tabulated by Vitos *et al.*³³ support the formation of that facet for Ni, Cu, Rh and Pd while making it questionable for Ir and Pt. For Au clusters they discard it totally. However, the profiles of gold clusters analyzed by Sundquist are

consistent with the occurrence of the (110) facet in the same way as in cases of Cu, Ni and Ag but one may wonder whether impurities or adsorbates could have perturbed the measurements.³² With respect to this, we stress that the present approach enables a direct determination of the particle shape of much smaller (nano-metric) particles and in better controlled conditions.

Adhesion energy at the Ag(100)–MgO(100) interface

The capability of the anisotropy ratios to serve as a basis to model the shape of Ag clusters shown in Fig. 2 and 3 can be tested by estimating the adhesion energy. Ag clusters on the flat MgO(100) surface that expose the (100) top facet (Fig. 2) are best defined by the aspect ratio H/D , where H is the height and D is the lateral size of the cluster, as directly measured on the supported particle (Fig. 5c). On a number of silver particles examined herein by HRTEM, this ratio was found to range between 0.50 and 0.63. The adhesion energy is given by $\beta_{100} = 2\gamma_{100}[1 - (H \times \gamma_{100})/(D \times \gamma_{111} \times \sin \theta)]$, where $\theta = 54.74^\circ$ is the angle between (111) and (100) orientations. Using the above $\gamma_{100}/\gamma_{111} = 1.03$ ratio, values of β_{100} range between $0.42\gamma_{100}$ and $0.74\gamma_{100}$ which, by taking $\gamma_{100} = 1.20 \text{ J m}^{-2}$,³³ corresponds to adhesion energies comprised between 0.49 and 0.89 J m^{-2} . On the other hand, quantitative characterization of Ag clusters sitting at the contact lines between stacked MgO cubes (Fig. 3) is not possible through the H/D aspect ratio because the Wulff center cannot be precisely located. Instead, using the heights H_{100} and H_{110} defined in Fig. 5d, the Wulff–Kaishew theorem gives $\beta_{100} = \gamma_{100}(1 - h_s/(H_{100} - h_s))$, with $h_s = (H_{100} - \gamma_{100}H_{100}/\gamma_{110})/[1 - \gamma_{100}\sqrt{2}/\gamma_{110}]$. From the cluster seen in Fig. 3b, a value of $\beta_{100} \sim 0.68\gamma_{100}$ (0.80 J m^{-2} with $\gamma_{100} = 1.20 \text{ J m}^{-2}$) is found. This value and the upper limit of the adhesion energy range ($0.49\text{--}0.89 \text{ J m}^{-2}$) – found by analyzing the clusters grown on flat MgO(100) surfaces – are in fair agreement with the values $\beta_{100} \sim 0.75\text{--}0.85 \text{ J m}^{-2}$ that were obtained by SDRS⁴⁹ and GISAXS^{47,48} analyses. In both these cases, silver clusters were grown on flat MgO(100) under ultra-high vacuum conditions and their sizes were found to be smaller than 10 nm. Thus, lower values obtained in our case ($<0.70 \text{ J m}^{-2}$) can be associated with Ag clusters of larger size. In agreement with theoretical prediction²⁶ the Ag/MgO cluster shape is seen to vary with the cluster size⁵⁵ as in the case of Ag/ α -Al₂O₃(1000).⁵⁶ The lowest values of the adhesion energy were found for Ag clusters of a few tens of nm in diameter for which the effect of size is expected to become marginal.^{26,51} Therefore, the value of $0.58 \pm 0.10 \text{ J m}^{-2}$ – that was averaged on different measurements – can be considered as a reference value of the Ag(100)/MgO(100) adhesion energy.

Relative stability of supported clusters

While most of the existing studies focused on metal particles on flat MgO terraces, Ag clusters in Fig. 3 are seen to appear mostly along the contact lines between stacking MgO crystallites and those in Fig. 4 favor stepped regions with respect to flat terraces. Indeed, the calculations show that stability of Ag clusters at the three considered surfaces of MgO substrate is sensibly different.

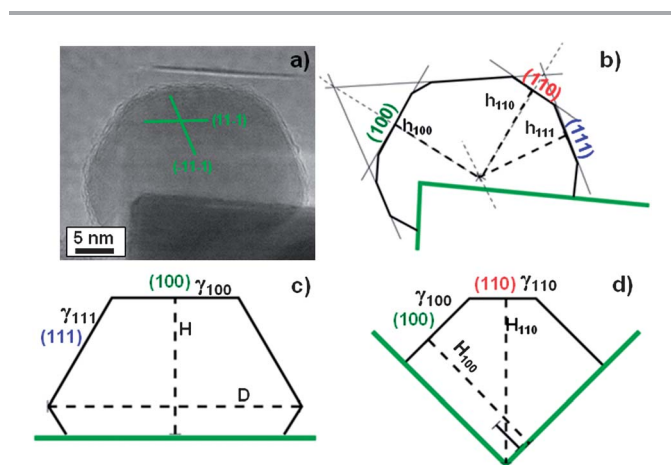


Fig. 5 Common Wulff construction for all analyzed silver clusters: (a) the Ag cluster which exposes enough well-defined facets to allow the determination (b) of the Wulff center through the geometric construction. Schematic representations of Ag clusters, corresponding to Fig. 2 and 3, are shown in (c) and (d) respectively. Structural characteristics used to quantify adhesion energy on the basis of the knowledge of surface anisotropies are indicated as: (i) H/D for an Ag cluster on a flat MgO surface and (ii) H_{100} and H_{110} for Ag on the contact line between two stacked MgO crystallites.

A clear preference is found for the location at the contact lines between two large MgO(100) facets (Fig. 3), while clusters on the stepped MgO surface (Fig. 4) appear to be the least stable. Low stability of Ag particles in the latter case is driven principally by the high density of steps used in the calculations, which implies a large number of exposed under-coordinated Ag atoms at the cluster periphery and at the Ag–MgO interface. Such a high step density may not be a direct representative for the present experimental situation. On the other hand, the enhanced stability of Ag clusters at the contact lines between stacked MgO cubes (Fig. 3) with respect to those on the flat MgO(100) surface can be explained with a simple liquid droplet model in which the total energy is a sum of bulk and surface terms only. For a given volume, the stability is determined by the surface term, including energies of both the free Ag surface and the Ag–MgO interface. Approximating the actual $\beta/\sigma = 0.7$ by $\beta/\sigma = 1$, the liquid droplet takes a semi-sphere shape (radius R_{flat}) and quarter of a sphere (radius R_{line}) on the flat surface and at the contact lines, respectively. At a given volume, the total energy ratio $E_{\text{flat}}/E_{\text{line}} = 2R_{\text{flat}}^2/R_{\text{line}}^2 = 2^{1/3} > 1$, showing that $E_{\text{flat}} > E_{\text{line}}$ is in agreement with the calculated cluster stability. In this simple model, the enhanced droplet stability at the contact lines between stacked particles is due to a significant increase of the interface area ($I_{\text{flat}}/I_{\text{line}} = 2^{-2/3} \sim 0.63$), which overrides the destabilizing effect due to a small increase of surface/volume ratio ($S_{\text{flat}}/S_{\text{line}} = 3 \times 2^{-5/3} \sim 0.94$). The preference for cluster location at the contact line may indeed be coherent with the experimental observation of higher density of clusters at these sites (Fig. 3a).

4 Conclusions

By combining TEM experiments and atomistic simulations of clusters of realistic size we have analyzed the morphology of silver nanoparticles supported on complex surfaces of MgO. These include stepped surfaces and contact lines between stacked crystallites. For all considered supported Ag clusters, the simulated particles reproduce remarkably well the experimental observations. The optimization/equilibration procedure results in cluster shapes consistent with the corresponding equilibrium shapes given by Wulff–Kaisew theorem. The agreement between experimental and simulated particle shapes proves that the Ag particles observed experimentally are close to their local equilibrium. The cube-on-cube epitaxy is systematically found at the Ag/MgO(100) interfaces, as expected from the energetic preference for that epitaxy. The top facet is parallel to the average orientation of the MgO substrate, (100) for flat MgO(100) and (110) for valleys between stacked MgO cubes. The calculations show that the stabilities of the three considered cluster locations are sensibly different. A clear preference is found for the location at the contact line between two large MgO(100) facets.

Silver clusters at equilibrium show (111), (100) and (110) facets with rather small anisotropy $\gamma_{100}/\gamma_{111} = 1.03 \pm 0.03$ and $\gamma_{110}/\gamma_{111} = 1.08 \pm 0.03$. In the case of Ag clusters large enough to escape surface stress effects, the Ag(100)/MgO(100) adhesion energy is found to amount to $0.58 \pm 0.10 \text{ J m}^{-2}$. The existence of

the open (110) facet in the case of silver raise the question of its occurrence in the equilibrium shape of clusters of other fcc metals – especially in the case of Au clusters, where the existing experimental and theoretical evidence is somewhat contradictory. This and the related questions can be unambiguously answered by our innovative approach which uses complex substrate morphology to enable direct observation of (110) facets.

Acknowledgements

The authors gratefully acknowledge the support from the French project ANR-11-BS10-006 MIGRANI.

Notes and references

- 1 *Handbook of Heterogeneous Catalysis*, ed. G. Ertl, H. Knözinger and J. Weitkamp, 1997, vol. 4.
- 2 *Environmental Catalysis*, ed. G. Ertl, H. Knözinger and J. Weitkamp, 1999.
- 3 J. M. Thomas and W. J. Thomas, *Principle and Practice of Heterogeneous Catalysis*, 1997.
- 4 S. A. Maier and H. A. Atwater, *J. Appl. Phys.*, 2005, **98**, 011101.
- 5 M. I. Stockman, *Phys. Today*, 2011, **64**, 39.
- 6 N. A. Frey, S. Peng, K. Cheng and S. H. Sun, *Chem. Soc. Rev.*, 2009, **38**, 2532.
- 7 C. R. Henry, *Surf. Sci. Rep.*, 1998, **31**, 231.
- 8 K. An and G. A. Somorjai, *ChemCatChem*, 2012, **4**, 1512.
- 9 G. Wulff, *Z. Kristallogr.*, 1901, **34**, 449.
- 10 W. L. Winterbottom, *Acta Metall.*, 1967, **15**, 303.
- 11 J. C. Heyraud and J. J. Métois, *J. Cryst. Growth*, 1980, **50**, 571.
- 12 L. D. Marks, *Rep. Prog. Phys.*, 1994, **57**, 603.
- 13 S. Giorgio, C. R. Henry, C. Chapon and J. M. Penisson, *J. Cryst. Growth*, 1990, **100**, 254.
- 14 S. Giorgio, C. Chapon, C. R. Henry, G. Nihoul and J. M. Penisson, *Philos. Mag. A*, 1991, **64**, 87.
- 15 B. Pauwels, G. Van Tendeloo, W. Bouwen, L. T. Kuhn, P. Lievens, H. Lei and M. Hou, *Phys. Rev. B: Condens. Matter Mater. Phys.*, 2000, **62**, 10383.
- 16 G. Renaud, R. Lazzari, C. Revenant, A. Barbier, M. Noblet, O. Ulrich, F. Leroy, J. Jupille, Y. Borensztein, C. R. Henry, J.-P. Deville, F. Scheurer, J. Mane-Mane and O. Fruchart, *Science*, 2003, **300**, 1416.
- 17 C. Revenant, G. Renaud, R. Lazzari and J. Jupille, *Nucl. Instrum. Methods Phys. Res., Sect. B*, 2006, **246**, 112.
- 18 C. Revenant, G. Renaud, R. Lazzari and J. Jupille, *Phys. Rev. B: Condens. Matter Mater. Phys.*, 2009, **79**, 235424.
- 19 R. Lazzari, G. Renaud, C. Revenant, J. Jupille and Y. Borensztein, *Phys. Rev. B: Condens. Matter Mater. Phys.*, 2009, **79**, 125428.
- 20 S. Giorgio, M. Cabie and C. R. Henry, *Gold Bull.*, 2008, **41**, 167.
- 21 J. Oviedo, J. F. Sanz, N. López and F. Illas, *J. Phys. Chem. B*, 2000, **104**, 4342–4348.
- 22 W. Vervisch, C. Mottet and J. Goniakowski, *Phys. Rev. B: Condens. Matter Mater. Phys.*, 2002, **65**, 245411.

- 23 C. Mottet, J. Goniakowski, F. Baletto, R. Ferrando and G. Tréglia, *Phase Transitions*, 2004, **77**, 101.
- 24 J. Goniakowski, C. Mottet and C. Noguera, *Phys. Status Solidi B*, 2006, **243**, 2516.
- 25 R. Ferrando, A. Fortunelli and R. L. Johnston, *Phys. Chem. Chem. Phys.*, 2008, **10**, 640.
- 26 R. Ferrando, G. Rossi, A. C. Levi, Z. Kuntova, F. Nita, A. Jelea, C. Mottet, G. Barcaro, A. Fortunelli and J. Goniakowski, *J. Chem. Phys.*, 2009, **130**, 174702.
- 27 J. Goniakowski, A. Jelea, C. Mottet, G. Barcaro, A. Fortunelli, Z. Kuntová, F. Nita, A. C. Levi, G. Rossi and R. Ferrando, *J. Chem. Phys.*, 2009, **130**, 174703.
- 28 S. Sao-Joao, S. Giorgio, C. Mottet, J. Goniakowski and C. R. Henry, *Surf. Sci.*, 2006, **600**, L86.
- 29 G. Glaspell, H. M. A. Hassan, A. Elzatahry, L. Fuoco, N. R. E. Radwan and M. S. El-Shall, *J. Phys. Chem. B*, 2006, **110**, 21387.
- 30 V. Resta, C. N. Afonso, E. Piscopiello and G. Van Tendeloo, *Phys. Rev. B: Condens. Matter Mater. Phys.*, 2009, **79**, 235409.
- 31 C. R. Henry, *Prog. Surf. Sci.*, 2005, **80**, 92.
- 32 B. E. Sundquist, *Acta Metall.*, 1964, **12**, 67.
- 33 L. Vitos, A. V. Ruban, H. L. Skriver and J. Kollár, *Surf. Sci.*, 1998, **411**, 186.
- 34 Y. Wang, W. Wang, K. N. Fan and J. Deng, *Surf. Sci.*, 2001, **490**, 125.
- 35 I. Galanakis, G. Bihlmayer, V. Bellini, N. Papanikolaou, R. Zeller, S. Blügel and P. H. Dederichs, *Europhys. Lett.*, 2002, **58**, 751.
- 36 W. Luo, W. Hu and S. Xiao, *J. Phys. Chem. C*, 2008, **112**, 2359.
- 37 L. Giordano, C. Di Valentin, J. Goniakowski and G. Pacchioni, *Phys. Rev. Lett.*, 2004, **92**, 096105.
- 38 H. M. Benia, X. Lin, H. J. Gao, N. Nilius and H. J. Freund, *J. Phys. Chem. C*, 2007, **111**, 10528.
- 39 S. Stankic, M. Cottura, D. Demaille, C. Noguera and J. Jupille, *J. Cryst. Growth*, 2011, **329**, 52.
- 40 R. P. Gupta, *Phys. Rev. B: Condens. Matter Mater. Phys.*, 1981, **23**, 6265.
- 41 V. Rosato, M. Guillopé and B. Legrand, *Philos. Mag. A*, 1989, **59**, 321.
- 42 F. Cyrot-Lackmann and F. Ducastelle, *Phys. Rev. B: Condens. Matter Mater. Phys.*, 1971, **4**, 2406.
- 43 F. Cleri and V. Rosato, *Phys. Rev. B: Condens. Matter Mater. Phys.*, 1993, **48**, 22.
- 44 A. Jelea, C. Mottet, J. Goniakowski, G. Rossi and R. Ferrando, *Phys. Rev. B: Condens. Matter Mater. Phys.*, 2009, **79**, 165438.
- 45 A. Jelea, C. Mottet, J. Goniakowski, G. Rossi and R. Ferrando, *Phys. Rev. B: Condens. Matter Mater. Phys.*, 2009, **79**, 165438.
- 46 J. Goniakowski and C. Mottet, *Phys. Rev. B: Condens. Matter Mater. Phys.*, 2010, **81**, 155443.
- 47 A. Ouahab, C. Mottet and J. Goniakowski, *Phys. Rev. B: Condens. Matter Mater. Phys.*, 2005, **72**, 035421.
- 48 F. Leroy, G. Renaud, A. Letoublon, R. Lazzari, C. Mottet and J. Goniakowski, *Phys. Rev. Lett.*, 2005, **95**, 185501.
- 49 R. Hacquart and J. Jupille, *J. Cryst. Growth*, 2009, **311**, 4598.
- 50 O. Robach, G. Renaud and A. Barbier, *Phys. Rev. B: Condens. Matter Mater. Phys.*, 1999, **60**, 5858.
- 51 N. Cabrera, *Surf. Sci.*, 1964, **2**, 320.
- 52 E. Vesselli, L. De Rogatis, X. L. Ding, A. Baraldi, L. Savio, L. Vattuone, M. Rocca, P. Fornasiero, M. Peressi, A. Baldereschi, R. Rosei and G. Comelli, *J. Am. Chem. Soc.*, 2008, **130**, 11417.
- 53 G. Peng, S. J. Sibener, G. C. Schatz and M. Mavrikakis, *Surf. Sci.*, 2012, **606**, 1050.
- 54 G. H. Jeong, M. Kim, Y. W. Lee, W. Choi, W. T. Oh, Q.-H. Park and S. W. Han, *J. Am. Chem. Soc.*, 2009, **131**, 1672.
- 55 S. Stankic *et al.*, unpublished data.
- 56 R. Lazzari and J. Jupille, *Nanotechnology*, 2012, **23**, 135707.

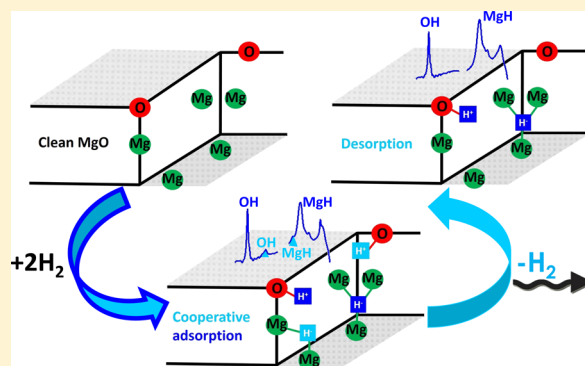
Interplay between Single and Cooperative H₂ Adsorption in the Saturation of Defect Sites at MgO Nanocubes

Francia Haque, Fabio Finocchi, Stephane Chenot, Jacques Jupille, and Slavica Stankic*[✉]

Sorbonne Université, CNRS, Institut des NanoSciences de Paris, INSP, F-75005 Paris, France

Supporting Information

ABSTRACT: The configurations associated with reversible and irreversible adsorption of hydrogen on MgO escape consensus. Here, we report the dissociation of H₂ on MgO nanocubes, which was examined by combining Fourier transform infrared spectroscopy and density functional theory (DFT)-based simulations. We found that the use of ultrahigh vacuum is essential for identifying the very first adsorption stages. Hydrogen pressure was varied from 10⁻⁸ mbar to near ambient, resulting in IR spectra of richer complexity than in current state of the art. Models with oxygen at regular corners (O_{3C}) and Mg at inverse corners (Mg_{1C}) were identified to be the most reactive and to split H₂ irreversibly already in the lowest pressure regime ($P_{\text{H}_2} < 10^{-3}$ mbar). The continuous increase in intensity of the corresponding IR bands (3712/1140 cm⁻¹) in the intermediate range of pressures (10⁻³–1 mbar), along with the appearance of bands at 3605/1225 cm⁻¹, was demonstrated to stem from cooperative adsorption mechanisms, which could be therefore considered as the main origin of irreversible hydrogen adsorption. At $P_{\text{H}_2} > 1$ mbar, fully reversible adsorption was shown to occur at O_{4C} (either on mono- or diatomic steps) and Mg_{3C} sites. Another OH/MgH couple (3697/1030 cm⁻¹) that became reinforced at high P_{H_2} but remained stable upon pumping was correlated to O_{3C} and Mg_{1C} in multiatomic steps. The difference in adsorption and desorption sequences confirmed the proposed cooperative adsorption of H₂ molecules. Our study provides new insights into the mechanisms that can be beneficial for understanding the chemistry of H₂ and other hydrogen-containing molecules, such as CH₄, on oxide surfaces, but also for the advancement of hydrogen-storage technologies.



1. INTRODUCTION

Understanding hydrogen adsorption and dissociation on oxide surfaces is central to unraveling many chemical and physical processes that involve hydrogen-containing molecules. A better comprehension of mechanisms for hydrogen storage is also necessary as to meet hydrogen storage requirements established by the Department of Energy. The prototypical system for studying the hydrogen interaction with oxide surface sites is represented by MgO nanocrystals. The formation of hydroxyl and hydride groups, as evidenced by infrared spectroscopy upon interaction of hydrogen with MgO powders, was first assigned to H⁺/H⁻ heterolytic dissociation on low-coordinated O²⁻/Mg²⁺ pairs, respectively.¹ This experimental study was followed by a series of computational works^{2–5} in which the chemical activity of MgO surface atoms was found to be in a strong correlation with their coordination number. In particular, at least one 3-coordinated site was judged as necessary for a stable hydrogen adsorption on the MgO surface.⁶ On highly dispersed MgO, two H₂-adsorption channels were identified to give rise for OH/MgH stretching vibrations with frequencies at 3712/1125 and 3460/1325 cm⁻¹.⁷ In the same study, the former couple was observed to be irreversible upon H₂ evacuation and was assigned to

homolytic H₂-splitting, a process that should involve paramagnetic O⁻/Mg⁺ species. Later, however, an electron paramagnetic resonance-based study discarded the existence of such species on a clean MgO surface and demonstrated that both of the IR-detected OH/MgH couples must stem from heterolytic dissociation processes.⁸ At $P_{\text{H}_2} \geq 1$ mbar, the irreversible OH/MgH couple was observed to reach its saturation limit, whereas the second one (3460/1325 cm⁻¹) starts growing at this pressure and can be completely removed upon H₂ evacuation, being, thus, referred as reversible.^{7,8}

Many efforts have been invested to establish a correlation between the two above-mentioned H₂ adsorption processes and appropriate surface configurations. 3-Coordinated Mg–O pairs (Mg_{3C}O_{3C}) including subsequent stabilization by H-bonding were first suggested by Knözinger et al.⁷ To explain the irreversible adsorption, H⁻ was proposed to adsorb at an inverse corner where it is shared between three Mg ions along with H⁺ being adsorbed at neighboring O_{4C}.^{9–11} The bonding of H⁻ at an inverse corner was then extended to the crossing

Received: April 4, 2018

Revised: June 29, 2018

Published: July 18, 2018

point of two monoatomic steps (H^- being bonded to two $\text{Mg}_{4\text{C}}$ and one $\text{Mg}_{5\text{C}}$) in combination with a $\text{O}_{4\text{C}}-\text{H}^+$ moiety.¹⁰ The reversible dissociative adsorption was attributed to $\text{O}_{4\text{C}}$ and Mg sites on two neighboring $\langle 100 \rangle$ steps⁹ or by placing the H^+ ion on the $\text{O}_{5\text{C}}$ atom situated at the bottom of the inverse corner.¹⁰ Finally, in ref 11, the irreversible adsorption of H^+/H^- fragments was associated with $\text{O}_{3\text{C}}$ and $\text{Mg}_{1\text{C}}$ (two $\text{Mg}_{4\text{C}}$ and one $\text{Mg}_{5\text{C}}$) sites. For reversible adsorption, this group of authors put forward an oxygen inverse corner in which H^+ is shared between three $\text{O}_{5\text{C}}$ atoms and H^- sitting shared between two adjacent $\text{Mg}_{5\text{C}}$ atoms. Among quite different surface structures reported so far, a common point is the key role suggested for inverse corners.^{7,9–11} These interpretations, with the exception of the work by Ricci et al.¹⁰ and Cavalleri et al.,¹² are solely based on experimental data. The proposed configurations vary mainly regarding the coordinate number of the anions (or cations) of which the corresponding inverse corner is built. Although the nature of the sites that are involved in H_2 is still controversial, a systematic approach combining theory and experiments is lacking. Moreover, on the experimental side, the partial pressures of hydrogen that have been used range between 1 and 100 mbar, which does not allow us to test the stability of the observed configurations over a large pressure range.

The present work reports on a combined Fourier transform infrared (FTIR) study and first-principles calculations on H_2 adsorption at MgO surface. MgO nanocrystals were synthesized via chemical vapor synthesis (CVS) to provide high surface area ($\geq 300 \text{ m}^2 \text{ g}^{-1}$) with a significant contribution of defects such as steps, edges, corners, and inverse steps and corners. Adsorption of H_2 was probed at partial pressures ranging from ultrahigh vacuum (UHV) (10^{-8} mbar) to almost ambient (100 mbar) to allow the determination of the pressure threshold. The objective is to identify microscopic H^+/H^- adsorption sites via frequencies and adsorption free energy estimated by ab initio calculations.

2. METHODS

2.1. Synthesis and FTIR Measurements. Measurements have been performed in a UHV apparatus involving a preparation chamber and a main chamber, both including working pressure in the 10^{-10} mbar range. Fourier transform infrared (FTIR) spectroscopy was performed on MgO pellets in the main chamber (through ZnSe windows) in the transmission mode by means of a Bruker Vertex 70 FTIR spectrometer equipped with a MCT detector. Blanks were collected prior to exposure and used as references. MgO powders were obtained via the CVS technique.¹³ The specific surface area of the resulting MgO material is $365 \text{ m}^2 \text{ g}^{-1}$ as determined by Brunauer–Emmett–Teller (LN_2) measurements. Transmission electron microscopy (TEM) analysis of the particles was achieved using a JEOL 2100 field emission transmission electron microscope operated at 200 kV with a 0.18 nm resolution. The statistics used to plot particle size distribution involved an observation of more than 300 particles. As a starting material, high-purity Mg pieces ($>99.98\%$) supplied by Goodfellow were used. The CVS-MgO powder was pressed into pellets with an applied pressure of less than 5 bar to avoid any changes in the specific surface area. Prior to being transferred in the main analysis chamber, MgO pellets were degassed at 1170 K in UHV for 1 h in the preparation chamber. The applied annealing treatment guarantees adsorbate-free MgO surfaces, which was confirmed

by the absence of any adsorbed impurity in the initial infrared spectrum of MgO only. Reference spectra used for the subtraction were recorded on the degassed MgO pellet in UHV. Hydrogen that was used for adsorption was supplied by Air Liquide with purity 99.999%. The IR spectra were recorded with a resolution of 4 cm^{-1} by averaging 250 interferogram scans to obtain a reasonable signal-to-noise ratio.

2.2. Density Functional Theory (DFT) Calculations.

The calculations were performed using the Quantum Espresso program suite,¹⁴ within the generalized gradient approximation (Perdew–Burke–Ernzerhof)¹⁵ to density functional theory (DFT).¹⁶ We accounted for the interaction between the ionic cores and the valence electrons by ultrasoft pseudopotentials (see Supporting Information for details).

The periodic slabs are at least seven atomic (001) layer thick, with one or two fixed central layers and a large enough void space. The defect sites were simulated through the use of shifted periodic boundary conditions: first, we built up the MgO(001) slabs. We then adopted peculiar base vectors to represent vicinal (01*n*) or (02*n*) surfaces ($n = 5–7$), with mono- or diatomic steps, and 4-fold-coordinated atoms on the ledge.¹⁷ To simulate defects with lower coordination numbers, we applied shifted periodic boundary conditions along the step direction, too. In this way, we could simulate corners and reverse corners on mono- and diatomic steps on MgO surfaces (Figure 1).

We studied other models for H_2 splitting, such as MgO(011) surfaces, which show straight ledges with an equal number of O and Mg ions along the $[100]$ direction. We also considered point defects, such as MgO divacancies in variable number NV_{MgO} ($\text{NV}_{\text{MgO}} = 1–3$) on terraces and monoatomic steps, as they are active sites for the dissociation of water and other molecules.¹⁸ Overall, we examined almost a hundred nonequivalent adsorption configurations.

In all cases, we checked that the computed H_2 adsorption energies are almost independent of the specific shifted boundary conditions that we used. In the limit of very low H_2 coverage, that is, a single H_2 molecule that splits at a given defect, the characteristics of the formed complexes are mostly influenced by the local conformation of the ions. In contrast, the coadsorption of several H_2 molecules or in the limit of high coverage depends on the defect geometry on a larger scale. For the most stable and representative adsorption configurations, we computed the dynamical matrix and the effective charge tensor within the density functional perturbation theory including up to third neighbors of the H^+ , H^- complexes. From these quantities, we determined the mode frequency and eigenvectors, as well as their relative intensities. To compare the computed with experimentally observed OH frequencies, the former ones were rescaled (see Supporting Information).

2.3. Ab Initio Adsorption Free Energy and Pressure.

The adsorption energy, ΔE_{ad} , at 0 K for $n\text{H}_2$ molecules has been computed through the difference of the total energy, E_{tot} , of the MgO(*ijk*) slab with adsorbed H and the sum of the total energies of the clean slab (with the same shifted periodic boundary conditions) and the isolated H_2 molecule as

$$\Delta E_{\text{ad}} = E_{\text{tot}}(2n\text{H}; \text{MgO}(ijk)) - nE_{\text{tot}}(\text{H}_{2(\text{gas})}) - E_{\text{tot}}(\text{MgO}(ijk)) \quad (1)$$

The molar adsorption energy is then obtained as $\Delta \epsilon_{\text{ad}} = \Delta E_{\text{ad}}/n$. A large negative $\Delta \epsilon_{\text{ad}}$ denotes the stability of the product (the surface with H adatoms) over the reactants (the clean

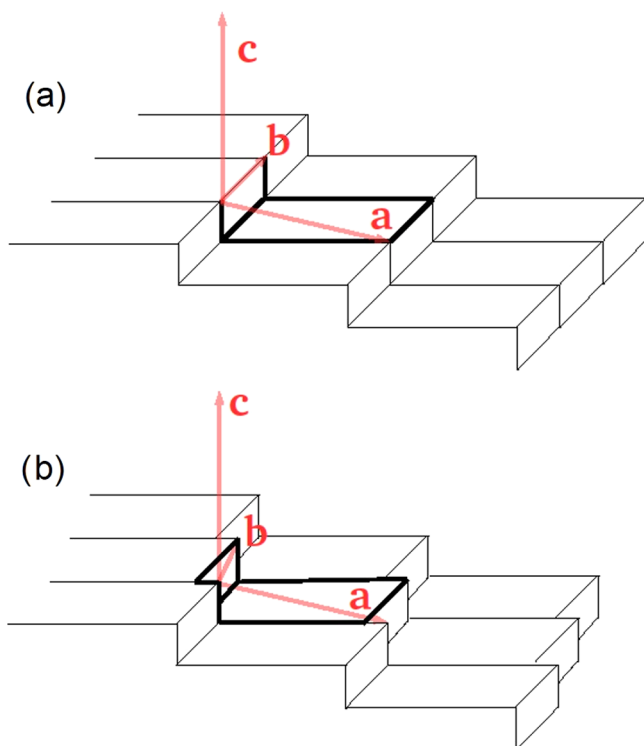


Figure 1. (A) High-index periodic surfaces represented through shifted periodic boundary conditions. Top: shifted periodic boundary conditions for vicinal surfaces with straight steps. In red are shown the base vectors: $a = a_0 (n_1, 0, -h)$; $b = a_0 (0, n_2, 0)$; and $c = a_0 (0, 0, n_3)$. n_1 is the width of the terrace, h the step height in units of the MgO lattice constant a_0 . (B) Shifted periodic boundary conditions for vicinal surfaces with kinks. Base vectors: $a = a_0 (n_1, 0, -h)$; $b = a_0 (-k, n_2, 0)$; and $c = a_0 (0, 0, n_3)$. k is the width of the kink on the step in units of the MgO lattice constant a_0 . In both cases, we draw only the topmost layer of the periodic surfaces. A thick line represents the repeated unit.

surface and the H_2 molecules in the gas phase). However, one cannot compare this standard procedure directly with experiments, which monitor adsorption as a function of the H_2 partial pressure, P . The pertinent quantity to look at is the Gibbs adsorption free energy, $\Delta g_{\text{ad}}(P, T)$, which is the difference between the thermodynamic potentials of products and reactants at a given pressure P and temperature T . $\Delta g_{\text{ad}}(P, T)$ can be approximated as

$$\Delta g_{\text{ad}}(P, T) = \Delta \varepsilon_{\text{ad}} - g_{\text{tra}}(P, T) - g_{\text{rot}}(P, T) \quad (2)$$

The translational $g_{\text{tra}}(P, T)$ and rotational $g_{\text{rot}}(P, T)$ contributions to the molar Gibbs free energy of the H_2 molecule in the gas phase were evaluated analytically within the ideal-gas approximation. More details can be found in the [Supporting Information](#).

For any temperature, we define the thermodynamic threshold pressure, P_{ad} , for H_2 dissociative adsorption on the actual surface defect as that for which $\Delta g_{\text{ad}}(P_{\text{ad}}, T) = 0$. Within the previous approximations, P_{ad} reads

$$P_{\text{ad}} = (k_{\text{B}}T^2/2\Theta\Lambda^3) \exp(\Delta \varepsilon_{\text{ad}}/RT) \quad (3)$$

where the characteristic rotational temperature for H_2 is $\Theta \sim 85$ K and $\Lambda = h/(2\pi M k_{\text{B}}T)^{1/2}$ is the thermal wavelength. The computed P_{ad} can then be compared with the onset of H_2 adsorption as experimentally measured, for each adsorption

configuration, under the hypothesis that adsorption and desorption of H_2 are mainly governed by thermodynamics. Moreover, we note that an error of 10 kJ/mol (or 0.1 eV/ H_2) on the molar adsorption energy, $\Delta \varepsilon_{\text{ad}}$, impacts P_{ad} by a factor ~ 50 at room temperature, which should be thus considered an estimate rather than a precise value.

3. EXPERIMENTAL RESULTS

The TEM image of MgO fabricated by CVS is presented in [Figure 2](#). The powder consists of cubical particles, which

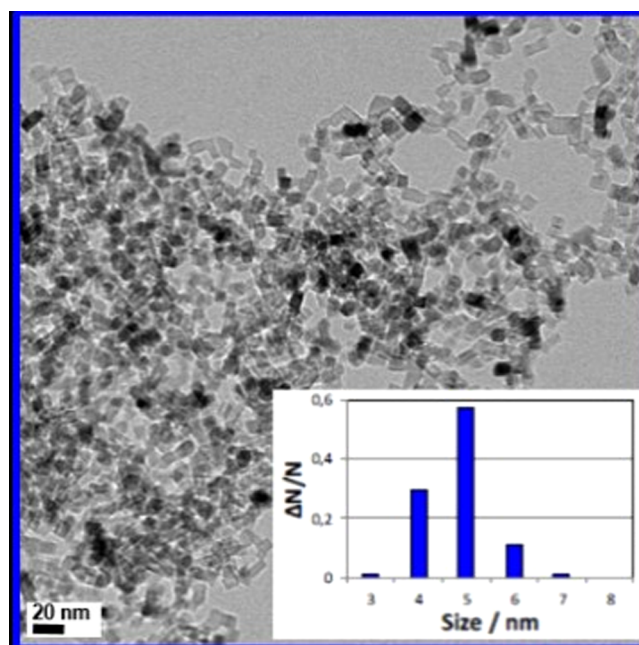


Figure 2. TEM image of MgO nanoparticles. The inset shows the diagram of particle size distribution.

exhibit a quite narrow size distribution of 5 ± 2 nm (inset of [Figure 2](#)). In addition, nanocubes appear as an ensemble of particles that share contact lines. These were found to serve as nucleation sites for the growth of metal clusters¹⁹ but also to systematically provide inverse corners, which are often invoked in the chemistry of hydrogen.^{9–11} The evolution of IR bands was monitored as a function of the hydrogen partial pressure, P_{H_2} , within the 10^{-8} –100 mbar pressure range. The appearance of infrared bands can be described according to three pressure domains: (i) low (up to 10^{-3} mbar), intermediate ($\sim 10^{-3}$ –1 mbar), and high (>1 mbar) that are indicated in blue, cyan, and green, respectively, in [Figure 3](#).

For the purpose of IR measurements, pellets of 25 mm in diameter were prepared out of 50 mg of MgO powder. Having the specific surface area of ~ 365 m² g⁻¹, it implies that such a pellet equals MgO surface of 15 m². Because exposures to hydrogen last 10 min, a pressure of $\sim 2 \times 10^{-5}$ mbar is required to saturate the pellets, by assuming a fast diffusion of hydrogen. Spectra recorded below 10^{-5} are therefore not quantitatively significant. IR bands at 3712, ~ 1140 and 863 cm⁻¹, as well as the shoulder at 3697 cm⁻¹ are the first that appear. Their intensity grows until the pressure reaches 1 mbar. Thereafter, the saturation limit is reached and no significant changes can be observed regarding the underlined bands. However, when the pressure changes from 10^{-3} mbar, a strong intensity boost is observed for all of these bands along with an appearance of

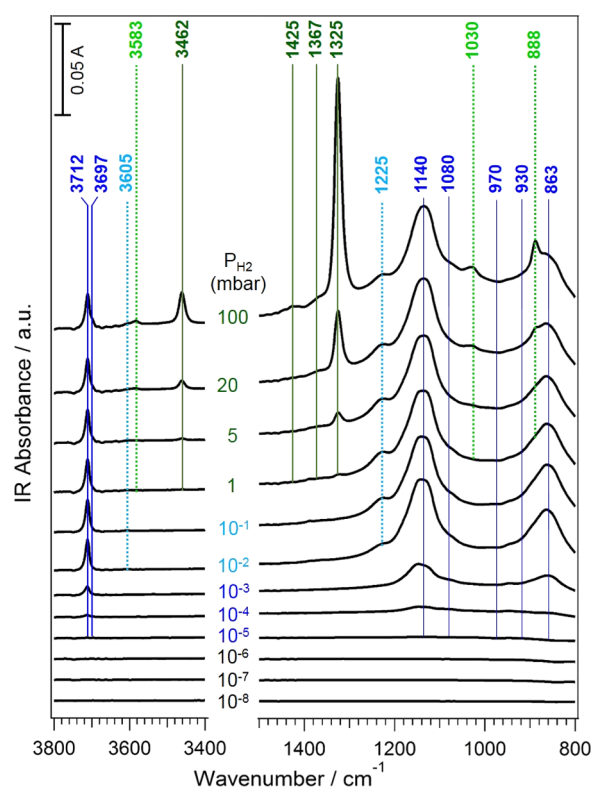


Figure 3. IR spectra of MgO exposed to $P_{\text{H}_2} = 10^{-8}$ –100 mbar. Three P_{H_2} regimes can be distinguished: low, $<10^{-2}$ mbar (blue); intermediate, $\sim 10^{-2}$ –1 mbar (cyan); and high, >1 mbar (green and light green).

new bands at ~ 3605 and 1225 cm^{-1} (marked cyan in Figure 3) with rather low intensity. The evolution of the band at $\sim 3605 \text{ cm}^{-1}$ is shown in Figure S1 (Supporting Information). At $P_{\text{H}_2} = 1$ mbar, bands at 3583 , 3462 , 1425 , 1325 , 1030 , and 888 cm^{-1} start to grow (marked green in Figure 3), whereas the shoulder at 3697 cm^{-1} increases in intensity.

To probe the stability of the IR bands formed in the presence of hydrogen, the FTIR spectrum obtained after H_2 -desorption ($P = 10^{-7}$ mbar) is compared with the one obtained at highest P_{H_2} (Figure 4). All of the species formed below 10^{-3} mbar are irreversibly adsorbed. The intensities of the bands at 3712 , 3697 , 1139 , and 863 cm^{-1} are unaffected by the removal of hydrogen from the gas phase, which is in line with already observed trends.⁸ Conversely, all of the features formed under higher H_2 pressures appear to be reversible, except the band at 1030 cm^{-1} that remains stable upon hydrogen removal.

4. SIMULATIONS

The observation of many new IR features with respect to the state of the art, the existence of four pressure regimes instead of two, and the stability in vacuum of a band (1030 cm^{-1}) that appears above 1 mbar, in a pressure range that is expected to give rise to only reversible adsorption, strongly question the current description of the H/MgO system. Simulations were undertaken on a large set of surface H^+/H^- configurations adsorbed on distinct surface defects to find the rationale of the pressure-dependent complexes with different stability. In the atomistic models, both monoatomic and diatomic steps with several surface defects, edges, corners, and inverse corners,

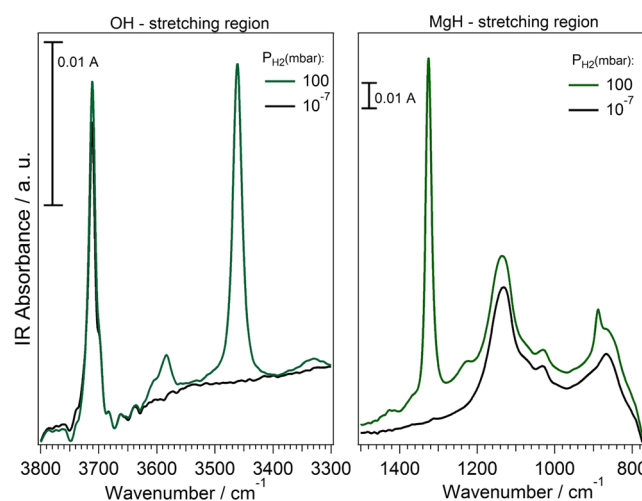


Figure 4. Comparison of the IR spectrum of MgO exposed to $P_{\text{H}_2} = 100$ mbar (green curve) to that obtained at $P_{\text{H}_2} = 10^{-8}$ mbar (black curve) after hydrogen desorption.

were considered for a total of about a hundred distinct surface configurations that were all optimized. For the configurations that correspond to negative adsorption energy, the vibrational frequencies were computed within the harmonic approximation.

4.1. Frequencies, Bond Lengths, and Coordination Numbers. The inverse correlation between bond lengths and stretching frequencies has been established in many polyatomic species,²⁰ solids containing hydroxyls²¹ and adsorbed hydroxyls.²² For a given kind of bond, the shorter the bond, the stiffer it is and, so, the higher the stretching frequency. Our theoretical results confirm the correlation for both O–H (Figure 5a) and H–Mg bonds (Figure 5b). Another important relationship is that bond lengths are increasing functions of the ion coordination numbers.^{23,24} As regards hydroxyls, the lower the coordination number of the O^{2-} anion to which the proton binds, the shorter and stronger the OH bond. Typically, the computed OH bond lengths range between 0.970 and 0.975 \AA for $\text{O}_{3\text{C}}$ sites (corners), whereas they are between 0.976 and 0.989 \AA for $\text{O}_{4\text{C}}$ (step edges). The Mg–H bond lengths range between 1.763 and 1.825 \AA for $\text{Mg}_{3\text{C}}$ sites at corners, between 1.786 and 1.920 \AA for $\text{Mg}_{4\text{C}}$ sites at step edges, and between 1.915 and 2 \AA for $\text{Mg}_{5\text{C}}$ sites at terraces.

As a trend, these two correlations enable us to deduce from the measured frequency the types of sites to which H^+ or H^- is bound. However, the presence of other weaker bonds, such as hydrogen bonds or, most importantly, $\text{H}_{\text{ads}}^+ \cdots \text{H}_{\text{ads}}^-$ interactions, may affect those robust guidelines, as discussed in Section 4.3.

4.2. Adsorption Enthalpies and Coordination Numbers. The stability of adsorbed groups is directly related to the adsorption enthalpy and thus to the critical pressure, P_{ad} , for H adsorption, as given in eq 3. Adsorption enthalpy can be approximately decomposed into the sum of distinct contributions from the O–H and H–Mg bonds that are created upon H_2 dissociation. However, the simulations provide the sum of these two contributions, which cannot be straightforwardly evaluated as singles. Nevertheless, we could obtain a rough estimate of the relative group stability as follows. For each specific surface conformation (mono- or diatomic steps, and

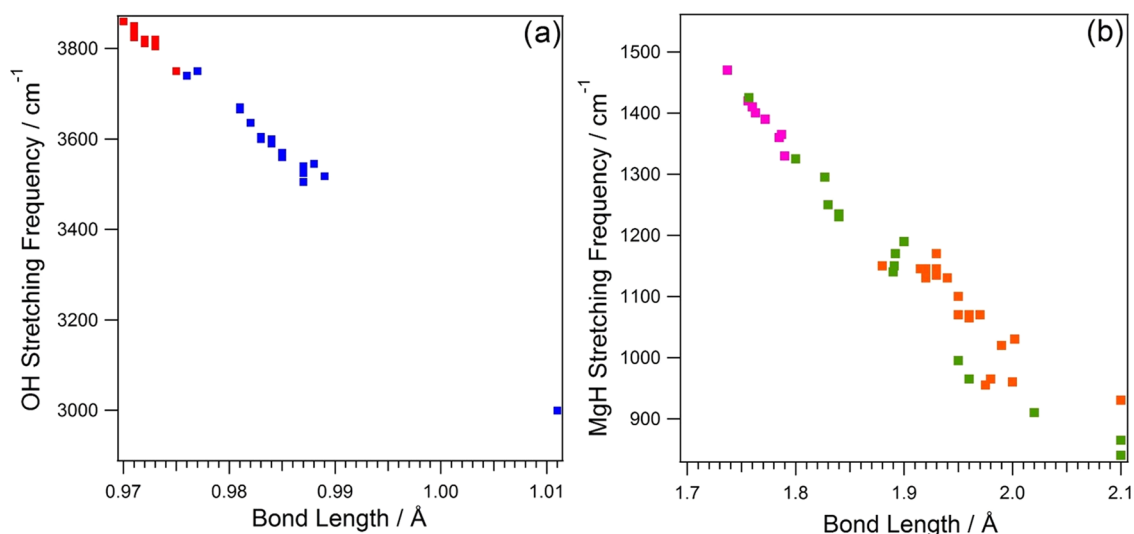


Figure 5. Correlation between computed (a) OH frequencies (not rescaled) and OH bond lengths and (b) MgH frequencies and MgH bond lengths. Squares: red for O_3C-H , blue for O_4C-H , pink for Mg_3C-H , green for Mg_4C-H , and orange for Mg_5C-H .

MgO divacancies in various numbers), we ranged the adsorption configurations from the highest to the lowest stability by increasing computed adsorption enthalpy. For adsorption configurations that differ just by a group (i.e., having either very similar O–H or H–Mg groups), we estimated the difference of the adsorption enthalpies when a group is replaced by another one. In such a way, we extracted the main trends in the relative stability of group subsets.

Regarding hydroxyl groups, adsorption of H^+ on corners is favored relative to step edges, which correlates well with the decreasing O_C-H bond length (Figure 5a). In contrast, the most stable H–Mg configurations are invariably those in which H^- is bound to three Mg cations, where it replaces a missing anion in the network. Then, a finer distinction exists for a similar H^- coordination number but variable Mg coordination number. The rule of thumb to obtain very stable adsorption configurations for H^- is to maximize the number of its bonds to cations having the lowest possible coordination number. As a consequence, the short-range conformation of the surface has an impact on the stability of H–Mg groups: for instance, H binds more tightly at inverse corners on monoatomic ($2Mg_{4C}$ and $1Mg_{5C}$) than at diatomic or polyatomic steps ($3Mg_{5C}$). This trend, which we observed for the heterolytic splitting of H_2 , is indeed more general, as monoatomic steps on MgO(001) surfaces are especially reactive toward water.^{22,25}

4.3. H^+H^- Proximity and Diffusion, Kinetics. The proximity of the H^+ , H^- fragments that originate from the heterolytic dissociation of H_2 can play a role in the adsorption. Our findings confirm that heterolytic H_2 adsorption is stabilized by the $H^+ \cdots H^-$ electrostatic interaction in agreement with ref 9. This opens the question of the role of proximity effects on the thermodynamic stability as well as on stretching frequencies of the OH and MgH groups. The contribution of the stabilizing $H^+ \cdots H^-$ interaction can be estimated by comparing the adsorption enthalpies between two adsorption configurations that only differ by d_{HH} . We have studied in detail the three following cases: the monoatomic step (schematized by the (015) surface), the sequence of monoatomic steps (the (011) surface), and the diatomic step (the (026) surface). Overall, the contribution of the electrostatic interaction to the adsorption enthalpy becomes

appreciable when the $H^+ \cdots H^-$ distance, d_{HH} , is smaller than about 2.0 Å. However, due to limited statistics, we can quantify these effects neither on the adsorption enthalpies nor on the O–H and Mg–H stretching frequencies, but only provide some examples.

The configuration in which the H^+ , H^- fragments are far apart is significantly less stable than that in which they are first neighbors. Irrespective of the kind of surface defect that dissociates H_2 , the resulting OH and MgH groups are stabilized by the $H^+ \cdots H^-$ Coulomb interaction. A paradigmatic case is the monoatomic step. At straight monoatomic steps, the adsorption enthalpy is negative when H^+ and H^- are first neighbors, whereas it is positive whenever the two species are far apart (unstable configuration). As pointed out by Giordano and Pacchioni, H_2 splits in two adjacent O_4C-H and Mg_4C-H groups at added atomic rows on MgO(001).²⁶ Our results on the H_2 splitting at the monoatomic step (MgO(015)) confirm their findings and show that the O_4C-H and Mg_4C-H groups are stabilized by the $H^+ \cdots H^-$ electrostatic interaction, with a remarkable short H^+H^- bond, $d_{HH} = 1.53$ Å. The strong $H^+ \cdots H^-$ interaction weakens both Mg–H and O–H bonds, stretches the remaining bonds in the MgO network inducing a big distortion of the step, and affects the frequencies: the O_4C-H group at equilibrium is 1.01 Å long and vibrates at a very low frequency, about 3000 cm^{-1} .

A very important issue in the present context is the role of kinetics in governing H_2 adsorption or diffusion. As far as adsorption is concerned, we found that for several defects it is possible to find a barrierless reaction path, starting from the physisorbed H_2 molecule and ending with split adsorbed H^+ and H^- . This occurs at MgO divacancies on terraces, monoatomic steps, and defects involving an O corner at diatomic steps. Although we did not carry out a systematic study of these reactions, it is reasonable to conclude that all defects involving corners and MgO divacancies are able to dissociate H_2 without activation barrier.

Once H_2 splits into H^+ and H^- , these species remain within the vicinity of the dissociation site unless they are able to diffuse. By increasing the $H^+ \cdots H^-$ distance, the attractive Coulomb interaction weakens. Therefore, diffusion is a favorable process only when another more stable adsorption

These, according to their onset and intensity evolution with pressure, can be classified into four P_{H_2} regimes. Their origin is discussed in correlation with surface defects obtained through the simulations. For choosing the best candidate, two main criteria were kept: (i) theoretical P_{H_2} should not much differ from the experimentally observed onset pressure, and (ii) computed frequencies of a given model should match best the IR spectra among all of the candidates. Such a double-check procedure yields an unprecedented and internally consistent classification because the configurations have been obtained independent of the experiments. Configurations that best fit the experimental data are collected in Table 1.

5.1. Adsorption of the Isolated Hydrogen Molecule ($P_{\text{H}_2} = 10^{-5}$ – 10^{-3} mbar). Configurations A–C (Table 1) are among the most stable that we found in the simulations. Including both mono- and diatomic steps on MgO surface, they could form at hydrogen pressures lower than 10^{-4} mbar. Their computed OH (3750 – 3710 cm^{-1}) and MgH (1145 – 1095 ; 965 – 850 cm^{-1}) stretching frequencies match well with the IR frequencies experimentally observed at the lowest P_{H_2} ($\sim 10^{-5}$ mbar, highlighted in blue in Figure 3). Although rather broad, the main MgH bands are experimentally observed to peak at 1139 and 863 cm^{-1} . By closer inspection, features can be also observed at 1080 , 970 , and 930 cm^{-1} , in particular, at pressure below 10^{-2} mbar (Figure 3). The calculations may account for the IR data in this frequency range. Configurations A–C involve systematically two components. First, H^+ is adsorbed always on 3-coordinated oxygen ($\text{O}_{3\text{C}}$), and the uniqueness of this adsorption site leads to a sharp band at 3712 cm^{-1} . An IR band at 3698 cm^{-1} is also observed. Unlike some reports,^{28,29} it cannot be attributed to brucite because such phase transformation cannot be expected under applied experimental conditions. We therefore explain the presence of IR band at 3698 cm^{-1} by configuration C, which is associated with diatomic steps and exhibits a slightly lower frequency than in the case of A and B (Table 1). In the three proposed models, H^- is mainly adsorbed at the Mg inverse corner (Mg_{IC}), in line with configurations previously suggested by other groups.^{7–11} In one of these,¹¹ a configuration similar to our model A (Table 1) is reported. H^- ions are in 3-fold coordination among (100), (010), and (001) faces and give rise to two almost degenerate frequencies (1095 – 1145 cm^{-1}) corresponding to the shorter and stiffer Mg–H bonds and a lower frequency (850 – 965 cm^{-1}) associated with the longer and weakest bond. An exception of this rule is represented by model C in which H^- is 2-fold-coordinated after being shared between two edges. However, this model fits this experimental range regarding both, the stability and frequencies.

The intensity of the two bands at 3712 and 1140 cm^{-1} boosts when P_{H_2} increases from 10^{-3} to 10^{-2} mbar. It keeps then increasing softly upon next shot of H_2 (10^{-2} – 10^{-1} mbar), whereas it finally saturates at $P_{\text{H}_2} = 1$ mbar, i.e., at the pressure which is several orders of magnitude higher than the onset H_2 -pressure ($< 10^{-5}$ mbar). This saturation limit was already reported by Diwald et al.,^{7,8} but the sudden change in intensity has not been interpreted so far. It cannot rely on thermodynamics because the configurations under study involve the most stable H^+ and H^- adsorption sites, $\text{O}_{3\text{C}}$ and Mg_{IC} , respectively. Indeed, these sites should be populated at the onset P_{H_2} along with no observable intensity increase, if thermodynamics solely controls adsorption. This is not the

case, and we attribute it, rather, to kinetics. Our calculations show that H_2 readily dissociates on neighboring O/Mg sites where H_2 heterolytically splits without barrier. In contrast, the dissociation on more remote $\text{O}_{3\text{C}}/\text{Mg}_{\text{IC}}$ sites is hindered by the activation energy of the diffusion of H^+/H^- from one $\text{O}^{2-}/\text{Mg}^{2+}$ adsorption site to another. Expecting the amount of neighboring $\text{O}_{3\text{C}}/\text{Mg}_{\text{IC}}$ to be rather low within the whole set of O corners and Mg inverse corners in the sample, another adsorption mechanism is needed to explain the saturation of the main peaks at medium pressures.

5.2. Cooperative Adsorption ($P_{\text{H}_2} = 10^{-3}$ – 1 mbar). The main change in the IR spectra within the $P_{\text{H}_2} = 10^{-3}$ – 10^{-2} mbar range is the intensity increase of peaks at 3712 cm^{-1} ($\text{O}_{3\text{C}}\text{--H}$) and at 1140 and 863 cm^{-1} ($\text{Mg}_{\text{IC}}\text{--H}$) along with the appearance of less intense features at 3605 and 1225 cm^{-1} . Furthermore, band intensities moderately increase up to a hydrogen pressure of 1 mbar (Figure S2). To explain these changes, we invoke the adsorption of two or more H_2 molecules on the basis of “hybrid configurations”. These consist of a stable site, such as the $\text{O}_{3\text{C}}\text{H}$ site or $\text{Mg}_{\text{IC}}\text{H}$ accompanied by a less stable site. Examples are given by configurations E and F in Table 1. Besides a $\text{Mg}_{\text{IC}}\text{H}$ site, the former involves an $\text{O}_{4\text{C}}\text{H}$ site whose frequency is calculated at 3545 cm^{-1} i.e., fairly close to the feature observed at 3605 cm^{-1} . In configuration F, the $\text{O}_{4\text{C}}\text{H}$ site is accompanied by a MgH, whose H^- is bound to one Mg on a terrace ($\text{Mg}_{5\text{C}}$) and one placed at the vertical edge of a diatomic step ($\text{Mg}_{4\text{C}}$). Its frequency, calculated at 1235 cm^{-1} , matches well the feature observed experimentally at 1225 cm^{-1} . However, the occurrence of configurations E and F does not explain the extremely low intensity of the features that appear at 3605 and 1225 cm^{-1} .

Until now, we have discussed the heterolytic splitting of single H_2 molecules on neighboring defects. However, at $P_{\text{H}_2} = 10^{-3}$ – 10^{-2} mbar, the cooperative absorption has to be considered. The lifetime of a molecule on a surface is $\tau \sim \nu_0^{-1} e^{E_{\text{ads}}/RT}$, where $\nu_0 \sim 10$ THz is the attempt frequency, E_{ads} is the adsorption energy, R is the gas constant, and T is the absolute temperature.³⁰ For E and F configurations, $\tau \sim 10^{-4}$ s by taking $E_{\text{ads}} \sim 0.5$ eV (Table 1). On the basis of $\tau \sim 10^{-4}$ s and working at $P_{\text{H}_2} \sim 10^{-2}$ mbar, the surface coverage would be close to one monolayer that means one H_2 molecule per surface atom. As a consequence, the probability that another molecule hits the surface close to the first one approaches unity. This suggests that at $P_{\text{H}_2} \geq 10^{-3}$ mbar the coadsorption of more than one H_2 molecule is a likely event. Such mechanism is already guessed by Gribov et al.,¹¹ relying heuristic arguments. The mechanism is examined here thanks to theoretical models consisting of two adsorbed H_2 molecules, such as in configuration X (Table 1) that gathers the above E and F configurations. The calculated frequency and the onset pressures of the X model fit the measured data even better than the previously discussed hybrid configurations. Regarding the stability, the X configuration is calculated to form at 0.8 mbar, which is 2 orders of magnitude above the onset at $P_{\text{H}_2} \sim 10^{-3}$ – 10^{-2} mbar under discussion. However, a typical error of 0.1 eV/ H_2 on the adsorption energy could affect the onset pressure by a factor 50 at room temperature so that an error of an order of magnitude is within the present accuracy of most DFT-based calculations. Moreover, the electrostatic attraction between the adsorbed H^- and H^+ on defective surface sites

could slightly increase the absolute adsorption energy and reinforce the stability of the cooperative adsorption.

Most importantly, the X configuration allows the recombination of hydrogen atoms adsorbed on O_{4C} and Mg_{4C} – Mg_{5C} sites, provided they are close enough to react. Indeed, the weak intensity of the features at $3605/1225\text{ cm}^{-1}$ indicates that the recombination is almost the rule and that the desorption process is quite fast. Therefore, the coadsorption of two or more H_2 molecules on hybrid configurations provides an effective mechanism to saturate many stable yet distant O_{3C} and Mg_{1C} sites, which is not possible through direct adsorption of isolated molecules. We stress that, although quite elementary arguments suggest that the surfaces of the nanopowders experience very many interactions with hydrogen per unit time, the coadsorption of several H_2 molecules has never been invoked so far as to quantitatively explain the IR spectra. Such a mechanism could be also at work when dissociating other H-containing molecules over MgO nanopowders, such as CH_4 recently reported by Schwach et al.³¹

5.3. Population of Mg_{3C} Corners ($P_{H_2} = 1$ – 100 mbar).

IR spectra recorded above 1 mbar (Figure 4, green frame) reveal two prominent and sharp peaks (3460 and 1325 cm^{-1}), the intensity of which promptly increases with pressure.^{7,8} Within this P_{H_2} range, the bands at 3712 and 1140 – 850 cm^{-1} do not vary anymore. Therefore, we can safely assume that the most stable and reactive sites for H_2 splitting (O_{3C} and Mg_{1C}) are completely saturated and other defect sites become responsible for the bands appearing in this P_{H_2} range. According to the above-described trend (Figure 5), the next most reactive O sites toward H^+ must be 4-fold-coordinated, whereas H^- should be coordinated to two or one surface Mg. Because the observed bands are very sharp and intense, well-defined configurations that exist in substantial number on hsa-MgO must lie in their origin. According to our calculations, they were associated with O_{4C} sites, either on monoatomic or diatomic steps, and Mg are sitting in corners (Mg_{3C}) because these sites provide Mg–H stretching frequencies higher than 1300 cm^{-1} . The proposed models are presented in Table 1 and denoted G, H, and I. The frequencies calculated for these models, OH between 3480 and 3510 cm^{-1} and MgH between 1390 and 1410 cm^{-1} , satisfy fairly the experimentally detected bands at 3460 and 1325 cm^{-1} as well as the weak feature observed at 1425 cm^{-1} . Compared to previous cases, agreement between computed and experimentally detected MgH frequencies is slightly less satisfactory; nevertheless, this assignment, in line with previous findings,¹² is perfectly consistent with the sharpness of the experimental peak at 1325 cm^{-1} , which in contrast would be quite a wide band for H bound to Mg_{4C} or Mg_{5C} . According to thermodynamics, there are as many Mg corners as O corners on MgO nanocrystals because the energetics of those defects hardly differs.¹⁷ Therefore, Mg corners must play a role at higher H_2 pressures, where the split molecule is stable. Interestingly, OH bands vibrating at 3576 – 3547 cm^{-1} were reported together with MgH bands at 1430 – 1418 cm^{-1} by Gribov et al.¹¹ In general agreement with the present work, these authors interpreted their observation on the basis of Mg_{3C} configurations to justify the high MgH frequency. However, for the H^+ -adsorption site, they suggested an inverse corner formed upon removing a Mg ion so that the proton becomes bonded to three oxygen ions (two O_{4C} and one O_{5C}). According to our simulations, structures similar to those are quite unstable.

Indeed, the OH bond length in hydroxyls rarely exceeds 1 \AA , which is necessary in such configuration where H^+ replaces a Mg^{2+} ion. In this pressure range, we note also an increase in intensity of the shoulder at 3698 cm^{-1} along with the appearance of additional weak features at 3583 , 1030 , and 888 cm^{-1} . They are assigned to hybrid structures with frequencies slightly different than those seen at a lower pressure. They would be marginal if a particular behavior of the band at 1030 cm^{-1} did not hold our attention. It is discussed below.

5.4. Desorption (100 – 10^{-8} mbar). We can see from Figure 4 that, except the band at 1030 cm^{-1} , all IR bands formed under higher H_2 pressures are completely removed upon pumping. In line with previous reports,^{8,9} this certainly applies to OH and MgH couple vibrating at 3460 and 1325 cm^{-1} , respectively, but also to all bands involved in hybrid structures (3605 – $3583/1225\text{ cm}^{-1}$). The intensity of the $3712/1140/863\text{ cm}^{-1}$ ensemble is essentially unchanged. This demonstrates that the thermodynamically most stable configurations, which include $O_{3C}H$ and $Mg_{1C}H$ parts, remain on the surface upon hydrogen evacuation, even those formed by progressive saturation as pressure increases from 10^{-3} to 1.0 mbar (Figure 3). The very important point to be mentioned is that the stable OH and MgH (irreversible IR bands) mostly result from cooperative adsorption over hybrid configurations, such as X and Y in Table 1.

Finally, although formed above $P_{H_2} > 1\text{ mbar}$, the band at 1030 cm^{-1} is stable upon hydrogen removal (Figure 4). This relatively narrow peak is likely related to a well-defined inverse corner that is both able to tightly bind H^- ions and unable to dissociate hydrogen directly so that cooperative adsorption is required. Seen along with the intensity increase of 3698 cm^{-1} , we hypothesize their correlation with multiautomatic steps: for instance, the oxygen corner of a multiautomatic step ($O_{3C}H$ with 3697 cm^{-1}) and the Mg_{1C} sites at the bottom of the multiautomatic step ($Mg_{1C}H$ with 1030 cm^{-1}). The corresponding calculated configuration is represented by model D in Table 1.

To explain desorption trends, we can argue that, at the highest $P_{H_2} = 100\text{ mbar}$, under-coordinated O and Mg sites are highly covered with adsorbed H^+ and H^- species. These progressively desorb as pressure decreases, starting from the less stable sites. In hybrid structures, hydrogen pumping leaves the most stable OH and MgH, namely, $O_{3C}H$ and $Mg_{1C}H$, which became irreversible irrespective of their mutual distance. The different behavior that is observed for adsorption and desorption sequences supports strongly the mechanism that involves hybrid structures and so the cooperative adsorption of two or more H_2 molecules at distinct defects.

5.5. Parallel between Hydrogen and Methane Adsorption on MgO. The nature of the active sites in the oxidative coupling of methane by Li-doped MgO catalysts is vividly debated. Spectroscopic³² and microscopic analyses^{33,34} as well as DFT calculations³⁵ have questioned the earlier suggestion of Li^+O^- sites.³⁶ Whereas no paramagnetic resonance was found to evidence Li^+O^- sites,³² lithium was shown to modify the morphology of MgO. Upon high-temperature treatments, the oxide powder initially dominated by (100) facets exposes an increased population of (110) and (111) facets and low-coordinated sites.^{33,34} Active sites of Li-doped MgO are therefore MgO sites, which raises the question of the involvement of corner and step sites.^{31,35} Upon exposure

of Li–MgO catalysts to 10 mbar of CH₄, the infrared spectrum of the OH stretching region exhibits bands at 3728, 3680, and 3660 cm⁻¹ that are reminiscent of the bands at 3712 and 3697 cm⁻¹ observed herein upon the formation of O_{3C}H corner moieties (Figure 3). The involvement of O_{3C} corner sites in the chemisorption of methane on MgO predicted by Kwapien et al. is clearly favored.³⁵

6. CONCLUSIONS

In summary, progressive adsorption of hydrogen molecules at the surface of MgO nanocubes was examined by combining IR spectroscopy and DFT simulations. Thermodynamic stability and the distinctive vibrational signatures of an exhaustive set of model configurations have been computed and critically compared with the experimental data obtained at H₂ pressures systematically increased from UHV to near ambient. The use of ultrahigh vacuum was shown to be essential for the identification of the very first adsorption stages. We select several atomistic models that account for the IR data in the various P_{H₂} regimes and explain the onset of H₂ splitting and the progressive saturation of diverse reactive sites. Thermodynamically most stable structures consist of O_{3C} (oxygen at regular corners) and Mg_{1C} (magnesium at inverse corners) and were shown to irreversibly split H₂ molecules in the lowest pressure range (up to 10⁻³ mbar). Our calculations show, however, that whenever H⁺/H⁻ adsorption sites are far apart and not neighbors, the dissociation becomes kinetically hindered, irrespective of the stability of the corresponding adsorption structure. Therefore, the population of distant defect sites at the MgO surface was proposed to proceed via cooperative adsorption of more than one H₂ molecule on hybrid structures combining sites of different reactivity and stability. Such scenario occurs already in the medium range of pressures (10⁻³–1 mbar) and, then, continues over highest P_{H₂} (1–100 mbar) where the fully reversibly dissociation at Mg_{3C} and O_{4C} sites of mono- and diatomic steps was also detected. The necessity of the coadsorption mechanism is further demonstrated by different adsorption and desorption sequences shown to occur at the involved defect sites. The coadsorption approach, demonstrated to be indispensable for progressive H⁺/H⁻ population of distant defect sites at MgO surfaces, can occur in a wider range of H-containing molecules.

In perspective, the present approach might also affect the issue of hydrogen storage that calls for a deeper understanding of the hydrogen adsorption/desorption cycles at the atomic scale. This would encourage new research efforts on defect engineering and doping of oxide nanopowders with high specific surface area in view of obtaining an alternative to the systems that are presently envisaged for hydrogen storage.

■ ASSOCIATED CONTENT

Supporting Information

The Supporting Information is available free of charge on the ACS Publications website at DOI: 10.1021/acs.jpcc.8b03192.

IR spectra of MgO (Figure S1); Plot of the integral area vs H₂ pressure for the IR bands (Figure S2) (PDF)

■ AUTHOR INFORMATION

Corresponding Author

*E-mail: slavica.stankic@insp.jussieu.fr.

ORCID

Slavica Stankic: 0000-0002-8711-9746

Notes

The authors declare no competing financial interest.

■ REFERENCES

- (1) Coluccia, S.; Boccuzzi, F.; Ghiotti, G.; Mirra, C. Evidence for Heterolytic Dissociation of H₂ on the Surface of Thermally Activated MgO Powders. *Z. Phys. Chem.* **1980**, *121*, 141–143.
- (2) Ito, T.; Kuramoto, M.; Yoshioka, M.; Tokuda, T. Active Sites for Hydrogen Adsorption on Magnesium Oxide. *J. Phys. Chem.* **1983**, *87*, 4411–4416.
- (3) Kobayashi, H.; Yamaguchi, M.; Ito, T. Ab Initio MO Study on Adsorption of a Hydrogen Molecule onto MgO(100) Surface. *J. Phys. Chem.* **1990**, *94*, 7206–7213.
- (4) Shluger, A. L.; Gale, J. D.; Catlow, C. R. A. Molecular Properties of the Magnesia Surface. *J. Phys. Chem.* **1992**, *96*, 10389–10397.
- (5) Anchell, J. L.; Morokuma, K.; Hess, A. C. An Electronic Structure Study of H₂ and CH₄ Interactions with MgO and Li-Doped MgO Clusters. *J. Chem. Phys.* **1993**, *99*, 6004–6013.
- (6) Kobayashi, H.; Salahub, D. R.; Ito, T. Dissociative Adsorption of Hydrogen Molecule on MgO Surfaces Studied by the Density Functional Method. *J. Phys. Chem.* **1994**, *98*, 5487–5492.
- (7) Knözinger, E.; Jacob, K.-H.; Hofmann, P. Adsorption of Hydrogen on Highly Dispersed MgO. *J. Chem. Soc., Faraday Trans.* **1993**, *89*, 1101–1107.
- (8) Diwald, O.; Hofmann, P.; Knözinger, E. H₂ Chemisorption and Consecutive UV Stimulated Surface Reactions on Nanostructured MgO. *Phys. Chem. Chem. Phys.* **1999**, *1*, 713–721.
- (9) Diwald, O.; Sterrer, M.; Knözinger, E. Site Selective Hydroxylation of the MgO Surface. *Phys. Chem. Chem. Phys.* **2002**, *4*, 2811–2817.
- (10) Ricci, D.; Di Valentin, C.; Pacchioni, G.; Sushko, P. V.; Shluger, A. L.; Giamello, E. Paramagnetic Defect Centers at the MgO Surface. An Alternative Model to Oxygen Vacancies. *J. Am. Chem. Soc.* **2003**, *125*, 738–747.
- (11) Gribov, E. N.; Bertarione, S.; Scarano, D.; Lamberti, C.; Spoto, G.; Zecchina, A. Vibrational and Thermodynamic Properties of H₂ Adsorbed on MgO in the 300–20 K Interval. *J. Phys. Chem. B* **2004**, *108*, 16174–16186.
- (12) Cavalleri, M.; Pelmenschikov, A.; Morosi, G.; Gamba, A.; Coluccia, S.; Martra, G. M. Dissociative Adsorption of H₂ on Defect Sites of MgO: A Combined IR Spectroscopic and Quantum Chemical Study. *Stud. Surf. Sci. Catal.* **2001**, *140*, 131–139.
- (13) Stankic, S.; Sternig, A.; Finocchi, F.; Bernardi, J.; Diwald, O. Zinc Oxide Scaffolds on MgO Nanocubes. *Nanotechnology* **2010**, *21*, No. 355603.
- (14) Giannozzi, P.; Baroni, S.; Bonini, N.; Calandra, M.; Car, R.; Cavazzoni, C.; Ceresoli, D.; Chiarotti, G. L.; Cococcioni, M.; Dabo, I.; et al. Quantum Espresso: A Modular and Open-Source Software Project for Quantum Simulations of Materials. *J. Phys.: Condens. Matter* **2009**, *21*, No. 395502.
- (15) (a) Perdew, J. P.; Burke, K.; Ernzerhof, M. Generalized Gradient Approximation Made Simple. *Phys. Rev. Lett.* **1996**, *77*, 3865. (b) Perdew, J. P.; Burke, K.; Ernzerhof, M. Generalized Gradient Approximation Made Simple [Phys. Rev. Lett. **77**, 3865 (1996)]. *Phys. Rev. Lett.* **1997**, *78*, 1396.
- (16) Kohn, W.; Sham, L. J. Self-Consistent Equations Including Exchange and Correlation. *Phys. Rev.* **1965**, *140*, A1133.
- (17) Finocchi, F.; Geysermans, P.; Bourgeois, A. The Role of Hydroxylation in the Step Stability and in the Interaction between Steps: A First-Principles Study of Vicinal MgO Surfaces. *Phys. Chem. Chem. Phys.* **2012**, *14*, 13692–13701.
- (18) Ealet, B.; Goniakowski, J.; Finocchi, F. Water Dissociation on a Defective MgO(100) Surface: Role of Divacancies. *Phys. Rev. B* **2004**, *69*, No. 195413.

(19) Stankic, S.; Cortes-Huerto, R.; Crivat, N.; Demaille, D.; Goniakowski, J.; Jupille, J. Equilibrium Shapes of Supported Silver Clusters. *Nanoscale* **2013**, *5*, 2448–2453.

(20) Zavitsas, A. A. Factors affecting the relation between stretching frequencies and bond lengths. Diatomic and polyatomic species without adjustable fitting parameters. *Spectrochim. Acta, Part A* **2015**, *151*, 553.

(21) Szalay, V.; Kovács, L.; Wöhlecke, M.; Libowitzky, E. Stretching Potential and Equilibrium Length of the OH Bond in Solids. *Chem. Phys. Lett.* **2002**, *354*, 56–61.

(22) Finocchi, F.; Hacquart, R.; Naud, C.; Jupille, J. Hydroxyl-Defect Complexes on Hydrated MgO Smokes. *J. Phys. Chem. C* **2008**, *112*, 13226–13231.

(23) Ferraris, G.; Catti, M. Generalization of Baur's Correlations between Bond Strength in Inorganic Structures. *Acta Crystallogr., Sect. B: Struct. Crystallogr. Cryst. Chem.* **1973**, *29*, 2006–2009.

(24) Finocchi, F.; Noguera, C. Structure and Bonding of Small Stoichiometric Lithium Oxide Clusters. *Phys. Rev. B* **1996**, *53*, 4989.

(25) Savio, L.; Smerieri, M.; Orzelli, A.; Vattuone, L.; Rocca, M.; Finocchi, F.; Jupille, J. Common Fingerprint of Hydroxylated non-polar Steps on MgO Smoke and MgO Films. *Surf. Sci.* **2010**, *604*, 252–257.

(26) Chen, H.-Y. T.; Giordano, L.; Pacchioni, G. From Heterolytic to Homolytic H₂ Dissociation on Nanostructured MgO(001) Films as a Function of Metal Support. *J. Phys. Chem. C* **2013**, *117*, 10623–10629.

(27) Wu, G.; Zhang, J.; Wu, Y.; Li, Q.; Chou, K.; Bao, X. Adsorption and Dissociation of Hydrogen on MgO Surface: A First-Principles Study. *J. Alloys Compd.* **2009**, *480*, 788–793.

(28) Martens, R.; Freund, F. The Potential Energy Curve of the Proton and the Dissociation Energy of the OH⁻ Ion in Mg(OH)₂. *Phys. Status Solidi A* **1976**, *37*, 97–104.

(29) Rywak, A. A.; Burlitch, J. M.; Loehr, T. M. Sol-Gel Preparation and Characterization of Magnesium Peroxide, Magnesium Hydroxide Methoxide, and Randomly and (111) Oriented MgO Thin Films. *Chem. Mater.* **1995**, *7*, 2028–2038.

(30) Israelachvili, J. N. *Intermolecular and Surface Forces*, 3rd ed.; Academic Press: Elsevier, 2011.

(31) Schwach, P.; Hamilton, N.; Eichelbaum, M.; Thum, L.; Lunkenbein, T.; Schlögl, R.; Trunschke, A. Structure Sensitivity of the Oxidative Activation of Methane over MgO Model Catalysts: II. Nature of Active Sites and Reaction Mechanism. *J. Catal.* **2015**, *329*, 574–587.

(32) Myrach, P.; Nilius, N.; Levchenko, S. V.; Gonchar, A.; Risse, T.; Dinse, K.-P.; Boatner, L. A.; Frandsen, W.; Horn, R.; Freund, H.-J.; et al. Temperature-Dependent Morphology, Magnetic and Optical Properties of Li-Doped MgO. *ChemCatChem* **2010**, *2*, 854–862.

(33) Zavyalova, U.; Weinberg, G.; Frandsen, W.; Girgsdies, F.; Risse, T.; Dinse, K.-P.; Schloegl, R.; Horn, R. Lithium as a Modifier for Morphology and Defect Structure of Porous Magnesium Oxide Materials Prepared by Gel Combustion Synthesis. *ChemCatChem* **2011**, *3*, 1779–1788.

(34) Luo, L.; Jin, Y.; Pan, H.; Zheng, X.; Wu, L.; You, R.; Huang, W. Distribution and Role of Li in Li-Doped MgO Catalysts for Oxidative Coupling of Methane. *J. Catal.* **2017**, *346*, 57–61.

(35) Kwapien, K.; Paier, J.; Sauer, J.; Geske, M.; Zavyalova, U.; Horn, R.; Schwach, P.; Trunschke, A.; Schloegl, R. Sites for Methane Activation of Lithium-Doped Magnesium Oxide Surfaces. *Angew. Chem., Int. Ed.* **2014**, *53*, 8774–8778.

(36) Lunsford, J. H. The Catalytic Oxidative Coupling of Methane. *Angew. Chem., Int. Ed.* **1995**, *34*, 970–980.



Cite this: DOI: 10.1039/c7cp01635b

ZnO powders as multi-facet single crystals†

 Francia Haque,^a Stéphane Chenot,^a Francesc Viñes,^{id}^b Francesc Illas,^{id}^b Slavica Stankic^{id}*^a and Jacques Jupille^a

 Received 14th March 2017,
 Accepted 20th March 2017

DOI: 10.1039/c7cp01635b

rsc.li/pccp

Oxides are most commonly found in divided forms with properties difficult to control since their crystallographic orientations usually escape analysis. To overcome this an appropriate model system can be provided by ZnO smoke which, obtained by combustion of Zn in air, exhibits nanoparticles with well-defined surface facets. The present work focuses on the interaction of water with ZnO smokes by combining density functional theory based simulations and infrared spectroscopy measurements with applied pressures from 10^{-7} to 1 mbar. We demonstrate that the use of ultra-high vacuum allows the analysis of the very first stages of the adsorption, and report on water structures on ZnO(11 $\bar{2}$ 0) for the first time. We further show that ZnO powders behave as multi-facet single crystals involving (10 $\bar{1}$ 0), (11 $\bar{2}$ 0), (0001), and (000 $\bar{1}$) surfaces with the polar orientations corresponding to 25% of the total surface area. A great deal of cross-agreements between experimental results and simulation provides a simple approach for the examination of hydroxylated/hydrated ZnO smokes and can be widely applied on other ZnO-related powders.

Introduction

The ubiquity of oxides in dispersed form has prompted research strategies in two directions: understanding the existing materials by means of appropriate reference systems and tailoring the desired properties through innovative syntheses.^{1–4} Approaches based on the comparison of powders exhibiting oriented facets with their single crystal forms have been stimulated to pinpoint the orientation-dependent properties.^{5–7} Alkaline earth oxides, MgO,^{8–11} CaO,^{9,12} SrO,⁹ and BaO,⁹ have long been studied in this context. The rock-salt structure leads to particles in the form of nanocubes closed by facets that show a unique (100) family of orientations that can be directly compared to single crystal surfaces.^{5,8–13} They offer a test bed for the study of water^{10,11,14–16} and hydrogen^{17,18} reactivity on sites of defined coordination^{9–11,17} as well as on specific defects that result from the contact between nanoparticles (NPs).¹⁹ High density of coordinatively unsaturated sites combined with quantum confinement effects,²⁰ specific sites,¹⁹ and electron trapping²¹ at particle–particle interfaces triggers non-trivial behaviours in the ensembles of nanoparticles and make them specific objects that deserve direct examination. Examples are a significant enhancement of the photocatalytic

efficiency of the P-25 titania powder when compared to any of its pure phases, rutile or anatase,²² and the cooperative mechanism between charge carriers and surface orientations which drives photoreactivity.²³ The study of those synergistic effects requires a morphological control of photocatalysts through syntheses that reliably favours one orientation or the other.^{23–25} A number of other oxides such as CeO₂, CuO, Co₃O₄, SnO₂, and Fe₂O₃ have been synthesized in the form of nanoparticles with well-defined facet orientations for the purpose of performing measurements of catalytic activity under controlled conditions.⁴

In this respect, zinc oxide nanoparticles appear as a quite challenging issue. ZnO is involved in numerous applications including paints, cements, ceramics, glasses, technical rubbers, sensors,^{26,27} optical coatings,²⁸ solar cells²⁹ and catalysts.^{30,31} It is, therefore, a massively produced material with global production of more than a million tons per year. The interest in this extremely useful material is boosted by the promising prospects in optoelectronics applications, although the difficulty of preparing p-type ZnO in a reproducible way is an obstacle for replacing GaN in devices.³² The hunt for a better understanding of highly dispersed ZnO deals, however, with an extreme complexity stemming from the large spectrum of morphologies that ZnO powders exhibit – sticks, tetrapods, platelets, discs, rings, ribbons and spirals.^{33,34} Despite the fact that both their growth and shaping are partly driven by the compensation required to stabilize polar orientations,^{35,36} there is still a sense of discouragement over a seemingly intractable puzzle regarding such a fascinating collection of ZnO nanoforms.

A way out may be offered by the fact that divided ZnO powders mostly show four facet orientations, two non-polar,

^a Sorbonne Universités, UPMC Univ Paris 06, CNRS-UMR 7588, Institut des NanoSciences de Paris, F-75252 Paris Cedex 05, France. E-mail: slavica.stankic@insp.jussieu.fr

^b Departament de Ciència de Materials i Química Física & IQTCUB, Universitat de Barcelona, c/ Martí i Franquès 1-11, 08028 Barcelona, Spain

† Electronic supplementary information (ESI) available. See DOI: 10.1039/c7cp01635b

(10 $\bar{1}$ 0) and (11 $\bar{2}$ 0), and two polar, (000 $\bar{1}$) and (0001), the former being expected to dominate^{37,38} in line with cleavage energies.³⁹ Water appears as an appropriate probe since comprehensive numerical simulations predict infrared spectra involving narrow infrared bands that are specific to each of the above orientations.³⁸ Given that powders are dominated by these orientations, water adsorption can act as a selective probe—as demonstrated by Kittaka and co-workers a long time ago.³⁹ In this work, infrared spectroscopy experiments are performed in the transmission mode on powders that are exposed to water from ultra-high vacuum conditions to near ambient pressure. In such a context, the application of ultra-high vacuum conditions is the key ingredient allowing a full control of the conditions upon adsorption. In a first row, it comprises the preparation of the required clean oxide surface and the observation of the very first stages of adsorption, and, in the second row, experimental data are then discussed in light of numerical simulations relying on a density functional approach aimed at the determination of energetically favourable water/ZnO surface configurations.

Results and discussion

Exposure of the ZnO smoke to water vapour

A representative SEM image of the ZnO smoke powder is shown in Fig. 1. These nanoparticles mostly adopt forms of sticks and tetrapods with sizes broadly varying. Stick and tetrapod morphologies are commonly observed in ZnO powders. In particular, tetrapods involve four prism-shaped wurtzite legs that extend in [0001] directions and present (10 $\bar{1}$ 0) and (11 $\bar{2}$ 0) facets on their sides. Surface energy calculations systematically show that sticks and tetrapods can be represented by Wulff construction that are dominated by (10 $\bar{1}$ 0) and (11 $\bar{2}$ 0) orientations with a minority of

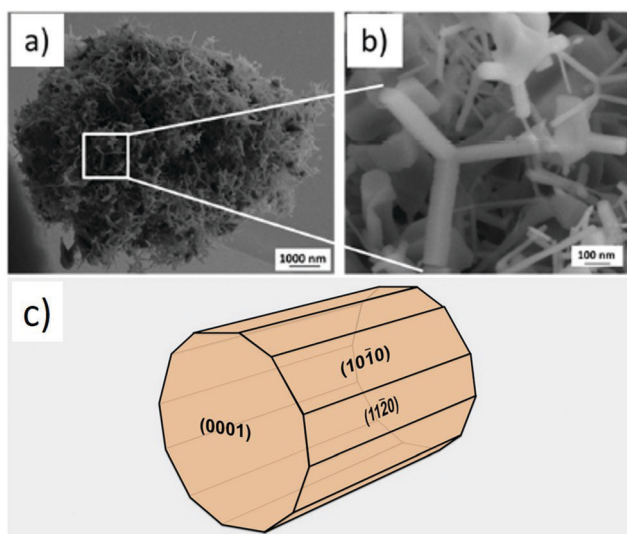


Fig. 1 Scanning electron microscope images of ZnO smoke: (a) an ensemble of nanoparticles and (b) a closer view of tetrapods and sticks present in the powder; (c) Wulff construction of ZnO stick derived from calculated surface energies⁴⁰ following Wulff shape construction,⁴¹ as previously described.⁴²

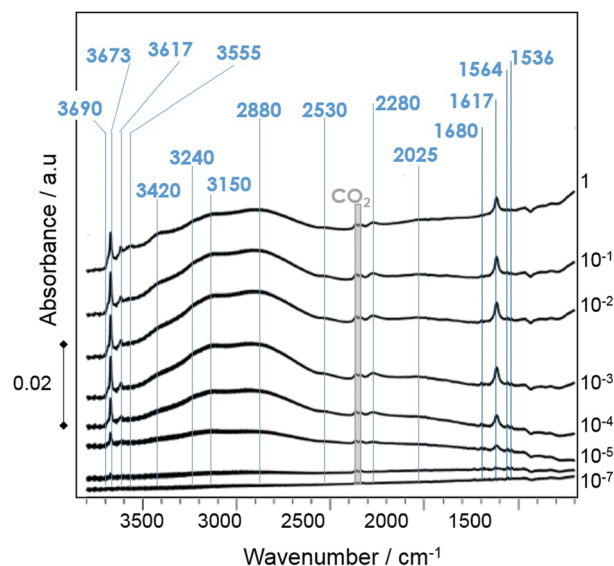


Fig. 2 Room-temperature FTIR spectra recorded in a vacuum (10^{-7} mbar) after exposure of ZnO smokes to $P_{\text{H}_2\text{O}} = 10^{-7}$ –1 mbar, as indicated on the right hand side, mbar. The observed bands are indicated by vertical bars on which frequencies are given in cm^{-1} .

polar orientations⁴⁰ (see Fig. 1c, ref. 43 and references therein), in agreement with transmission electron microscopy.^{40,44} ZnO smoke powders were exposed to increasing partial pressures of water vapour and the corresponding room-temperature Fourier transform infrared (FTIR) spectra recorded at $P_{\text{H}_2\text{O}} = 1 \times 10^{-7}$ –1 mbar are presented in Fig. 2. The observation of IR bands at very low pressures highlights the interest of performing experiments under ultra-high vacuum conditions. Frequencies shown in Fig. 2 are listed in Table S1 (see ESI†) where they are compared to measurements reported in ref. 6.

FTIR spectra recorded after exposure at a pressure of up to 1×10^{-1} mbar show a stable profile with bands progressively increasing in intensity. The spectra recorded after 300 s at 1×10^{-4} mbar (5000 L) and after exposures at 1 mbar show an astonishing similarity to the spectra recorded by Noei *et al.* after an exposure of 9000 L and after exposure to a partial pressure of 4 mbar of water vapour in helium,⁶ respectively. The only difference is the absence of the sharp band at 3441 – 3448 cm^{-1} while the broad band at 3420 cm^{-1} is systematically observed. Such an agreement between the IR spectra recorded on ZnO smoke of the present work and the commercial ZnO powder⁶ discards any fortuitous matching. Since water adsorption on ZnO leads to strongly orientation-dependent vibrational spectra,³⁸ the resemblance of the two IR spectra likely reflects a profound similarity of the orientation of the facets present on the two types of ZnO powders, which call for a detailed analysis.

Nevertheless, the adsorption of water on a given orientation may not lead to a unique configuration, as on ZnO(10 $\bar{1}$ 0) on which both fully dissociated and alternative half-dissociated arrangements of similar energy have been observed.^{6,38,46–49} This has prompted us to compare the experimental data presented in Fig. 2 to theory, on the basis of a full theoretical review of the configurations that can be taken by water on the (10 $\bar{1}$ 0), (11 $\bar{2}$ 0),

(0001), and (000 $\bar{1}$) facets, *i.e.* on the orientations expected to be dominant on ZnO nanoparticle surfaces.^{37,38,45}

Comparison between experiment and simulation

ZnO(000 $\bar{1}$)-O and ZnO(0001)-Zn polar orientations. Firstly, it has been found that the water adsorption gives rise to only one structure on each basal plane. Experiment and theory fully agree about water adsorption on the polar (000 $\bar{1}$) orientation (Fig. 3). Hydroxyl groups are expected to stand up on this surface giving rise to a unique OH stretching band in the frequency region under study.³⁸ In the present work, it is found at 3617 cm⁻¹—matching well with the values recorded by HREELS on a ZnO(000 $\bar{1}$) single crystal and by FTIR on ZnO powder, *i.e.* 3621 and 3620 cm⁻¹, respectively.⁶ The hydroxylation of the zinc-terminated ZnO(0001)-Zn surface is not expected to be observed in the IR spectra since the intensity of the related O-H stretching band is predicted to be too weak.³⁸

ZnO(10 $\bar{1}$ 0) orientation. On the ZnO(10 $\bar{1}$ 0) orientation, four calculated configurations have been selected (Fig. 4). Additional structures were found as well, but the present choice was limited to those configurations which can unambiguously explain at least one experimentally observed IR band.

Those correspondences are discussed first. The (2 × 1) structure (labelled (2 × 1)_A), in which every second water molecule

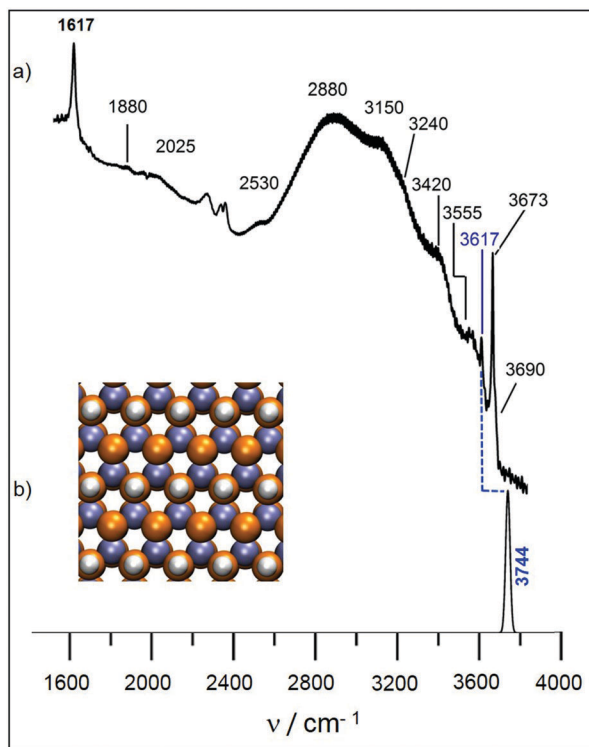


Fig. 3 Comparison between (a) IR spectrum recorded on ZnO smoke at RT after exposure to $P_{\text{H}_2\text{O}} = 1$ mbar—representative of the spectra shown in Fig. 2—and (b) calculated spectra associated with the H₂O adlayer structure determined by the DFT approach for the ZnO(000 $\bar{1}$) surface which involves a unique ν_{OH} stretching frequency (see the text). On the left, schematic representation of the surface structure in which, substrate Zn, substrate O, and H atoms are represented by blue, orange, and grey, respectively.

is dissociated,^{38,47–49} is confirmed by the present DFT approach to be the most stable configuration for water adsorption on ZnO(10 $\bar{1}$ 0) (Fig. 4b). The dissociation, which is partly triggered by hydrogen bonds between water molecules, gives rise to free O_w-H groups attached to surface zinc atoms Zn_s of a Zn-O dimer row and to a proton adsorbed on a surface oxygen atom O_s of a neighbouring dimer row. The resulting O_s-H groups are hydrogen-bonded across the [11 $\bar{2}$ 0] trenches to the free O_w-H. DFT predicts stretching frequencies of 3763 and 3139 cm⁻¹ for Zn_s-O_wH and O_s-H, respectively. The corresponding experimental modes are at 3673 and 3150 cm⁻¹ (Fig. 4a), which

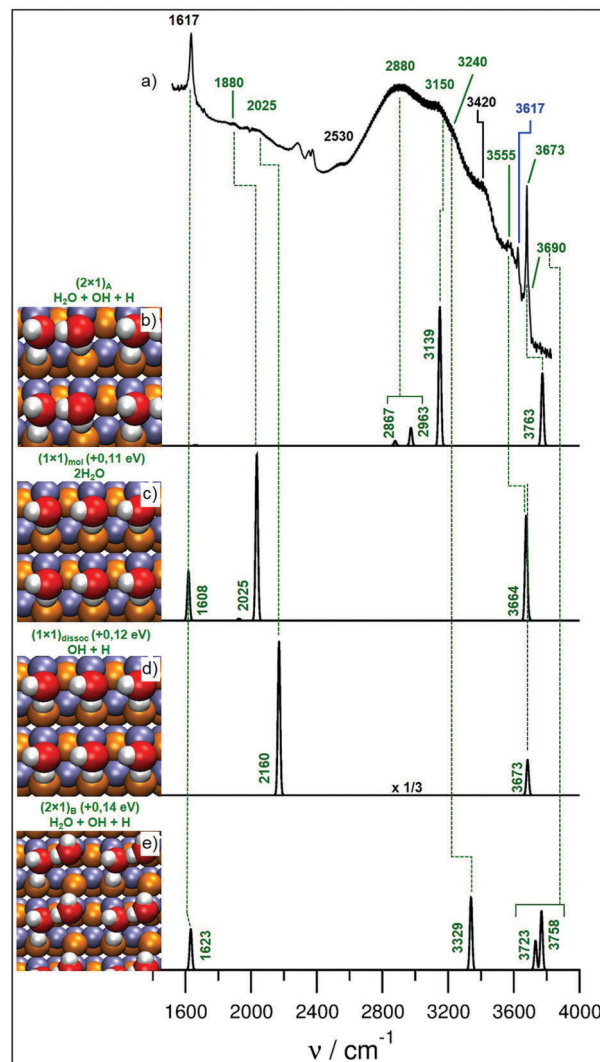


Fig. 4 Comparison between (a) IR spectrum recorded on ZnO smoke at RT after exposure to $P_{\text{H}_2\text{O}} = 1$ mbar—representative of the spectra shown in Fig. 2—and calculated spectra associated to H₂O adlayer structures determined by DFT approach for ZnO(10 $\bar{1}$ 0) surface: (b) (2 × 1)_A, (c) (1 × 1)_{mol}, (d) (1 × 1)_{dissoc} and (e) (2 × 1)_B. The four calculated structures are presented in the figure on the left hand side of these spectra. The extra energy involved in those structure with respect to the (2 × 1)_A structure are indicated. Oxygen and zinc atoms from the substrates appear as blue and orange spheres, respectively, whereas oxygen and hydrogen from the adsorbed water molecules are represented by red and light grey, respectively. Blue highlighted frequency corresponds to ZnO(000 $\bar{1}$)-O orientation.

parallel values of 3670 and 3195 cm^{-1} recorded on the (10 $\bar{1}$ 0) surface of a ZnO single crystal (see the ESI†).^{6,46} The comparison with the vibrational spectra recorded on single crystal surfaces makes the assignment quite reliable. The non-dissociated water molecules involved in the (2 × 1)_A structure are hydrogen-bonded to both neighbouring free OH and surface oxygen atoms of the next ZnO dimer rows, which is expected to give rise to DFT symmetric and asymmetric stretches at 2963 and 2867 cm^{-1} , respectively (Fig. 4b). The experimental counterpart is the broad band at 2880 cm^{-1} (Fig. 4a). This interpretation contradicts the assignment of the mode seen at 3690 cm^{-1} to a non H-bonded O_w-H of the intact water molecule.⁴⁶ The origin of this mode is discussed in connection with the additional configurations of water adsorbed on ZnO(10 $\bar{1}$ 0) (see below). Calculations reveal the existence of three additional H₂O/ZnO(10 $\bar{1}$ 0) superstructures that are energetically almost degenerate with the above (2 × 1)_A. These involve fully molecular (1 × 1)_{mol} (Fig. 4c), fully dissociated (1 × 1)_{dissoc} (Fig. 4d), and alternative half-dissociated (2 × 1)_B structures (Fig. 4e). They are higher in energy than the (2 × 1)_A structure only by 0.11, 0.12 and 0.14 eV per molecule, respectively. The coexistence of the (1 × 1)_{mol} structure with the half-dissociated (2 × 1)_A has already been postulated on the basis of STM observations supported by DFT calculations.⁴⁷ In the (1 × 1)_{mol} structure, water molecules occupy similar sites to the non-dissociated water molecules of the (2 × 1)_A arrangement (Fig. 4c and ref. 47). The calculated bands at 1608 and 1623 cm^{-1} can be assigned to the deformation mode of water, whose main feature is observed experimentally at 1617 cm^{-1} . Discussion about this mode requires, however, a complete overview of all the configurations that are identified in the IR spectra of the hydroxylated ZnO smoke and is, therefore, given at the end of this section. The two bands of the calculated vibrational spectrum, at 3664 and 2025 cm^{-1} , correspond to the free O_w-H and the hydrogen-bonded O_w-H, respectively. The former is associated with the well-defined experimental feature observed at 3555 cm^{-1} (Fig. 4a) which, in the same way as in the calculated spectra, is shifted by about a hundred wave numbers with respect to the intense stretching Zn_s-O_wH band (3673 cm^{-1}) related to the (2 × 1)_A structure (Fig. 4a). The calculated 2025 cm^{-1} band is related to the experimental mode observed at 1880 cm^{-1} (Fig. 4a).

Direct observation by STM⁴⁷ of (1 × 1)_{mol} makes very likely the occurrence of both, the fully dissociated (1 × 1)_{dissoc} (Fig. 4d) and the alternative half-dissociated (2 × 1)_B (Fig. 4e) since being of similar energy to (1 × 1)_{mol}. DFT predicts that the dissociation of the molecules of (1 × 1)_{mol} yields the (1 × 1)_{dissoc} structure which involves free O_w-H (3673 cm^{-1}) and hydrogen-bonded O_s-H (2160 cm^{-1}) groups (Fig. 4d). The DFT value of 2160 cm^{-1} is related to the experimental 2025 cm^{-1} (Fig. 3a). (Because of the systematic blue shift of the calculated frequencies, it is consistent to assign the calculated 2025 cm^{-1} ((1 × 1)_{mol}, Fig. 4c) and 2160 cm^{-1} ((1 × 1)_{dissoc}, Fig. 4d) to the experimental bands at 1880 cm^{-1} and 2025 cm^{-1} , respectively.) Moreover, the two calculated bands are the only counterparts that can be found in the whole set of calculated spectra for the modes that are observed in the 1850–2025 cm^{-1} range. Finally, in the additional half-dissociated (2 × 1)_B (Fig. 4e), adsorbed moieties occupy similar sites to those in (2 × 1)_A, except that each water molecule draws a

free O_w-H outward instead of being doubly hydrogen-bonded (Fig. 3a), which results in two O_w-H stretches with DFT values of 3723 and 3758 cm^{-1} . Together with the free O_w-H mode of the (1 × 1)_{dissoc} structure (a DFT value of 3673 cm^{-1}), these modes can be related to the IR features experimentally observed at 3690–3700 cm^{-1} (this work and ref. 44) and 3656 cm^{-1} ,⁴⁶ in the vicinity of the sharp Zn_s-O_wH band (3673 cm^{-1} in the experimental spectra) that dominates the (2 × 1)_A configuration. The occurrence of these features in the HREELS spectrum of the ZnO(10 $\bar{1}$ 0) crystal surface⁶ definitely demonstrates that they are related to hydroxylated ZnO(10 $\bar{1}$ 0). Although precise assignments cannot be provided, the experimental observation of additional bands at 3639, 3656, and 3690 cm^{-1} (Fig. 4a and ref. 6) around the intense Zn_s-O_wH mode at 3673 cm^{-1} ((2 × 1)_A configuration, Fig. 4b) supports the existence of the (1 × 1)_{dissoc} (Fig. 4d) and (2 × 1)_B (Fig. 4e) configurations that provide calculated counterparts to the observed frequencies. Finally, H-bonded O_s-H of (2 × 1)_B (Fig. 4e) is blue-shifted (DFT: 3329 cm^{-1}) with respect to that of (2 × 1)_A (DFT 3139 cm^{-1}) and it is attributed to the broad although well-defined mode experimentally observed at 3240 cm^{-1} (Fig. 4a).

ZnO(11 $\bar{2}$ 0) orientation. In contrast to the ZnO(10 $\bar{1}$ 0) surface, there exist no experimental data for water adsorption on the ZnO(11 $\bar{2}$ 0) single crystal surface. To our knowledge, the interaction between water and the ZnO(11 $\bar{2}$ 0) surface has been discussed only through theoretical approaches.^{38,49–51} By comparison with experiment (Fig. 5a), the present DFT calculations

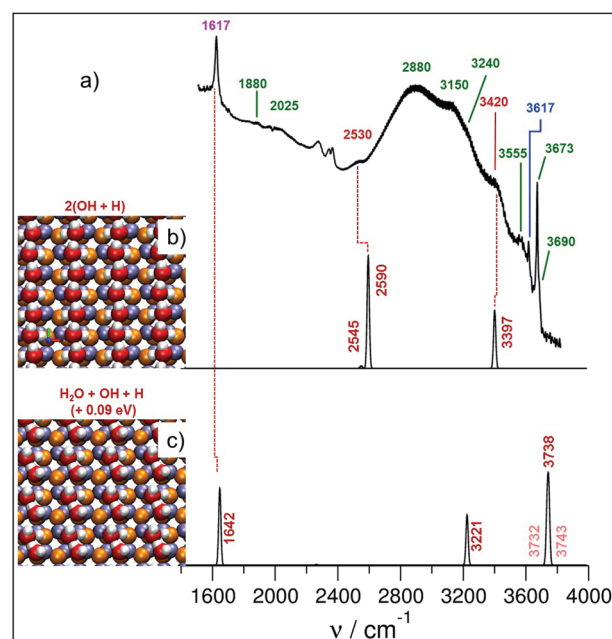


Fig. 5 Comparison between (a) IR spectrum recorded on ZnO smoke at RT after exposure to $P_{\text{H}_2\text{O}} = 1$ mbar—representative of the spectra shown in Fig. 2—and the calculated spectra associated with H₂O adlayer structures determined by the DFT approach for the ZnO(11 $\bar{2}$ 0) surface and representative structures: (b) (2 × 1)_{fully-dissoc}, (c) (2 × 1)_{half-dissoc}. The same colour code as in Fig. 3 and 4 is used for spheres representative of atoms. The blue and green highlighted frequencies correspond to ZnO(000 $\bar{1}$)-O and ZnO(10 $\bar{1}$ 0) orientations, respectively. The deformation frequency (1617 cm^{-1}) of the water molecule is highlighted in violet.

favour the full dissociative adsorption of water molecules (Fig. 5b) by 0.09 eV with respect to a half-dissociation (Fig. 5c) similar to that observed on ZnO(10 $\bar{1}$ 0)—that is in agreement with the calculations of other groups.^{49,50} Although the view is not unanimous,⁵¹ all groups agree that the configuration of lowest energy is any of the two above structures and that their energy separation is ~ 0.1 eV per molecule or less. The fully molecular adsorption is discarded since its difference in energy with the structure of lowest energy lies between 0.25 eV per water molecule (this work) and 0.85 eV per water molecule in ref. 43. As in the case of water-covered ZnO(10 $\bar{1}$ 0), the small difference in energy between fully dissociated and half-dissociated configurations points to coexisting superstructures. The fully dissociated (2 \times 1) involves only hydrogen bonded OH groups (Fig. 5b) predicted to give rise to modes at 3397 and 2590 cm⁻¹ as well as a fairly weak mode at 2545 cm⁻¹. These are associated with experimentally recorded bands at 3420 and 2530 cm⁻¹, respectively (Fig. 5a). The assignment is meaningful since the two bands could not be explained by any other water structure among those that are presented herein, which is a necessary condition to support the reliability of the configuration proposed for adsorption of water on ZnO(11 $\bar{2}$ 0). In the second structure suggested herein, the half-dissociated (2 \times 1) (Fig. 5c) vibrational modes are expected at 3738, 3221, and 1642 cm⁻¹. None of these can be singled out on the basis of the experimental IR spectra, although they do not contradict the experimentally observed data (Fig. 5a). Despite the fact that this structure has no unambiguous counterpart in the experimental infrared spectrum, its existence is assumed because of its very small difference in energy with the fully dissociated (2 \times 1).

According to calculations, the deformation mode of water molecules, exhibiting a rather high intensity, does not appear in any of the most stable water configurations—the (2 \times 1)_A structure for ZnO(10 $\bar{1}$ 0) (Fig. 4b) and the fully dissociated (2 \times 1) for ZnO(11 $\bar{2}$ 0) (Fig. 5b). Four bands are identified in the experimental spectrum, at 1536, 1564, 1617, and 1680 cm⁻¹ (Fig. 2). A consistent DFT counterpart is offered by the three modes found in the calculated configurations, at 1608 cm⁻¹ ((1 \times 1)_{mol}, Fig. 4c), 1623 cm⁻¹ ((2 \times 1)_B, Fig. 4e) and 1642 cm⁻¹ (half-dissociated (2 \times 1), Fig. 5c), although unambiguous assignments are not possible. Finally, by comparing the calculated intensities (Fig. 4 and 5 and ref. 38) to the experiment, a non-polar/polar ratio of 75/25 is determined. It is close to other estimates^{37,38} and consistent with the general expectation that the non-polar (10 $\bar{1}$ 0) and (11 $\bar{2}$ 0) are dominant orientations on the ZnO surface exhibiting lowest cleavage energy.⁴⁵

Experimental and computational methods

Experimental

The present work deals with ZnO nanopowders obtained by burning zinc in an air atmosphere. This method allows for the formation of oxide particles at temperatures high enough to be close to the equilibrium shape.¹¹ Similar to MgO smokes,⁵² also

the obtained ZnO smoke powders include nanoparticles of a broadly dispersed size while being mostly in the form of sticks and tetrapods that are commonly encountered in ZnO powders (Fig. 1). ZnO smokes are deposited on $\sim 25 \times 25$ mm² silicon wafers that are set above the burning zinc ribbon. Silicon supports allow *in situ* FTIR analysis by transmission since silicon is transparent in the frequency range of relevance.⁵³ ZnO smokes show a rather low specific area of 4 m² g⁻¹, as determined by nitrogen sorption measurements. This modest specific area has a remarkable advantage regarding reactivity measurements. Typically, ZnO deposited on the $\sim 25 \times 25$ mm² Si wafer amounts to ~ 1 mg, which corresponds to an area of 40 cm². On the basis of the kinetic theory of gases, this means that ~ 10 s are required at a partial pressure of 1×10^{-6} mbar for an exposure of the surface of the oxide as a whole to 1 Langmuir (symbol L, exposure of 1.33×10^{-6} mbar during 1 second which corresponds to a full monolayer if the sticking probability is assumed to be one). Exposures being systematically of 300 s ensure that, even at the smallest pressure used herein (1×10^{-7} mbar), all the surface sites of the powder have been visited more than once by the gas under study. This makes possible to achieve a rather homogeneous coverage of the powders' surface as a whole. After preparation, the ZnO-covered silicon wafer is immediately inserted into the ultra-high vacuum (UHV) set-up, consisting of the main analysis chamber and a preparation one – both of them affording a residual pressure of less than 10^{-9} mbar. Prior to exposure to water, ZnO powders are thermally activated at 700 K. Fourier Transform Infrared Spectroscopy (FTIR) is performed in the transmission mode on a Bruker Vertex 70 FTIR spectrometer equipped with a MCT detector, spectra were obtained by averaging 100 scans at a resolution of 4 cm⁻¹. Blanks are collected prior to exposure and used as references.

Computational methods

ZnO NPs have been modelled as a combination of most stable surfaces: (10 $\bar{1}$ 0), (11 $\bar{2}$ 0), (000 $\bar{1}$), and (0001). These have been represented *via* periodic slabs adding a vacuum region of 10 Å between translationally repeated slabs along the surface direction, following a previously utilized procedure.³⁸ Test calculations with double vacuum yielded variations in adsorption energies below 0.001 eV, and of at most 2 cm⁻¹ in computed vibrational frequencies. Briefly, periodic density functional theory (DFT) calculations have been carried out using the VASP code,⁵⁴ while using the projector augmented wave (PAW) method to represent atomic cores.⁵⁵ A plane wave basis set of kinetic energy of up to 415 eV was employed with a tetrahedron method algorithm for smearing. Geometry optimizations were performed using a conjugate gradient algorithm, yet final energies obtained were corrected to 0 K (no smearing). Surface structures were considered optimized when forces acting on atoms were below 0.01 eV Å⁻¹. Calculations were carried out in a non-spin-polarized fashion using the Perdew–Burke–Ernzerhof (PBE) exchange–correlation functional,⁵⁶ known to be appropriate to model wurtzite ZnO bulk and surfaces,⁴⁵ as well as interactions of atomic hydrogen, hydroxyl moieties, and water molecules thereon.⁴⁸

Polar (000 $\bar{1}$) and (0001) surfaces, as well as nonpolar (11 $\bar{2}$ 0) surface, are known to display a (1 \times 1) perfect arrangement when fully hydrated.^{38,57,58} However, for the nonpolar (10 $\bar{1}$ 0) surface a (2 \times 1) unit cell is needed, as theoretically and experimentally determined in the past^{47,59} and very recently by Kenmoe and co-workers.⁶⁰ These surfaces have been represented using eight-layered slabs, whose bottom most layers are kept as in the pre-optimized bulk positions, whereas uppermost four layers, together with H, OH, or H₂O moieties, are fully relaxed. Different arrangements have been explored for H₂O adsorbed on these surfaces, including situations where half or all the H₂O molecules are dissociated, as well as cases where all water remain intact, considering different surface locations of water molecules and H and/or OH groups as well. In all cases, a 17 \times 17 \times 1 Monkhorst–Pack *k*-points mesh was used, and so, variations in total energy due to the computational setup are below 0.001 eV, as found in tests with stringent conditions. Adsorption energies are already found in the literature,³⁸ and so here only differences in adsorption energy per H₂O unit are shown. From the found structural energy minima, harmonic frequencies were gained by numerical calculations and diagonalization of the Hessian matrix by independent displacements of 0.03 Å of the adsorbate, and in the case of H adsorbed on a surface O atom, O_s, by taking this into account as well. Shorter displacements lead to variations in frequencies below 4 cm⁻¹, and coupling with substrate is expected to be negligible given that phonon frequencies are in the 100–600 cm⁻¹ range.⁶¹ Notice that neglecting anharmonicity may translate into overestimated frequencies, with a difference of \sim 100 cm⁻¹ for frequencies above 3500 cm⁻¹.^{38,62} Simulated IR spectra were obtained by estimating the band intensity *via* a change in the vibration dipole moment component normal to surface, and a peak Gaussian convolution of 100 cm⁻¹ half-width has been applied.

Conclusions

In summary, by combining infrared spectroscopy and DFT approaches, it is demonstrated that ZnO smoke behaves as multi-facet single crystals. Along with the identification—for the first time—of water structures on ZnO(11 $\bar{2}$ 0), and of new water structures on ZnO(10 $\bar{1}$ 0), the present work highlights that highly dispersed ZnO is dominated by a few well-defined low-index orientations and that water adsorption can serve as a discriminant probe to specifically identify oriented facets in those ZnO materials. All the significant infrared bands seen in the experimental spectra of ZnO smoke exposed to water vapour have been directly assigned to calculated modes for water adsorbed on (10 $\bar{1}$ 0), (11 $\bar{2}$ 0), (0001), and (000 $\bar{1}$) surfaces and, conversely, all the calculated vibrational modes match an experimental counterpart. Cross-agreements between the experimental results and simulations raise confidence in the validity of the assignments. Moreover, the similarity of the infrared spectra collected here to those recorded by Noei *et al.* on another type of ZnO nanopowder⁶ suggests that the very simple image emerging

from the examination of hydroxylated/hydrated ZnO smokes could be widely applied. The proposed approach differs markedly from common practice. Instead of constraining the synthesis to favour one facet or another, the powder is analysed as it is. This gives a great deal of generality to the present conclusions. In line with the similarity of the infrared spectra collected here with those recorded by Noei *et al.*⁶ on a different ZnO powder, this gives a great deal of generality to the present conclusions. The above combined theoretical and experimental approach appears as a robust basis for addressing the surface structure of divided zinc oxide and suggests a wide application for the very simple image emerging from the examination of hydroxylated/hydrated ZnO smokes.

Acknowledgements

We thank Dr Dominique Demaille (INSP, Paris) for recording SEM images shown in Fig. 1 as well as Dr Jacek Goniakowski (INSP, Paris) and Dr Remi Lazzari (INSP, Paris) for fruitful discussions, comments and proofreading. This work has been supported by Spanish Ministry of Economy and Competitiveness (MINECO) and Fondo Europeo de Desarrollo Regional (FEDER) CTQ2015-64618-R grant and partly by Generalitat de Catalunya grants 2014SGR97, and XRQTC. The research in this work is in the framework of the NOMAD Center of Excellence project which received funding from the European Union's Horizon 2020 research and innovation programme under grant agreement No. 676580. F. V. thanks MINECO for a postdoctoral Ramón y Cajal (RyC) research contract (RYC-2012-10129). F. I. acknowledges additional support from the 2015 ICREA Academia Award for Excellence in University Research.

References

- 1 C. Burda, X. Chen, R. Narayanan and M. A. El-Sayed, *Chem. Rev.*, 2005, **105**, 1025.
- 2 G. A. Somorjai and R. M. Rioux, *Catal. Today*, 2005, **100**, 201.
- 3 A. Zecchina, E. Groppo and S. Bordiga, *Chem. – Eur. J.*, 2007, **13**, 2440.
- 4 K. Zhou and Y. Li, *Angew. Chem., Int. Ed.*, 2012, **51**, 602.
- 5 G. Spoto, E. N. Gribov, G. Ricchiardi, A. Damin, D. Scarano, S. Bordiga, C. Lamberti and A. Zecchina, *Prog. Surf. Sci.*, 2004, **76**, 71.
- 6 H. Noei, H. Qiu, Y. Wang, E. Löffler, C. Wöll and M. Muhler, *Phys. Chem. Chem. Phys.*, 2008, **10**, 7092.
- 7 P. Borghetti, E. Meriggio, G. Rousse, G. Cabailh, R. Lazzari and J. Jupille, *J. Phys. Chem. Lett.*, 2016, **7**, 3223.
- 8 S. Coluccia, A. J. Tench and R. L. Segall, *J. Chem. Soc., Faraday Trans. 1*, 1979, **75**, 1769.
- 9 E. Garrone, A. Zecchina and F. S. Stone, *Philos. Mag. B*, 1980, **42**, 683.
- 10 E. Knözinger, K.-H. Jacob, S. Singh and P. Hofmann, *Surf. Sci.*, 1993, **290**, 388.
- 11 R. Hacquart, J.-M. Krafft, G. Costentin and J. Jupille, *Surf. Sci.*, 2005, **595**, 172.

- 12 S. Stankic, J. Bernardi, O. Diwald and E. Knözinger, *J. Phys. Chem. B*, 2006, **110**, 13866.
- 13 A. F. Moodie and C. E. Warble, *J. Cryst. Growth*, 1971, **10**, 26.
- 14 R. Hacquart and J. Jupille, *Chem. Phys. Lett.*, 2007, **439**, 91.
- 15 P. Geysersmans, F. Finocchi, J. Goniakowski, R. Hacquart and J. Jupille, *Phys. Chem. Chem. Phys.*, 2009, **11**, 2228.
- 16 G. Cabailh, R. Lazzari, J. Jupille, L. Savio, M. Smerieri, A. Orzelli, L. Vattuone and M. Rocca, *J. Phys. Chem. A*, 2011, **115**, 7161.
- 17 E. Knözinger, K.-H. Jacob and P. Hofmann, *J. Chem. Soc., Faraday Trans.*, 1993, **89**, 1101.
- 18 O. Diwald and E. Knözinger, *J. Phys. Chem. B*, 2002, **106**, 3495.
- 19 N. Siedl, D. Koller, A. K. Sternig, D. Thomele and O. Diwald, *Phys. Chem. Chem. Phys.*, 2014, **16**, 8339.
- 20 V. H. Grassian, *J. Phys. Chem. C*, 2008, **112**, 18303.
- 21 K. P. McKenna and A. L. Shluger, *Nat. Mater.*, 2008, **7**, 859.
- 22 D. C. Hurum, A. G. Agrios, K. A. Gray, T. Rajh and M. C. Thurnauer, *J. Phys. Chem. B*, 2003, **107**, 4545.
- 23 J. Pan, G. Liu, G. Q. Lu and H.-M. Cheng, *Angew. Chem., Int. Ed.*, 2011, **50**, 2133.
- 24 H. G. Yang, C. H. Sun, S. Z. Qiao, J. Zou, G. Liu, S. C. Smith, H. M. Cheng and G. Q. Lu, *Nature*, 2008, **453**, 638.
- 25 C. Deiana, M. Minella, G. Tabacchi, V. Maurino, E. Fois and G. Martra, *Phys. Chem. Chem. Phys.*, 2013, **15**, 307.
- 26 P. S. Shewale and Y. S. Yu, *J. Alloys Compd.*, 2016, **684**, 428.
- 27 D. Chakraborty, R. Gayen, S. Hussain, R. Bhar, A. K. Ghoshal and A. K. Pal, *J. Phys.: Conf. Ser.*, 2012, **390**, 012065.
- 28 R. Knut, R. Lindblad, S. Grachev, J.-Y. Faou, M. Gorgoi, H. Rensmo, E. Søndergard and O. Karis, *J. Appl. Phys.*, 2014, **115**, 043714.
- 29 K. Kalyanasundaram, *J. Phys. Chem. C*, 2014, **118**, 16303.
- 30 C. T. Campbell, K. A. Daube and J. M. White, *Surf. Sci.*, 1987, **182**, 458.
- 31 K. Maeda and K. Domen, *Chem. Mater.*, 2010, **22**, 612.
- 32 Ü. Özgür, Y. I. Alivov, C. Liu, A. Teke, M. A. Reshchikov, S. Dogan, V. Avrutin, S.-J. Cho and H. Morkoç, *J. Appl. Phys.*, 2005, **98**, 041301.
- 33 Z. L. Wang, *Mater. Today*, 2004, **7**, 26.
- 34 A. B. Djurisić and Y. H. Leung, *Small*, 2006, **2**, 944.
- 35 P. X. Gao and Z. L. Wang, *J. Appl. Phys.*, 2005, **97**, 044304.
- 36 G. R. Li, T. Hu, G. L. Pan, T. Y. Yan, X. P. Gao and H. Y. Zhu, *J. Phys. Chem. C*, 2008, **112**, 11859.
- 37 D. Scarano, G. Spoto, S. Bordiga, A. Zecchina and C. Lamberti, *Surf. Sci.*, 1992, **276**, 281.
- 38 F. Viñes, A. Iglesias-Juez, F. Illas and M. Fernandez-García, *J. Phys. Chem. C*, 2014, **118**, 1492.
- 39 S. Kittaka, T. Sasaki and N. Fukuhara, *Langmuir*, 1992, **8**, 2598.
- 40 A. Iglesias-Juez, F. Viñes, O. Lamiel-García, M. Fernández-García and F. Illas, *J. Mater. Chem. A*, 2015, **3**, 8782.
- 41 G. Wulff, *Z. Kristallogr. Mineral.*, 1901, **34**, 449.
- 42 F. Viñes, J. R. B. Gomes and F. Illas, *Chem. Soc. Rev.*, 2014, **43**, 4922.
- 43 H. F. Wilson, C. Tang and A. S. Bernard, *J. Phys. Chem. C*, 2016, **120**, 9498.
- 44 T. Sato, T. Tanigaki, H. Suzuki, Y. Saito, O. Kido, Y. Kimura, C. Kaito, A. Takeda and S. Kaneko, *J. Cryst. Growth*, 2003, **255**, 313.
- 45 B. Meyer and D. Marx, *Phys. Rev. B: Condens. Matter Mater. Phys.*, 2003, **67**, 035403.
- 46 Y. Wang, M. Muhler and C. Wöll, *Phys. Chem. Chem. Phys.*, 2006, **8**, 1521.
- 47 O. Dulub, B. Meyer and U. Diebold, *Phys. Rev. Lett.*, 2005, **95**, 136101.
- 48 B. Meyer, H. Rabaa and D. Marx, *Phys. Chem. Chem. Phys.*, 2006, **8**, 1513.
- 49 D. J. Cooke, A. Marmier and S. C. Parker, *J. Phys. Chem. B*, 2006, **110**, 7985.
- 50 D. Raymand, A. C. T. van Duin, D. Spångberg, W. A. Goddard III and K. Hermansson, *Surf. Sci.*, 2010, **604**, 741.
- 51 S. G. Holthaus, S. Köppen, T. Frauenheim and L. C. Ciacchi, *J. Chem. Theory Comput.*, 2012, **8**, 4517.
- 52 S. Stankic, M. Cottura, D. Demaille, C. Noguera and J. Jupille, *J. Cryst. Growth*, 2011, **329**, 52.
- 53 F. Finocchi, R. Hacquart, C. Naud and J. Jupille, *J. Phys. Chem. C*, 2008, **112**, 13226.
- 54 G. Kresse and J. Furthmüller, *Phys. Rev. B: Condens. Matter Mater. Phys.*, 1996, **54**, 11169.
- 55 P. E. Blöchl, *Phys. Rev. B: Condens. Matter Mater. Phys.*, 1994, **50**, 17953.
- 56 J. P. Perdew, K. Burke and M. Ernzerhof, *Phys. Rev. Lett.*, 1996, **77**, 3865.
- 57 M. Kunat, S. Gil-Girol, T. Becker, U. Burghaus and C. Wöll, *Phys. Rev. B: Condens. Matter Mater. Phys.*, 2002, **66**, 081402.
- 58 T. Becker, S. Hövel, M. Kunat, C. Boas, U. Burghaus and C. Wöll, *Surf. Sci.*, 2001, **486**, L502.
- 59 B. Meyer, D. Marx, O. Dulub, U. Diebold, M. Kunat, D. Langenberg and C. Wöll, *Angew. Chem., Int. Ed.*, 2004, **43**, 6642.
- 60 S. Kenmoe and P. U. Biedermann, *Phys. Chem. Chem. Phys.*, 2017, **19**, 1466.
- 61 B. H. Bairamov, A. Heinrich, G. Irmer, V. V. Toporov and E. Ziegler, *Phys. Status Solidi B*, 1983, **119**, 227.
- 62 S. Manzhos, T. Carrington Jr. and K. Yamashita, *Surf. Sci.*, 2011, **605**, 616.



Cite this: *Nanoscale*, 2019, **11**, 5102

Defect-related multicolour emissions in ZnO smoke: from violet, over green to yellow†

Miao Zhang,^{a,b} Frédéric Averseng,^a Francia Haque,^b Patrizia Borghetti,^b Jean-Marc Krafft,^a Benoît Baptiste,^c Guylène Costentin^{ID}*^a and Slavica Stankic^{ID}*^b

The nature of defects in ZnO smoke was studied at different stages of the material's history by combining photoluminescence (PL) and electron paramagnetic resonance (EPR) spectroscopy. In contrast to studies previously reported on ZnO nanopowders, high vacuum conditions ($P < 10^{-5}$ mbar) have been applied during sample storage, handling and spectroscopic investigations. Two pairs of violet-PL/EPR signals (2.88 eV/ $g = 1.956$ and 2.80 eV/ $g = 1.960$) were observed in the as-synthesized ZnO powder and attributed to surface (dominant) and bulk zinc interstitials (Zn_i^+). Upon annealing in O_2 -poor conditions, green-PL emission (2.41 eV) and EPR signal at $g = 2.002$ develop along with EPR signals specific of superoxide radicals (O_2^-). In the absence of any external O_2 supply, the oxygen necessary for the creation of a notable amount of O_2^- is provided by the lattice of ZnO smoke, so that the green emission and its EPR counterpart are unambiguously assigned to singly charged oxygen vacancies (V_O^+). Annealing at high P_{O_2} results in a broad PL emission (~ 2.07 eV) without an EPR counterpart. This yellow emission was assigned to peroxide-like surface species (O_2^{2-}). Overall, this study shows that the visible emissions in ZnO smoke nanopowders can range from violet, over green to yellow as a function of sample history and that the corresponding PL/EPR fingerprints can serve as guidelines for the recognition of defects in other ZnO types.

Received 10th December 2018,
Accepted 11th February 2019

DOI: 10.1039/c8nr09998g

rsc.li/nanoscale

1. Introduction

The properties and, thus, technological potential of any semiconductor (chemical, optical, magnetic, *etc.*) are highly governed by the atomic-scale defects it contains. This applies to both the nature and quantity of defects that are present. A semiconducting metal oxide, ZnO, finds applications as a transparent conducting oxide for solar cells,^{1,2} piezoelectric for various electronic devices,³ transparent thin film for gas sensors,^{4,5} nanowire-based gas sensor for NO_x or H_2 ,⁶ UV optical emitter in LEDs,⁷⁻⁹ and dilute magnetic semiconductor for spintronics.^{10,11} The presence of lattice defects is known to impact the performance of ZnO in most of these application fields. In particular, defects are highly undesirable in ZnO when used as an UV optical emitter in LEDs since their presence reduces luminescence efficiency when compared to a

defect-free material. Hence, fundamental knowledge on ZnO defects is required in order to tune the ZnO performances for a variety of novel high-tech applications.

Point defects are present in all crystalline materials in the form of missing (vacancies), interstitial (interstitials) or substituted (anti-sites) ions and are, generally, electronically charged. They induce local changes and lattice relaxations and new electronic states are generated within the band gap. An identification of crystal defects is, however, not a simple task. This can be illustrated by highly controversial assignments of photoluminescence (PL) and electron paramagnetic resonance (EPR) data reported for ZnO, with several defects proposed for a given signal or several signals ascribed to a given defect. This concerns in particular, the after discussed green luminescence (centered ~ 2.17 – 2.5 eV) that was controversially assigned to various ZnO defects (V_O , O_{Zn} , O_i , V_{Zn}).¹²⁻¹⁹ The absence of consensus results from both, an inadequate comparison of samples of different origins (for instance single crystals vs. nanostructured ZnO) and/or the variability of experimental conditions applied during the synthesis, processing and measurements. The nature and concentration of a given defect depend strongly on all stages of the sample's history (from synthesis, over processing to measurements) and the corresponding spectroscopic properties are thus expected to vary. This particularly concerns nanostructured ZnO (nano-

^aSorbonne Université, CNRS, Laboratoire de Réactivité de Surface, LRS, F-75005 Paris, France. E-mail: guylene.costentin@upmc.fr

^bSorbonne Université, CNRS, Institut des NanoSciences de Paris, INSP, F-75005 Paris, France. E-mail: slavica.stankic@insp.jussieu.fr

^cSorbonne Université, CNRS, Institut de Minéralogie, de Physique des Matériaux et de Cosmochimie, IMPMC, F-75005 Paris, France

†Electronic supplementary information (ESI) available. See DOI: 10.1039/c8nr09998g

particles, thin films) where, for instance, the measurements in air can strongly differ from those in vacuum.^{20,21} Transformation of an existing defect into a new one can occur through the change of its oxidation state *via* the interaction with surrounding molecules, which finally leads to the disappearance of its specific spectroscopic signal. For instance, oxygen vacancies can be efficiently passivated by water – as clearly demonstrated in FTIR studies on ZnO nanoparticles.^{22–24} Therefore, exposing ZnO nanoparticles to a water containing environment is likely to severely hinder the identification of native oxygen vacancies initially present in the sample.

Also, while theoretical calculations may provide useful information for the identification of lattice defects in ZnO, one should keep in mind that they are commonly performed at $T = 0$ K, *i.e.* far from the conditions usually achieved in experiments. Additionally, nanostructured systems are usually obtained and studied far from thermodynamic equilibrium. Thus, the straightforward application of such theoretical results for discussing the existence of given defects is at least questionable. For example, because the formation energy of singly charged oxygen vacancies (V_{O^+}) was calculated to be rather high in ZnO,²⁵ the V_{O^+} is therefore considered to be a defect rather difficult to create. Yet the present study will unambiguously prove otherwise.

In this contribution, by using highly controlled experimental conditions, we will demonstrate a close correlation of PL/EPR fingerprints observed in ZnO smoke nanopowder at different stages (as-synthesized, in the presence of O₂ and H₂O molecules, after thermal post-growth treatments) to corresponding point defects. In that context, we applied the following strategy:

(i) Use of a clean synthesis route to exclude extrinsic defects thus limiting the investigation to the sole intrinsic ones.

(ii) Application of high-vacuum conditions ($P < 10^{-5}$ mbar) during the storage, handling, and spectroscopic characterization studies.

Such a strategy allowed us to identify the nature of defects that are natively present in ZnO smoke and to follow their evolution as well as the appearance of new ones at different processing stages.

2. Experimental details

2.1. Synthesis and storage

ZnO smoke nanopowder was produced by the metal combustion method in a glovebox where the ignition of metallic Zn-foil of high purity (99.99%, 0.125 mm thickness, Advent Research Materials Ltd) was resistively induced.²⁶ As confirmed by XPS analysis, these synthesis conditions ensure that the formation of extrinsic defects was avoided. The white powder was collected on a glass plate and, then, transferred into a quartz-glass cell dedicated to PL or EPR measurements. The powder was constantly maintained under dynamic vacuum ($P < 10^{-5}$ mbar) during the storage and *in situ* spectroscopic measurements.

2.2. Electron microscopy

For the purpose of microscopy studies, as-synthesized ZnO powders were directly deposited on TEM grids, preventing the use of any solvent. Transmission electron microscopy (TEM) measurements were performed on a JEOL 2100 field emission transmission electron microscope operating at 200 kV with a 0.18 nm resolution. Scanning electron microscopy (SEM) images were recorded on a field emission Zeiss Supra 40 scanning electron microscope.

2.3. X-Ray diffraction

X-Ray powder diffraction measurements were carried out at the X-ray diffraction platform of IMPMC on a Panalytical XpertPro MPD diffractometer using a Co K α radiation source ($\lambda_{K\alpha 1} = 1.78897$ Å, $\lambda_{K\alpha 2} = 1.79285$ Å) and an X'Celerator detector. The samples were prepared within a glovebox and mounted in a homemade chamber allowing XRD measurements under controlled, anoxic conditions.

Cell parameters, mean coherent domain sizes and micro-strain were refined using the Rietveld method as implemented in Fullprof software. Since the peak width was larger than the instrumental resolution, Lorentzian isotropic size (Y) and Lorentzian isotropic strain (X) parameters were refined. The two effects can be decoupled on the diagram measured over a wide angular range because the first induces a peak broadening as $Y/\cos(\theta)$ whereas the second as $X/\tan(\theta)$.

2.4. Electron paramagnetic resonance (EPR)

In order to strictly control the different thermal treatments and subsequent EPR measurements, the following procedure has been followed: (i) a homemade setup equipped with a tubular oven has been used for all thermal treatments. High-vacuum ($P < 10^{-5}$ mbar) was reached using a turbo-molecular pump. Connections also permitted the controlled addition and removal of gases, such as O₂ and H₂O vapor, during or after the thermal treatments. (ii) The ZnO sample was treated and measured in a suprasil quartz tube (5 mm external diameter), combined with a high-vacuum bellows-type metal-glass stopper and ball joint, which allowed for a continuous connection with the homemade setup during all treatments, measurements, avoiding any unwanted external contamination.

The EPR measurements were performed on a JEOL FA300 computerized spectrometer working at ~ 9.3 GHz (X-band). All spectra were recorded placing the powders under dynamic vacuum ($P < 10^{-5}$ mbar) at 77 K, using an insertion dewar containing liquid nitrogen, applying a microwave power of 2 mW and 100 kHz field modulation and presented, as is usual, as the first derivative of the absorbance. In order to avoid the overmodulation and subsequent alteration of narrow EPR signals (resulting in signal broadening, loss of close peaks or multiplets, *etc.*), a modulation width/amplitude of 0.1 mT was systematically used. The g -factors were calibrated by using solid 2,2-diphenyl-1-picrylhydrazyl (DPPH, $g = 2.0037$) and care

was taken to always keep the same height of powder in the EPR tube (~ 2 cm).

Additionally, the g -factor of solids can be anisotropic (value differs among the considered direction), and is thus described as a tensor (3×3 matrix with zero non-diagonal terms, and g_x , g_y and g_z diagonal terms). Three cases may then occur: rhombic ($g_x \neq g_y \neq g_z$), axial ($g_z \neq g_x = g_y$), or isotropic ($g_z = g_x = g_y = g$) symmetry.²⁷ Computer simulations of the spectra were performed using the EPRsim32 program.²⁸

2.5. Diffuse reflectance UV-vis (DR UV-Vis)

The spectra were recorded at room temperature using a Varian Cary 5000 spectrometer equipped with an integrating sphere, while a sample of barium sulfate (BaSO_4) with $\sim 100\%$ reflectance was used as a reference.

2.6. Photoluminescence (PL)

Room-temperature experiments were performed on a FluoroLog II fluorometer (Jobin–Yvon) equipped with a 450 W Xe lamp as an excitation source. Photoluminescence emission spectra were obtained fixing the excitation energy at 4.13 eV (300 nm) and using a WG-320 cut-off filter on the emission side to prevent the contributions of the first and second order coming from excitation light. The PL band fitting analyses were done by using IGOR.

Photoluminescence and UV-vis diffuse reflectance measurements were carried out in a quartz glass tube that was connected to the same homemade high vacuum line ($P < 10^{-5}$ mbar) as that used for EPR measurements.

To investigate the impact of annealing steps in an oxygen rich atmosphere (section 3.2.2), the sample was alternatively annealed in $P_{\text{O}_2} = 100$ mbar, then outgassed at room temperature to $P < 10^{-5}$ mbar for 1 h before the PL/EPR spectra were recorded under dynamic vacuum as usual. The same procedure was repeated in the second and third cycles.

2.7. Raman

The same quartz glass cell as described for PL and UV experiments was used for Raman investigations. Raman spectra were recorded at room temperature on a Jobin–Yvon triple-stage T64000 Raman spectrometer equipped with a CCD camera. An argon laser monochromatic source ($\lambda = 514.5$ nm) was used.

2.8. X-ray photoelectron spectroscopy (XPS)

XPS spectra were recorded with a non-monochromatic Al $K\alpha$ source (photon energy, $h\nu = 1486.7$ eV) and a hemispherical analyzer Phoibos 100 with a pass energy of 20 eV at normal emission. The stoichiometric ratio n_1/n_2 between two species distributed homogeneously in the sample is obtained through the following equation: $n_1/n_2 = I_1 (\sigma_2 \times \lambda_2 \times T_2) / I_2 (\sigma_1 \times \lambda_1 \times T_1)$, where I is the integration areas of the peak Zn 3s and that of the component of O 1s corresponding to lattice oxygen in ZnO, T is the transmission function of the analyzer tabulated for the analyzer Phoibos 100, λ_{Zn} and λ_{O} are provided by the NIST standard reference database for the ZnO material,^{29,30} while σ_{Zn} and σ_{O} are taken from ref. 31.

3. Results

3.1. As-prepared ZnO smoke nanoparticles

3.1.1. Morphological, structural and optical properties.

Fig. 1a and b show representative TEM images of the as-prepared ZnO smoke nanoparticles. Rods (white arrow in Fig. 1a) and tetrapods, with the latter being slightly dominant, were systematically observed in ZnO smoke micrographs. Such tetrapod-like structures of CdSe, were shown to exhibit particular electron transport properties³² and thus have recently gained great attention. In these structures, four individual rod-like crystals (tetrapod-arms) grow from a common core and arrange together in the form of a tetrahedron. The length of the arms is larger than 100 nm while the diameter is clearly smaller than

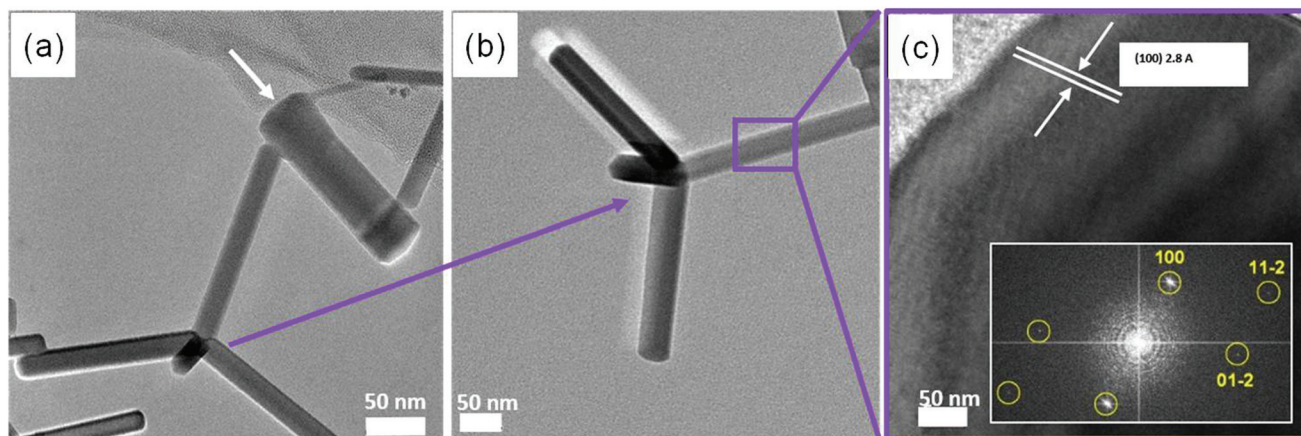


Fig. 1 Representative TEM (a, b) and HRTEM (c) images of the as-synthesized ZnO smoke sample. HRTEM image (c) corresponds to the ZnO tetrapod arm viewed along a [021] zone axis of the wurtzite structure. The inset in (c) shows SAED of the selected HRTEM zone in violet.

50 nm. The high-resolution TEM (HRTEM) image of such a tetrapod arm seen along the [021] zone axis is presented in Fig. 1c. It illustrates that the tetrapod arms grow along the [0001] direction and have a wurtzite structure. No disordered areas were observed and the lattice spacing was found to be 0.281 nm, which matches with the d -spacing of {1011} ZnO planes. The high crystal quality of particles is demonstrated by the selected area electron diffraction (SAED) pattern (inset in Fig. 1c).

The X-ray diffraction pattern (Fig. 2a) and lattice parameters calculated by Rietveld refinement analysis ($a = b = 3.250 \text{ \AA}$, $c = 5.207 \text{ \AA}$, see Table 2 in section 3.2.1) confirm the wurtzite phase. The intense and narrow diffraction peaks reflect the high crystal quality of the sample and a mean coherent domain size of $\sim 90 \text{ nm}$. The microstrain, estimated by the Williamson–Hall method³³ to be 3%, indicates that the distances between the relevant crystal planes are not identical, pointing out some stress probably induced by the presence of defects. The Raman spectrum (Fig. 2b) reveals two intense peaks centered at 100 cm^{-1} (E_2^{low}) and 439 cm^{-1} (E_2^{high}). E_2^{low} and E_2^{high} Raman modes are particularly sensitive to the motion of zinc and

oxygen in the lattice, respectively,^{34,35} and represent a direct measure of ZnO crystal quality. Additionally, two less intense peaks are observed at ~ 490 and at $\sim 600 \text{ cm}^{-1}$. The former peak is usually detected on nanostructured ZnO and attributed to the surface optical phonon (SOP).³⁶ The broad and weak signal at 600 cm^{-1} can be correlated with the $E_1(\text{LO})$ peak previously detected on ZnO single crystals at $\sim 590 \text{ cm}^{-1}$ and assigned to intrinsic lattice defects.³⁵ In ZnO thin films grown under Zn-rich conditions, such a Raman mode at $\sim 580\text{--}590 \text{ cm}^{-1}$ was systematically attributed to an excess of zinc in the ZnO lattice, in line with the growth conditions.^{37,38}

The as-synthesized ZnO smoke powder exhibits a white color and the related diffuse reflectance UV-visible spectrum (Fig. 2c) shows an absorption threshold at $\sim 380 \text{ nm}$. From the corresponding Tauc plot (Fig. SI-1†), the band gap energy (E_{BG}) was estimated to be 3.26 eV in line with values commonly reported for nanostructured ZnO ($3.2\text{--}3.3 \text{ eV}$).^{39,40}

3.1.2. PL and EPR fingerprints of the as-prepared ZnO smoke. The room temperature PL emission spectrum of the as-synthesized ZnO-smoke (Fig. 3a) was recorded using an exci-

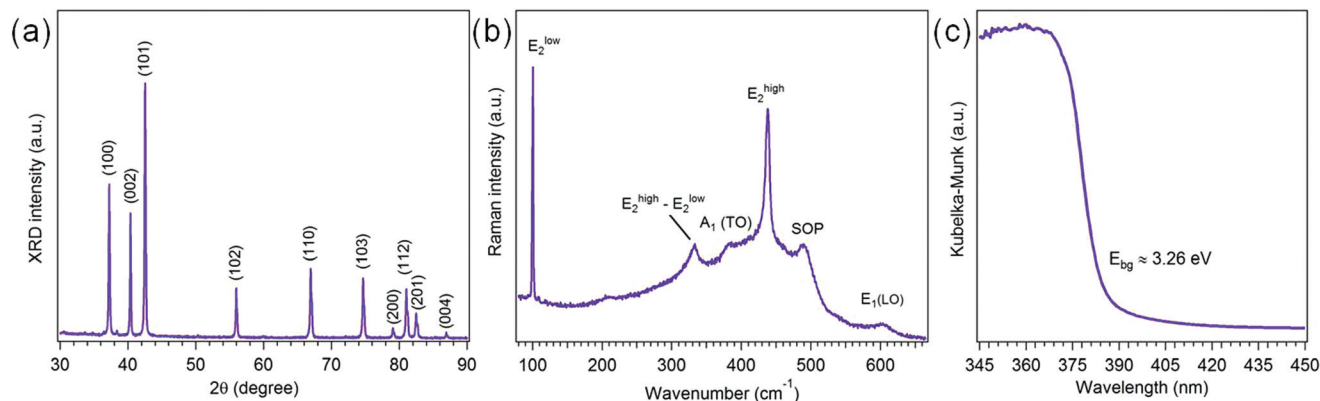


Fig. 2 XRD pattern (a), Raman (b) and DR UV-Vis spectrum (c) of the as-synthesized ZnO smoke.

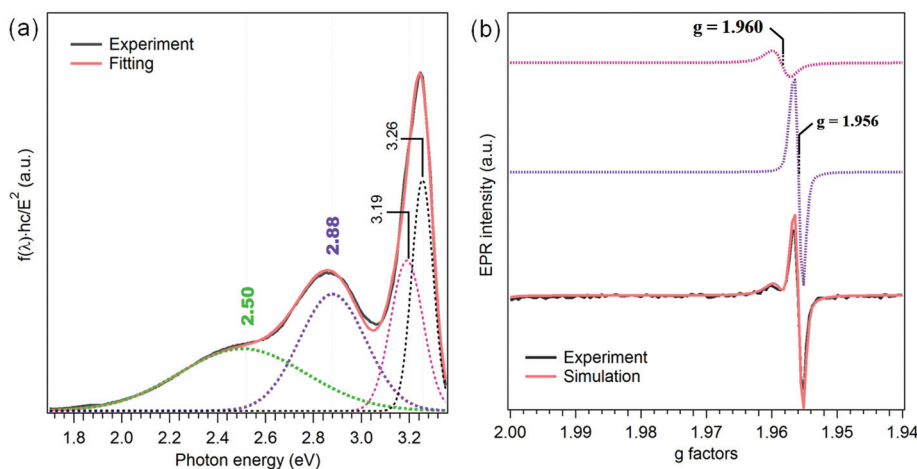


Fig. 3 As-synthesized ZnO smoke: (a) PL spectra (black curve) and corresponding band-fitting analysis (red). The contribution of each emission is represented by dotted curves in black, magenta, violet and green. (b) Experimental (black curve) and simulated (red curve) EPR spectra. Violet and magenta dotted curves show the contribution of the two paramagnetic species (A and B).

tation energy of 4.13 eV that slightly exceeds the E_{BG} estimated from the Tauc plot (Fig. SI-1†). The PL spectrum consists of a strong and sharp UV-band and a broad, low-intensity one in the visible domain. The UV-emission results from band-to-band transitions¹³ and its high intensity reflects the good crystal quality demonstrated above by HRTEM, XRD and Raman data. The existence of an emission band in the visible domain, despite its low intensity, yet reflects that additional states exist in the band gap of the as-grown sample. Given the applied synthesis conditions, the native defects evidently present in ZnO smoke can only be of the intrinsic nature.

Band fitting analysis (Fig. 3a) shows that the PL spectrum can be nicely reproduced by a set of a four Gaussian bands. The UV emission requires two Gaussians of a similar energy (3.19 eV and 3.26 eV) – both close to the estimated value of E_{BG} (Fig. SI-1†). The width of the excitonic band and so the necessity of two Gaussian curves for its adequate reproduction come from the morphological heterogeneity of the sample (Fig. 1a). The visible emission can also be successfully fitted by a pair of Gaussians. The first one is centered at 2.50 eV (495 nm), which corresponds to green luminescence (GL) commonly reported for ZnO and, so far, attributed to all defects likely to be present in ZnO.^{41–44} We will not discuss this PL band in the present paper since it is a subject of another ongoing study. The second Gaussian band reveals a slightly higher contribution and peaks at 2.88 eV (430 nm), an energy that matches with violet luminescence (VL). VL is less frequently measured on ZnO but if observed then usually on samples produced under non-equilibrium conditions followed by an ultra-rapid reactive quenching.⁴⁵ Unlike GL, for which no uniform recombination model was calculated, transitions between 2.75 and 2.90 eV have been quite consistently calculated to arise from

energy states related to interstitial zinc (Zn_i).^{46–48} The same assignment can also be found in several experimental studies.^{38,49,50} VL observed in the PL spectrum of the as-synthesized ZnO smoke fits well to this interval suggesting Zn_i to be the defect specific of the applied synthesis method. This is not surprising since metal combustion synthesis occurs far from the equilibrium and includes rapid quenching conditions that, as mentioned above, favor Zn-rich ZnO. Such an excess of Zn, in at least the first few nanometers (~ 5 nm), of the as-synthesized ZnO smoke surface was confirmed by XPS analysis ($\text{Zn}/\text{O} = 1.26 \pm 0.15$).

The EPR spectrum (Fig. 3b) of the as-prepared sample consists of two signals: an intense and narrow signal at $g = 1.956$ (species A) and a weaker one at $g = 1.960$ (species B). EPR signals with a g -value close to 1.960 have been often observed on ZnO yet without a consensus on their origin, so far.^{51–57} Only a few studies report an EPR signal at $g = 1.956$ on ZnO,^{58–60} yet Morazzoni and coworkers assigned it to Zn_i .⁶⁰ One should notice that this EPR signal prevails in the EPR spectrum of the as-prepared ZnO smoke in the same way that VL was shown to dominate the visible domain of the PL spectrum.

Considering the Zn-excess determined by XPS, the maximum of the visible PL and the synthesis conditions, we assign the two main PL/EPR features of the as-grown ZnO smoke (couple I: 2.88 eV/ $g = 1.956$) to Zn_i . Additionally, the proximity in g -values of the two EPR signals (1.960 vs. 1.956) may point to the same type of species (*i.e.* Zn_i) yet experiencing a somewhat different crystallographic environment. In order to get more insights on that point, the impact of molecular oxygen on these two signals was further investigated since only defects located at the surface can be available for such an interaction that would modify their corresponding signals.

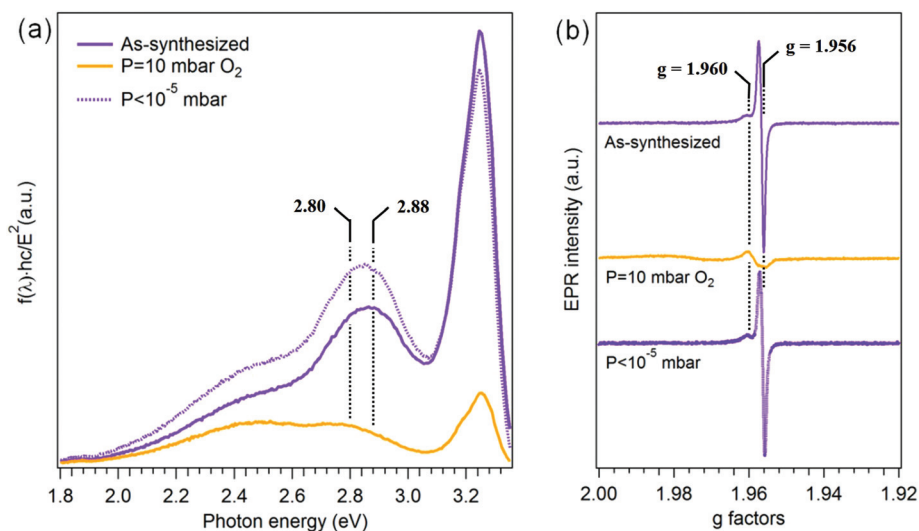


Fig. 4 PL (a) and EPR (b) spectra of the as-synthesized ZnO smoke in a vacuum (solid violet curve), in the presence of O_2 (solid orange curve, $P_{\text{O}_2} = 10$ mbar) and after pumping out O_2 (dotted violet curve, $P < 10^{-5}$ mbar).

3.1.3 Adsorption of O₂ at RT. Fig. 4a compares the PL spectra of the as-synthesized ZnO (violet, solid line), in the presence of O₂ (orange, $P_{O_2} = 10$ mbar) and after pumping out oxygen (violet, dotted line). Overall, the PL intensity decreases in the presence of O₂. It is well known that the adsorption of an e⁻ acceptor (such as O₂) on a semiconductor surface leads to an upward band bending that, consequently, results in the generation of a depletion layer near the surface.^{61,62} Such a depletion layer determines the depth of the active PL and, so, the photoluminescence yield. This explains why the otherwise dominant light emission mechanism measured for the as-prepared ZnO smoke (UV-emission) is almost one order of magnitude weaker in the presence of O₂. In the case of nanoparticles such an effect is even more pronounced, since much of the material is close to the surface and, thus, more affected by band bending. Similar effects occurring upon O₂ admission were reported for ZnO nanowires by Reshchikov and coworkers⁶³ who measured a much higher intensity of excitonic emission in a vacuum than in ambient air pressure. The influence of oxygen on the intensity and shape of PL spectra illustrates how important it is to perform such measurements under dynamic vacuum as to prevent misleading interpretation due to O₂ interfering effects.

On the other hand, a strong decrease of VL upon interaction with O₂ implies that the underlying defect (*i.e.* Zn_i⁺) transforms into an optically inactive center. To be able to interact with gaseous O₂, Zn_i⁺ defects must be located at the surface. Additionally, a PL band emerges at 2.80 eV (VL_B) upon O₂ adsorption. This band belongs also to the violet emission domain and was most probably already present in the spectrum of the as-synthesized sample yet, its contribution was hardly distinguishable from the close and much more intense (four times) band at 2.88 eV. Hence, in a similar way to the coexisting EPR signals at rather close *g*-factors ($g = 1.956$ and 1.960), the two close violet bands (2.80 eV *vs.* 2.88 eV) are associated with defects of the same nature, yet localized in different environments – which is confirmed by their different reactivity towards oxygen.

In the EPR spectrum recorded in presence of O₂ ($P = 10$ mbar) (Fig. 4b), the two close EPR signals ($g = 1.956$ and 1.960) also show opposite behaviors: while the one at $g = 1.956$ (species A) disappears almost completely (similarly to VL contribution in the PL spectrum) the signal at $g = 1.960$ (species B) remains mainly unaffected (similarly to VL_B contribution in the PL spectrum). After pumping O₂ out, the signal at $g = 1.956$ recovers back to its former state (dotted violet curve in Fig. 4b), which points out a reversible process. Such a reversible broadening or, in our case, a complete disappearance (and recovery) of an EPR signal in the presence (and removal) of physically adsorbed O₂ – *i.e.* close enough to interact with the related paramagnetic species – is well reported in the literature.^{64,65} Hence, the intensity decrease of the signal at $g = 1.956$ can be explained by strong dipolar interactions between adsorbed O₂ and paramagnetic Zn_i⁺ from the surface.

Apart from being the dominant contributions in the initial spectra, VL at 2.88 eV and the EPR signal at $g = 1.956$ also show a similar sensitivity towards O₂. The two spectroscopic signals (couple I) are therefore both assigned to surface Zn_i⁺ and identified as the main native defect in ZnO smoke. We also note the recovery of couple I signals to their initial state after pumping the O₂ out (dotted violet curves in Fig. 4). This points towards rather weak O₂ adsorption and reversible electron transfer.

The pairing of the second couple (2.80 eV/ $g = 1.960$; couple II) is based on a similar reasoning: relatively lower contributions in initial PL/EPR spectra compared to those associated with couple I, and similar tendencies in presence of O₂ addition. Couple II exhibits PL maximum and *g*-value only slightly different from those of couple I. At the same time, it shows an opposite trend in the interaction with O₂. Therefore, it can be attributed to the same type of defect, *i.e.* Zn_i⁺, yet present deeper in the bulk. This is in agreement with a recent work by Erdem *et al.*,⁶⁶ in which an EPR signal at $g = 1.96$ was suggested to originate from core defects of ZnO.⁶⁷

3.2 Effects of annealing treatments

In order to follow the outcome of the Zn_i⁺ native defects and the eventual creation of new defects, the as-synthesized sample was annealed either in an O₂-poor or O₂-rich conditions. The newly observed spectroscopic features and the associated species or defect assignments are gathered in Table 1. The related processing protocols were adopted in line with formation energies calculated for various point defects in ZnO over a wide range of O₂ partial pressures.^{25,68}

3.2.1 Annealing in low P_{O_2}

Annealing in a high vacuum. Compared to the as-synthesized ZnO smoke, no substantial morphological or structural changes were observed on the sample annealed at $T = 773$ K in a high vacuum ($P < 10^{-5}$ mbar) (Fig. SI-2†). Though the crystalline mean size domain noticeably decreases, the lattice parameters remain unchanged and the micro-strain moderately increases from 3 to 6% (Table 2), which may be due to the formation of new defects in the ZnO crystal.

In the corresponding Raman spectrum (Fig. 5, green curve), we observe that the E_2^{high} peak (439 cm⁻¹), specific of lattice-oxygen motions, is strongly affected by such thermal treatment whereas a new $E_1(\text{LO})$ peak, specific of intrinsic defects, emerges at ~560 cm⁻¹.

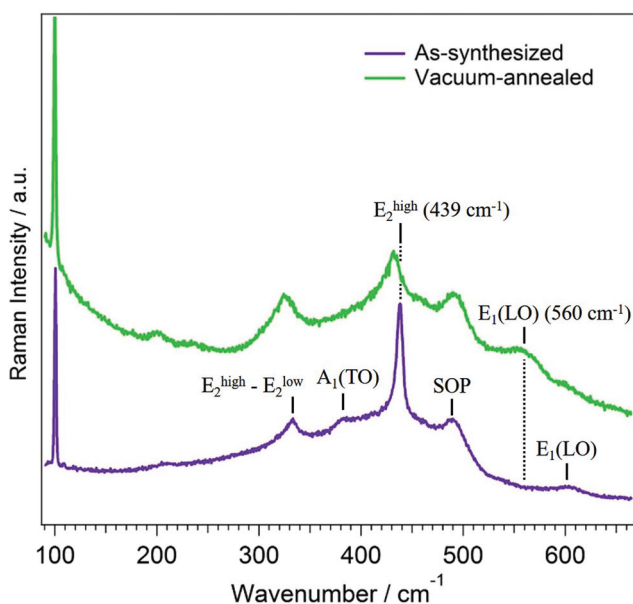
The initially intense UV-emission (see Fig. 3a) is strongly reduced after annealing ZnO smoke in high vacuum (Fig. 6a) implying that a significant amount of defects is formed in the crystal where they provide new channels for electron–hole recombination. More interestingly, such an annealing treatment results in a new PL band (Fig. 6a) that can be reproduced by a single Gaussian curve centered at 2.41 eV (515 nm). Although mathematically not necessary for the resulting fit, one can notice that the VL ~2.80 eV may neverthe-

Table 1 List of the linked (couple I, II and III) and non-linked EPR/PL signals detected in ZnO smoke in function of sample's history (as-synthesized, and upon subsequent post-treatments) and their proposed assignments

$E_{\text{emiss}} (E_v)/g$ value	Conditions for detection	Assignment
Couple I	2.88 eV/ $g = 1.956$ As-synthesized smoke and Zn annealed sample (in a lower relative amount) (<i>sensitive to O_2 adsorption</i>)	Surface Zn_i^+
Couple II	2.80 eV/ $g = 1.960$ As-synthesized smoke and vacuum annealed and Zn vapor annealed samples (<i>insensitive to O_2 adsorption</i>)	Bulk Zn_i^+
Couple III	~ 2.41 eV/ $g \sim 2.002$ Vacuum and Zn-vapor annealed samples (high intensity) and oxygen annealed sample (weak intensity) (<i>sensitive to water adsorption</i>)	Oxygen vacancy V_O^+
EPR	$g_z = 2.047-2.043$; $g_y = 2.009$; $g_x = 2.003$ Vacuum annealed sample (<i>disappearance upon long time pumping</i>)	Superoxide species (O_2^-) adsorbed on the ZnO surface
PL	2.0 eV Oxygen annealed sample (<i>disappearance after long time pumping associated with simultaneous recovery of surface Zn_i^+ features</i>)	Peroxide-like species O_2^{2-} in interaction with the ZnO surface
PL	2.5 eV As-synthesized smoke	To be discussed in a forthcoming paper

Table 2 Comparison of lattice parameters, microstrain and mean coherent domain size of the as-synthesized and vacuum-annealed (773 K, $P < 10^{-5}$ mbar) samples, obtained via Rietveld analysis

	Lattice parameters (Å)	Microstrain (%)	Mean coherent domain size (nm)
As-synthesized	$a = 3.25019$ (5) $b = 3.25019$ (5) $c = 5.20709$ (10)	3	90
Vacuum-annealed	$a = 3.25009$ (8) $b = 3.25009$ (8) $c = 5.20700$ (14)	6	51

**Fig. 5** Raman spectra of the as-synthesized and annealed (773 K, $P < 10^{-5}$ mbar) ZnO smoke.

less be present in a small contribution within the new PL band. On the contrary, the VL ~ 2.88 eV remains rather undetectable.

The corresponding EPR spectrum is shown in Fig. 6b. When compared to that obtained on the as-synthesized sample (zoom in Fig. 6b vs. Fig. 3b), the signal at $g = 1.956$ is not anymore detectable, whereas the signal at $g = 1.96$ is comparatively not modified. The behavior of the former signal upon high-vacuum annealing and in the interaction with O_2 is comparable to that of VL (2.88 eV). This strongly confirms the attribution of both spectroscopic features (couple I) to the same defect.

Simultaneously with the disappearance of the EPR signal at $g = 1.956$, a new signal is observed at $g > 2.00$. The EPR spectrum is rather complex in this range and the simulation (Fig. 5b) shows contribution of three overlapping signals:

- I. $g_{\text{iso}} = 2.002$ (species C, green dotted)
- II. $g_z = 2.043$, $g_y = 2.009$ and $g_x = 2.003$ (species D, yellow dotted)
- III. $g_z = 2.047$, $g_y = 2.009$ and $g_x = 2.003$ (species E, brown dotted)

The origin of an isotropic EPR signal (species C) detected on ZnO with the g -value close to 2.00 remained a matter of great debate until now. Besides resonating close to the value of free electrons ($g = 2.002$) – attribution adopted by some authors^{69,70} – defects such as $V_{Zn}:Zn_i$ complexes,⁷¹ Zn_i^+ ,⁷² V_O^+ (ref. 69) and O_s^- (ref. 73) were also suggested. The other two signals detected in the EPR spectrum of the vacuum-annealed sample (species D and E) present a pseudo-axial rhombic symmetry consistent with superoxide species (O_2^-) adsorbed on ZnO.^{60,74–76} The g_z component is known to be the most sensitive to the environment of the paramagnetic species, so that its variation in species D and E may point out different localizations of O_2^- – yet both on the surface. The presence of superoxide anions on the sample only annealed in a high vacuum and measured at constant pumping ($P < 10^{-5}$ mbar) is, at first, surprising since the generation of such radicals generally occurs when a previously reduced surface is contacted with gaseous O_2 .^{75–77} It is therefore evident that, here, for the creation of a notable amount of O_2^- in the course of high-vacuum annealing, oxygen must have an intrinsic origin – *i.e.* it must come from the lattice of ZnO smoke. The evident loss of lattice

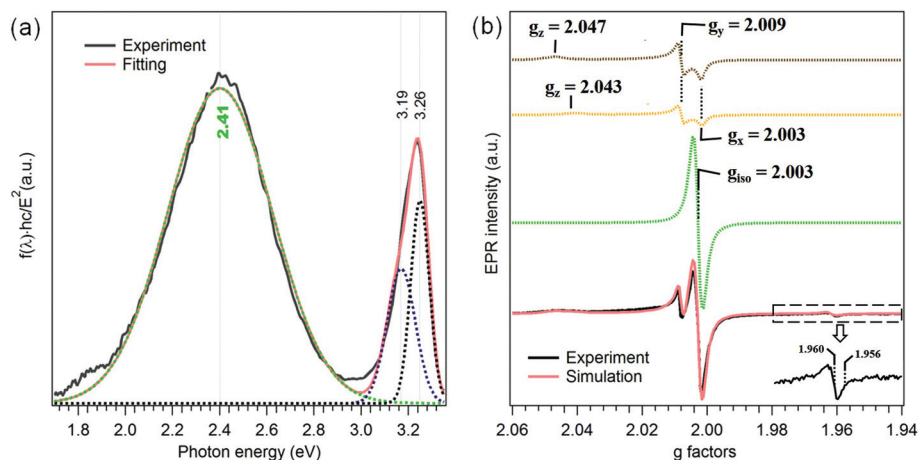
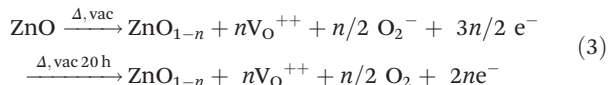
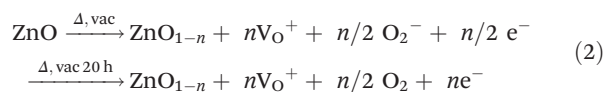
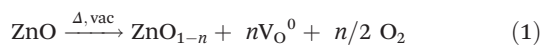


Fig. 6 PL spectrum with corresponding band fitting (a) and experimental and simulated EPR spectra (b) of ZnO smoke annealed at 773 K in a high vacuum ($P < 10^{-5}$ mbar). Despite being shown in arbitrary units, the y-scales in Fig. 6 are almost one order of magnitude lower than those in Fig. 3.

oxygen can proceed *via* one of the following processes, each of them involving the concomitant formation of an oxygen vacancy (V_{O}^0 , V_{O}^+ or V_{O}^{++}):



Pathway (1) considers the formation of a neutral oxygen vacancy. There is no associated electron release required for the formation of O_2^- , that is observed *via* corresponding EPR signals, nor any paramagnetic species that might stand for the EPR signal at $g = 2.002$ observed along with those of O_2^- . Pathway (3) implies the formation of a doubly charged oxygen vacancy V_{O}^{++} , fulfilling the conditions of e^- release and potentially explaining the formation of O_2^- . Yet, it still does not explain the signal at $g = 2.002$. Thus, only pathway (2) can fully explain the changes observed in EPR spectra after high-vacuum annealing: departure of oxygen from the lattice and release of electrons associated with the formation of O_2^- and of paramagnetic V_{O}^+ species.

Considering the calculated formation energies of oxygen vacancies in ZnO^{47,78,79} the absolute values greatly differ as a function of the calculation method. However, irrespective of the calculation method used, the trend in E_f is rather constant in these studies: while the neutral oxygen vacancy was systematically reported to exhibit the highest E_f value, the formation of V_{O}^{++} was shown to be favorable under O-poor conditions.^{25,68,78} The formation energy of a neutral oxygen vacancy V_{O}^0 was calculated in ref. 25 and 80 to be ~ 3.5 eV that should prohibit its presence even under extremely O-poor conditions. Nevertheless, when passing to nanostructured systems the for-

mation energy of the defect can be considerably lowered – as recently shown for V_{O} in ZrO_2 ⁸¹ and on ZnO.⁸² Still, one has to be careful not to rely too strictly on these results since calculations are performed at $T = 0$ K, generally far from most experimental conditions, and especially ours. For instance, although the V_{O}^+ is consistently reported as unstable and observable only under irradiation,⁸⁰ thus, at first, seemingly contradicting our experimental evidence, the EPR signals specific O_2^- shown in our experiment strongly support the presence of singly charged oxygen vacancy in vacuum annealed ZnO smoke.

In conclusion, we cannot exclude any of the reaction pathways represented by (1)–(3), but only pathway (2) can explain the changes observed in EPR spectra upon high-vacuum annealing: (i) release of electrons necessary for the formation of O_2^- (specific EPR signals observed) and (ii) formation of an additional paramagnetic species which resonates at $g = 2.002$. Thus the EPR signal at $g = 2.002$ as well as its PL counterpart, that appears in parallel with the maximum at 2.41 eV, can be quite assuredly assigned to V_{O}^+ (couple III). We also note that the PL peak is rather broad and, although it can be represented by a lone Gaussian curve, it cannot be totally excluded that other contributions also take part – for instance, those that can be correlated to V_{O} and V_{O}^{++} , and which can be simultaneously formed following 1–3 pathways. This will be discussed in relation to the 2.5–2.2 eV PL emissions in a forthcoming paper.

Similar assignments for peaks of couple III can be found in several studies.^{83,84} For instance, an emission band peaking at 2.43 eV was proposed to result from the recombination between an e^- from an isolated V_{O}^+ vacancy and a photoexcited hole.⁸⁵ More recently, the PL band at 2.45 eV was suggested to result from the $V_{\text{O}}^+ \rightarrow$ valence band transition.⁸⁶ However, since it was detected under extremely different and mostly uncontrolled experimental conditions, no consensus is yet reached for its assignment. In addition, different transitions matching this energy were calculated by several groups.^{87–89} Finally, this led to the fact that several defects likely existing in

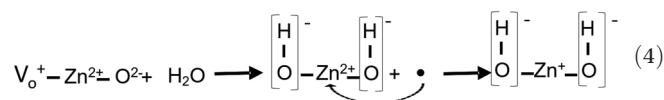
ZnO were suggested as candidates for this PL band. The attribution of the EPR signal at $g = 2.002$ is, on the other hand, hindered by the fact that it lies very close to the value usually reported for free electrons ($g \sim 2.00$). However, the *in situ* (dynamic vacuum, $P < 10^{-5}$ mbar) detection of O_2^- specific EPR signals in our experiment confirms that oxygen is released from the Zn–O network. Hence, oxygen vacancies must have been subsequently formed – and, thus, related to the signals of Couple III.

We have furthermore noticed that the O_2^- specific EPR signals, detected in the course of high-vacuum annealing, disappear when the sample is subjected to a longer pumping time at room temperature ($t > 20$ h). Evidently, O_2^- species can be fully removed in the form of O_2 through a fully reversible electron transfer at room temperature – a typical behavior of superoxide species. In contrast, the 2.41 eV and $g = 2.002$ couple (couple III) were still detected after 20 h pumping at RT, indicating that the V_O^+ vacancy is stable over time.

The loss of lattice oxygen, which occurs at high-vacuum annealing, explains also the intensity decrease of the signals related to surface Zn_i^+ (couple I). Indeed, apart from the fraction of released electron necessary for O_2^- formation, pathway (2) also provides electrons that may interact with surface Zn_i^+ and transform them into Zn^0 . Part of this Zn^0 is most probably sublimated at these temperatures and, thus, removed from the system. Indeed, once the annealing treatment was completed a greyish deposit was observed on the cold part of either the PL or EPR cells. This is supported by XPS indicating a decrease of the Zn/O ratio of the annealed sample (1.10) compared to that obtained on the as-synthesized ZnO smoke (1.26). Fig. 7

reports a synoptic proposal for the interconnected redox processes that take place during the high-vacuum annealing and which explain the disappearance of some native defects and generation of new ones.

The assignment of couple III to V_O^+ is further tested *via* its expected reactivity towards water^{23,88} and the results are shown in Fig. 8. Water splitting fills up the V_O^+ vacancy, leading to the intensity decrease of couple III. Moreover, the associated released electron interacts with surface Zn^{2+} and forms Zn^+ , explaining the concomitant intensity increase of couple I (VL at 2.88 eV and $g = 1.956$), as described in eqn (4):



Annealing in Zn-vapor. PL and EPR spectra of ZnO smoke annealed in a Zn-rich atmosphere are shown in Fig. 9a and b, respectively. Both PL and EPR spectra show signals (at 2.41 eV (515 nm) and $g = 2.002$ (species C)) identical to those of couple III observed on vacuum annealed ZnO smoke. This is not surprising since the formation of oxygen vacancies is expected under such experimental conditions – *i.e.* Zn-rich atmosphere. As in the case of the vacuum annealed sample, the electron release upon the formation of V_O^+ may once more explain the intensity decrease of spectroscopic fingerprints related to surface Zn_i^+ (couple I). The main difference compared to annealing in a vacuum is that D and E EPR species specific of O_2^- radicals are not detected in spectrum recorded of the sample annealed in Zn-vapor (Fig. 6b, Table 1). Such an

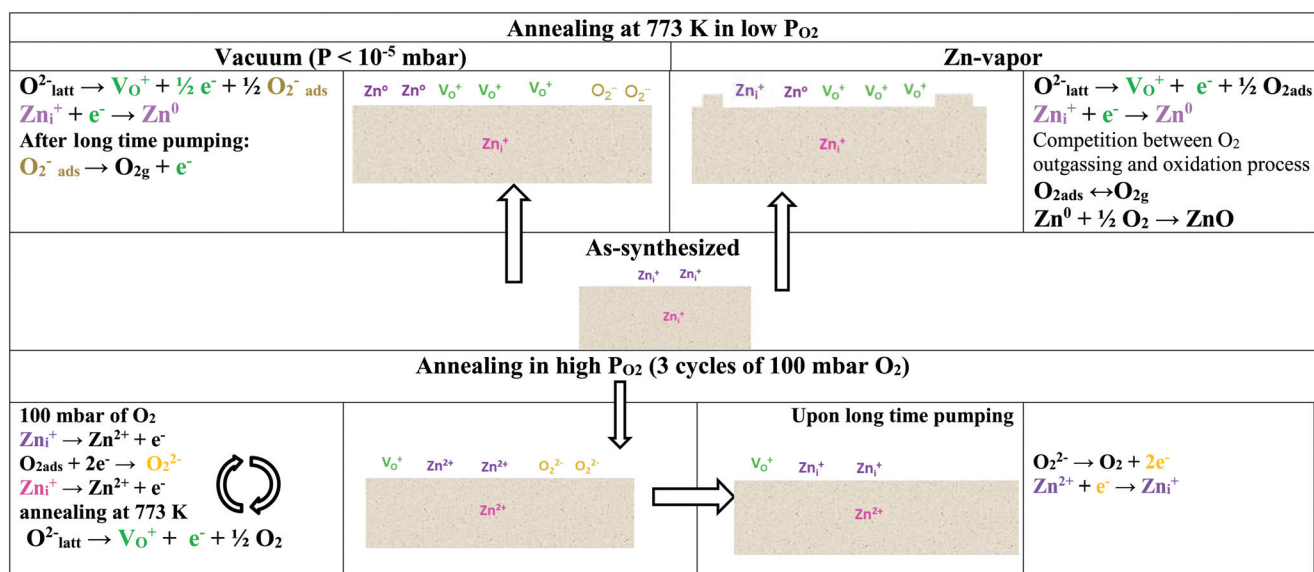


Fig. 7 Diagrammatical representation of the defects detected along the history of the ZnO smoke, starting from as-synthesized to annealed – either in low P_{O_2} (high-vacuum and Zn-vapor) or in high P_{O_2} atmospheres – and in relation with the qualitatively interconnected redox processes that take place depending on the processing conditions. Native defects in ZnO smoke, *i.e.* bulk and surface Zn_i^+ are reduced upon annealing in low P_{O_2} by electrons released in the course of oxygen vacancies formation. During the annealing in high P_{O_2} , antagonistic processes occur leading, on the one hand, to the oxidation of Zn_i^+ defects and formation of peroxide-like species, and, on the other, to oxygen vacancy formation.

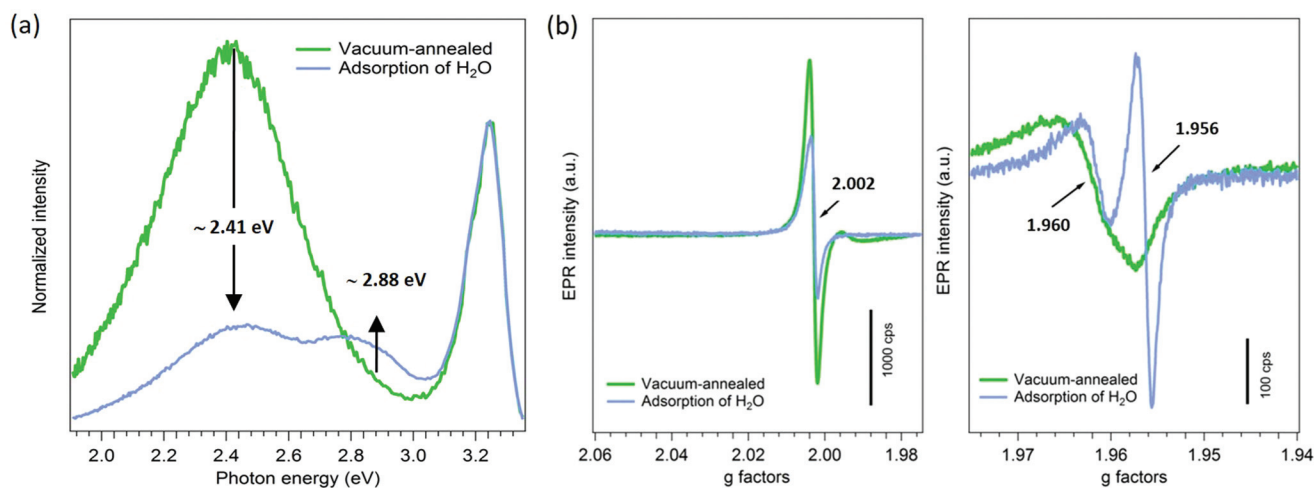


Fig. 8 (a) PL spectra and (b) EPR spectra of high vacuum annealed ZnO smoke (773 K and $P < 10^{-5}$ mbar) and after exposing this powder to water ($P_{\text{H}_2\text{O}} = 10$ mbar).

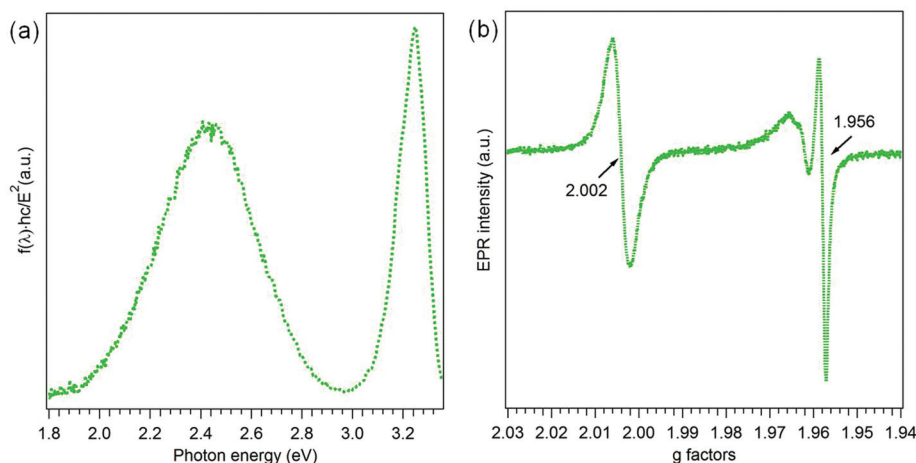


Fig. 9 PL (a) and EPR (b) spectra obtained on ZnO smoke annealed at 773 K in the presence of Zn-vapor ($P_{\text{Zn}} \sim 100$ mbar).

absence of the O_2^- specific signals is yet not surprising since Zn is present in excess in the gas phase and, now, the newly formed O_2 can rapidly react with gaseous Zn to form new ZnO entities (Fig. 7).

3.2.2 Annealing in high P_{O_2} . In another set of experiments, the sample was repeatedly annealed in oxygen and then outgassed. The PL spectra obtained after each of the 3 cycles are presented in Fig. 10a. After the first cycle (brown curve), the intensity of VL (2.88 eV, surface Zn_i^+) decreased along with an intensity increase in the lower energy part (< 2.5 eV) of the spectrum. The effect is reinforced with every additional O_2 annealing/outgassing cycle. After the third cycle, VL is completely absent, which can be explained by the oxidation of Zn_i^+ that is thus transformed into optically inactive Zn^{2+} centers. The intense PL band that develops at ~ 2.0 eV *i.e.* in the yellow part of the optical spectrum (600 nm, yellow luminescence (YL)) is

rather broad and can be decomposed into more than one PL emission (Fig. SI-3[†]). Besides YL contribution at 2.07 eV, the one at 2.41 eV is also present, – as well as the EPR signal at $g = 2.002$ (not shown) (Table 1). Interestingly, YL disappears after a longer pumping time (24 h instead of usual 1 h) (Fig. 10b), suggesting that the underlying defect is weakly bound to ZnO.

Whereas the evolution of yellow luminescence (YL) is not surprising – since it was systematically measured in oxygen rich conditions and on all forms of ZnO (single crystals,⁹⁰ thin films⁹¹ and nanoparticles^{20,92,93}) the coexistence of the V_O^+ related PL/EPR fingerprints appears unusual at first glance (Table 1). However, considering the applied experimental conditions the competition between three processes should be assumed: (i) formation of V_O (due to high annealing T), (ii) passivation of V_O (due to the presence of O_2) and (iii) formation of defects related to YL emission (due to high P_{O_2})

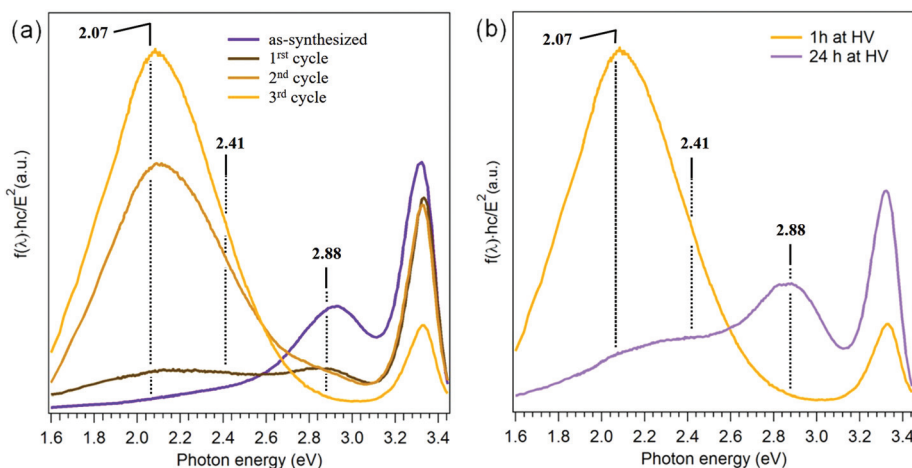


Fig. 10 PL spectra (a) of ZnO smoke repeatedly annealed in O_2 ($T_{\text{ann}} = 773$ K, $P_{O_2} = 100$ mbar) then outgassed at RT. (b) Comparison of PL spectra of the ZnO after three cycles recorded after 1 h (yellow) and 24 h pumping (light violet).

(Fig. 7). Indeed, though O_2 is present during annealing, a competition between the generation and passivation of oxygen vacancies occurs, as demonstrated by Drouilly *et al.*⁹⁴

Despite the rather high formation energies calculated for O_i -type defects, DFT stability diagrams show^{25,78} that these defects can be significantly favored in an O_2 rich atmosphere. Therefore, the yellow luminescence was principally assigned to oxygen interstitials – more precisely to singly charged ones (O_i^-).^{95–97} Based on the absence of a new EPR signal along with the YL, a paramagnetic nature of this defect must be excluded. According to theory,^{25,98} O_i may not only be isolated, yet located close to lattice oxygen ions, giving rise to a molecular-like diatomic entity. Such an entity would exhibit fully occupied $p\pi^*$ orbitals,^{25,98} with an electronic structure similar to that of O_2^{2-} peroxide species. Therefore, in contrast to the generally accepted picture of singly charged oxygen interstitials (O_i^-) being assigned to yellow emission,^{95,97} we instead propose a peroxide-like entity stabilized at the surface of ZnO nanoparticles where it acts as the recombination center for YL. A similar scenario is demonstrated also in the case of the NiO surface in Ref. 99. Once at the surface, the oxygen molecule can be reduced to surface bidentate O_2^{2-} by electrons provided either *via* the oxidation of Zn_i^+ or from oxygen vacancies – the formation of which was shown to be as one of the competing processes in this sample processing. Not dissociated, such peroxide-species can easily leave the surface as was confirmed by the disappearance of YL upon more efficient pumping (light violet curve in Fig. 10b). In the same spectrum, the reversibility of such a process can be observed through the recovery of the Zn_i^+ characteristic signal. The attribution of YL to such O_2^{2-} -bidentate, localized at the surface instead of being embedded in ZnO crystal – as suggested by Janotti *et al.*²⁵ – may be questioned except if one considers the nano-nature of ZnO (Table 1, Fig. 7). At the same time, it opens up basis for new computational strategies.

4. Conclusions

By combining electron paramagnetic resonance (EPR) and photoluminescence (PL) spectroscopy, we have studied the nature of native defects in ZnO nanopowders prepared *via* the metal combustion technique. Several processing protocols have been applied to follow the outcome of the existing defects and the eventual creation of new ones. Thanks to the strict control of the experimental conditions during all stages of sample storage, processing and measurements, crystal defects are identified in correlation with the condition specific PL/EPR fingerprints.

We demonstrate here how important it is to precisely detail the experimental conditions in which spectra were recorded. Performing EPR and PL under controlled conditions allows the spectroscopic fingerprints to be unambiguously attributed to the corresponding defects. An example is couple I (2.88 eV/ $g = 1.956$) that otherwise escapes detection in nanostructured ZnO due to measurements performed in conditions different than high-vacuum *i.e.* in an O_2 or H_2O containing environment. The same is true for the identification of V_O^+ that could be missed if the corresponding measurements were not performed under conditions that ensure the detection of O_2^- specific signals *i.e.* in a dynamic high vacuum ($P < 10^{-5}$ mbar). Moreover, thanks to the detection of O_2^- , the doubtless assignment of EPR at $g = 2.002$ to V_O^+ species provided a basis to exclude these defects to be present in the as-synthesized sample and to attribute the observed couple I exclusively to Zn_i^+ – as additionally supported also by XPS results. We also showed that the use of probe molecules, such as O_2 , may provide efficient discrimination between same defects yet localized in different crystallographic environments, namely surface or bulk.

Bulk and surface Zn_i^+ were identified as native defects specific of the applied synthesis method. The formation of singly charged oxygen vacancies (V_O^+) at the surface of ZnO was undoubtedly demonstrated to occur upon annealing in an

O₂-poor atmosphere. Annealing in high P_{O₂} was shown to lead to antagonism effects relative to high temperature and atmosphere, respectively. Apart from the relatively small contribution of V_O⁺ as due to the high-annealing temperature applied, defects specific of O₂-rich conditions are produced in the form of peroxide-like diatomic oxygen. The various defects identified in this study were shown to produce color specific PL emissions that range from violet (Zn_i⁺), over green (V_O⁺) to yellow (O₂²⁻) visible domain. Hence, under strictly controlled conditions, ZnO smoke can represent an appropriate model system for studying crystal defects. A great deal of cross-agreement between strictly controlled experimental conditions and PL/EPR fingerprints provides a simple approach that can be used for studying and/or identifying defects in other ZnO types.

Conflicts of interest

There are no conflicts to declare.

Acknowledgements

Dr Miao Zhang wants to thank the China Scholarship Council (CSC) for the three years Ph.D. funding. The authors are also grateful to: Vincent Losinho from Laboratoire de Réactivité de Surface, Sorbonne Université, (LRS) for his help in designing and building the set up used for EPR and PL *in situ* studies and Stephane Chenot from Institut des NanoSciences de Paris, Sorbonne Université, (INSP) for the maintenance of synthesis chamber and high-vacuum storage lines.

References

- 1 S. Jung, J. Lee, J. Seo, U. Kim, Y. Choi and H. Park, *Nano Lett.*, 2018, **18**, 1337–1343.
- 2 H. Li, L. K. Schirra, J. Shim, H. Cheun, B. Kippelen, O. L. Monti and J.-L. Bredas, *Chem. Mater.*, 2012, **24**, 3044–3055.
- 3 S. Vishniakou, R. Chen, Y. G. Ro, C. J. Brennan, C. Levy, E. T. Yu and S. A. Dayeh, *Adv. Mater. Technol.*, 2018, **3**, 1700279.
- 4 M. S. Yao, W. X. Tang, G. E. Wang, B. Nath and G. Xu, *Adv. Mater.*, 2016, **28**, 5229–5234.
- 5 J.-W. Kim, Y. Porte, K. Y. Ko, H. Kim and J.-M. Myoung, *ACS Appl. Mater. Interfaces*, 2017, **9**, 32876–32886.
- 6 A. Katoch, J.-H. Kim, Y. J. Kwon, H. W. Kim and S. S. Kim, *ACS Appl. Mater. Interfaces*, 2015, **7**, 11351–11358.
- 7 W. Zhao, X. Xiong, Y. Han, L. Wen, Z. Zou, S. Luo, H. Li, J. Su, T. Zhai and Y. Gao, *Adv. Opt. Mater.*, 2017, **5**, 1700146.
- 8 R. Bao, C. Wang, Z. Peng, C. Ma, L. Dong and C. Pan, *ACS Photonics*, 2017, **4**, 1344–1349.
- 9 M. D. Marcantonio, S. Gellner, J. E. Namanga, J. Frohleichs, N. Gerlitzki, F. Vollkommer, G. Bacher and E. Nannen, *Adv. Mater. Technol.*, 2017, **2**, 1600215.
- 10 A. Behan, A. Mokhtari, H. Blythe, D. Score, X. Xu, J. Neal, A. Fox and G. Gehring, *Phys. Rev. Lett.*, 2008, **100**, 047206.
- 11 Z. Sun, X. Yang, C. Wang, T. Yao, L. Cai, W. Yan, Y. Jiang, F. Hu, J. He and Z. Pan, *ACS Nano*, 2014, **8**, 10589–10596.
- 12 H.-L. Guo, Q. Zhu, X.-L. Wu, Y.-F. Jiang, X. Xie and A.-W. Xu, *Nanoscale*, 2015, **7**, 7216–7223.
- 13 P. Camarda, F. Messina, L. Vaccaro, S. Agnello, G. Buscarino, R. Schneider, R. Popescu, D. Gerthsen, R. Lorenzi and F. M. Gelardi, *Phys. Chem. Chem. Phys.*, 2016, **18**, 16237–16244.
- 14 R. Gurwitz, R. Cohen and I. Shalish, *J. Appl. Phys.*, 2014, **115**, 033701.
- 15 T. M. Borseth, B. G. Svensson, A. Y. Kuznetsov, P. Klason, Q. X. Zhao and M. Willander, *Appl. Phys. Lett.*, 2006, **89**, 262112.
- 16 K. H. Tam, C. K. Cheung, Y. H. Leung, A. B. Djuricic, C. C. Ling, C. D. Beling, S. Fung, W. M. Kwok, W. K. Chan, D. L. Phillips, L. Ding and W. K. Ge, *J. Phys. Chem. B*, 2006, **110**, 20865–20871.
- 17 B. Lin, Z. Fu and Y. Jia, *Appl. Phys. Lett.*, 2001, **79**, 943.
- 18 Z. Wang, X. Zu, S. Zhu and J. Wang, *Phys. E*, 2006, **35**, 199.
- 19 J. Lv and C. Li, *Appl. Phys. Lett.*, 2013, **103**, 232114.
- 20 A. R. Gheisi, C. Neygandhi, A. K. Sternig, E. Carrasco, H. Marbach, D. Thomele and O. Diwald, *Phys. Chem. Chem. Phys.*, 2014, **16**, 23922–23929.
- 21 B. Fabbri, A. Gaiardo, A. Giberti, V. Guidi, C. Malagù, A. Martucci and M. Sturaro, *Procedia Eng.*, 2014, **87**, 148–151.
- 22 C. Drouilly, J.-M. Krafft, F. Averseng, H. Lauron-Pernot, D. Bazer-Bachi, C. Chizallet, V. Lecocq and G. Costentin, *Catal. Today*, 2013, **205**, 67–75.
- 23 H. Noei, H. Qiu, Y. Wang, E. Löffler, C. Wöll and M. Muhler, *Phys. Chem. Chem. Phys.*, 2008, **10**, 7092–7097.
- 24 F. Haque, S. Chenot, F. Viñes, F. Illas, S. Stankic and J. Jupille, *Phys. Chem. Chem. Phys.*, 2017, **19**, 10622–10628.
- 25 A. Janotti and C. G. Van de Walle, *Phys. Rev. B: Condens. Matter Mater. Phys.*, 2007, **76**, 165202.
- 26 S. Stankic, M. Cottura, D. Demaille, C. Noguera and J. Jupille, *J. Cryst. Growth*, 2011, **329**, 52–56.
- 27 J. A. Weil and J. R. Bolton, *Electron Paramagnetic Resonance-Elemental Theory and Practical Applications*, John Wiley & Sons, Inc., Hoboken, New Jersey, 2nd edn, 2007.
- 28 T. Spalek, P. Pietrzyk and Z. Sojka, *J. Chem. Inf. Model.*, 2005, **45**, 18–29.
- 29 C. J. Powell and A. Jablonski, *NIST Electron Effective-Absorption-Length Database - Version 1.3*, National Institute of Standards and Technology, Gaithersburg, MD, 2011.
- 30 X. Llovet, F. Salvat, D. Bote, F. Salvat-Pujol, A. Jablonski and C. J. Powell, *NIST Database of Cross Sections for Inner-Shell Ionization by Electron or Positron Impact, Version 1.0*, National Institute of Standards and Technology, Gaithersburg, Maryland, 2014.
- 31 J. J. Yeh, *Atomic calculation of photoionization cross-sections and asymmetry parameters*, 1985.
- 32 M. Karakus, Y. Sung, H. I. Wang, Z. Mics, K. Char, M. Bonn and E. Cánovas, *J. Phys. Chem. C*, 2017, **121**, 13070–13077.

- 33 P. Bindu and S. Thomas, *J. Theor. Appl. Phys.*, 2014, **8**, 123–134.
- 34 S. Kumar and P. Sahare, *Nano*, 2012, **7**, 1250022.
- 35 R. Cuscó, E. Alarcón-Lladó, J. Ibanez, L. Artús, J. Jimenez, B. Wang and M. J. Callahan, *Phys. Rev. B: Condens. Matter Mater. Phys.*, 2007, **75**, 165202.
- 36 H. Zeng, W. Cai, B. Cao, J. Hu, Y. Li and P. Liu, *Appl. Phys. Lett.*, 2006, **88**, 181905.
- 37 G. J. Exarhos and S. K. Sharma, *Thin Solid Films*, 1995, **270**, 27–32.
- 38 D. Thapa, J. Huso, J. L. Morrison, C. D. Corolewski, M. D. McCluskey and L. Bergman, *Opt. Mater.*, 2016, **58**, 382–389.
- 39 M. Miyake, M. Sugino, N. Narahara, T. Hirato and P. V. Braun, *Chem. Mater.*, 2017, **29**, 9734–9741.
- 40 G. Ou, D. Li, W. Pan, Q. Zhang, B. Xu, L. Gu, C. Nan and H. Wu, *Adv. Mater.*, 2015, **27**, 2589–2594.
- 41 F. Leiter, H. Alves, A. Hofstaetter, D. Hofmann and B. Meyer, *Phys. Status Solidi B*, 2001, **226**, R4–R5.
- 42 A. B. Djurišić, W. C. Choy, V. A. L. Roy, Y. H. Leung, C. Y. Kwong, K. W. Cheah, T. Gundu Rao, W. K. Chan, H. Fei Lui and C. Surya, *Adv. Funct. Mater.*, 2004, **14**, 856–864.
- 43 M. Li, G. Xing, G. Xing, B. Wu, T. Wu, X. Zhang and T. C. Sum, *Phys. Rev. B: Condens. Matter Mater. Phys.*, 2013, **87**, 115309.
- 44 K. E. Knutsen, A. Galeckas, A. Zubiaga, F. Tuomisto, G. C. Farlow, B. G. Svensson and A. Y. Kuznetsov, *Phys. Rev. B: Condens. Matter Mater. Phys.*, 2012, **86**, 121203.
- 45 S. Polarz, A. Roy, M. Merz, S. Halm, D. Schröder, L. Schneider, G. Bacher, F. E. Kruis and M. Driess, *Small*, 2005, **1**, 540–552.
- 46 P. Erhart, K. Albe and A. Klein, *Phys. Rev. B: Condens. Matter Mater. Phys.*, 2006, **73**, 205203.
- 47 S. Zhang, S.-H. Wei and A. Zunger, *Phys. Rev. B: Condens. Matter Mater. Phys.*, 2001, **63**, 075205.
- 48 D. C. Look, G. C. Farlow, P. Reunchan, S. Limpijumnong, S. Zhang and K. Nordlund, *Phys. Rev. Lett.*, 2005, **95**, 225502.
- 49 H. Zeng, G. Duan, Y. Li, S. Yang, X. Xu and W. Cai, *Adv. Funct. Mater.*, 2010, **20**, 561–572.
- 50 M. Chen, Z. Wang, D. Han, F. Gu and G. Guo, *J. Phys. Chem. C*, 2011, **115**, 12763–12773.
- 51 K. Vanheusden, W. Warren, C. Seager, D. Tallant, J. Voigt and B. Gnade, *J. Appl. Phys.*, 1996, **79**, 7983–7990.
- 52 W. K. Liu, K. M. Whitaker, A. L. Smith, K. R. Kittilstved, B. H. Robinson and D. R. Gamelin, *Phys. Rev. Lett.*, 2007, **98**, 186804.
- 53 V. Ischenko, S. Polarz, D. Grote, V. Stavarache, K. Fink and M. Driess, *Adv. Funct. Mater.*, 2005, **15**, 1945–1954.
- 54 J. Qu, Y. Ge, B. Zu, Y. Li and X. Dou, *Small*, 2016, **12**, 1369–1377.
- 55 C. G. Van de Walle, *Phys. Rev. Lett.*, 2000, **85**, 1012.
- 56 S. Cox, E. Davis, S. Cottrell, P. King, J. Lord, J. Gil, H. Alberto, R. Vilao, J. P. Duarte and N. A. de Campos, *Phys. Rev. Lett.*, 2001, **86**, 2601.
- 57 A. W. Cohn, N. Janßen, J. M. Mayer and D. R. Gamelin, *J. Phys. Chem. C*, 2012, **116**, 20633–20642.
- 58 D. Hofmann, H. Zhou, D. Pfisterer, H. Alves, B. Meyer, P. Baranov, N. Romanov, C. de Mello Donega, A. Meijering and S. Orinskii, *Phys. Status Solidi C*, 2004, **1**, 908–911.
- 59 L. Larina, N. Tsvetkov, J. Yang, K.-S. Lim and O. Shevchuk, *ECS Trans.*, 2010, **28**, 161–167.
- 60 F. Morazzoni, R. Scotti and S. Volontè, *J. Chem. Soc., Faraday Trans.*, 1990, **86**, 1587–1591.
- 61 Z. Zhang and J. T. Yates Jr., *Chem. Rev.*, 2012, **112**, 5520–5551.
- 62 S. Ma, M. E. Reish, Z. Zhang, I. Harrison and J. T. Yates Jr., *J. Phys. Chem. C*, 2017, **121**, 1263–1271.
- 63 M. A. Reshchikov, A. Behrends, A. Bakin and A. Waag, *J. Vac. Sci. Technol., B: Microelectron. Nanometer Struct.–Process., Meas., Phenom.*, 2009, **27**, 1688–1692.
- 64 R. Iyengar, V. S. Rao and A. Zettlemoyer, *Surf. Sci.*, 1969, **13**, 251–262.
- 65 V. J. Joly, K. Takahara, K. Takai, K. Sugihara, T. Enoki, M. Koshino and H. Tanaka, *Phys. Rev. B: Condens. Matter Mater. Phys.*, 2010, **81**, 115408.
- 66 E. Erdem, *J. Alloys Compd.*, 2014, **605**, 34–44.
- 67 P. Jakes and E. Erdem, *Phys. Status Solidi RRL*, 2011, **5**, 56–58.
- 68 R. Vidya, P. Ravindran, H. Fjellvåg, B. Svensson, E. Monakhov, M. Ganchenkova and R. M. Nieminen, *Phys. Rev. B: Condens. Matter Mater. Phys.*, 2011, **83**, 045206.
- 69 D. Liu, Y. Lv, M. Zhang, Y. Liu, Y. Zhu, R. Zong and Y. Zhu, *J. Mater. Chem. A*, 2014, **2**, 15377–15388.
- 70 A. J. Reddy, M. Kokila, H. Nagabhushana, J. Rao, C. Shivakumara, B. Nagabhushana and R. Chakradhar, *Spectrochim. Acta, Part A*, 2011, **81**, 59–63.
- 71 A. Pöppel and G. Völkel, *Phys. Status Solidi A*, 1991, **125**, 571–581.
- 72 X. Xu, C. Xu, J. Dai, J. Pan and J. Hu, *J. Phys. Chem. Solids*, 2012, **73**, 858–862.
- 73 X. Chen, Y. Li, X. Pan, D. Cortie, X. Huang and Z. Yi, *Nat. Commun.*, 2016, **7**, 12273.
- 74 S. Moribe, T. Ikoma, K. Akiyama, Q. Zhang, F. Saito and S. Tero-Kubota, *Chem. Phys. Lett.*, 2007, **436**, 373–377.
- 75 Z. Hao, L. Fen, G. Lu, J. Liu, L. An and H. Wang, *Appl. Catal., A*, 2001, **213**, 173–177.
- 76 J. Cope and I. Campbell, *J. Chem. Soc., Faraday Trans. 1*, 1973, **69**, 1–9.
- 77 C. Gionco, M. C. Paganini, E. Giamello, R. Burgess, C. Di Valentin and G. Pacchioni, *Chem. Mater.*, 2013, **25**, 2243–2253.
- 78 F. Oba, A. Togo, I. Tanaka, J. Paier and G. Kresse, *Phys. Rev. B: Condens. Matter Mater. Phys.*, 2008, **77**, 245202.
- 79 S. Clark, J. Robertson, S. Lany and A. Zunger, *Phys. Rev. B: Condens. Matter Mater. Phys.*, 2010, **81**, 115311.
- 80 F. Gallino, G. Pacchioni and C. Di Valentin, *J. Chem. Phys.*, 2010, **133**, 144512.
- 81 A. R. Puigdollers, F. Illas and G. Pacchioni, *J. Phys. Chem. C*, 2016, **120**, 4392–4402.

- 82 S. Lany and A. Zunger, *Phys. Rev. B: Condens. Matter Mater. Phys.*, 2010, **81**, 113201.
- 83 N. Hsu, W. Hung and Y. Chen, *J. Appl. Phys.*, 2004, **96**, 4671–4673.
- 84 V. Subramanian, E. E. Wolf and P. V. Kamat, *J. Phys. Chem. B*, 2003, **107**, 7479–7485.
- 85 K. Vanheusden, C. Seager, W. t. Warren, D. Tallant and J. Voigt, *Appl. Phys. Lett.*, 1996, **68**, 403–405.
- 86 S. Vempati, J. Mitra and P. Dawson, *Nanoscale Res. Lett.*, 2012, **7**, 470.
- 87 T. K. Kundu, N. Karak, P. Barik and S. Saha, *Int. J. Soft Comput. Eng.*, 2011, **1**, 19–24.
- 88 W. Zhu, S. Kitamura, M. Boffelli, E. Marin, E. Della Gaspera, M. Sturaro, A. Martucci and G. Pezzotti, *Phys. Chem. Chem. Phys.*, 2016, **18**, 9586–9593.
- 89 N. Kondal and S. K. Tiwari, *Mater. Res. Bull.*, 2017, **88**, 156–165.
- 90 E. Epie and W. Chu, *Appl. Surf. Sci.*, 2016, **371**, 28–34.
- 91 F. Stavale, N. Nilus and H.-J. Freund, *J. Phys. Chem. Lett.*, 2013, **4**, 3972–3976.
- 92 C. Chandrinou, N. Boukos, C. Stogios and A. Travlos, *Microelectron. J.*, 2009, **40**, 296–298.
- 93 W.-C. Sun, Y.-C. Yeh, C.-T. Ko, J.-H. He and M.-J. Chen, *Nanoscale Res. Lett.*, 2011, **6**, 556.
- 94 C. Drouilly, J. M. Krafft, F. Averseng, S. Casale, D. Bazer-Bachi, C. Chizallet, V. Lecocq, H. Vezin, H. Lauron-Pernot and G. Costentin, *J. Phys. Chem. C*, 2012, **116**, 21297–21307.
- 95 P. Rauwel, M. Salumaa, A. Aasna, A. Galeckas and E. Rauwel, *J. Nanomater.*, 2016, **2016**, 19.
- 96 M. Liu, A. Kitai and P. Mascher, *J. Lumin.*, 1992, **54**, 35–42.
- 97 X. Wu, G. Siu, C. Fu and H. Ong, *Appl. Phys. Lett.*, 2001, **78**, 2285–2287.
- 98 S. Limpijumnong, X. Li, S.-H. Wei and S. Zhang, *Appl. Phys. Lett.*, 2005, **86**, 211910.
- 99 S. Sugiura, Y. Shibuta, K. Shimamura, M. Misawa, F. Shimojo and Y. Shu, *Solid State Ionics*, 2016, **285**, 209–214.

Effects of Water and Cell Culture Media on the Physicochemical Properties of ZnMgO Nanoparticles and Their Toxicity toward Mammalian Cells

Jasmina Vidic,^{*,†} Francia Haque,^{‡,§} Jean Michel Guigner,^{||,⊥} Aurore Vidy,[†] Christophe Chevalier,[†] and Slavica Stankic^{*,‡,§}

[†]Virologie et Immunologie Moléculaires, Institut de la Recherche Agronomique, UR 892, Bât. Biotechnologies, Jouy en Josas F-78350, France

[‡]CNRS, Institut des Nanosciences de Paris, UMR 7588, 4 place Jussieu, 75252 Paris Cedex05, France

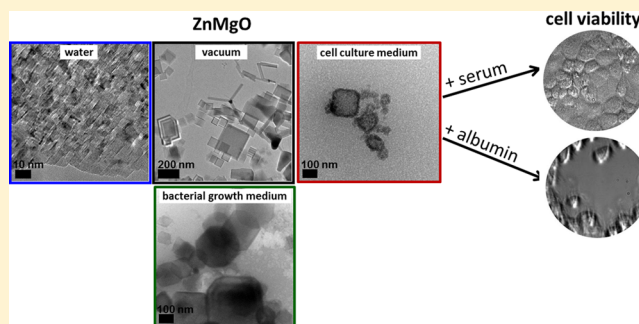
[§]UPMC – Université Paris 06, INSP, UMR 7588, 4 place Jussieu, 75252 Paris Cedex05, France

^{||}IMPMC – Institut de Minéralogie et de Physique des Milieux Condensés, Université Pierre et Marie Curie, UMR7590, 4 place Jussieu, 75252 Paris Cedex05, France

[⊥]CNRS, IMPMC-UMR7590, Paris F-75005, France

S Supporting Information

ABSTRACT: ZnMgO nanoparticles have shown potential for medical applications as an efficient antibacterial agent. In this work, we investigate the effect of water and two commonly used cell culture media on the physicochemical properties of ZnMgO nanoparticles in correlation with their cytotoxicity. In vacuum, ZnMgO nanopowder consists of MgO (nanocubes) and ZnO (nanotetrapods and nanorods) particles. Upon exposure to water or the Luria–Bertani solution, ZnO characteristic shapes were not observable while MgO nanocubes transformed into octahedral form. In addition, water caused morphological alternations in form of disordered and fragmented structures. This effect was directly reflected in UV/vis absorption properties of ZnMgO, implying that formation of new states within the band gap of ZnO and redistribution of specific sites on MgO surfaces occurs in the presence of water. In mammalian culture cell medium, ZnMgO nanoparticles were shapeless, agglomerated, and coated with surrounding proteins. Serum albumin was found to adsorb as a major but not the only protein. Adsorbed albumin mainly preserved its α -helix secondary structure. Finally, the cytotoxicity of ZnMgO was shown to strongly depend on the environment: in the presence of serum proteins ZnMgO nanopowder was found to be safe for mammalian cells while highly toxic in a serum-free medium or a medium containing only albumin. Our results demonstrate that nanostructured ZnMgO reaches living cells with modified morphology and surface structure when compared to as-synthesized particles kept in vacuum. In addition, its biocompatibility can be modulated by proteins from biological environment.



INTRODUCTION

Nanostructured metal oxides are being incorporated into almost all fields of technology: fabrication of microelectronic circuits, sensors, piezoelectric devices, fuel cells, coatings for the passivation of surfaces against corrosion, and as catalysts.^{1,2} This is due to their electronic structure which can exhibit a metallic, semiconducting or insulating character. Metal oxide nanoparticles are furthermore used to enhance the quality of cosmetic and food industry products, whereas medical purposes include their applications such as therapeutics, diagnostics, imaging, or drug deliveries.^{3–5} Metal oxides, such as ZnO, MgO, CuO, or TiO₂, have a particular potential for the use in medicine due to their strong antimicrobial activity against a range of bacteria.^{6–9} Several mechanisms of antibacterial action have been proposed, such as mechanical damaging of bacterial

membranes, cell penetration and binding to specific intracellular targets, and/or generation of reactive oxygen species.⁷ These findings suggested that metal oxide nanoparticles may provide novel modes of action when compared to existing antibiotics, and so they can potentially be applied against strains of bacteria with gained antibiotic resistance. To date, however, their biocompatibility and the safety for mammalian cells remain under debate. Some mammalian cells can uptake and metabolize metal oxides nanoparticles,^{10,11} but other findings emphasize risks for human and mammalian cells.^{12,13} Understanding the physicochemical behavior of nanostructured metal

Received: April 17, 2014

Revised: July 25, 2014

Published: September 3, 2014

oxides in biological media and fluids is therefore essential for their applications in medicine.

Physicochemical properties that govern reactivity of nanostructured metal oxides are determined by particle size, shape, crystal structure, and crystallographic orientation of exposed facets, parameters which are mainly under the scope of surface science investigations. These studies are, however, restricted to the systematic use of single crystalline samples and to experiments in ultrahigh vacuum, that is, to conditions that are far from physiological. However, it is well-known that when exposing metal oxide nanostructures to water their surfaces undergo a series of chemical reactions which in turn modify nanoparticle morphology, their dissolution properties or lead to the formation of new crystallographic phases. For instance, the most stable surfaces of MgO are by far those of (100) orientations leading to cubic crystallites with (100) facets. However, octahedra with (111) facets were found upon MgO dissolution in ultrapure water.^{14,15} Shape transformation was also observed for TiO₂ nanoparticles, where an excess dilution with deionized water caused partial dissolution of the cubic-like TiO₂ nanocrystals and, consequently, its transformation into spherical ones.¹⁶ The solubility of nanoparticles was found to depend not only on their chemical properties but also on the particles size, shape, surface properties and crystal structure.¹⁷ In contact with water a thermodynamically stable hydroxide layer is formed on the ZnO surface preventing further penetration of water into the bulk.¹⁸ However, in nanostructured form, ZnO possesses a greater propensity for dissolution in water.¹⁹

In biological environments, the presence of plasma proteins, salt composition, and pH value affect additionally morphology, surface chemistry, dissolution, and aggregation degree of nanoparticles. When suspended in biological fluids nanoparticles rapidly associate with a series of proteins that form a dynamical layer all over the particle.²⁰ The formation of this so-called "protein-corona" layer modifies the original physicochemical properties of nanoparticles and determines their biocompatibility. The presence of serum proteins was shown to modify aggregation properties of different nanoparticles and consequently alters their reactivity.^{20–24} Initially, nanoparticles are coated by the most abundant proteins as albumin, immunoglobulins, and fibrinogen. These can be displaced over time by less abundant but higher affinity proteins in processes that are also in a function of the nanoparticles sizes and surface properties.^{25–27} Finally, proteins bound to nanoparticles may undergo conformational and functional changes which in turn may alter their own reactivity.^{26,28,29}

Recently, we have shown that ZnMgO nanoparticles exhibit an efficient antibacterial activity while being safe for human HeLa cells.⁸ In this work, alternations in shape, surface structure, and optical activity of ZnMgO nanoparticles were studied upon dissolution in water and some commonly used cell culture media. Attention was paid to the interaction between ZnMgO nanoparticles and serum proteins, in particular serum albumin (BSA). Those interactions were correlated with the nanoparticles toxicity toward mammalian cells.

■ EXPERIMENTAL SECTION

Synthesis of ZnMgO Nanoparticles. ZnMgO nanoparticles were fabricated by burning 10 wt % Mg/Zn alloy (Mg90/Zn10, 10 wt %, Goodfellow) in a glovebox made of stainless steel and rigid plastic designed to afford vacuum ($P \sim 1$ mbar). The combustion of alloy

ribbons was started by a thin Ni–Cr wire held in contact with the extremity of the ribbon which could be resistively heated. Prior to the measurements, powders were kept and transported under vacuum ($P < 10^{-5}$ mbar) in order to prevent any contact with the ambient air.

Chemicals and Proteins. NaCl (99.9% purity), HEPES, Luria–Bertani broth (LB) medium, Crystal Violet, and bovine serum albumin (BSA) were purchased from Sigma-Aldrich. Fetal bovine serum (FBS) was purchased from Perbio. Before use, Crystal Violet was dissolved in Milli-Q water (0.05% w/v) and filtered at 0.22 nm. BSA was additionally purified using size-exclusion chromatography and a Superdex S200 column with an enhanced separation for molecular weights in the range 15–100 kDa. After purification, the BSA monomer concentration was determined using the extinction coefficient deduced from the protein composition of $\epsilon = 43\,824\text{ M}^{-1}\cdot\text{cm}^{-1}$.

Transmission Electron Microscopy (TEM). Measurements were achieved by using a LaB6 JEOL JEM 2100 (JEOL, Japan) field emission transmission electron microscope operated at 200 kV and with 0.18 nm resolution. For cryo-TEM analysis, the microscope was equipped with a cryo pole piece and a drop of solution was deposited on a Quantifoil grid (MicroTools GmbH, Germany). The excess of solution was then blotted out with filter paper, and before evaporation the grid was quench-frozen in liquid ethane to form a thin vitreous ice film. The grid was then maintained all the time at 90 K to prevent evaporation and crystallization of the ice film. The images were taken with an ultrascan 2k CCD camera (GATAN) and with a JEOL low dose system (Minimum Dose System, MDS) to protect the thin ice film from any irradiation before imaging and to reduce irradiation during the image capture.

UV/Vis Spectroscopy. UV/vis absorption spectra of liquid and solid nanoparticles samples were collected on a UV-vis-NIR Varian Cary 5000 spectrophotometer. Diffuse reflectance mode and an integrating sphere were used for measurements on powders, whereas the Kubelka–Munk model was applied to derive the absorbance values from the respective reflectance values.

Tryptophan Fluorescence Measurements. Fluorescence measurements were performed with a FP-6200 spectrofluorimeter (JASCO, Tokyo, Japan) connected with a thermostated cell holder at 20 °C, using a 1 cm path length quartz cell. BSA (6 μM) was incubated with ZnMgO nanoparticles (ranging from 0.01 to 0.5 mg/mL) in HBS buffer (10 mM HEPES, 150 mM NaCl, pH 7.4) for 2 h before measurements. The fluorescent spectra were acquired in the range of 290–450 nm when excited at 280 nm, at a scanning rate 125 nm/min and a bandwidth 5 nm.

Circular Dichroism (CD). Far-UV (180–260 nm) CD spectra were measured on a JASCO J-810 spectropolarimeter using a 1 mm path length quartz cell. BSA (6 μM) was incubated with 0.1–1 mg/mL ZnMgO in HBS buffer, pH 7.4, for 24 h before recording. Spectra were collected at a scanning rate of 100 nm/min, with a bandwidth of 1.0 nm and a resolution of 100 mdeg. Measurements were done at 20°. Each spectrum was an average of eight scans. All spectra were corrected for the contribution of the buffer.

Dynamic Light Scattering. Dynamic light scattering (DLS) measurements were performed on a Zetasizer Nano serie (Malvern, U.K.) using a helium–neon laser wavelength of 633 nm and detection angle of 173°. The scattering intensity data were processed using the instrumental software to obtain the hydrodynamic diameter (R_H) and the size distribution of particles in each sample. The R_H of the particles was estimated from the autocorrelation function, using the Cumulants method. A total of 10 scans with an overall duration of 5 min were obtained for each sample. All measurements were done in HBS buffer, pH 7.4, at 20 °C.

Cell Cultures and Cytotoxicity Tests. Madin-Darby canine kidney (MDCK) cells were used to test ZnMgO cytotoxicity. Cells were purchased from the American Type Culture Collection (Manassas, VA) and grown in MEM medium (minimum essential medium) supplemented with Earle's Salts without L-glutamine (PPA The Cell Culture Company, Austria), completed with 10% heat-inactivated FBS, 2 mM L-glutamine, penicillin (100 units/mL), and streptomycin (0.1 mg/mL), according to the American Type Culture

Collection recommendations. Cells were maintained at 37 °C in a 5% CO₂ incubator. In some tests, cells were washed with FBS-free medium before incubation with nanoparticles.

Cell death was quantified by acridine orange staining followed by flow cytometry analysis (Becton FACSCalibur, Dickinson and Company, USA), as explained elsewhere.⁸ Briefly, the cells were collected, washed in PBS (8 mM Na₂HPO₄, 1.5 mM KH₂PO₄, 150 mM NaCl, 3 mM KCl, pH 7.4), and then resuspended in the cellular medium containing acridine orange (0.1 μg/mL) in the dark. Stained cells were fixed with 3.2% paraformaldehyde in PBS and then collected and resuspended in PBS. Each test was done on 5 × 10⁴ cells.

A cytotoxicity test with the crystal violet staining was done on MDCK cells incubated with ZnMgO nanoparticles overnight. MDCK cellular monolayers were then fixed with 10% formol and subsequently stained with crystal violet for 30 min.

Particles Incubation with Cell Culture Medium and SDS-PAGE Analysis. ZnMgO (1 mg) was incubated with RPMI medium complemented with 10% FBS overnight (total volume, 1 mL). The particle–protein complexes were purified as previously explained.^{27,28} Briefly, samples were centrifuged at 14 000g to pellet particle–protein complexes. The pellets were extensively washed in PBS buffer to remove all nonbound proteins. In the final step pellets were resuspended in the Laemmli buffer and boiled for 5 min at 100 °C to eluted bound proteins from the particles. NuPage BisTris 12% polyacrylamide gels (Invitrogen, France) were used for SDS-PAGE. All experiments were produced at least twice to ensure reproducibility of the particle–protein complex.

RESULTS AND DISCUSSION

ZnMgO in Water: Morphology and Optical Properties.

Prior to the study of ZnMgO under physiological conditions, the water effects on ZnMgO morphology and optical properties were investigated since water represents the major constituent in biological fluids and media. For this purpose, ZnMgO nanoparticles were treated with deionized water for 24 h and subsequently annealed at 1270 K under high vacuum conditions. This thermal treatment provides a completely dehydroxylated and adsorbate free surface of nanoparticles and represents an essential precondition in surface science investigation of highly dispersed metal oxides.³⁰ TEM images of as-synthesized and water-treated ZnMgO nanopowders are compared in Figure 1. As recently reported,⁸ as-synthesized ZnMgO exhibits shapes that are characteristic of both of its pure components, MgO-cubes and ZnO-tetrapods and rods (Figure 1a). In the same work, X-ray diffraction measurements were also conducted on the as-synthesized ZnMgO powder showing the coexistence of both crystal phases, cubic and hexagonal. Thus, it was confirmed that ZnMgO powder represents a two-component system. Such ZnMgO morphology is characteristic for the synthesis route applied, which moreover provides particles with low degree of aggregation³¹ due to the particles generation in the gas-phase in combination with the above-described annealing treatment. Upon water treatment, most MgO cubes undergo corrosion, preferentially at corner and edge sites, which results in the loss of their regular cubic shape and the appearance of octahedral shape, as designated by blue circle in Figure 1b. The observed cubic to octahedral transformation of MgO shape fully agrees with both theoretical calculations^{14,32,33} and experimental evidence reported previously.¹⁵ It was shown that, when immersed in water, MgO cubic crystallites limited by (100) facets first reveal average (110) cuts of the edges. These are followed by (111) cuts, giving the crystallites an octahedral form. As for ZnO-part, the tetrapod- and nanorod-like shapes, which are characteristic for as-synthesized ZnMgO nanopowders (Figure 1a), could not

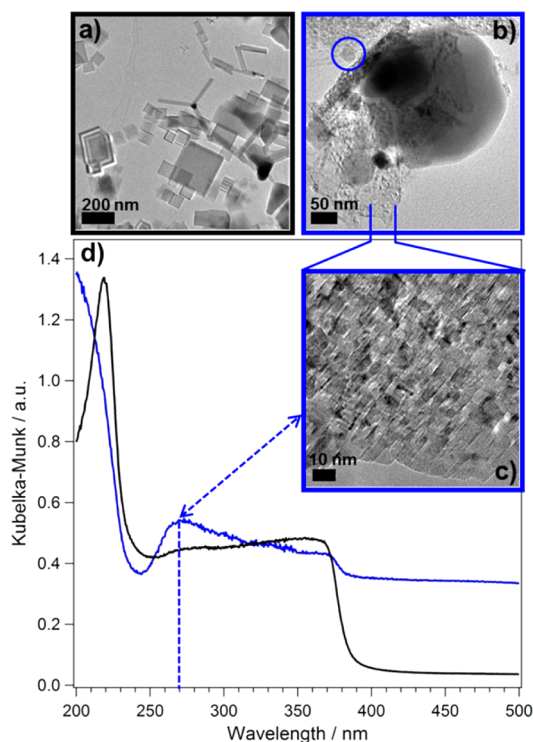


Figure 1. TEM images (a–c) and diffuse reflectance UV/vis spectra (d) of as-synthesized ZnMgO nanopowders (black border and black curve) and water-treated (blue borders and blue curve). Powders were annealed ($T = 1270$ K, $P < 10^{-5}$ mbar) and kept in vacuum ($p < 10^{-5}$ mbar) prior to measurements. The blue circle in (b) surrounds crystallites of octahedral form to point out nonobservable structures in as-synthesized powders. A region with disordered and fragmented structures in (b) was recorded at higher magnification, and is presented in (c) in the close-up view. The blue arrow correlates morphological modifications (fragmented structures) with the corresponding optical feature in the diffuse reflectance UV/vis spectrum.

be detected any longer after the powder was treated with water (Figure 1b). This implies that ZnO nanoparticles partially dissolve in water. In addition, the pH value of ZnMgO water solution was measured to be ~ 9 , indicating the formation OH⁻ ions. As a matter of fact, ZnO is one of the metal oxides most soluble in water and its major cytotoxicological impact is usually correlated with the released Zn²⁺ ions in a given biological environment.^{34–36} Finally, disordered and fragmented structures were also detected in water treated ZnMgO, as presented in a close-up view in Figure 1c. Interestingly, such structures were not reported for water treated pure MgO¹⁵ or pure ZnO.⁶

Morphological changes of nanostructured materials result in the redistribution of specific surface sites and, therefore, can be easily tracked in their optical properties.³⁷ Diffuse reflectance UV/vis spectra obtained on as-synthesized and on water-treated ZnMgO powders are compared in Figure 1d. As expected, the spectrum of as-synthesized ZnMgO nanopowder represents a superimposition of spectra characteristic of pure oxides: two absorption bands, at 222 nm (band I) and 270 nm (band II), that correspond to MgO nanopowders and the absorption edge at about 375 nm which refers to ZnO. The absorption bands I and II were previously attributed to localized electronic transitions occurring at 4-fold and 3-fold coordinated oxygen anions in edges and corners of MgO cubes,

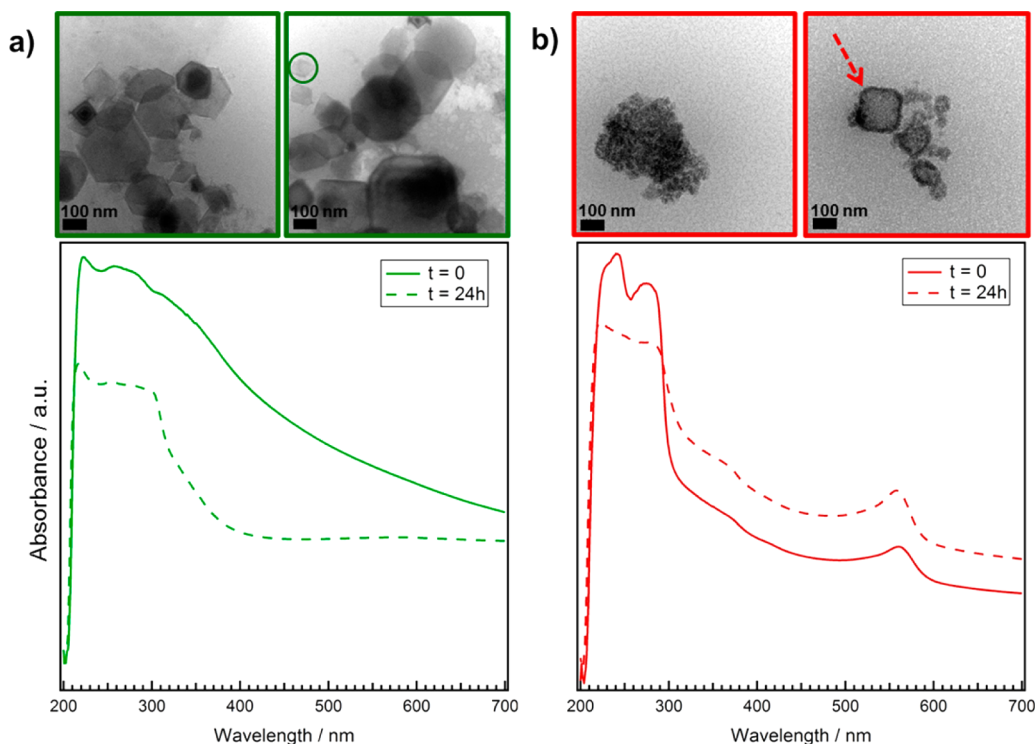


Figure 2. Cryo-TEM images and UV/vis spectra of ZnMgO nanopowder admixed into (a) a LB bacterial medium (green) and (b) a RPMI mammalian cell culture medium supplemented with 10% FBS (red). Nanoparticles were incubated for 24 h within each medium before electron microscopy observations. The green circle indicates cubic to octahedral shape transformation occurred in LB medium. The red arrow indicates a form close to cubic. UV/vis spectra were recorded immediately (solid lines) and after 24 h (dashed lines) that ZnMgO was suspended.

respectively.^{37,38} In as-synthesized ZnMgO powder, the absorption band I shows a relatively high intensity while the absorption band II can only be noticed as an inflection (black curve in Figure 1d). Upon water treatment, an intensity enhancement was measured for the absorption band I. Additionally, it became broader with the maximum shifted below the wavelength accessible in nonevacuated spectrometers ($\lambda > 200$ nm), enabling its complete characterization (blue curve in Figure 1d). However, the observed broadening of the band I suggests that some of MgO edges were affected by water. The water treatment significantly increased the intensity of the absorption band II. Detection of this absorption band was shown to be possible only on MgO nanopowders with high concentration of 3-coordinated oxygen ions in corner position of MgO cubes.³⁷ Therefore, the intensity increase of band II indicates that the erosion of MgO nanocrystals upon water treatment results in formation of corner sites. This finding is consistent with the TEM observation of disordered/fragmented structures in Figure 1c. The blue arrow in Figure 1 associates the morphological modification with its corresponding reflection in the optical spectrum. Although ZnO specific nanorods and tetrapods were not microscopically detected in the water treated ZnMgO, the absorption edge characteristic of pure ZnO (~ 375 nm) was measured as slightly red-shifted (Figure 1d, blue curve). Unlike MgO where electronic transitions are precisely assigned to certain surface sites, optical transitions in ZnO are delocalized within the whole bulk. The absorption intensity was seen to increase in $\lambda > 375$ nm, suggesting that new gap states in ZnO bulk were formed upon water treatment. Interestingly, such enhancement of absorption intensity was not observed for pure ZnO treated with water (Figure S-1, Supporting Information). The results demonstrate

that both the ZnO-specific and the MgO-specific spectroscopic characteristics of nanostructured ZnMgO are affected by water. This supports the microscopic evidence of morphological alternations observed in water treated ZnMgO samples.

ZnMgO Behavior in Biological Media. The behavior of the ZnMgO nanopowder in two biological environments, LB bacteria growth and RPMI mammalian cell culture media, was investigated by cryo-TEM visualization and UV/vis spectroscopy. The measurements were done directly in the solution in order to approach physiological conditions. Cryo-TEM images in Figure 2a (upper panel) reveal that the morphology of ZnMgO suspended in LB bacterial medium for 24 h was altered in a similar way as after water treatment. Indeed, most of MgO crystallites, which initially exhibit an exceptionally regular cubic shape, were transformed into octahedral forms; whereas ZnO nanorods and nanotetrapods, initially present in ZnMgO smoke powders, were not evidenced. However, unlike water treated samples, ZnMgO did not show disordered and fragmented structures in the LB medium. Admixing ZnMgO into the LB medium did not change its physiological pH (pH = 7.4). A recent dissolution kinetics study of nano-ZnO has shown that Zn^{2+} ions are hardly released from the oxide at neutral pH.³⁶ Thus, different pH in water and the LB medium may contribute to diverse structural modifications observed for ZnMgO nanocrystals in two environments.

The UV/vis absorption spectrum of ZnMgO dissolved in LB medium (Figure 2a) shows no optical features specific of ZnMgO nanopowder (Figure 1d). The main contribution to optical absorption of ZnMgO-LB solution originates from molecules present in the LB medium (Figure S-2a, Supporting Information). LB contains many amino acids, especially tryptophan, NaCl (5 g/L), and yeast extract. An intensity loss

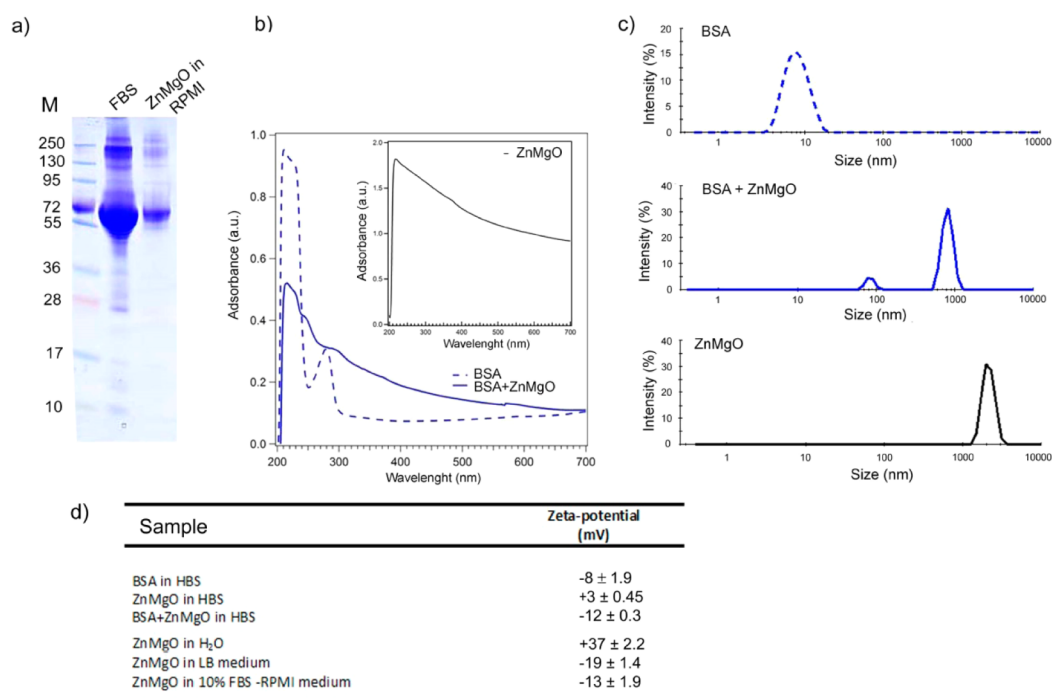


Figure 3. Interaction between ZnMgO nanoparticles and BSA. (a) Illustration of SDS-PAGE gel analysis of ZnMgO-associated proteins from RPMI medium supplemented with 10% FBS. (b) UV/vis spectra of pure BSA (0.4 mg/mL) dissolved in water and after admixing ZnMgO (1 mg/mL). Inset: UV/vis spectrum of ZnMgO in water (1 mg/mL). (c) Size distributions of monomeric BSA, BSA-ZnMgO mixture, and pure ZnMgO nanoparticles in HBS buffer pH 7.4, monitored by DLS. All solutions were incubated for 24 h at room temperature before measurements. (d) Zeta potential of ZnMgO nanoparticles in different media used in this work.

was observed in the spectrum recorded after 24 h compared to spectrum recorded immediately upon adding nanoparticles (Figure 2a). Similarly, an intensity decrease was found in UV/vis spectra of pure components, MgO and ZnO (Figure S-3a, Supporting Information). This intensity loss indicates that the concentration of molecules from medium decreases which may be explained by their binding to nanoparticles. The adsorption of these molecules will affect the reactivity of nanoparticles, since further interactions of nanoparticles will be mediated by the layer formed on their contact surface. Indeed, it was previously reported that the minimal antibacterial inhibitory concentration of nano-ZnO was around two orders of magnitude smaller in pure water than in the bacteria growth medium.³⁹ The authors proposed that molecules from the medium may compete with the bacterial membrane to bind the nanoparticle which, in consequence, decreases the antibacterial efficiency of nano-ZnO.

After being dissolved in the mammalian cell culture RPMI medium complemented with 10% FBS, ZnMgO nanoparticles exhibited disordered and agglomerated structures (Figure 2b, upper panel). ZnO specific nanotetrapods and nanorods disappeared also in this medium, while MgO nanocubes were seen to be strongly damaged and to expose particularly irregular surfaces. However, some forms close to cubic were still recognizable, as highlighted by the red arrow in Figure 2b. The pH value of RPMI medium after admixing ZnMgO remained physiological. This indicates that medium buffer capacity neutralized hydroxide ion release observed in pure water solution. We assume that alternations of nanoparticle morphology in the mammalian cell culture medium comprise (i) crystal fragmentation upon contact with water, (ii) adsorption of molecules from the medium, and (iii) agglomeration of the formed entities. Agglomeration of

nanoparticles due to the high ionic strength of the biological environment is one of the main effects that accompany interaction between nanoparticles and biological molecules.²³ Nanoparticles are reported to be rapidly coated by various biomolecules, especially proteins, when dissolved in biological fluids and media.^{16,40} Indeed, cryo-TEM images in Figure 2b show shapeless structures which can be assumed to be serum proteins forming corona over ZnMgO.

Similarly to the case of LB, also in this medium UV/vis spectroscopy did not reveal optical transitions that are typical of a ZnMgO nanopowder (Figure 2b), but mainly due to molecules of which the medium consists (Figure S-2b, Supporting Information). After 24 h incubation of ZnMgO in completed-RPMI medium, absorption intensities decreased for the part of the spectrum between 200 and 300 nm while a quite visible intensity enhancement was observed in the range of higher wavelengths (Figure 2b). This intensity increase indicates the occurrence of new electronic transitions, which strongly suggests the formation of complexes between ZnMgO and molecules from the medium. Interestingly, such intensity increase was not observed in absorption spectra of pure MgO and ZnO (Figure S-3b, Supporting Information).

To verify ZnMgO–protein complex formation, a SDS-PAGE analysis was applied on ZnMgO nanoparticles incubated with the RPMI medium supplemented with 10% FBS. After 24 h of incubation, the solution was centrifuged to collect protein–nanoparticle complexes and pellets were subjected to gel migration. The obtained protein profile in Figure 3a indicates that the most abundant serum proteins, especially BSA with a molecular weight of about 66 kDa, were adsorbed on ZnMgO nanopowders.

ZnMgO–BSA Interaction. BSA is reported to be rapidly associated with a range of nanoparticles of various composition

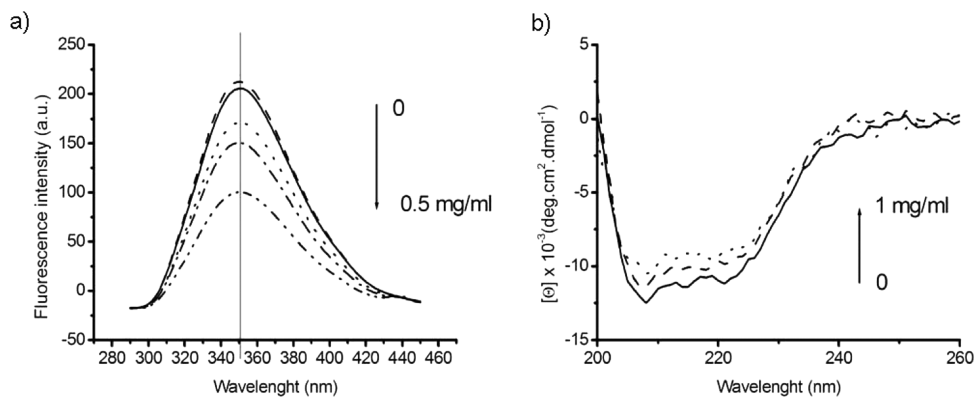


Figure 4. (a) Fluorescence spectra of BSA (0.4 mg/mL) alone and in the presence of different ZnMgO concentrations (0.01–0.5 mg/mL). Measurements were done in HBS buffer solution, pH 7.4. Note the decrease in protein fluorescence with increasing nanoparticle concentration. (b) Circular dichroism spectra of BSA in the absence (solid line) and in the presence of 0.1 mg/mL ZnMgO (3-point segment) and 1 mg/mL ZnMgO (2-point segment).

and size.^{41–43} By far, the most abundant protein in blood serum, albumin, is also the most abundant protein in the FBS supplemented RPMI medium (0.4 mg/mL according to manufacturers' specification). The UV/vis absorption spectrum of pure BSA and BSA incubated with ZnMgO nanoparticles for 24 h is presented in Figure 3b. Pure BSA gives two characteristic absorption peaks: an intense one between 190 and 210 nm which is due to the transition in polypeptide backbone structure and the less intensive one at 280 nm attributed to absorption of aromatic amino acids.⁴⁴ Admixing ZnMgO to BSA clearly decreased the intensity of the absorption band centered at ~ 220 nm, while intensity enhancement was seen in the full range of $\lambda > 260$ nm. This latter absorption was observed in the UV/vis spectrum recorded on water dissolved ZnMgO (inset in Figure 3b) and thus can be assigned to absorption properties of ZnMgO nanoparticles in an aqueous solution. Significant differences between UV/vis spectra of pure BSA and BSA–ZnMgO system, both quantitative and qualitative, support the finding that BSA binds to ZnMgO nanocrystals.

Binding of BSA to ZnMgO was expected since one of the biological roles of this protein is to nonspecifically bind and carry various molecules in blood. The interaction BSA–ZnMgO may be governed by electrostatic attractions between nanoparticles surface charges and those of the protein amino acids. In addition, surrounding water molecules can facilitate these bindings as it was predicted from computer simulations of protein adsorption to the MgO surface.⁴⁵ The interaction between nanoparticles, water, and proteins from the medium may in turn influence the formation of agglomerates in solutions. Thus, DLS measurements were performed to find the mean hydrodynamic radius (R_H) of the BSA admixed to ZnMgO. As shown in Figure 3c, the R_H of monomeric BSA in the buffer solution was about 8 nm which was expected for a globular protein of 66 kDa. Upon addition of ZnMgO, new peaks were observed, showing species with apparent higher sizes of $R_H = 85$ and 820 nm (Figure 3c). Interestingly, ZnMgO nanoparticles alone gave large microscale clusters with $R_H > 2100$ nm. DLS data suggest that BSA stabilized dispersion of ZnMgO particles in the aqueous solution. A similar stabilizing effect of BSA on nanoparticle aggregation was previously reported for ZnO in water.²¹

To verify whether BSA–ZnMgO interaction can be governed by electrostatic interaction, zeta potential measurements were

performed in HBS buffer. The zeta potential is a key indicator of the stability of colloidal dispersions and represents the overall charge a particle acquires in a solution. As shown in Figure 3d, BSA had a negative surface charge while ZnMgO had a positive one. The ZnMgO–BSA complex had a negative surface charge with higher magnitude of zeta potential when compared to those obtained on two systems separately (Figure 3d). This suggests the formation of a BSA–ZnMgO complex and confirms the proposed implication of electrostatic interactions in their binding. For comparison, the zeta potential of ZnMgO was determined in water, LB medium, and RPMI medium (Figure 3d). Relatively high values of zeta potential were measured for ZnMgO in water and LB medium (37 and -19 mV, respectively,) indicating that nanoparticles resist aggregation in these solutions as observed in TEM images in Figures 1b,c and 2a. In contrast, the zeta potential of ZnMgO dissolved in RPMI supplemented with serum proteins was relatively small (-13 mV). This indicates that nanoparticles tend to coagulate or flocculate in complete RPMI medium, which is in agreement with our microscopic measurements in Figure 2b.

Certain proteins change their conformation and denature after being adsorbed on nanoparticles.^{26,28,46} By fluorescence spectroscopy, we investigated whether the conformation of BSA is modified upon its adsorption on ZnMgO. Figure 4a shows the fluorescent emission spectra of BSA alone and when incubated with ZnMgO in the concentration range from 0 to 0.5 mg/mL. The main contribution to the fluorescence of BSA is by tryptophan (Trp) which is very sensitive to the polarity of its environment.⁴⁷ In hydrophilic solutions, as when Trp is in contact with surrounding water molecules, its emission maximum is at about 355 nm. In a hydrophobic environment, as happened when Trp is not flexible but within the polypeptide ordered secondary structures, this maximum is blue-shifted.⁴⁷ As shown in Figure 4a upon admixing ZnMgO to the BSA solution, the maximum of Trp fluorescence did not shift but the intensity of the emission gradually decreased. The observed fluorescence quenching can result from the protein secondary structure rearrangement or by the formation of a nonfluorescent ground state complex between Trp and ZnMgO. To verify whether BSA undergoes secondary structure alternations upon binding to ZnMgO, CD spectra in the far-UV region were recorded (Figure 4b). Two negative bands at 208 and 222 nm characteristic for α -helix structure of BSA are

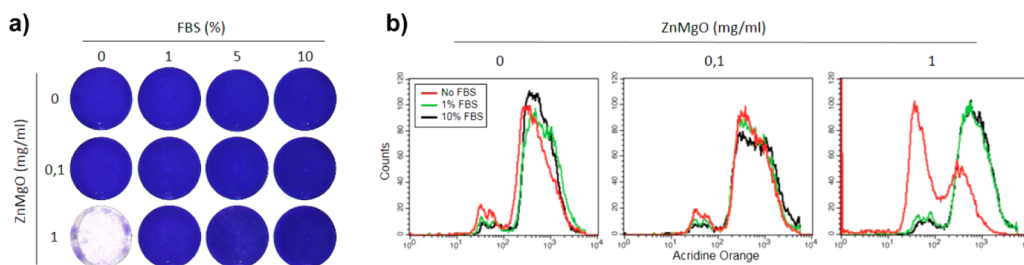


Figure 5. ZnMgO effects on cell viability. MDCK cells were incubated with ZnMgO nanopowders in a cell culture medium containing various concentrations of serum proteins for 24 h. MDCK cell monolayers were then (a) stained with crystal violet or (b) subjected to the flow cytometry analysis after acridine orange staining. Note that cell death was detected only in FBS-free medium for high nanoparticle concentration (1 mg/mL).

clearly visible in the spectra of BSA alone. Both of the negative minimums decreased in intensity by adding 0.1 and 1 mg/mL of nano-ZnMgO, whereas the peak shapes and positions were almost unaffected. This implies that, upon binding to ZnMgO, BSA preserves its initial structure but the protein α -helical content slightly decreases. A constant position of the Trp fluorescent maximum and a relatively small CD spectra alternation in Figure 4 suggest that the interactions between ZnMgO nanoparticles and BSA are weak.

ZnMgO Toxicity toward Mammalian Cells. Finally, the toxicity of ZnMgO nanoparticles toward mammalian cells was investigated as a function of surrounding medium. The MDCK cells were incubated for 24 h with ZnMgO nanoparticles (0.1 and 1 mg/mL concentrations) in a medium containing various concentrations of serum proteins. MDCK cells were chosen for their robust growth in a serum-free medium. After incubation with nanoparticles, MDCK cell monolayers were stained with crystal violet to visualize the cytotoxic effect (Figure 5a). ZnMgO at 0.1 mg/mL showed no toxicity regardless of the serum protein concentration in the medium. However, complete cell death was observed for 1 mg/mL ZnMgO nanoparticles in FBS-free medium (Figure 5a). The cytotoxicity of ZnMgO was further evaluated using acridine orange fluorescent staining to quantify damaged cells. MDCK cells incubated with ZnMgO were stained with acridine orange, and the fluorescence was measured in a flow cytometer (Figure 5b). The acridine orange derived fluorescence intensity of untreated MDCK cells and cells treated with 0.1 mg/mL ZnMgO was unaffected regardless of the medium composition. In contrast, at 1 mg/mL in the absence of FBS, ZnMgO nanoparticles killed about 85% of the treated MDCK cells. These findings strongly suggest that serum proteins have a protective role against ZnMgO nanoparticle toxicity. Interestingly, 1% FBS was sufficient to fully protect MDCK cell from ZnMgO toxicity (Figure 5). Probably, even at low serum concentration, the ZnMgO surface is fully covered by serum proteins. A similar effect was previously observed during the formation of the protein corona on nanoparticles at different plasma concentrations.⁴⁸

Since albumin was detected as a major component in ZnMgO protein corona, we also tested the role of albumin in preventing cytotoxicity. For this purpose, we replaced serum by with BSA at 0.4 mg/mL (equivalent BSA concentration in the medium). When MDCK cells grown in BSA complemented medium were incubated with ZnMgO nanoparticles, less than 7% cells survived, compared to 98% in medium containing FBS (Figure S-4, Supporting Information). This suggests only a weak BSA protecting effect and indicates that BSA alone cannot prevent ZnMgO cytotoxicity. Probably other, less abundant

serum proteins exert the protective role against ZnMgO cytotoxicity. Likewise, the dynamic formation of protein corona was shown to be a collective process that resulted in a creation of a stable heterogeneous layer at the nanoparticles surface.⁴⁸ Additional studies are, however, necessary to characterize other serum proteins binding to ZnMgO nanoparticles.

We previously have shown that 1 mg/mL ZnMgO was safe for human HeLa cells in a cellular medium containing 10% FBS.⁸ This is in accordance with the ZnMgO biocompatibility observed here for MDCK cells in serum-containing medium. However, in bacterial growth LB medium, 1 mg/mL ZnMgO completely irradiated Gram-positive but not Gram-negative bacteria.⁸ It appears, thus, that ZnMgO cellular toxicity depends on the cell type and can be modulated by the composition of the surrounding medium.

CONCLUSIONS

ZnMgO nanoparticles were observed to undergo morphological changes when admixed to aqueous solutions. In a complex cell culture medium, the majority of nanoparticles become shapeless, agglomerated, and coated with surrounding proteins. Consequently, mammalian cells encounter morphologically modified ZnMgO nanoparticles whose contact surfaces are altered by the proteins in the corona. We conclude that the corona governs the cytotoxicity of the nanoparticles since the cellular damages caused by ZnMgO may be obstructed by proteins from surrounding media. We envisage that our overall results may shed light on the factors to be considered before applying metal oxide nanoparticles as new therapeutics.

ASSOCIATED CONTENT

Supporting Information

Diffuse reflectance UV/vis spectra of as-synthesized and water treated ZnO nanoparticles; UV/vis spectra of pure LB and RPMI medium; UV/vis spectra of pure MgO and ZnO dissolved in LB and RPMI medium; MDCK cells incubated with a ZnMgO nanopowder in the cell culture medium complemented with either FBS (10%) or BSA (0.4 mg/mL) for 24 h. This material is available free of charge via the Internet at <http://pubs.acs.org>.

AUTHOR INFORMATION

Corresponding Authors

*E-mail: jasmina.vidic@jouy.inra.fr. Tel: + 33134652623. Fax: +33134652621.

*E-mail: slavica.stankic@insp.jussieu.fr. Tel: + 33144274650. Fax: + 33144273982.

Notes

The authors declare no competing financial interest.

ACKNOWLEDGMENTS

We thank Charles-Adrien Richard (INRA, Jouy en Josas) for his help with size-exchange chromatography, David Portehault (LCMCP, Paris) for helping with zeta potential measurements, and Prof. Philippe Depondt (INSP, UPMC, Paris) for comments and proofreading.

REFERENCES

- (1) Henrich, V. E.; Cox, P. A. *The Surface Chemistry of Metal Oxides*; Cambridge University Press: Cambridge, UK, 1994.
- (2) Rodríguez, J. A.; Fernández-García, M. E. *Synthesis, Properties and Applications of Oxide Nanoparticles*; Wiley: Hoboken, NJ, 2007.
- (3) Chertok, B.; Moffat, B. A.; David, A. E.; Yu, F.; Bergemann, C.; Ross, B. D.; Yang, V. C. Iron oxide nanoparticles as a drug delivery vehicle for MRI monitored magnetic targeting of brain tumors. *Biomaterials* **2008**, *29*, 487–496.
- (4) Kievit, F. M.; Zhang, M. Surface engineering of iron oxide nanoparticles for targeted cancer therapy. *Acc. Chem. Res.* **2011**, *44*, 853–862.
- (5) Tassa, C.; Shaw, S. Y.; Weissleder, R. Dextran-coated iron oxide nanoparticles: A versatile platform for targeted molecular imaging, molecular diagnostics, and therapy. *Acc. Chem. Res.* **2011**, *44*, 842–852.
- (6) Brayner, R.; Dahoumane, S. A.; Yepremian, C.; Djediat, C.; Meyer, M.; Coute, A.; Fievet, F. ZnO nanoparticles: synthesis, characterization, and ecotoxicological studies. *Langmuir* **2010**, *26*, 6522–6528.
- (7) Hajipour, M. J.; Fromm, K. M.; Ashkarran, A. A.; Jimenez de Aberasturi, D.; de Larramendi, I. R.; Rojo, T.; Serpooshan, V.; Parak, W. J.; Mahmoudi, M. Antibacterial properties of nanoparticles. *Trends Biotechnol.* **2012**, *30*, 499–511.
- (8) Vidic, J.; Stankic, S.; Haque, F.; Ciric, D.; Le Goffic, R.; Vidy, A.; Jupille, J.; Delmas, B. Selective antibacterial effects of mixed ZnMgO nanoparticles. *J. Nanopart. Res.* **2013**, *15*, 1595.
- (9) Applerot, G.; Lellouche, J.; Lipovsky, A.; Nitzan, Y.; Lubart, R.; Gedanken, A.; Banin, E. Understanding the antibacterial mechanism of CuO nanoparticles: Revealing the route of induced oxidative stress. *Small* **2012**, *8*, 3326–3337.
- (10) Arbab, A. S.; Wilson, L. B.; Ashari, P.; Jordan, E. K.; Lewis, B. K.; Frank, J. A. A model of lysosomal metabolism of dextran coated superparamagnetic iron oxide (SPIO) nanoparticles: implications for cellular magnetic resonance imaging. *NMR Biomed.* **2005**, *18*, 383–389.
- (11) Taylor, E.; Webster, T. J. Reducing infections through nanotechnology and nanoparticles. *Int. J. Nanomed.* **2011**, *6*, 1463–1473.
- (12) Shi, J.; Karlsson, H. L.; Johansson, K.; Gogvadze, V.; Xiao, L.; Li, J.; Burks, T.; Garcia-Bennett, A.; Uheida, A.; Muhammed, M.; Mathur, S.; Morgenstern, R.; Kagan, V. E.; Fadeel, B. Microsomal glutathione transferase 1 protects against toxicity induced by silica nanoparticles but not by zinc oxide nanoparticles. *ACS Nano* **2012**, *6*, 1925–1938.
- (13) Turney, T. W.; Duriska, M. B.; Jayaratne, V.; Elbaz, A.; O'Keefe, S. J.; Hastings, A. S.; Piva, T. J.; Wright, P. F.; Feltis, B. N. Formation of zinc-containing nanoparticles from Zn²⁺ ions in cell culture media: implications for the nanotoxicology of ZnO. *Chem. Res. Toxicol.* **2012**, *25*, 2057–2066.
- (14) Geysmans, P.; Finocchi, F.; Goniakowski, J.; Hacquart, R.; Jupille, J. Combination of (100), (110) and (111) facets in MgO crystals shapes from dry to wet environment. *Phys. Chem. Chem. Phys.* **2009**, *11*, 2228–2233.
- (15) Hacquart, R.; Jupille, J. Hydrated MgO smoke crystals from cubes to octahedra. *Chem. Phys. Lett.* **2007**, *439*, 91–94.
- (16) Gao, Y.; Elder, S. A. TEM study of TiO₂ nanocrystals with different particle size and shape. *Mater. Lett.* **2000**, *44*, 228–232.
- (17) Misra, S. K.; Dybowska, A.; Berhanu, D.; Luoma, S. N.; Valsami-Jones, E. The complexity of nanoparticle dissolution and its importance in nanotoxicological studies. *Sci. Total Environ.* **2012**, *438*, 225–232.
- (18) Hu, X.; Masuda, Y.; Ohji, T.; Kato, K. Dissolution–recrystallization induced hierarchical structure in ZnO: Bunched roselle and core–shell-like particles. *Cryst. Growth Des.* **2010**, *10*, 626–631.
- (19) Bian, S. W.; Mudunkotuwa, I. A.; Rupasinghe, T.; Grassian, V. H. Aggregation and dissolution of 4 nm ZnO nanoparticles in aqueous environments: influence of pH, ionic strength, size, and adsorption of humic acid. *Langmuir* **2011**, *27*, 6059–6068.
- (20) Lynch, I.; Dawson, K. A. Protein–nanoparticle interactions. *Nano Today* **2008**, *3*, 40–47.
- (21) Churchman, A. H.; Wallace, R.; Milne, S. J.; Brown, A. P.; Brydson, R.; Beales, P. A. Serum albumin enhances the membrane activity of ZnO nanoparticles. *Chem. Commun.* **2013**, *49*, 4172–4174.
- (22) Murdock, R. C.; Braydich-Stolle, L.; Schrand, A. M.; Schlager, J. J.; Hussain, S. M. Characterization of nanomaterial dispersion in solution prior to in vitro exposure using dynamic light scattering technique. *Toxicol. Sci.* **2008**, *101*, 239–253.
- (23) Prasad, R. Y.; Wallace, K.; Daniel, K. M.; Tennant, A. H.; Zucker, R. M.; Strickland, J.; Dreher, K.; Kligerman, A. D.; Blackman, C. F.; Demarini, D. M. Effect of treatment media on the agglomeration of titanium dioxide nanoparticles: impact on genotoxicity, cellular interaction, and cell cycle. *ACS Nano* **2013**, *7*, 1929–1942.
- (24) Hsiao, I. L.; Huang, Y. J. Effects of serum on cytotoxicity of nano- and micro-sized ZnO particles. *J. Nanopart. Res.* **2013**, *15*, 1829.
- (25) Barran-Berdon, A. L.; Pozzi, D.; Caracciolo, G.; Capriotti, A. L.; Caruso, G.; Cavaliere, C.; Riccioli, A.; Palchetti, S.; Lagana, A. Time evolution of nanoparticle-protein corona in human plasma: Relevance for targeted drug delivery. *Langmuir* **2013**, *29*, 6485–6494.
- (26) Cedervall, T.; Lynch, I.; Lindman, S.; Berggard, T.; Thulin, E.; Nilsson, H.; Dawson, K. A.; Linse, S. Understanding the nanoparticle-protein corona using methods to quantify exchange rates and affinities of proteins for nanoparticles. *Proc. Natl. Acad. Sci. U.S.A.* **2007**, *104*, 2050–2055.
- (27) Lundqvist, M.; Stigler, J.; Elia, G.; Lynch, I.; Cedervall, T.; Dawson, K. A. Nanoparticle size and surface properties determine the protein corona with possible implications for biological impacts. *Proc. Natl. Acad. Sci. U.S.A.* **2008**, *105*, 14265–14270.
- (28) Maiorano, G.; Sabella, S.; Sorce, B.; Brunetti, V.; Malvindi, M. A.; Cingolani, R.; Pompa, P. P. Effects of cell culture media on the dynamic formation of protein–nanoparticle complexes and influence on the cellular response. *ACS Nano* **2010**, *4*, 7481–7491.
- (29) Simon-Vazquez, R.; Lozano-Fernandez, T.; Peleteiro-Olmedo, M.; Gonzalez-Fernandez, A. Conformational changes in human plasma proteins induced by metal oxide nanoparticles. *Colloids Surf., B* **2014**, *113*, 198–206.
- (30) Muller, M.; Stankic, S.; Diwald, O.; Knozinger, E.; Sushko, P. V.; Trevisanutto, P. E.; Shluger, A. L. Effect of protons on the optical properties of oxide nanostructures. *J. Am. Chem. Soc.* **2007**, *129*, 12491–12496.
- (31) Stankic, S.; Cottura, M.; Demaille, D.; Noguera, C.; Jupille, J. Nucleation and growth concepts applied to the formation of a stoichiometric compound in a gas phase: The case of MgO smoke. *J. Cryst. Growth* **2011**, *329*, 52–56.
- (32) Pojani, A.; Finocchi, F.; Goniakowski, J.; Noguera, C. A theoretical study of the stability and electronic structure of the polar {111} face of MgO. *Surf. Sci.* **1997**, *387*, 354–370.
- (33) Refson, K.; Wogelius, R. A.; Fraser, D. G.; Payne, M. C.; Lee, M. H.; Milman, V. Water chemisorption and reconstruction of the MgO surface. *Phys. Rev. B* **1997**, *52*, 10823–10826.
- (34) Auffan, M.; Rose, J.; Wiesner, M. R.; Bottero, J. Y. Chemical stability of metallic nanoparticles: A parameter controlling their potential cellular toxicity in vitro. *Environ. Pollut.* **2009**, *157*, 1127–1133.
- (35) Zhang, H.; Ji, Z.; Xia, T.; Meng, H.; Low-Kam, C.; Liu, R.; Pokhrel, S.; Lin, S.; Wang, X.; Liao, Y. P.; Wang, M.; Li, L.; Rallo, R.

Damoiseaux, R.; Telesca, D.; Madler, L.; Cohen, Y.; Zink, J. I.; Nel, A. E. Use of metal oxide nanoparticle band gap to develop a predictive paradigm for oxidative stress and acute pulmonary inflammation. *ACS Nano* **2012**, *6*, 4349–4368.

(36) Chusueia, C. C.; Wub, C.-H.; Mallavarapua, S.; Houc, F. Y. S.; Hsud, C.-M.; Winiarze, J. G.; Aronstamb, R. S.; Huangb, Y.-W. Cytotoxicity in the age of nano: The role of fourth period transition metal oxide nanoparticle physicochemical properties. *Chem.-Biol. Interact.* **2013**, *206*, 319–326.

(37) Stankic, S.; Muller, M.; Diwald, O.; Sterrer, M.; Knozinger, E.; Bernardi, J. Size-dependent optical properties of MgO nanocubes. *Angew. Chem., Int. Ed. Engl.* **2005**, *44*, 4917–4920.

(38) Hacquart, R.; Krafft, J.-M.; Costentin, G.; Jupille, J. Evidence for emission and transfer of energy from excited edge sites of MgO smokes by photoluminescence experiments. *Surf. Sci.* **2005**, *595*, 172–182.

(39) Apperlot, G.; Lipovsky, A.; Dror, R.; Perkas, N.; Nitzan, Y.; Lubart, R.; Gedanken, A. Enhanced antibacterial activity of nanocrystalline ZnO due to increased ROS-mediated cell injury. *Adv. Funct. Mater.* **2009**, *19*, 842–852.

(40) Yang, S. T.; Liu, Y.; Wang, Y. W.; Cao, A. Biosafety and bioapplication of nanomaterials by designing protein–nanoparticle interactions. *Small* **2013**, *9*, 1635–1653.

(41) Allemann, E.; Gravel, P.; Leroux, J. C.; Balant, L.; Gurny, R. Kinetics of blood component adsorption on poly(D,L-lactic acid) nanoparticles: Evidence of complement C3 component involvement. *J. Biomed. Mater. Res.* **1997**, *37*, 229–234.

(42) Lundqvist, M.; Stigler, J.; Cedervall, T.; Berggard, T.; Flanagan, M. B.; Lynch, I.; Elia, G.; Dawson, K. The evolution of the protein corona around nanoparticles: A test study. *ACS Nano* **2011**, *5*, 7503–7509.

(43) Mahmoudi, M.; Lynch, I.; Ejtehadi, M. R.; Monopoli, M. P.; Bombelli, F. B.; Laurent, S. Protein–nanoparticle interactions: Opportunities and challenges. *Chem. Rev.* **2011**, *111*, 5610–5637.

(44) Layne, E. Spectrophotometric and turbidimetric methods for measuring proteins. *Methods Enzymol.* **1957**, *3*, 447–455.

(45) Cormack, A. N.; Lewis, R. J.; Goldstein, A. H. Computer simulation of protein adsorption to a material surface in aqueous solution: biomaterials modeling of a ternary system. *J. Phys. Chem. B* **2004**, *108*, 20408–20418.

(46) Clift, M. J.; Bhattacharjee, S.; Brown, D. M.; Stone, V. The effects of serum on the toxicity of manufactured nanoparticles. *Toxicol. Lett.* **2010**, *198*, 358–365.

(47) Li, Q.; Chevalier, C.; Henry, C.; Richard, C. A.; Moudjou, M.; Vidic, J. Shadoo binds lipid membranes and undergoes aggregation and fibrillization. *Biochem. Biophys. Res. Commun.* **2013**, *438*, 519–525.

(48) Monopoli, M. P.; Walczyk, D.; Campbell, A.; Elia, G.; Lynch, I.; Bombelli, F. B.; Dawson, K. A. Physical-chemical aspects of protein corona: relevance to in vitro and in vivo biological impacts of nanoparticles. *J. Am. Chem. Soc.* **2011**, *133*, 2525–2534.